Early Diagenetic Silicon Cycling in a Changing Arctic Ocean

James Patrick Joseph Ward

Supervised by Dr Katharine R. Hendry (University of Bristol), Dr Sandra Arndt (Université Libre de Bruxelles), Dr Christian März (University of Leeds)

May 17, 2022

A dissertation submitted to the University of Bristol in accordance with the requirements for award of the degree of Doctor of Philosophy in the Faculty of Science, School of Earth Sciences.

Word count: 62,750

Early Diagenetic Silicon Cycling in a Changing Arctic Ocean

James Ward

Abstract

The Arctic Ocean silicon (Si) cycle is under considerable pressure from natural and anthropogenic forcings. For example, the Barents Sea has experienced a 20-30% reduction in the concentration of dissolved silicic acid (DSi) in inflow waters since 1990, in addition to the most rapid rates of warming and sea-ice retreat in the Arctic, largely driven by a northward expansion of Atlantic Water. These factors have contributed to a shift in phytoplankton spring bloom community compositions towards temperate flagellate species, as conditions become less favourable for Si-based diatoms. The Arctic seafloor represents an important biogeochemical reactor, supplying a similar flux of DSi to the ocean as pan-Arctic rivers. However, current understanding of the regional Si budget is partially limited by a lack of data in this area, leading to an isotopic imbalance. It is crucial to resolve this discrepancy, in order to better anticipate the implications of further perturbations.

This thesis presents a dataset of stable Si isotopes (δ^{30}Si) measured in the sediment pore water DSi pool and reactive solid phases, coupled to steady state and transient reaction-transport models, used to gain a comprehensive understanding of the current state of early diagenetic Si cycling in the Barents Sea. This research uncovers a strong mineralogical control on the benthic Si cycle, with DSi derived from the dissolution of lithogenic silicate minerals contributing an estimated 13-98% of the pore water DSi pool alongside biogenic silica (BSi), as well as a coupling of the Si cycle with iron-redox cycling. Furthermore, pore water DSi δ^{30}Si and cation concentrations reveal a reprecipitation of dissolving DSi (3-37%) as authigenic clays (AuSi). By using a reaction-transport model to quantify these processes, this thesis presents an isotopically balanced budget for the Barents Sea, pointing to AuSi burial as a possible missing sink of isotopically light Si in the pan-Arctic Ocean budget. Transient reaction-transport modelling also reveals that seasonal variability in BSi deposition is reflected within the seafloor through tight benthic-pelagic coupling. The dissolution of fresh phytodetritus is estimated to contribute approximately one-third of the total annual DSi benthic flux, which will be subject to change as pelagic phytoplankton community compositions further adjust to changing conditions.

Declaration

I declare that the work in this dissertation was carried out in accordance with the requirements of the University's Regulations and Code of Practice for Research Degree Programmes and that it has not been submitted for any other academic award. Except where indicated by specific reference in the text, the work is the candidate's own work. Work done in collaboration with, or with the assistance of, others, is indicated as such. Any views expressed in the dissertation are those of the author.

Signed _____ **Date** _____

Acknowledgements

My first and greatest thanks go to my primary supervisor, Kate Hendry. I can't thank Kate enough for her unwavering support, encouragement and advice from day one. Kate's guiding hand helped me navigate the choppy waters of a pandemic, take on a once in a lifetime opportunity to join a research cruise in the fjords of Greenland, attend multiple amazing conferences and work alongside my PhD in an internship that has led directly to my current role. I will be forever grateful for her supervision.

Secondly, a huge thank you to my supporting supervisors, Sandra Arndt and Christian März. I am grateful to Sandra for her instruction and patience in teaching me how to use BRNS and to her family for their hospitality on many research trips to Brussels. Sandra and Christian have both provided me with invaluable advice and facilitated discussions that developed and improved my thoughts and ideas.

I owe a debt of gratitude to my journal article co-authors and the wider Changing Arctic Ocean Seafloor (ChAOS) team. Thank you also to all the amazing people of the University of Bristol Earth Sciences department, in particular the Bristol Isotope Group (BIG) and Bristol Oceans Past and Present (BOPP) group. I am thankful to Hong Chin Ng, Jade Hatton, Helena Pryer, Lucie Cassarino, Holly Welsby, Chris Coath, Adam McAleer and Felipe Sales de Freitas for their support and instruction on all things isotopes and reaction-transport modelling.

I would also like to thank the UK Natural Environment Research Council (NERC), who funded this research through the Changing Arctic Ocean programme (grant no. NE/P005942/1), as well as the Geochemistry Group who financially supported my travel to the 2019 Goldschmidt Conference in Barcelona.

To all my friends, including the South Wolds boys, Bellevue boys, Locusts, Holi-Baes, G47, Bristol undergrads and the rest of my PhD intake. Thank you for all the good times, I am lucky to be surrounded by such great people. Finally, a special dedication to my family. Without their support, I would not be in a position to begin a PhD, much less complete one. Dad, thanks for always motivating me to 'save the planet' and for being first in line to 'check my spelling'. Mum, thanks for continually tackling the imposters syndrome, reminding me to get a wriggle on and for teaching me that nothing is worth doing unless it's done right. Thanks to my step-parents and four step-siblings for their love and support, in particular to Jayne and Keith for proof reading my personal statement

and for the GCSE maths lessons all those years ago, both of which got me through the door at Bristol! To Jules' family, thank you for your support and for taking me in as one of the 'blow-ins'. To Jules (and Nemo), I can't quite put the words together to express my gratitude for your love, unshakeable support, and for being there whenever the doubts crept in. And a final tribute to my grandparents, especially Harold Joseph Ward, who personified the Commando spirit. Completing this PhD has been a long road, but he would've been reminding me along the way to have patience and not spoil this ship for a ha'porth of tar. This thesis is dedicated to him.

Contents

List of Figures

List of Tables

Acronym Glossary

Acronym	Definition
ChAOS	Changing Arctic Ocean Seafloor project
CAO	Central Arctic Ocean
AW	Atlantic Water
ArW	Arctic Water
BSW	Barents Sea Water
NCCW	Norwegian Coastal Current Water
MW	Meltwater
BSB	Barents Sea Basin
BSO	Barents Sea Opening
BSX	Barents Sea Exit
PF	Oceanic Polar Front
MIZ	Marginal ice zone
TOC	Total organic carbon
TSOC	Total Sediment Oxygen Consumption
HNLC	High Nutrient Low Chlorophyll
SWI	Sediment-water interface
PW	Pore water
CT	Core-top water
SW	Seawater
BSi	Biogenic silica
DSi	Dissolved silicic acid
LSi	Lithogenic silica
AuSi	Authigenic clay
FeSi	Si adsorbed to metal oxides
Si-Alk	Mild alkaline leachable Si
Si-HCl	Mild acid leachable Si
Si-NaOH	Harsh alkaline leachable Si
cmbsf	cm below seafloor

mbss	m below sea surface
BRNS	Biogeochemical Reaction Network Simulator
RTM	Reaction-transport model
SSB	Standard-sample bracketing
ICP-OES	Inductively coupled plasma - optical emission spectrometry
MC-ICP-MS	Multicollector inductively coupled plasma mass spectrometry
SEM	Scanning Electron Microscopy
EDX	Energy Dispersive X-Ray Analysis
MRP	Mass resolving power
LOD	Limit of detection
LOQ	Limit of quantification
SEM	Standard error of the mean
(R)SD (σ)	(Relative) Standard deviation
(N)RMSE	(Normalised) Root Mean Square Error
ANOVA	Analysis of variance

Chapter 1

Introduction

Some text and figure captions of this chapter are included in an article accepted for publication at Geochimica et Cosmochimica Acta ('Stable Silicon Isotopes Uncover a Mineralogical Control on the Benthic Silicon Cycle in the Arctic Barents Sea', doi.org/10.1016/j.gca.2022.05.005) and another in revision at Biogeosciences ('Benthic Silicon Cycling in the Arctic Barents Sea: a Reaction-Transport Model Study', doi.org/10.5194/bg-2022-51), both by Ward et al.

1.1 The marine silicon cycle

Silicon (Si) is the second most abundant element on Earth, accounting for ∼27% of the lithosphere by mass (Sutton et al., 2018; Tréguer et al., 1995). The reaction between silicate minerals of the lithosphere and CO_2-enriched meteoric water (forming carbonic acid) regulates Earth's climate over geological timescales (Walker et al., 1981) (equation 1.1). This chemical weathering process liberates dissolved silicic acid (hereby referred to as DSi), which results in 6.2±1.8 Tmol Si yr^{-1} carried to the ocean by rivers. The riverine DSi flux represents the biggest single source to the global ocean Si budget (55% of the total), with submarine groundwater and dissolution of silicate minerals representing the second and third most significant Si inputs (2.3±1.1 and 1.9±0.7 Tmol Si yr^{-1} respectively) (Tréguer et al., 2021).

$$CaSiO_3 + 2\,CO_2 + H_2O \longrightarrow Ca^{++} + 2\,HCO_3^- + SiO_2 \tag{1.1}$$

Silica is a key nutrient in the marine environment for Si-based primary producers such as diatoms, silicoflaggelates and radiolarians, as well as larger organisms like sponges. The presence of DSi is therefore fundamental to the functioning of marine ecosystems. Diatoms, a major group of phytoplankton, build skeletons or cell walls (i.e. frustules) of biogenic silica (or 'opal', hereby referred to as BSi) through the uptake of DSi present in seawater, 95% of which is in the form of orthosilicic acid (H_4SiO_4) (Tréguer et al.,

1995). BSi is dense and acts as a ballast, which can efficiently ferry organic carbon from the surface ocean to depth, coupling the benthic and pelagic realms. It is estimated that approximately half of the export flux of organic carbon from the surface ocean occurs due to the sinking of diatomaceous aggregates (Nelson et al., 1995; Rickert, 2000; Tréguer et al., 2018). Therefore, Si is an element intrinsically connected to the biological pump through silicifying organisms, thus it is thought of as a co-regulating factor of atmospheric CO_2 concentrations (Loucaides et al., 2010; März et al., 2015).

The importance of BSi with respect to the carbon cycle is not only associated to carbon export from the photic zone. The two main materials that allow for vertical transport of organic carbon in the oceanic water column are calcium carbonate ($CaCO_3$) and BSi, with a minor role played by lithogenic material (Honjo et al., 2008). According to Honjo et al. (2008), just 20% of the ocean can be defined by a BSi:$CaCO_3$ ballast material ratio of >1. These regions, termed 'the silica ocean' (subarctic North Pacific and the Southern Ocean) are considered more beneficial for the earth's atmospheric CO_2 balance than the rest of the ocean (the 'carbonate ocean'). $CaCO_3$ precipitated by coccolithophores and foraminifera removes alkalinity from the surface ocean, which results in a net flux of CO_2 into the atmosphere, partially offsetting that which is taken up through the organic carbon biological pump.

The so-called 'silica' and 'carbonate' oceans have characteristically distinct BSi preservation regimes. In diatomaceous sediments concentrated beneath silica oceans, BSi accumulation represents 15-25% of that which is produced in the surface ocean. However, the majority of BSi production (75-90%) occurs in the rest of the ocean (80% by area), where very little of the surface BSi production is preserved (Rickert, 2000). The weighted average of these regimes results in a global mean BSi burial of 3% in ocean sediments (as a proportion of BSi produced in the surface ocean), half of which occurs in the Southern Ocean (Rickert, 2000). This divergence in preservation regimes is thought to be associated with the production of thicker-walled diatom frustules in high nutrient low chlorophyll (HNLC) regions of the Southern Ocean and subarctic Pacific Ocean (Hutchins and Bruland, 1998; Rickert, 2000).

1.1.1 Early diagenetic cycling of silicon

Seawater is undersaturated with respect to BSi, therefore as silicifiers sink to the seafloor on average >95% are remineralised back to DSi (Tréguer and De La Rocha, 2013). Crucially, one-third of this remineralisation occurs at or near the sediment-water interface (SWI) during early diagenesis, creating strong DSi concentration gradients between the upper pore and bottom waters, driving return fluxes back to the water column. Ng et al. (2020) also presented evidence for the dissolution of sponge-derived BSi in marine sediments, which has previously been thought to be resistant to dissolution (Maldonado et al., 2005, 2019). This benthic-pelagic coupling is critical for the maintenance of subsequent

phytoplankton blooms in shallow settings and where benthic-derived DSi can be admixed into the photic zone by entrainment in water masses (Loucaides et al., 2012a). In addition to the dissolution of BSi in marine sediments, DSi can be liberated by dissolution of primary and secondary lithogenic silicate minerals (LSi) (Geilert et al., 2020a; Jeandel and Oelkers, 2015). This is especially the case in the North Atlantic and Central Arctic Ocean, where bottom water concentrations are typically below the solubility of many silicate minerals (März et al., 2015; Tréguer et al., 1995). Recent work has demonstrated the importance of this process in beach and ocean margin settings, representing a new source of DSi to the global ocean (Ehlert et al., 2016b; Fabre et al., 2019). Indeed, it is estimated that the dissolution of river-derived LSi particulates and basaltic glass in seawater represents the third largest input of DSi to the global ocean (1.9±0.7 Tmol Si yr^{-1}) (Tréguer et al., 2021).

The build-up of sediment pore water DSi in marine sediments through BSi and LSi dissolution is curbed by uptake during the precipitation of authigenic clay minerals (AuSi) (Ehlert et al., 2016a; Geilert et al., 2020a; Loucaides et al., 2010; Michalopoulos and Aller, 1995; Sutton et al., 2018). Thus, the magnitude of the DSi benthic return flux across the sediment-water interface (SWI), largely depends on the balance between the aforementioned processes. The precipitation of AuSi can operate either through the dissolution of LSi and subsequent coprecipitation of DSi with dissolved aluminium (Al), or alternatively through a 'typical' reverse weathering pathway, whereby BSi reacts with Al/iron (Fe)-rich (oxyhydr)oxides and major cations present in pore waters (Ehlert et al. (2016a) and references therein). This reaction pathway forms potassium (K), magnesium (Mg) and Fe enriched aluminosilicates described as 'green clay', or glauconite, which is a common BSi weathering product (Aller, 2014; Ehlert et al., 2016a; Loucaides et al., 2010) (equation 1.2). It is generally accepted that AuSi precipitation requires a source of both Al and Si, however typically a build-up of Al in solution is not often observed, thus it is thought that AuSi precipitation instead proceeds through a near-instantaneous dissolution-precipitation reaction (Michalopoulos and Aller, 1995). This near-instantaneous process is thought to account for the fact that Al is considered immobile under low temperature weathering regimes (Michalopoulos and Aller, 1995), given this would allow for a lack of observable change in either dissolved or bulk solid phase Al.

AuSi precipitation has been evidenced in previous studies through sediment pore water Si isotopic compositions ($\delta^{30}Si_{DSi-PW}$) (see section 1.3) and concentration profiles of cations (Cassarino et al., 2020; Ehlert et al., 2016a; Geilert et al., 2020a, 2014; Georg et al., 2009; Ng et al., 2020; Rude and Aller, 1994). Although, a lack of cation uptake does not necessarily preclude the presence of AuSi precipitation, as the dissolution of LSi can interfere with the concentration of these key elements. Ng et al. (2020) hypothesised that a lack of concurrent uptake of pore water K^+ with Mg^{2+}, was due to precipitation of a clay phase with a stoichiometry that differed from that expected of a typical reverse weathering

pathway. Indeed, Odin and Matter (1981) studied the neoformation of glauconite and found that the initial, poorly crystalline phase is relatively K depleted, which increases as the clay matures (Michalopoulos and Aller, 1995).

There is no doubt that the early diagenetic solid phase conversion of BSi to AuSi enhances the preservation potential of BSi and can act as a sink for many elements and alkalinity in seawater (Aller, 2014; Dunlea et al., 2017). However, the degree to which reverse weathering provides a sink of Si to the global ocean is debated. Prior to the last decade, reverse weathering was poorly understood. AuSi precipitation at the SWI was previously thought to be a slow reaction, occurring over 10-100 kyr, that represented a minor sink term in the ocean Si budget ($\sim$0.5 Tmol Si yr^{-1}) (DeMaster, 1981). Instead, more recent evidence suggests that reverse weathering proceeds on the order of months and is active ubiquitously across the global ocean seafloor, representing a sink of 4.7$\pm$2.3 Tmol Si yr^{-1}, potentially accounting for the additional Si sink required to close the global ocean Si budget (Cassarino et al., 2020; Ehlert et al., 2016a; Geilert et al., 2020a; März et al., 2015; Michalopoulos and Aller, 1995; Ng et al., 2020; Pickering et al., 2020; Rahman et al., 2016, 2017; Tréguer et al., 2021). However, DeMaster (2019) argue that while AuSi precipitation is occurring in deltaic sediments, the burial of reactive diatomaceous BSi alone can account for complete removal of all DSi delivered to the oceans. It has therefore been suggested that AuSi precipitation does not constitute a significant Si sink, as this precipitation reaction represents an early diagenetic solid phase conversion of BSi, rather than a sink per se (DeMaster, 2019; Frings et al., 2016). It is likely that whether AuSi can be considered a true sink of ocean Si or not, depends entirely on the depositional context. If AuSi traps sediment pore water DSi within the surface sediment, where macrofaunal mixing (through bioirrigation and bioturbation) and concentration gradients would typically allow for exchange with overlying bottom waters, reverse weathering would be considered a sink.

$$\begin{aligned} \mathit{Reactive}\mathrm{SiO_2} + \mathrm{Al(OH)_4}^- + (\mathrm{Fe}^{2+3+}, \mathrm{Mg}^{2+}, \mathrm{K}^+, \mathrm{Li}^+) + \mathrm{F}^- + \mathrm{HCO_3}^- \\ \longrightarrow \mathit{AuSi} + \mathrm{CO_2} + \mathrm{H_2O} \end{aligned} \tag{1.2}$$

1.2 The Arctic Ocean Si budget

DSi is a key nutrient in high latitude marine ecosystems. Primary production in the Arctic Ocean is characterised by a diatom-dominated spring bloom event, which despite lasting just a few weeks, accounts for a significant portion of average annual primary production (Krause et al., 2019). As a result, the spring bloom (and thus the activity of diatoms) partially governs the capacity for the Arctic Ocean to uptake and sequester atmospheric CO_2, and is highly influential for regional food web dynamics. However, pre-bloom DSi stocks have waned over recent decades, leading to a reduction in the maximum diatom biomass production and likely exacerbating the kinetic limitation of growth by ambient

DSi concentrations observed across the Arctic Ocean (Giesbrecht and Varela, 2021; Krause et al., 2018, 2019). It has been hypothesised that the observed westward redistribution of certain fish species across the subarctic Atlantic region is a consequence of the reduction in late-winter DSi concentrations (Krause et al., 2019; Pacariz et al., 2016). It is therefore crucial to fully understand the current distribution of DSi across the Arctic Ocean, to better anticipate the impacts of any climate-induced perturbations that may exacerbate these factors.

Previous Si budgets for the Arctic Ocean suggest that DSi inputs and outputs are in balance, or that the Arctic Ocean represents a slight net exporter of DSi (1.08 and 1.57 Tmol Si yr^{-1} respectively) (Anderson et al., 1983; Jones and Coote, 1980; Torres-Valdés et al., 2013). The two main inputs of DSi to the region are through the Bering Strait from the North Pacific Ocean and across the Barents Sea from the North Atlantic Ocean. The predominant water mass outflows are through the Davis and Fram Straits into the North Atlantic.

The Arctic Ocean seafloor represents an important biogeochemical reactor, with previous work estimating that the contribution of the benthic recycling flux to the overlying water column (0.35-0.42 Tmol Si yr^{-1}) is equal to the total input from all pan-Arctic rivers (0.41 Tmol Si yr^{-1}) (Holmes et al., 2012; März et al., 2015). For reference, the supply of DSi to the ocean from rivers outside of the Arctic is 5.4 Tmol Si yr^{-1} (Tréguer et al., 2021). There is also some suggestion that benthic nutrient fluxes could be influential distally from their source. Jones and Anderson (1986) hypothesised that nutrient maxima observed across the Arctic Ocean at the halocline are fed by dense waters formed through brine rejection during sea ice formation on continental shelf seas, which flow downslope, entraining regenerated nutrients exuding from shelf sediments (Hulth et al., 1996; Jones and Anderson, 1986). Despite these observations, until recently the recycling and burial of BSi from the seafloor has been overlooked in Si budgets of the Arctic Ocean (Brzezinski et al., 2021; März et al., 2015). In part, this omission was due to an underestimation of the magnitude of the benthic DSi flux. However, the solid phase origins of the sediment pore water DSi pool that emanates from Arctic Ocean sediments within the benthic flux have not been fully elucidated, with the assumption made that the benthic flux is fuelled entirely through BSi dissolution (März et al., 2015). Unlike other global oceans, the North Atlantic and Arctic Ocean sediment pore waters generally remain undersaturated with respect to many primary and secondary silicate minerals, which could enable their dissolution. Dissolution of such material would represent a source of 'new' Si to the budget, rather than representing an internal recycling process.

The exclusion of seafloor processes from Arctic Ocean Si budgets was not only due to a misunderstanding of the benthic DSi flux, but also a result of the underestimation of the BSi burial rate. Previous estimates of Arctic Ocean sedimentation rates (a few mm kyr^{-1}) (Backman et al., 2004), coupled with generally low BSi contents (<5 wt%) (März

et al., 2015), implied a negligible rate of BSi burial. Following a revision of the age models, sediment accumulation rates have since been reviewed (10-30 mm kyr^{-1}), leading to the incorporation of BSi burial in the most recent iteration of the Arctic Ocean Si budget (Brzezinski et al., 2021).

Brzezinski et al. (2021) used the Si budget of Torres-Valdés et al. (2013) to carry out an assessment of the Arctic Ocean Si isotopic budget. The Si isotopic dataset for the Arctic Ocean has grown significantly over the last decade, however the majority of existing data is focussed on water column DSi (Brzezinski et al., 2021; Giesbrecht and Varela, 2021; Liguori et al., 2020; Varela et al., 2016), with some complimentary measurements of sediment trap BSi, as well as the composition of the two largest fluvial contributors of freshwater to the Arctic Ocean (the Yenisey and Lena Rivers) (Mavromatis et al., 2016; Pokrovsky et al., 2013; Sun et al., 2018). Brzezinski et al. (2021) hypothesise that the cycling of Si within the Arctic Ocean has little net impact on the isotope budget, indicated by the similarity of the Si isotopic composition of water mass in and outflows (see section 5.4.5). However, current understanding of the Arctic Ocean Si cycle is not sufficient to close the isotope budget, which is missing a permanent sink of isotopically light Si, required to compensate for the isotopically light input from Arctic rivers (Brzezinski et al., 2021).

Significant data gaps currently exist, which must be filled if we are to close the Arctic Ocean Si budget. Specifically, there is a notable paucity of data pertaining to the isotopic composition of BSi within the seafloor, as well as other reactive pools of solid phase sedimentary Si. This is consistent with a compilation of benthic nutrient fluxes, which highlighted a scarcity of DSi benthic flux data on Arctic shelf seas of the eastern hemisphere (Fig. 1.1) (Bourgeois et al., 2017). Furthermore, while measurements exist for the Si isotopic composition of the Davis and Bering Straits inflows, there is a lack of information from other major gateways, including the Fram Strait and Barents Sea.

1.2.1 The Barents Sea Si cycle

The Barents Sea Si cycle is in a state of flux, driven by a combination of natural and anthropogenically-driven perturbations. The Barents Sea shelf lies on the doorstep of the Arctic Ocean, representing one of just two gateways through which Atlantic Water can enter. The Atlantic Water mass dominates the central and southern regions of the Barents Sea, while colder Arctic Waters prevail in the north of the region (Fig. 1.2). These two main water masses are delineated by a key hydrographic feature, the oceanic polar front, a site of intense physical mixing and interleaving of water masses. Since 1980, the volumetric inflow rate of Atlantic Water across the Barents Sea opening onto the shelf has doubled and the temperature has increased by 1.4^{o}C, in a process termed 'Atlantification' (Årthun et al., 2012; Oziel et al., 2016; Polyakov et al., 2017). The increased heat content of the basin has contributed to the rapid rate of winter sea ice loss observed across the shelf (Årthun et al., 2012). The Barents Sea has seen a reduction in the winter

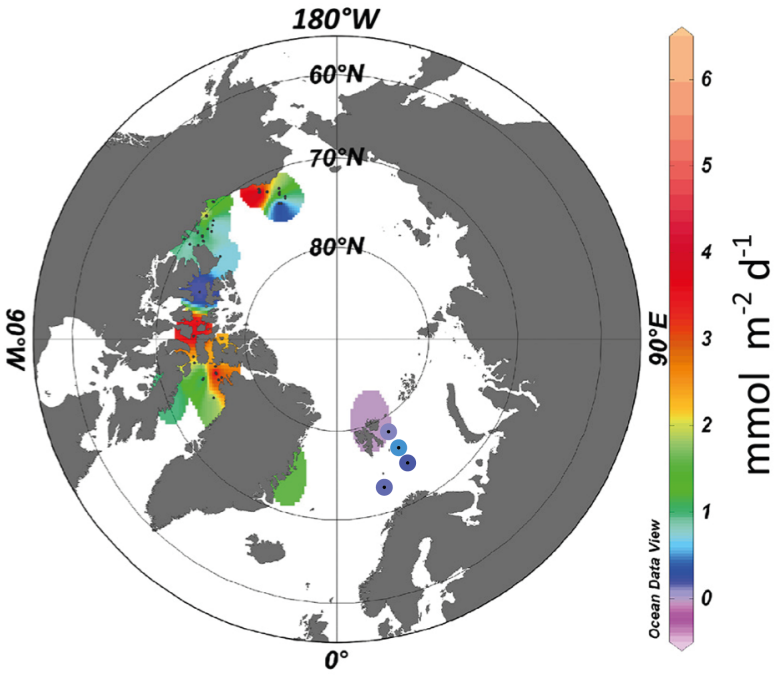

Figure 1.1: Pan-Arctic benthic DSi flux compilation modified from Bourgeois et al. (2017) (see references therein) to include data from this study (stations B03, B13, B14, B15). DSi fluxes (n=61) in mmol m^{-2} day^{-1}. Note the density of data on shelves of the western Arctic relative to the scarcity of data from the European and Siberian Arctic Ocean sectors.

maximum sea ice extent (March) of 54% since 1979, representing the highest rate of the pan-Arctic region (11,300 km^{-2} yr^{-1}) (Bailey et al., 2021; Lind et al., 2018; Stroeve and Notz, 2018). The northern Barents Sea region is soon expected to complete its transition from a highly stratified Arctic Water regime to a warm, sea ice free, well-mixed Atlantic Water-dominated regime (Lind et al., 2018).

Despite the fact that the North Atlantic and european sector of the Arctic Ocean are defined as part of the 'carbonate ocean' (Honjo et al., 2008), diatoms currently dominate the community compositions of the Barents Sea and wider Arctic Ocean phytoplankton spring blooms. The spring bloom forms in April/early May as a combination of solar radiation and sea ice meltwater stratify the nutrient-rich photic zone (Wassmann et al., 1999). The spring bloom is a cornerstone event, making up a significant proportion of annual primary productivity across the region, especially in seasonally ice covered areas (Krause et al., 2018). Estimates suggest that the spring bloom contributes approximately half of net annual primary production in the Barents Sea (Dalpadado et al., 2014). However, the northward-advancing oceanic polar front caused by expansion of the Atlantic Water realm, is leading to an invasion of temperate phytoplankton species in the previously Arctic-Water dominated areas (Neukermans et al., 2018; Orkney et al., 2020). Between 2002-2018, an increasing contribution of prymnesiophytes (*Phaeocystis pouchetii* and *Emiliania huxleyi*) to Barents Sea phytoplankton blooms have been observed, in favour of diatom growth

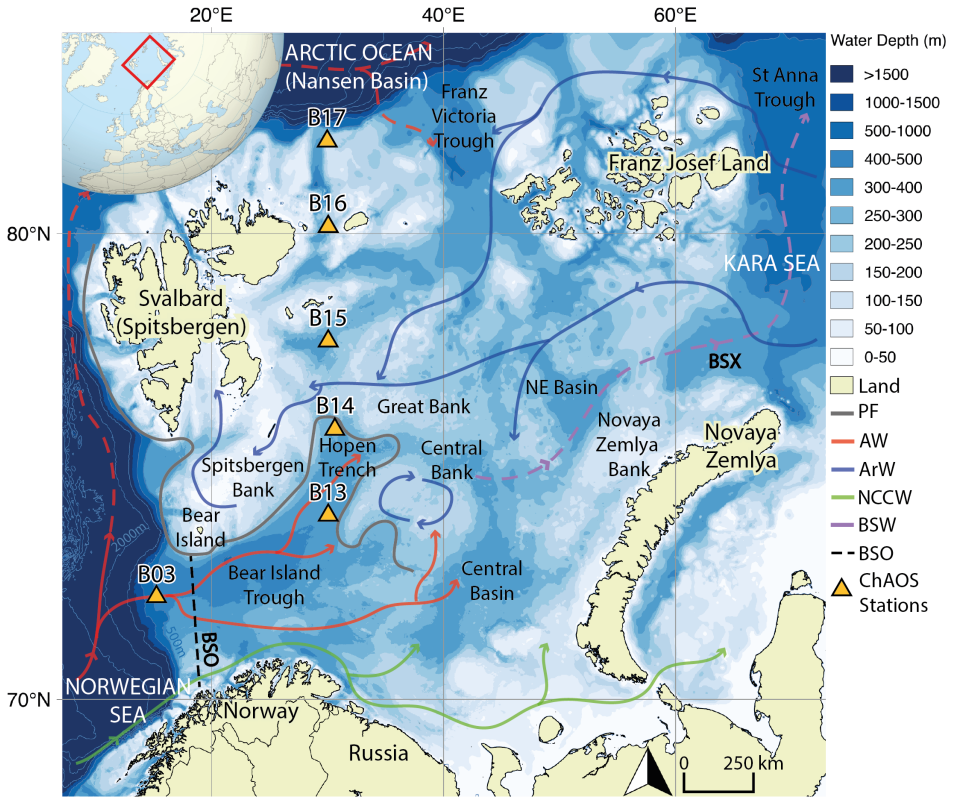

Figure 1.2: Map of ChAOS sampling stations and schematic of water mass circulation in the Barents Sea (PF- Polar Front (oceanic), AW- Atlantic Water, ArW- Arctic Water, NCCW- Norwegian Coastal Current Water, BSW- Barents Sea Water, BSO- Barents Sea Opening, BSX- Barents Sea Exit. Dotted current paths represent subducted water masses (Lien et al., 2013)). The Barents Sea has a mean water depth of 230 m and is the largest of seven shelf seas encircling the Arctic Ocean, covering 1.4×10^6 km^2 (Sakshaug, 1997). NCCW and warm AW flow northwards through the BSO, while colder, relatively nutrient poor ArW flows southwards (Årthun et al., 2012; Oziel et al., 2016). The PF delineates the northern, ArW sector which is seasonally ice-covered (August-September minima, March-April maxima) and the AW dominated region to the south, which is kept perennially ice-free by the warmth of the AW. The bathymetry of the Barents Sea is characterised by the juxtaposition of deep troughs and shallow banks, which topographically constrain the PF in the western shelf, rendering it's position relatively stable (Oziel et al., 2016). This is in contrast to the eastern branch of the PF, which presents with significant positional variability on seasonal and interannual timescales (Smedsrud et al., 2013). The mixing of water masses, coupled with brine rejection from sea ice formation on the shallow banks forms denser BSW, which cascades to greater depths in a northeasterly direction, draining into the Arctic Ocean through the BSX (Smedsrud et al., 2013). BSW is thought to be critical for ventilation of the deep Arctic Ocean and for regional atmospheric CO_2 sequestration (Oziel et al., 2016; Smedsrud et al., 2013). Bathymetry data is from the GEBCO 2014 dataset (Jakobsson et al., 2012).

(Neukermans et al., 2018; Orkney et al., 2020). In addition, Lomas et al. (2019) demonstrated that diatoms grown in cold, polar temperatures have a higher Si density than warmer water species. These temperate species are forecast to become the resident bloom formers of the european sector of the Arctic Ocean due to Atlantification (Neukermans et al., 2018).

Furthermore, since 1990, the concentration of DSi in Atlantic inflow waters has been in decline (∼20%) and at a much faster rate than nitrates (Rey, 2012), consistent with a wider trend observed across the North Atlantic Ocean over the last 30 years (Hátún et al., 2017). Krause et al. (2018) recently uncovered the kinetic limitation of diatom growth around Svalbard and in the central Barents Sea by ambient DSi. Krause et al. (2018) note that the diatom species assemblage around Svalbard was less well adapted for growth at low DSi concentrations (<2 μM) compared to species of the North Atlantic Subtropical Gyre. The phenomena observed by Rey (2012) and Hátún et al. (2017) is resulting in a reduction of pre-bloom DSi stocks, which will most likely have negative implications for the spatial and temporal coverage of diatom blooms. Therefore, this process represents a compounding factor to the water-mass driven shift in primary producers, generating even less favourable conditions for diatom-growth.

The implications of these shifts in phytoplankton community compositions could also be significant for the wider Barents Sea ecosystem, including higher trophic levels. These consequences are thus far unquantified, which will likely impact marine mammals and commercial fishing (Lind et al., 2018; Rey, 2012). The major fisheries of the region are currently reliant upon the seasonal production of copepod zooplankton stocks, which are in turn tightly coupled to the diatom spring bloom (Rey, 2012). Furthermore, Faust et al. (2020) hypothesise that the Barents Sea seafloor represents an important sink of organic carbon, which is sensitive to shifts in vertical organic carbon deposition fluxes. Recent long and short-term sediment trap observations from north and west of Svalbard have illustrated the importance of diatom growth on the export of carbon. Dybwad et al. (2021) and Fadeev et al. (2021) revealed a two-fold higher organic carbon export underneath diatom-dominated blooms formed in seasonally ice covered zones, compared with that measured in sinking *P. pouchetii* aggregates in ice-free areas. Collected diatomaceous aggregates were twice as large and found to sink two-times faster than the ice-free region aggregates (Fadeev et al., 2021). Furthermore, meter-long filaments of the sympagic (ice-associated) diatom species *Melosira Arctica*, have been found anchored to sea-ice north of Franz Josef Land (Boetius et al., 2013). Crucially, these filaments are not consumed as food in the pelagic water column, thus they are able to sink rapidly to the seafloor and contributed >85% of organic carbon export at the sampling stations in 2012 (Boetius et al., 2013). Similar filaments have previously been found lying on the seafloor of the Barents Sea (Wassmann et al., 2006a). A shift in phytoplankton species composition and the knock-on effects on carbon export to the deep ocean, could therefore have significant implications

for the efficacy of the Barents Sea benthos as a store of organic carbon, not only on the cycling of Si.

1.3 Silicon isotope geochemistry

Stable Si isotopes have been used to reconstruct Si weathering regimes, as paleoproxies of primary productivity, to estimate rates of organic carbon export from the surface ocean, identify sources and sinks of Si and to trace water mass mixing (Brzezinski et al., 2021; de Souza et al., 2012; Frings et al., 2016; Hendry and Brzezinski, 2014; Opfergelt and Delmelle, 2012; Sutton et al., 2018; Trower and Fischer, 2019). Early diagenetic processes pertaining to Si can leave a perceptible imprint on the isotopic composition of the DSi pool by changing the relative abundance (i.e. a fractionation) of the three stable isotopes of Si (^{28}Si, ^{29}Si, ^{30}Si) between multiple components of the system. Stable Si isotopic compositions (δ^{30}Si) are reported in δ notation in units of per mille (‰, International Union of Pure and Applied Chemistry (IUPAC)) (equation 1.3), which represents a deviation of the ^{30}Si/^{28}Si ratio of the sample relative to the international Si standard NBS28. Si isotopic fractionation on earth's surface is mass-dependent and can be described by two mechanisms. Equilibrium fraction refers to isotopic exchange driven by differences in mass, between two components in chemical equilibrium. The fractionation factor ($^{30}\varepsilon$) in this scenario can be calculated using equation 1.4. Kinetic fractionation represents a mass-dependent fractionation of isotopes in a system that is out of chemical and isotopic equilibrium, whereby reaction rates in both directions are not identical and could be unidirectional if the products are isolated (Young et al., 2002). $^{30}\varepsilon$ in a kinetic reaction is calculated using equation 1.5, where ^{L}k and ^{H}k represent the lighter and heavier isotope-specific reaction rate constants.

$$\delta^{n}Si = \left(\frac{(^{n}Si/^{28}Si)_{sample}}{(^{n}Si/^{28}Si)_{standard}} - 1 \right) \times 1000 \tag{1.3}$$

$$\alpha_{A-B} = \frac{(^{n}Si/^{28}Si)_{A}}{(^{n}Si/^{28}Si)_{B}} \tag{1.4}$$

$$\alpha_{L-H} = \frac{^{L}k}{^{H}k} \tag{1.5}$$

$$^{n}\varepsilon_{A-B} = \Delta^{n}Si_{A-B} = \delta^{n}Si_{A} - \delta^{n}Si_{B} = 1000 \ln \alpha_{A-B} \tag{1.6}$$

1.3.1 Silicon isotopes in the natural environment

Isotopic fractionation effects provide a powerful tool with which to trace the biogeochemical cycling of Si within the benthos. In this thesis I employ this tool to map Barents Sea

benthic Si cycling through measurement of both the sediment pore water dissolved and solid phases.

The degree of stable Si isotope fractionation at high temperatures is limited to 0.2 to 0.5‰, equivalent to the range of δ^{30}Si values measured in igneous rocks (-0.5, -0.35 and ∼0‰ for the bulk silicate earth, mantle and felsic crust respectively) (Ding et al., 1996; Savage et al., 2010, 2012). However, this tool is particularly effective for low-temperature reactions, as earth surface processes are able to fractionate Si isotopes to a wide range of δ^{30}Si value, from -6 to +6‰ (Chemtob et al. (2015); Wang et al. (2019) and references therein).

Isotopic fractionation during the uptake of DSi for diatom growth is thought to average -1.1‰, depleting the residual DSi pool of the lighter isotope (De La Rocha et al., 1997), initially assumed to be independent of species and temperature (Reynolds et al., 2006). However, studies since have demonstrated that this process is potentially highly species dependent, with $^{30}\varepsilon$ ranging from -0.4 to -2.2‰ across temperate and polar species (Sun et al., 2014; Sutton et al., 2013). δ^{30}Si values measured in deep and surface seawater DSi range from +0.5 to +3.5‰, averaging ∼+1.5‰, with a significantly reduced range in the deep ocean (Sun et al. (2014); Sutton et al. (2018) and references therein) (Fig. 1.3). Corresponding δ^{30}Si values in diatom-derived BSi range from -0.7 to +3.5‰ (Sun et al. (2014); Sutton et al. (2018); Varela et al. (2016) and references therein). Additional forms of BSi include radiolaria and sponge-derived opal. The degree of isotopic fractionation during uptake of DSi by radiolaria is similar to modern diatoms, with $^{30}\varepsilon$ ranging from -0.05 to -1.2‰, corresponding to δ^{30}Si values of +0.54 to +1.75‰ (Doering et al., 2021). Sponge spicules on the other hand, present with the largest range in δ^{30}Si values of oceanic BSi, ranging from -5.7 to +0.9‰ (averaging -2.1‰) (Sutton et al. (2018) and references therein), with apparent $^{30}\varepsilon$ of -6.7 to -1.5‰ (Cassarino et al., 2018; De la Rocha, 2003; Hendry et al., 2010; Hendry and Robinson, 2012). The typical inverse relationship between water column depth profiles of DSi concentration and δ^{30}Si is driven by the growth of silicifiers (Cassarino, 2018). Lower DSi concentrations are generally found in the surface ocean due to uptake in the photic zone, which increases with depth as BSi remineralises. Similarly, isotopically heavier compositions of DSi are generally observed in the surface ocean due to the preferential biotic uptake of ^{28}Si, which then tends to decrease with water depth (Cassarino (2018); Liguori et al. (2020); Varela et al. (2016) and references therein).

The change in δ^{30}Si of the BSi phase and DSi pool as it is consumed can be described by two models. The first is a Rayleigh-style (closed) system, the second is a steady-state (open) system, both of which take into account the fraction of DSi utilised from the initially available DSi pool (Fig. 1.4). In the former, there is no additional supply of nutrients, thus fractionation proceeds under a Rayleigh-type distillation regime. Whereas, under the latter conditions, a state of dyanmic equilibrium is achieved, whereby there is a continuous supply of fresh DSi to the system. Here there is a balance between the supply

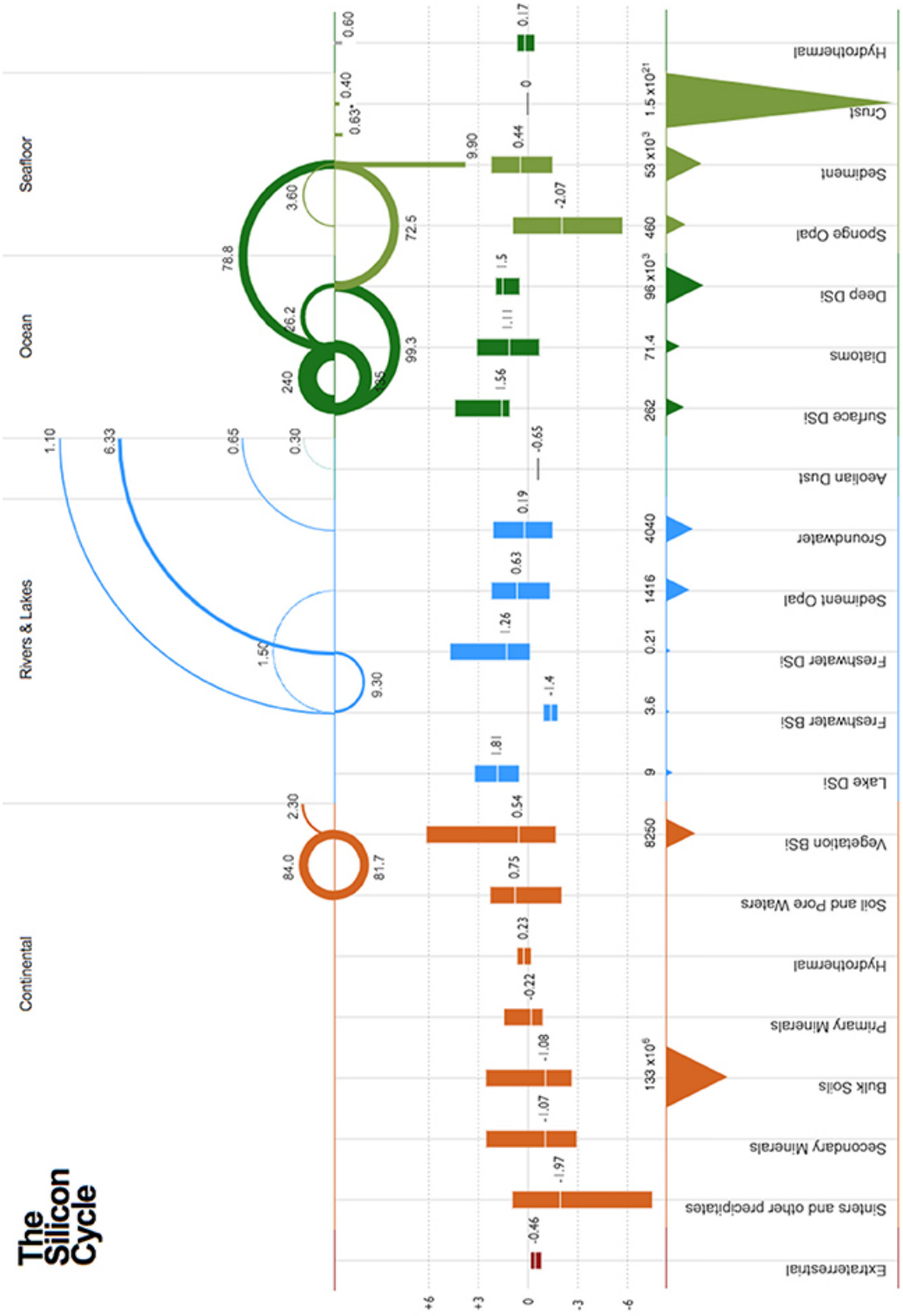

Figure 1.3: Global Si cycle schematic from (Sutton et al., 2018). Illustrates the transfer of Si between reservoirs,the compositional range of analysed media (references therein) and reservoir sizes. Fluxes given in 10^{12} *mol* yr^{-1}*;* $Tmol^{-1}$ yr^{-1}.

of DSi (input) and the output (the residual DSi and forming BSi). Reynolds et al. (2006) determined that DSi uptake during diatom growth in highly stratified surface waters of the subpolar North Pacific represents an in-situ example of a closed system. In contrast, Reynolds et al. (2006) found that the same process in the North Pacific subtropical gyre was best represented by an open system fractionation model, due to vertical water column mixing and lateral transport of DSi through strong surface currents. However, it is unlikely that in-situ conditions ever reflect ideal examples of one of the two endmember conceptual models of isotopic fractionation.

Closed system:

$$\delta^{30}Si_{DSi-obs} = \delta^{30}Si_{DSi-init} + {}^{30}\varepsilon \cdot ln(f) \tag{1.7}$$

$$\delta^{30}Si_{BSi-inst} = \delta^{30}Si_{DSi-obs} + {}^{30}\varepsilon \tag{1.8}$$

$$\delta^{30}Si_{BSi-acc} = \delta^{30}Si_{DSi-init} - {}^{30}\varepsilon \cdot \frac{(fln(f))}{(1-f)} \tag{1.9}$$

Open system:

$$\delta^{30}Si_{DSi-obs} = \delta^{30}Si_{DSi-init} - {}^{30}\varepsilon \cdot (1-f) \tag{1.10}$$

$$\delta^{30}Si_{BSi} = \delta^{30}Si_{DSi-init} + {}^{30}\varepsilon \cdot f = \delta^{30}Si_{DSi-obs} + {}^{30}\varepsilon \tag{1.11}$$

where the enrichment factor, $f = [DSi]_{obs}/[DSi]_{init}$. $\delta^{30}Si_{DSi-obs}$ and $\delta^{30}Si_{DSi-init}$ represent the Si isotopic composition measured in the water column and in the initial DSi source (when $f = 1$) respectively. $\delta^{30}Si_{BSi-inst}$ and $\delta^{30}Si_{BSi-acc}$ respectively refer to the isotopic composition of the instantaneously formed BSi at each time interval and the time-integrated composition of that which accumulates. Under a Rayleigh model, $\delta^{30}Si_{BSi-inst}$ differs from $\delta^{30}Si_{BSi-acc}$, although the δ^{30}Si of the accumulated BSi pool can never exceed $\delta^{30}Si_{DSi-init}$. Whereas in the open system, $\delta^{30}Si_{BSi}$ has a homogeneous composition that remains in equilibrium with the DSi source pool at all times. The difference between $\delta^{30}Si_{DSi-obs}$ and $\delta^{30}Si_{BSi}$ (or $\delta^{30}Si_{BSi-inst}$) is equal to ${}^{30}\varepsilon$.

Previous work looking into isotopic fractionation during the dissolution of BSi is limited, with some suggestion that this process occurs in isotopic equilibrium, without fractionation (${}^{30}\varepsilon$ of 0‰) (Wetzel et al., 2014). Conversely, Demarest et al. (2009) suggest that dissolution of BSi invokes a slight enrichment in the lighter isotope in the dissolved Si phase (${}^{30}\varepsilon$ of -0.55‰).

Authigenic minerals forming through kinetic precipitation reactions do not do so in isotopic equilibrium. Instead, these phases preferentially uptake the lighter isotope (^{28}Si), leaving the residual sediment pore waters relatively heavy in isotopic composition (i.e. ^{30}Si enriched)(DePaolo, 2011; Frings et al., 2016). A ${}^{30}\varepsilon$ of -2.05‰ has been derived for the formation of 2:1 clays of the Amazon Basin (Hughes et al., 2013), which is consistent with

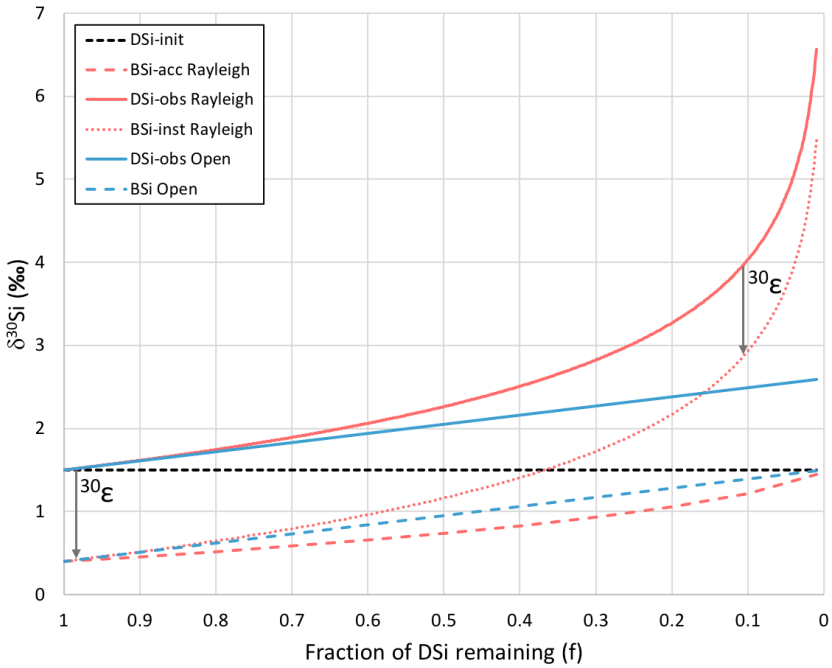

Figure 1.4: Schematic demonstrating the change in Si isotopic compositions of the DSi and BSi pools as DSi is consumed during diatom growth, across two fractionation models. Red lines depict $\delta^{30}Si$ evolution under a Rayleigh/closed system regime, while the blue lines show fractionation in an open/steady-state system where there is a continuous supply of reactant. Dashed black line represents the $\delta^{30}Si$ measured in the initial DSi pool. In both models, the difference between the instantaneous BSi $\delta^{30}Si$ and the $\delta^{30}Si$ of the DSi pool is -1.1‰, which is the mean fractionation factor associated with the uptake of DSi by marine diatoms (De La Rocha et al., 1997). At $f = 0$, all reactant has been consumed, thus the composition of the accumulated BSi pool is equal to $\delta^{30}Si_{DSi-init}$.

estimates for the precipitation of Kaolinite (-2.2‰) (Ziegler et al., 2005b) and formation of allophane (-1.8‰) (Ziegler et al., 2005a). However, $^{30}\varepsilon$ can reach -3.0‰ depending on the number of dissolution-precipitation cycles that occur (Opfergelt and Delmelle, 2012). A similar effect is observed during adsorption of DSi onto Fe (oxyhydr)oxides, which also preferentially retain the lighter isotope ($^{29}\varepsilon$ -0.55 to -0.81‰, approximately -1.06 to -1.59‰ $^{30}\varepsilon$ for ferrihydrite and goethite respectively) (Delstanche et al., 2009) and incorporation into Fe(III)-Si gels, thought to represent a precursor to Precambrian banded iron formations (-2.3 to -3.23‰) (Zheng et al., 2016). The findings of Delstanche et al. (2009) indicate that $^{30}\varepsilon$ increases with the degree of crystallinity and therefore mineral maturity, while in a similar fashion to clay mineral precipitation, Opfergelt and Delmelle (2012) indicate that the final enrichment can reach -3.0‰ depending on successive adsorption-desorption cycles.

Continental waters are generally isotopically heavier than the Si isotope composition of the bedrock. It is thought that most of this discrepancy can be accounted for by AuSi precipitation and DSi adsorption onto metal oxides, with biotic uptake in terrestrial plants and freshwater diatoms also contributing (Fig. 1.3) (Opfergelt and Delmelle, 2012; Sutton et al., 2018). This hypothesis is consistent with the inverse relationship between weathering rates and average fluvial catchment δ^{30}Si uncovered by (Georg et al., 2007) in Iceland. δ^{30}Si values measured in freshwater samples collected from rivers and lakes range from -0.58 to +4.66‰ (averaging +1.26‰) (Hatton et al. (2019); Sutton et al. (2018) and references therein). The lightest isotopic compositions of this compilation were observed by Hatton et al. (2019) in glacial river samples from across the northern hemisphere, in which δ^{30}Si values were found to range from -0.58 to +0.78‰ (averaging +0.16‰), similar to the bedrock composition. This isotopically light composition of glacial relative to non-glacial rivers results from an intense physical weathering regime, which facilitates the dissolution of fine-grained glacial flour (Hatton et al., 2019).

1.4 Thesis aims and hypotheses

It is imperative that we improve our understanding of the Arctic Ocean Si cycle as Atlantification continues to expand the Atlantic Water-dominated regime of the Barents Sea and DSi concentrations of inflow waters continue to decline. In order to accurately anticipate the impact of future climatic, physical and chemical perturbations, we must improve our mechanistic understanding of the processes involved in the biogeochemical cycling of Si. Currently, there are significant data gaps precluding closure of the Arctic Ocean Si isotope budget, including observations from key gateways, such as the Barents Sea, and isotopic compositions measured in BSi of seafloor sediment (Brzezinski et al., 2021). Furthermore, while the pelagic system has been receiving increasingly more attention with regard to nutrient delivery, primary productivity and export production, much

less is known of the benthic Si cycle. This precludes a holistic understanding of how the Si cycle may respond to future changes in sea ice cover and water mass distribution.

This thesis will use reaction-transport modelling, coupled with stable Si isotopes measured in both the solid and dissolved phase of sediment cores of the Barents Sea inflow shelf, to disentangle and improve our understanding of the main drivers of the benthic Si cycle. Recent work has begun to develop a better understanding of early diagenetic cycling of Si through measurement of stable Si isotopes and reaction-transport modelling (Cassarino et al., 2020; Ehlert et al., 2016a; Geilert et al., 2020a; Ng et al., 2020), however this is the first study of its kind within the Arctic circle and the first time that Si isotopes have been measured in solid phase reactive Si pools alongside the pore water phase.

Here I present laboratory measurements from samples collected from three stations of the Barents Sea that span the key hydrographic domains (Arctic Water and Atlantic Water) and features (oceanic polar front), over three consecutive years, to study the interannual variability and spatial heterogeneity of the benthic Si cycle. Gaining a comprehensive understanding of the biogeochemical baseline of both hydrographic regimes will allow for an assessment of future conditions under continued Atlantification, with the potential to use the warmer, ice free southern region as an analogue for future conditions in the north.

Aim 1 (Chapter 3): Produce a δ^{30}Si dataset of operationally-defined reactive Si pools in Barents Sea sediments and investigate the effect of differing sample preparation techniques on those compositions.

Recent work by Pickering et al. (2020) demonstrates the presence of three operationally-defined reactive pools of Si in marine sediments that can be accessed through a novel sequential sediment digestion protocol. Previous studies that employ stable Si isotopes to study the benthic Si cycle measure the dissolved phase pore water DSi pool and sometimes present complimentary analysis of the sediment BSi component (Cassarino et al., 2020; Ehlert et al., 2016a; Geilert et al., 2020a; Ng et al., 2020). This thesis presents a δ^{30}Si dataset, including measurements of all three operationally-defined reactive pools of Si across three stations. In order to obtain a comprehensive understanding of the benthic Si cycle, an assessment must be made of not only the isotopic composition of the pore water DSi stock, but also of all the reactive solid phase pools that are able to contribute to it. This thesis also represents the first isotopic study of the Arctic Ocean seafloor, which will begin to fill a key knowledge gap that remains in closing the wider Arctic Ocean Si budget (Brzezinski et al., 2021).

Sample preparation techniques during experiments to determine sediment BSi content and to study reactive Si pools in marine sediment are inconsistent, with some laboratories opting to freeze/oven-dry and grind/powder sediment prior to analysis (Carter and Colman, 1994; Cassarino et al., 2020; Conley, 1998; Ehlert et al., 2016a; Gallinari et al., 2008; Geilert et al., 2020a; Kamatani and Oku, 2000; Liu et al., 2017b; Rosén et al., 2010; Wu

et al., 2017; Xu et al., 2020) and others simply thawing samples to room temperature from frozen (Michalopoulos and Aller, 2004; Pickering et al., 2020; Presti and Michalopoulos, 2008; Qin et al., 2012) (references are not exhaustive). Michalopoulos and Aller (2004) demonstrated that grinding sediment can artificially increase the estimated BSi content when using a traditional alkaline leach methodology (DeMaster, 1981), due to an increase in the surface area of exposed, fresh BSi accessible to the leachate. This thesis aims to use Si isotopes to unravel the influence of differing sample preparation techniques on the composition of three reactive Si pools, with the goal of advocating for methodological consistency to allow for reliable interlaboratory comparison across future published work.

Hypotheses:

1. Sediment BSi contents will be similar to adjacent Kara and Norwegian Seas (<1 wt%) and approximately +1.5‰, similar to measurements of δ^{30}Si in BSi at <800 m depth across the Arctic Ocean (Liguori et al., 2020; Varela et al., 2016).

2. Sediment BSi content will be higher under the oceanic polar front than in the Arctic and Atlantic Water-dominated regions to the north and south, following observations by Wassmann and Olli (2004) that frontal mixing in the Barents Sea enhances the delivery of organic carbon to depth.

3. Grinding sediment samples will increase the estimated BSi content relative to frozen samples (Michalopoulos and Aller, 2004) and introduce cross-contamination between the operationally-defined reactive Si pools, altering the measured δ^{30}Si.

Aim 2 (Chapter 4): Produce a δ^{30}Si dataset of Barents Sea sediment core top waters and pore water depth profiles to determine the processes responsible for pore water DSi build-up.

Si isotopic analysis of marine sediment pore waters began in 2016 with samples collected from the Peruvian margin upwelling region (Ehlert et al., 2016a) to study isotopic fractionation and constrain the processes involved in the early diagenesis and turnover of Si. Over the last 5 years this work has expanded to include the Gulf of California (Geilert et al., 2020a), West Antarctic Peninsula (Cassarino et al., 2020), western Greenland margin and the Labrador Sea (Ng et al., 2020). This thesis expands the growing dataset to the Arctic circle. Until now, research on the benthic Si cycle of the Arctic Ocean has been limited to analysis of BSi content and sediment pore water DSi concentrations (März et al., 2015). DSi concentrations in sediment pore waters are useful for inferring at what depths dissolution and uptake processes are active, for example, März et al. (2015) hypothesise that BSi and Fe (oxyhydr)oxide dissolution drive increases in DSi, and suggest that authigenic clay minerals take up DSi at depth. However, a more powerful tool, such as Si isotopes,

is required to provide direct evidence and elucidate specific sources and sinks. Benthic Si cycling is complex and can involve the release of DSi from multiple phases, including BSi, LSi and metal oxides, as well as uptake into AuSi and adsorption reactions. Indeed, the growing body of pore water Si isotopic data is one of a few geochemical tools that has contributed to the realisation that reverse weathering may be occurring ubiquitously across the global seafloor (Pickering et al., 2020; Tréguer et al., 2021), rather than just in high sedimentation rate microenvironments (Michalopoulos and Aller, 1995).

Just as the composition of BSi within Arctic Ocean seafloor sediments represents a significant knowledge gap that must be filled to assist in closing the regional Si budget, we must also constrain the isotopic composition of the benthic DSi flux through measurement of pore waters. This thesis will allow for a better estimation of the extent to which an additional sink of isotopically light Si is required to balance the regional isotope budget (Brzezinski et al., 2021). Furthermore, if direct evidence of the reverse weathering inferred by März et al. (2015) can be afforded by measurement of Si isotopes, this process would represent a sink of isotopically light Si previously unaccounted for in Arctic Ocean shelf sediments.

Hypotheses:

1. Pore water asymptotic DSi concentrations will be similar to those measured in the Central Arctic Ocean and Beaufort Sea margin (70-100 μM) (März et al., 2015).

2. Arctic Ocean sediment pore water DSi concentrations (70-100 μM) (März et al., 2015) are lower than the solubility of AuSi assumed in previous studies (220-330 μM) (Cassarino et al., 2020; Dixit et al., 2001; Ehlert et al., 2016a; Krissansen-Totton and Catling, 2020; Loucaides et al., 2010). However, AuSi precipitation has previously been inferred to explain the uptake of DSi at depth in Arctic Ocean sediment cores (März et al., 2015). Evidence for this may be observed as a downcore increase in δ^{30}Si.

3. If the Barents Sea sediments are not influenced by AuSi precipitation, pore water δ^{30}Si profiles will tend towards the composition of the dissolving solid phases downcore (likely a combination of the BSi and LSi operational pool δ^{30}Si).

Aim 3 (Chapter 5): Simulate the early diagenetic cycling of Si to quantify rates of reaction to inform a Barents Sea Si budget and explore whether seasonal deposition of fresh BSi can perturb the pore water DSi pool.

Stable Si isotopes provide a powerful tool with which to elucidate specific Si sources and sinks involved in the early diagenetic turnover of Si in marine sediments. However, this thesis aims to gain a holistic understanding of the mechanistic processes involved, therefore

I use a numerical reaction-transport model to replicate the early diagenetic cycling of Si by fitting the observational dataset. Simulating the benthic Si cycle allows for rates of reaction to be quantified (BSi and LSi dissolution, AuSi precipitation, Si desorption from Fe (oxyhydr)oxides) and isotopic fractionation factors associated with each reaction to be constrained. These parameters are necessary to calculate a Si budget for the Barents Sea.

Application of a reaction-transport model in this thesis will allow for a direct comparison of the steady state simulations with previous studies that have applied similar models in different settings, including the Peruvian upwelling zone, Gulf of California and West Antarctic Peninsula (Cassarino et al., 2020; Ehlert et al., 2016a; Geilert et al., 2020a). However, for the first time, this thesis employs a transient version of the steady state model to investigate the influence of seasonal deposition of fresh phytodetritus on the benthic Si cycle. The Barents Sea spring bloom is an important process that contributes over 50% of the Barents Sea annual net primary production (Dalpadado et al., 2014) and is subject to change as Atlantification proceeds and pre-bloom DSi stocks continue their decline (Årthun et al., 2012; Hátún et al., 2017; Oziel et al., 2016; Rey, 2012). It is therefore crucial to establish whether this process is expressed in the benthos through tight benthic-pelagic coupling (Dale et al., 2021; Ragueneau et al., 2001), or if the seafloor represents a relatively stable Si repository unaffected by seasonal variability in BSi deposition (Sayles et al., 1996; Schlüter and Sauter, 2000). Quantification of this process will allow for a better understanding of the influence of changes in phytoplankton community compositions over time (Neukermans et al., 2018; Orkney et al., 2020).

Hypotheses:

1. Given the low pore water DSi concentrations observed in Arctic Ocean sediments, additional sources of DSi to BSi (such as LSi) will be required to reproduce the DSi and δ^{30}Si pore water depth profiles.

2. Best model-data fits will require input from the Fe redox cycle, the influence of which has been inferred in similar previous studies (Ehlert et al., 2016a; Geilert et al., 2020a; März et al., 2015; Ng et al., 2020).

3. Periodic deposition of fresh bloom-derived BSi will drive discernible increases in surface sediment pore water DSi concentrations.

Chapter 2

Materials and methods

Some text and figure captions of this chapter are included in an article accepted for publication at Geochimica et Cosmochimica Acta ('Stable Silicon Isotopes Uncover a Mineralogical Control on the Benthic Silicon Cycle in the Arctic Barents Sea', doi.org/10.1016/j.gca.2022.05.005) and another in revision at Biogeosciences ('Benthic Silicon Cycling in the Arctic Barents Sea: a Reaction-Transport Model Study', doi.org/10.5194/bg-2022-51), both by Ward et al.

2.1 Site description, core sampling and data acquisition

This thesis presents an isotopic investigation into the early diagenetic cycling of Si at three sampling sites on the Barents Sea shelf (B13, B14, B15), and uses supporting information from an additional three stations (B03, B16, B17) (Fig. 1.2). These sampling stations lie along a 30^{o}E transect between 74 and 81^{o}N, which crosses a sea ice gradient and the main hydrographic domains (Atlantic Water, Arctic Water) and features (oceanic Polar Front). Samples were collected between late June and early August across three cruises (JR16006 in 2017, JR17007 2018 and JR18006 2019) aboard the RRS *James Clark Ross*. Cruise reports are available, which include all accompanying details and complementary data (Barnes, 2019; Hopkins, 2018; Solan, 2018). Stations are bioturbated to varying degrees (Solan et al., 2020) and sampling was targeted at sites of similar fine-grained silty-mud sedimentary composition for optimal core recovery. Due to hydrodynamic sorting this sediment is typically concentrated in deep glacial troughs carved out by the Eurasian ice sheet during the Last Glacial Maximum, therefore sampling water depths were also similar between the stations and range from 280-370 m.

A suite of physical, chemical and biological parameters were analysed across a range of discrete water column depths (Barnes, 2019; Dumont et al., 2019; Solan, 2018). Water column sample collection was carried out through casts of the ships CTD rosette system, which included a Sea-Bird Scientific SBE 911plus CTD, including mounted 12 L and 20 L Niskin bottles (Fig. 2.1). Sampling for sediment, pore water and core top water

analysis was carried out with a Megacorer from the UK National Marine Facilities (National Oceanography Centre), containing up to 12 core tubes. This device allowed for sampling of the upper 30-40 cm of sediment, including the overlying core top water and in-tact sediment-water interface. At the Changing Arctic Ocean Seafloor (ChAOS) stations, eight core tubes were set up in the Megacorer, four or five of which were pre-drilled for pore water sampling. At each station, at least three 'replicate' Megacorer deployments were carried out, with a minimum of 20 m distance between each one to account for spatial heterogeneities. After deployment, 2 L of core top water was sampled from each core tube during cruise JR16, smaller volumes were collected during JR17 and JR18, which were insufficient for Si isotope analysis. For solid phase sampling, the core tubes were placed onto a manual core extruder and slices were taken in 0.5 cm resolution to 2 cm below the seafloor (cmbsf) and 1 cm thereafter.

Pore water samples were taken with Rhizon filters (0.15 μm pores) attached to 50 mL syringes. Spacers were used to maintain the vacuum during sampling. For each Megacorer deployment, samples were combined to ensure adequate sample volume and stored in acid-cleaned vials. Samples for Si isotopic analysis were acidified with 20 μL of distilled, concentrated HCl (10 M) and stored at 4^{o}C. Sample resolution was high: 1 cm intervals between 0-2 cmbsf, 2 cm to 20.5 cmbsf and 5 cm to the base of the core (30-35 cmbsf). Macronutrient (NH_4^+, NO_3^-, PO_4^{3-}, SiO_2) concentration analysis of pore water and water column samples (and core incubation samples on JR18) were carried out onboard using a Lachat QuikChem 8500 flow injection autoanalyser (Hach Lange) using internationally certified reference materials for seawater nutrients to monitor analyser performance (KANSO Co. Ltd., Japan. Batch CG for JR16, CD for JR17 and batches CI for seawater and CF for pore water on JR18). An additional standard reference solution from low nutrient concentration seawater was also analysed throughout the analysis (OSIL batch 25 for JR16, batch 26 for JR17 and batch 27 for JR18) in addition to the KANSO reference standards measured at the start and end of the cruises. The mean error of the macronutrient analysis across the three cruises was 1.2% (Sian Henley, pers. comm. 2019). Prior to autoanalyser measurements, all samples were filtered using a clean nylon mesh (pore size 200 μm) to eliminate zooplankton.

Solid phase Mn, Fe, K and Al analysis was carried out using a Phillips PW-2400 WD-X-ray fluorescence (XRF) spectrometer at the University of Oldenburg (analytical precision and accuracy was better than 5% (Faust et al., 2020)). Pore water element concentrations (Fe, Mn, Mg and K) were analysed at the University of Leeds using a Thermo Scientific iCAP 7400 Radial ICP-OES (uncertainty <3%). As with the nutrient data, pore water trace and major elemental concentrations were determined for all Megacorer events. Profiles discussed here will correspond to those events and stations selected for Si isotopic analysis.

Each Megacorer deployment was attributed an event number and one core was taken

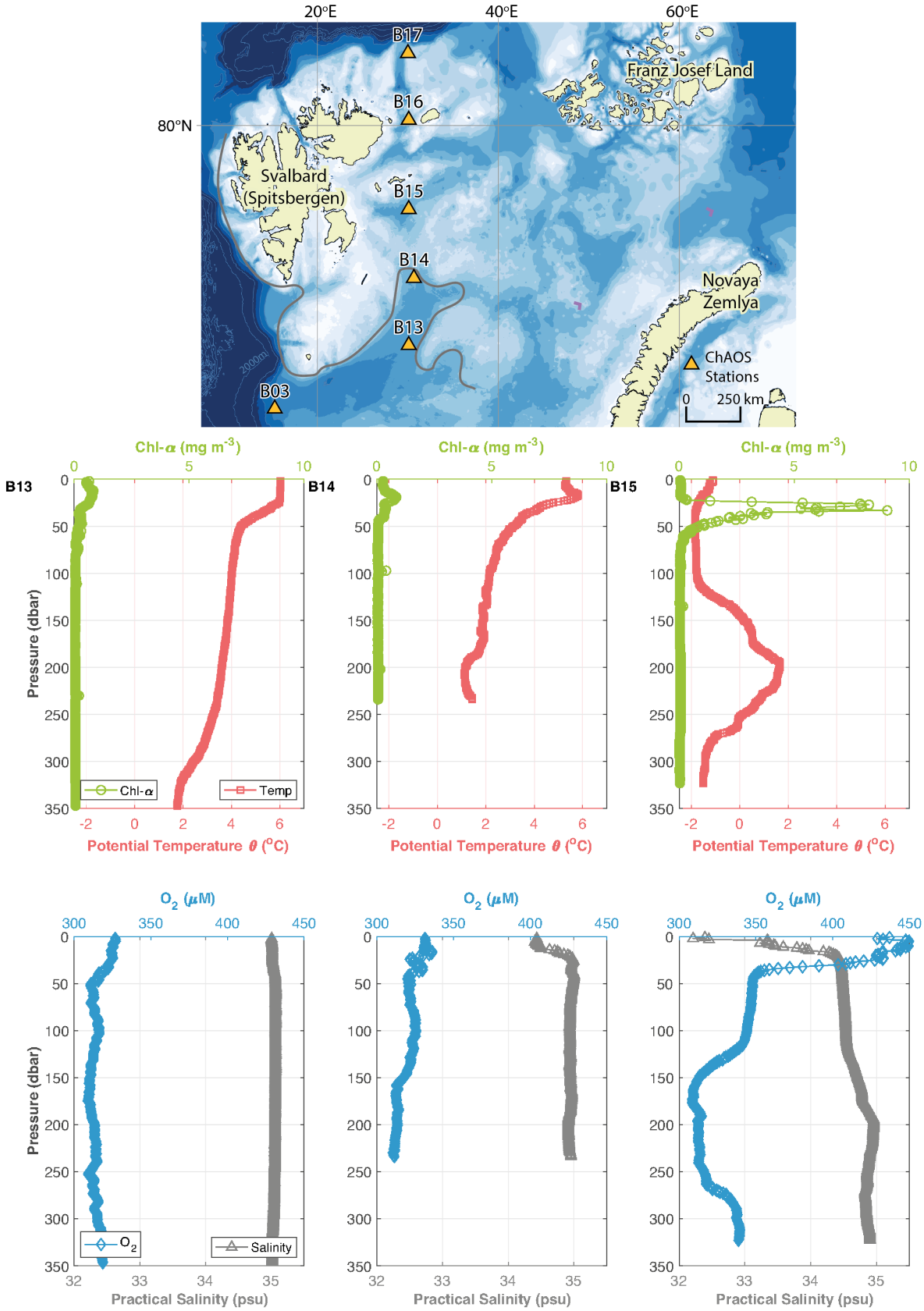

Figure 2.1: Sampling station locations and representative CTD profiles (2017) of potential temperature, fluorescence (Chl-α), salinity and dissolved O_2. Left to right columns: B13, B14, B15.

from three deployments at each site to be analysed for macronutrients (including [DSi]) for all three cruises. Samples collected from stations B13, B14 and B15 were prioritised for Si isotopic analysis in this study to allow for characterisation of the two major hydrographic domains of the Barents Sea and a key feature (Atlantic Water, Polar Front and Arctic Water respectively). Sampling coordinates indicate that for all three sites, two of the three cores analysed for $\delta^{30}Si_{DSi-PW}$ were collected within 100-400 m of each other between cruise years, while the third core, namely JR17 B13, JR18 B14 and JR17 B15, were collected 25 km south, 0.9 km north and 15 km southwest respectively of the two clustered cores (Fig. 1.2). Therefore, we have an indication of intra and inter site spatial variability, with some inference into interannual temporal variability where sampling between the cruises is within a reasonable distance.

Sediment core incubations were carried out on cruise JR18 in order to quantify benthic nutrient fluxes, associated with the benthic Si cycle (this study) and organic matter degradation (ammonium and phosphate) (Freitas et al., 2020). One core for each sampling station was selected from the Megacorer deployments and stored in a dark room of constant temperature (4^oC). An air tight cap was sealed over the top of the core tube, which incorporated a plastic tube where a 60 mL syringe could be connected for sample collection. A magnetic stirrer was attached to the base of the cap to continuously homogenise the core top water. The incubation was run over a 24 hour period, with 50 mL samples extracted through a filter (Acrodisc PF Syringe filter, 0.8/0.2 μm supor membrane) at three hour intervals. After each extraction, the height of the core top water was noted down to enable calculation of the benthic flux magnitude.

2.2 Pre-concentration of sediment core top and pore water samples

Prior to isotopic analysis, water column, sediment core top and pore water samples were required to undergo a pre-concentration step. This procedure was carried out in a clean setting at the University of Bristol's Bristol Isotope Group (BIG) laboratory. The volume of sample required to achieve a 2 ppm Si solution after column chemistry was calculated prior to sample preparation, assuming a 100% sample yield. Sample pre-concentration was then carried out by the Mg-induced co-precipitation (MAGIC) method, broadly following Karl and Tien (1992) and de Souza et al. (2012). This method involves the adsorption of Si onto brucite ($MG(OH_2)$) as it precipitates from seawater. This process concentrates the Si and reduces the cation and anion matrix by up to two orders of magnitude, allowing for the effective use of cation exchange resin columns (de Souza et al., 2012). This precipitation is induced by the step-wise addition of 1 M NaOH (Titripur Reag. Ph Eur grade) to pH-neutral samples. Prior to addition of 1 M NaOH the pH of samples was tested. As would be expected, seawater and core-top water samples were found to have a pH of $\sim$7, however

pore water samples were acidified with 20 μL of distilled HCl (10 M) after sample collection to prevent the precipitation of solid Fe-(oxyhydr)oxide minerals in vials during storage. In addition, for some particularly Fe-rich samples, further acidification was required before MAGIC due to the presence of fine-grained Fe-precipitates in the base of the sample vials. In this case, 0.1% v/v 10 M in-house distilled HCl was added and the samples were left for 24 hours to ensure complete dissolution. Samples were then neutralised using 1 M NaOH to pH ~5-7 to allow for adequate brucite precipitation and left for 24 hours to equilibrate.

Following equilibration, samples were transferred in their required volumes to acid-cleaned 15 or 50 mL centrifuge tubes ('A') and 1.2% v/v 1 M NaOH was added to the solution. The tubes were shaken with an IKA Mixer Lab Dancer Vortex every ten minutes for one hour and left for 36 hours in total. Samples were then centrifuged at 3000 rpm for three minutes and the supernatant was poured into a second acid-cleaned centrifuge tube ('B'), at which point 1% v/v 1 M NaOH was added to centrifuge tube B, which was again mixed every ten minutes for one hour. The new centrifuge tube was left for a further 36 hours for precipitation to extract any remaining Si. The 'B' centrifuge tubes were centrifuged at 3000 rpm for three minutes and the supernatant was discarded. After centrifugation, 1 mL or 5 mL of 0.001 M NaOH solution was added to the 15 mL and 50 mL centrifuge B tubes respectively to re-suspend the precipitate, which was then drawn up into an acid-cleaned pipette tip and added to the centrifuge tube A, recombining the sample. The re-combined precipitate was then rinsed with 0.001 M NaOH three times. Each time, 1 mL or 5 mL of 0.001 M NaOH was added to the samples, which were mixed by vortex and centrifuged at 3000 rpm for three minutes, following which the supernatant was discarded.

This rinsing procedure removes excess cations and anions (Na^+, Cl^-, $SO_4{}^{2-}$, Ca^{2+}, K^+) (Ng et al., 2020). Typically, samples are then left in their stable precipitate form until the day of column chemistry, however pore water samples of certain Barents Sea stations are Fe-rich, resulting in the precipitation of a fine Fe (oxyhydr)oxide in the centrifuge tubes after precipitate re-dissolution. As a result, distilled 10 M HCl was added to pore water samples at an earlier stage, which were left for 36 hours prior to column chemistry. Samples that were analysed with the fine Fe (oxyhydr)oxide material present prior to column chemistry presented with isotopically heavier compositions (Fig. 2.2), likely due to the preferential adsorption of DSi onto solid phase Fe minerals (Delstanche et al., 2009; Zheng et al., 2016).

In order to re-dissolve samples from their precipitate form, 50 μl and 80 μl distilled HCl (10 M) was added to the 15 mL and 50 mL centrifuge tubes respectively, which were then diluted to 1 mL with 18.2 MΩ Milli-Q water. This ensures consistency across sample matrices. Precipitates derived from larger volume samples (50 mL centrifuge tubes) were often found to retain solution from the 0.001 M NaOH rinse stage, thereby increasing the volume of solution from the desired 1 mL. Therefore, where required, samples were

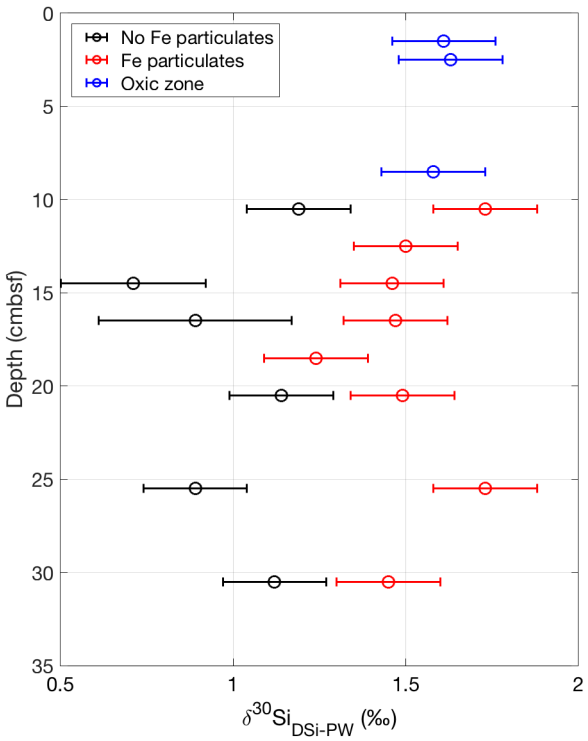

Figure 2.2: Influence of Fe oxide precipitates formed in B15 JR16 pore water sample bottles on $\delta^{30}Si_{DSi-PW}$. Blue data points are samples collected from oxic sediment layers, where pore water Fe concentrations are close to zero (Fig. 4.11). Red samples were analysed despite the presence of a fine-grained deposit in the centrifuge tubes, assumed to be composed of Fe (oxyhydr)oxides. Black data points represent reanalysis of the samples initially analysed (red data points), after having been further acidified and left for sufficient time to allow for Fe dissolution.

placed in acid-cleaned Teflon beakers and placed onto a hot plate at 90^{o}C to reduce the volume and ensure the intended mass of Si was available for column chemistry. ALOHA standards were dried down intermittently alongside the samples to ensure there was no isotopic fractionation associated with the evaporation process.

2.2.1 Cation Exchange Chromatography

The pre-concentrated water samples, as well as all solid phase leachates and standards were passed through cation exchange columns, following Georg et al. (2006) (Fig. 2.3). A resin is used for the chromatographic separation of Si from the seawater matrix (i.e. sea salt) (de Souza et al., 2012). The proportion of the 1 mL pre-concentrated solution to be passed through the column is calculated, based on obtaining the desired final concentration in a sample prepared for instrument analysis (usually 2 ppm Si, but can vary depending on available sample volume). For example, a 1 mL ∼6.8 ppm Si post-MAGIC solution would require the entire volume to be passed through the column and eluted with 2 mL Milli-Q water, in order to produce a post-column solution of ∼2.3 ppm Si. This allows for doping associated with sample preparation for instrument analysis, which dilutes the sample to ∼2 ppm Si. For analysis of sediment leachates, the concentration of Si was analysed using the molybdate blue spectophotometry method, following which the volume of sample to pass 7.2 μg of Si through the column resin was calculated. Sample was dried down at 90^{o}C if required, to allow for a Milli-Q elution of at least 1.8 mL (equivalent to the resin volume), for a final purified sample volume of 3.6 mL.

New resin (Bio-Rad AG50W-X12, 200-400 mesh cation exchange resin in H^+ form) was thoroughly cleaned prior to use, alternating between 6 M distilled HCl and Milli-Q three times. If the resin had been used for column chemistry three times, it was dried and discarded, if not the columns (including resin) were cleaned following the procedure in Table 2.1. Gradually increasing the strength of the acid passed through the column prevents rapid expansion of the resin, which would create vesicles and cavities, potentially inhibiting the free flow of solution. To set up a new column, 1.8 mL of resin was pipetted into Bio-Rad polypropylene columns. The required sample volume was then loaded onto the columns and eluted with the required volume of Milli-Q to produce a solution of 3 mL at ∼1-2 ppm (depending on available sample volume). All standards and samples were treated with this procedure. This method retains all ambient cations (e.g. Na^+, Mg^{2+}, Fe^{2+}) from the solution and does not attract dissolved Si as non-ionic orthosilicic acid (H_4SiO_4), or the negatively charged species $H_3SiO_4^-$, which are in equilibrium between pH range 2-8 (Georg et al., 2006) (Fig. 2.3). Samples were collected with acid-cleaned Nalgene 8 mL LDPE bottles and were analysed within 48 hours of column chemistry.

Use of a cation exchange resin was preferred in this study to the alternative anion exchange method (Wickbold, 1959), previously used in the determination of Si isotope ratios (Engström et al., 2006). In the latter methodology, to ensure successful separation

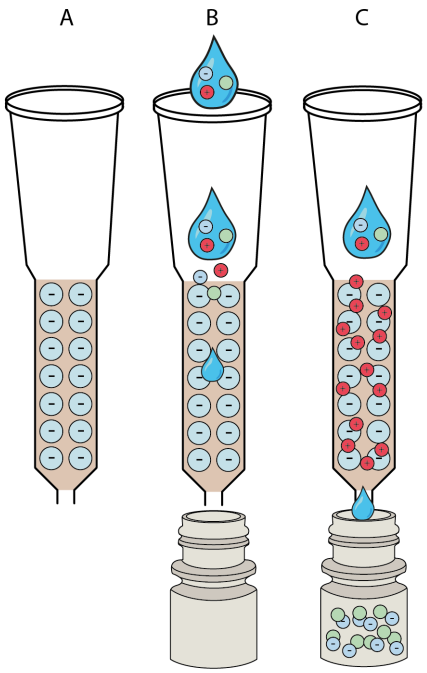

Figure 2.3: Cation exchange chromatography schematic. A) Immobilised anion surface of Bio-Rad resin. B) Sample and standards flow through the column into 8 mL Nalgene vials. C) Cations bind to anion surface, while non-ionic and negatively charged dissolved silica species pass through the resin.

of Si in solution from ambient ions, Si must be converted to H_2SiF_6, which dissociates to form an exchangeable species ($SiF_6{}^{2-}$), which has a high affinity for the resin (Engström et al., 2006). While Si recovery through this method is found to be >97%, the use of hydrofluoric acid (HF) presents significant complications when determining isotopic ratios by multi-collector inductively coupled plasma mass-spectrometry (MC-ICPMS). Previous work has found that HF-free solutions by way of a cation exchange method can increase instrument sensitivity by 30-40% (Georg et al., 2006).

2.3 Silicon isotope analysis

Stable Si isotopes (^{28}Si, ^{29}Si, ^{30}Si) were measured in sediment pore, core top and seawater samples, as well as solid phase leachates using a Finnigan Neptune Plus High Resolution MC-ICP-MS by Thermo Fisher Scientific in the Bristol Isotope Group laboratory at the University of Bristol. Analysis was carried out in both wet and dry plasma mode, in medium or high resolution, so as to resolve common interferences on masses 28 (e.g. $^{14}N^{14}N^+$, $^{12}C^{16}O^+$), 29 ($^{14}N^{15}N^+$, $^{13}C^{16}O^+$, $^{12}C^{17}O^+$, $^{14}N^{14}N^1H$, $^{12}C^1H^{16}O$) and 30 ($^{15}N^{15}N^+$, $^{13}C^{17}O^+$, $^{12}C^{18}O^+$, $^{14}N^{16}O$) (Cardinal et al., 2003; Hendry et al., 2011) (Fig. 2.4, Table 2.2). Data acquisition was carried out through numerous sessions over two years. Si solution was transferred from the autosampler via a PFA (perfluoroalkoxy) Savillex C-

Table 2.1: Si separation scheme using cation exchange chromatography, including resin preparation and cleaning. This example is for an LMG standard (21 ppm) passed through the resin to produce a 7 mL solution of ∼2.3 ppm Si, which allows for dilution to 2 ppm after the doping procedure used during preparation for MC-ICP-MS instrument analysis. Steps 1-4 are carried out only for new resin. After new resin is transferred into polypropylene columns it used up to three times, after which it is discarded. Steps 5-10 are used to clean the resin between uses.

Step	Eluent	Volume	Function
1	6 M HCl	Fill Teflon pot	Initial clean
2	Milli-Q	”	”
3	Repeat ×3	”	”
4	3 M HCl	”	Storage
5	3 M HCl	10 mL	Clean and condition
6	6 M HCl	10 mL	”
7	10 M HCl	5 mL	Clean
8	6 M HCl	5 mL	”
9	3 M HCl	5 mL	”
10	Milli-Q	10 mL	Rinse
11	Sample (e.g. LMG)	0.76 mL	Cation exchange
12	Milli-Q	6.24 mL	Si elution

flow nebuliser (100 μL min^{-1}) connected either to a PFA Teflon barrel spray chamber (wet plasma) or an Apex IR Desolvating Nebulizer (dry plasma), both from Elemental Scientific. The PFA spray chamber was stored in 8 M HNO_3 and rinsed thoroughly with Milli-Q water prior to use. The Apex IR quartz flowpath was rinsed with 0.1 M HCl prior to every use to prevent the build up of deposits in the spray chamber, which were found occasionally to result in sporadic spikes in the ^{24}Mg blank intensity. If ^{24}Mg intensity spikes were observed, the analytical session was halted and the Apex IR was thoroughly rinsed to remove any deposits. Typically, quartz spray chambers and injectors are avoided for measurement of Si isotopes due to the potential for Si contamination, however Si intensity in the blank was carefully monitored and we found no evidence of adverse effects of a quartz flowpath on the composition of measured standards. Furthermore, while the intensity of Si was generally higher in the blank with an Apex IR compared to a PFA spray chamber, the sample signal intensity increased by a greater proportion, helping to ensure that blank levels remained below the 1% threshold. Typical blank intensities were ∼0.02 V for ^{28}Si with wet plasma, increasing to ∼0.06 V when in dry plasma mode. If the intensity of the blank solution (0.1 M in-house distilled HCl) neared 1% of the intensity in the tuning solution, the nebuliser was left in the wash solution until such time as the blank had reduced in intensity.

Nebulised sample was delivered into the plasma by a sapphire injector, which passed through sample and skimmer cones that form the interface between the plasma and MC-ICP-MS. While in wet plasma mode, standard sample and nickel-X skimmer cones (R

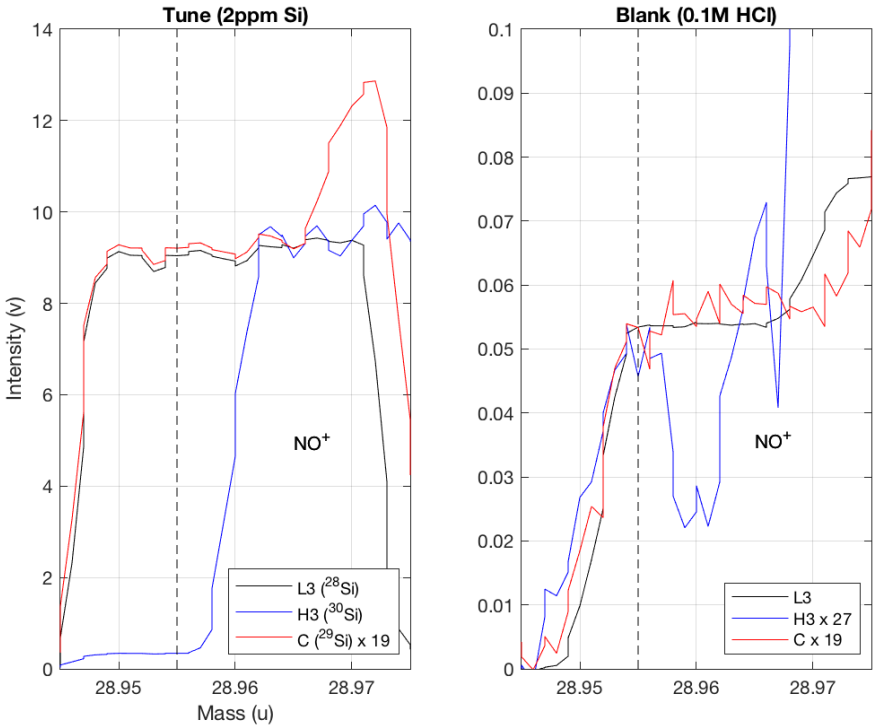

Figure 2.4: Peak scans of stable Si isotopes in medium resolution, wet plasma mode. Peaks from a 2 ppm NBS-based tuning solution (left) and a 0.1 M HCl blank (right). Note the difference in y axis scales and exaggeration of the intensities on cups C and H3. Measurements were carried out on the lower mass side of the peak to avoid interferences (dashed black line). The centre mass was carefully selected, taking into account proximity to the shoulder and $^{14}N^{16}O$ interference of the sample peak, as well as the negative inflection on the blank curve.

Table 2.2: Mass spectrometer operating conditions and configuration used for Si isotopic analysis of standards and samples.

Running Parameter	Typical Setting	
	Wet Plasma Mode	*Dry Plasma Mode*
Mass spectrometer	Neptune	”
Forward power (W)	1150-1210	”
Resolution	Med/High	”
Auxiliary gas (L min^{-1})	∼0.8	∼1.0
Sample gas (L min^{-1})	0.85-0.98	1.0-1.1
Sample cone	Standard	Pt-tipped Jet
Skimmer cone	Nickel X	Pt-tipped Nickel X
Spray chamber	PFA Barrel	Apex-IR
Nebuliser	Savilex C-flow	”
Uptake rate (μL min^{-1})	100	”
Uptake mode	Self-aspirating	”
Injector	Sapphire	”
Sample matrix	0.1M HCl	”
Cycles per block	20	”
Integration time (s)	4.2	”
Wash time (s)	60	90
Idle time (s)	3	”
Uptake time (s)	40	90
2ppm solution ^{28}Si intensity (V)	≤10	≥20
Blank ^{28}Si intensity (V)	∼0.02	∼0.06
Amplifiers	$10^{11}\Omega$ resistor	”
Faraday cup configuration		
Low 4	^{26}Mg	
Low 3	^{28}Si	
Axial (C)	^{25}Mg, ^{29}Si	
High 3	^{30}Si	
High 4	^{24}Mg	

A Chilton ICP-MS Cones Ltd.) were used, whereas when the switch was made to dry plasma there was also a change in cones to a jet-sample cone and nickel X-skimmer cone (both platinum-tipped, Thermo Fisher Scientific from ICP-MS Cones Ltd.). Prior to sampling, instrument tuning (e.g. torch position, sample and auxiliary gas flow rates, peak shape) was carefully adjusted using a purified Si solution of NBS28 standard to ensure a stable signal of anticipated intensity. Typical intensity of a 2 ppm Si solution in medium resolution and wet plasma mode was $\leq$10 V for ^{28}Si, but at least 20 V in dry plasma mode. The decision to switch from wet to dry plasma mode resulted from the discovery that the increased intensity afforded by the Apex IR resolved sporadic complications with high Mg corrections driven by matrix sensitivities.

Si peak shapes were adjusted during the tuning process to increase the mass range at which the centre cup could be positioned. A quantitative quality control of the peak shape was carried out by calculation of the mass resolving power (MRP) (equation 2.1), where m is the mass number of the observed mass (28 in this case) and Δm represents the mass difference between 95% and 5% of the peak slope (95%−5%) (Fig. 2.5):

$$MRP = \frac{m}{\Delta m} \tag{2.1}$$

If the MRP was found to be <4000 and could not be improved in either medium or high resolution, the slit was replaced before analysis was considered. Prior to every analytical sequence, peak centering was manually carried out on ^{28}Si, ^{24}Mg, ^{25}Mg and ^{26}Mg to correct for any drift in the mass calibrations. Selection of the centre cup mass was carried out carefully, taking into account: the discussed interferences that are clearly visible in medium and high resolution, the negative inflection on the 0.1 M HCl blank and proximity to the peak shoulder (Fig. 2.4). Typically the centre cup mass ranged from 28.959 to 28.961.

Samples were analysed using a standard-sample bracketing (SSB) technique (De La Rocha, 2002) (order: Blank - Standard (NBS28) - Sample - Standard (NBS28) - Blank) and intensity matching of Si and Mg between standard and sample was typically within 10%. Providing intensities are well matched between the standard and sample, this method allows for the avoidance of issues associated with polyisobaric interferences, as they influence both of the former to a similar degree (Cardinal et al., 2003). Prior to any mass bias correction, the intensities of all the isotopes measured (^{28}Si, ^{29}Si, ^{30}Si, ^{24}Mg, ^{25}Mg, ^{26}Mg) were corrected for background levels of Si and Mg by removing the mean intensities in the bracketing blank solutions from the standard/sample (see example for ^{28}Si in equation 2.2).

$$^{28}Si_{blank\,corrected} = ^{28}Si_{measured} - mean\left(^{28}Si\right)_{bracketing\,blanks} \tag{2.2}$$

In addition to SSB, each standard and sample was doped with Mg (50 μL 10 ppm

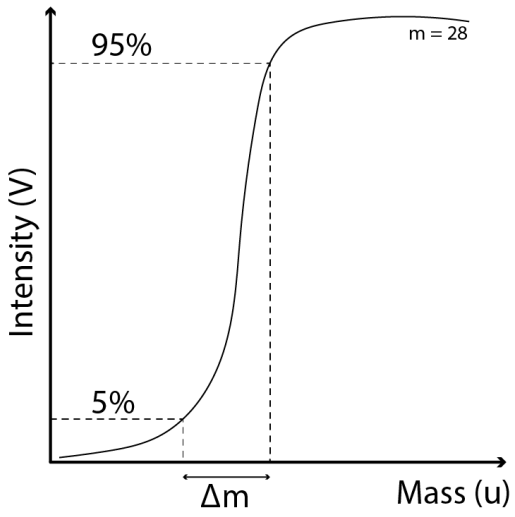

Figure 2.5: Schematic showing the calculation of mass resolving power (MRP). A minimum of 4000 was required before analysis was considered.

Inorganic Ventures 1484 Mg Standard per 1 mL of sample) to further address mass bias and instrumental drift through internal standard normalisation (Cardinal et al., 2003). Mass bias is a significant and unavoidable problem in mass spectrometry, especially ICP-MS. The net result of instrumental mass bias is the preferential transmission of heavier isotopes through the mass spectrometer, causing non-uniform sensitivities across the mass range and inaccurate measurement of samples and standards as a result (Cardinal et al., 2003; Yuan et al., 2016). This phenomena is not perfectly understood, therefore in order to tackle this issue it must be directly measured (Andrén, 2004). Mass bias correction through SSB alone is predicated on the assumption that a temporal drift in mass bias is predictable and therefore stable between the bracketing standards, which may not always be the case (Araújo et al., 2017; Mason et al., 2004). Mg represents a reasonable element for internal standardisation of Si, as the isotopes are of a similar atomic mass and the initial isotopic composition of the solution is known. We can therefore measure the isotopic composition of the Mg doped in every standard and sample and use that as a continuous quantification of mass bias and thus apply a correction (fractionation factor f_{Mg}) through use of the fractionation exponential law (equation 2.3) (Cardinal et al., 2003). This correction factor is derived from the $^{25}Mg/^{24}Mg$ ratio and applied to the Si isotope ratios (equation 2.4), which assumes that Mg and Si isotope ratios are behaving in a similar fashion.

$$f_{Mg} = ln\left(\frac{\left(\frac{^{25}Mg}{^{24}Mg}\right)_{true}}{\left(\frac{^{25}Mg}{^{24}Mg}\right)_{measured}}\right) \Big/ ln\left(\frac{Mass^{25}Mg}{Mass^{24}Mg}\right) \tag{2.3}$$

$$\left(\frac{^{29}Si}{^{28}Si}\right)_{true} = \left(\frac{^{29}Si}{^{28}Si}\right)_{measured} \times \left(\frac{Mass^{29}Si}{Mass^{28}Si}\right)^{f} \tag{2.4}$$

A constant linear relationship between measured ^{29}Si/^{28}Si *vs* ^{25}Mg/^{24}Mg ratios is expected, with a slope of 0.8588 (Cardinal et al., 2003). Fig. 2.6 demonstrates that over a prolonged period of time, the linear relationship between isotope ratios is consistent with that expected, however the slope and y intercept can vary on shorter temporal scales, both between and within analytical sessions. Therefore, while linearity may apply within a given session (i.e. constant f_{Si}/f_{Mg}), the absolute value of the mass bias fractionation correction factor can differ (Cardinal et al., 2003). However, it is thought that the effects of this are negligible when SSB is used in conjunction with Mg internal normalisation. Amongst other reasons, this is because analysis of all six isotopes in dynamic mode allows for a near-instantaneous correction of the mass bias (Cardinal et al., 2003).

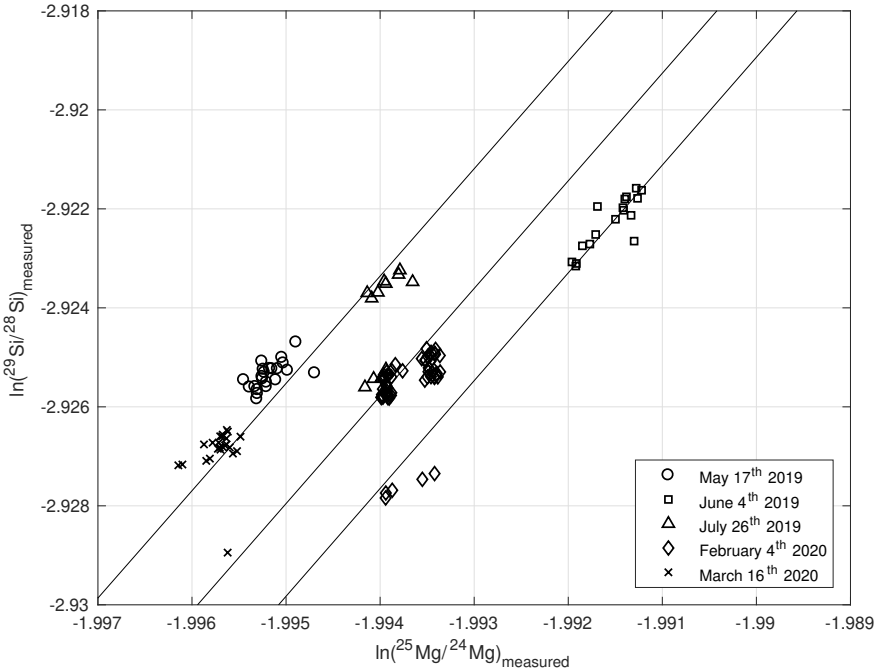

Figure 2.6: Long-term measured Si ($^{29}Si/^{28}Si$) vs Mg isotope ratios ($^{25}Mg/^{25}Mg$) plot in standards and samples from a random selection of MC-ICP-MS runs from this study. Three straight lines plotted are theoretical lines for when $f_{Si} = f_{Mg}$ (as assumed in equation 2.4), which have a gradient of 0.8588 for ($^{29}Si/^{28}Si$)/($^{25}Mg/^{24}Mg$) (Cardinal et al., 2003). Lines were visually fit to the data through variation of the y intercept.

Samples and standards were also doped with 50 μL 0.001 M H_2SO_4 (ROMIL-UpA) and 1 M HCl (in-house distilled) per 1 mL of sample, so as to counteract any distortion of the ionisation efficiency and instrumental mass bias by anionic matrices (SO_4^{2-} and Cl^-) (Hughes et al., 2011; Van Den Boorn et al., 2009). Cation exchange chromatography does not remove these problematic anionic species, however it is possible to add a relatively large

volume of artificial anionic matrix to the sample and bracketing standards, to overwhelm the signal and ensure that any influence on the measured isotope ratios is consistent across the two. We can then use the internally normalised Si isotope ratios from the standards and samples to calculate the δ^{30}Si value using equation 1.3.

Each sample, standard and blank was analysed for 20 individual measurement integrations (or 'cycles') with an integration time of 4.2 s and an idle time of 3 s. This was carried out in dynamic mode, allowing for the measurement of Mg and Si isotope peaks in each cycle, with 20 cycles per 'block'. When using the PFA spray chamber (wet plasma), the uptake time was 40 s and a 60 s wash (a pot of 0.1 M HCl in addition to the blank) was carried out before each of the SSB components listed above. However, when using the Apex IR (dry plasma), a longer wash and uptake time was required (both 90 s) to account for the longer Apex IR flowpath relative to that of the PFA spray chamber.

Data quality was assessed through the correlation between δ^{29}Si and δ^{30}Si of all standards and samples analysed. All samples exhibit a strong correlation between δ^{29}Si and δ^{30}Si (R^2 0.997) and fall on a mass dependent fractionation line of gradient 0.5123 (Fig. 2.7), which is in between that expected of mass dependent kinetic (0.5092) and equilibrium (0.518) Si isotope fractionation (Reynolds et al., 2007). This observation indicates that mass independent fractionation induced by instrumental mass bias has been adequately managed. Certain data points were omitted from the dataset where they did not meet the following strict quality control criteria. Any data with a calculated Mg correction factor of >0.25‰ were removed. Mg corrections of 0.2-0.25‰ were used, providing δ^{30}Si values of replicate measurements were within long term reproducibility of standards (±0.14‰). Furthermore, any data points with a difference of ≥0.15‰ between the predicted mass dependent and measured δ^{29}Si values were omitted, as were any samples with propagated internal errors of >0.2. Omitted samples were re-analysed if there was adequate sample volume remaining.

Regular standard analysis was also carried out in each analytical session in addition to the SSB and internal normalisation protocols, in order to quantify the long-term external reproducibility of sample measurements and to monitor any drift in the tuning or performance of the MC-ICP-MS (Fig. 2.8). Such changes include, but are not limited to, shifts in peak position or signal stability. Every sequence within an analytical session would be bracketed by calibrated standards (either Diatomite or LMG08), which were also included approximately every five samples throughout the sequence. In addition, a seawater standard ($ALOHA_{1000}$ or $ALOHA_{300}$) was analysed at least twice in each analytical session, which was used as a quality control for the seawater Si pre-concentration procedure, to ensure it was not inducing any isotopic fractionation.

Diatomite standard (Celpure) is produced from purified diatomite, which has undergone inter-laboratory testing and has an average δ^{30}Si composition of +1.26 ±0.2‰ (2σ) (Reynolds et al., 2007). LMG08 is a standard derived from a sponge collected from An-

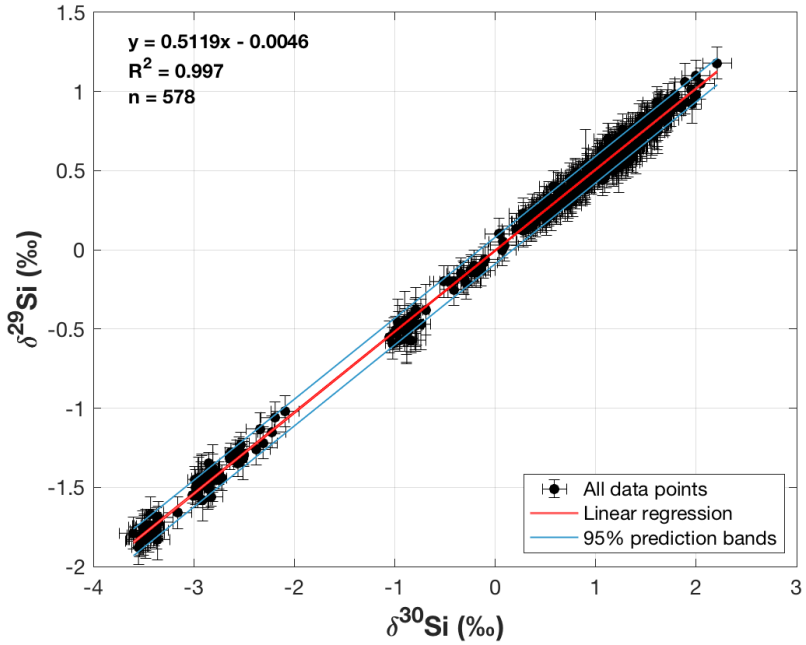

Figure 2.7: Three isotope plot of $\delta^{29}Si$ vs $\delta^{30}Si$ for all samples and standards analysed throughout this study, to assess control of instrumental mass bias (n=578). Error bars denote long term reproducibility of standards (Diatomite) $\pm 2\sigma$ (± 0.14‰ for $\delta^{30}Si$ and ± 0.09‰ for $\delta^{29}Si$). Linear regression (red line) has an R^2 of 0.997 and gradient of 0.5119. Light blue lines depict the 95% prediction intervals of the linear regression. 95% confidence intervals fall within the line thickness of the linear regression.

vers Island (West Antarctic Peninsula), which has been analysed extensively in multiple laboratories and has an average δ^{30}Si of -3.43 ±0.15‰ (Hendry et al., 2011; Hendry and Robinson, 2012). These published values agree well with those analysed in this study, with average δ^{30}Si values of +1.24 ±0.14‰ (n=116) for Diatomite and -3.47 ±0.13‰ (n=46) for LMG08. ALOHA seawater is sampled from the North Pacific subtropical gyre (Station ALOHA) at 1000 m and 300 m water depths as part of the GEOTRACES programme, which has undergone inter laboratory calibration. $ALOHA_{1000}$ and $ALOHA_{300}$ present with published average δ^{30}Si compositions of +1.24 ±0.2‰ and +1.68 ±0.35‰ (2σ) respectively (Grasse et al., 2017). These values also compare well to those analysed in this study, with average δ^{30}Si values of +1.23 ±0.17‰ (n=30) and +1.54 ±0.16‰ (2σ) (n=4) respectively (Fig. 2.8).

2.4 Solid phase sequential leach extractions

Operationally-defined reactive pools of Si were analysed in surface sediment samples following Pickering et al. (2020). An additional study was also carried out to assess the influence of drying and grinding sediment samples prior to analysis, as well as to assess the requirement for pre-treatment with H_2O_2. This sequential digestion procedure separates Si into operational pools based on the conditions, kinetics (time dependent) and sequence of the reaction (DeMaster, 1981; Michalopoulos and Aller, 2004; Pickering et al., 2020; Rahman et al., 2016). These pools are defined as follows: acid leachable (Si-HCl), mild alkaline leachable (Si-Alk) and harsh alkaline leachable (Si-NaOH) (Michalopoulos and Aller, 2004; Pickering et al., 2020).

Frozen sediment samples were slowly thawed to room temperature (T ~22^oC), then 50-100 mg was weighed in triplicate into acid cleaned 50 mL polyethylene Falcon centrifuge tubes. In addition, subsamples were weighed in duplicate into petri dishes and stored in a drying cabinet at 60^oC for 24 hours to obtain wet/dry weight ratios in order to correct the measured sediment BSi contents. 36 mL of 0.1 M HCl (in-house distilled) was added to each sample tube and procedural blanks were prepared in triplicate for each analytical session. Tubes were sealed with parafilm, vortexed and sonicated for 20 minutes. Sample tubes were then vortexed periodically and left on their side overnight to ensure maximum contact between leachate and sample, for a total leach time of 18 hours. Michalopoulos and Aller (2004) found no perceptible difference in measured BSi content when samples were periodically *vs* constantly shaken throughout the leaching process.

Sample tubes were centrifuged at 4000 rpm for 10 minutes and 36 mL of supernatant was pipetted into new acid cleaned 50 mL tubes, being careful to ensure sediment sample loss was minimal. 10 mL of Milli-Q water was then pipetted into each of the sediment sample tubes, which were vortexed and centrifuged (4000 rpm for 10 minutes) to remove any residual acid. The supernatant was pipetted to waste, as Rahman et al. (2016) found

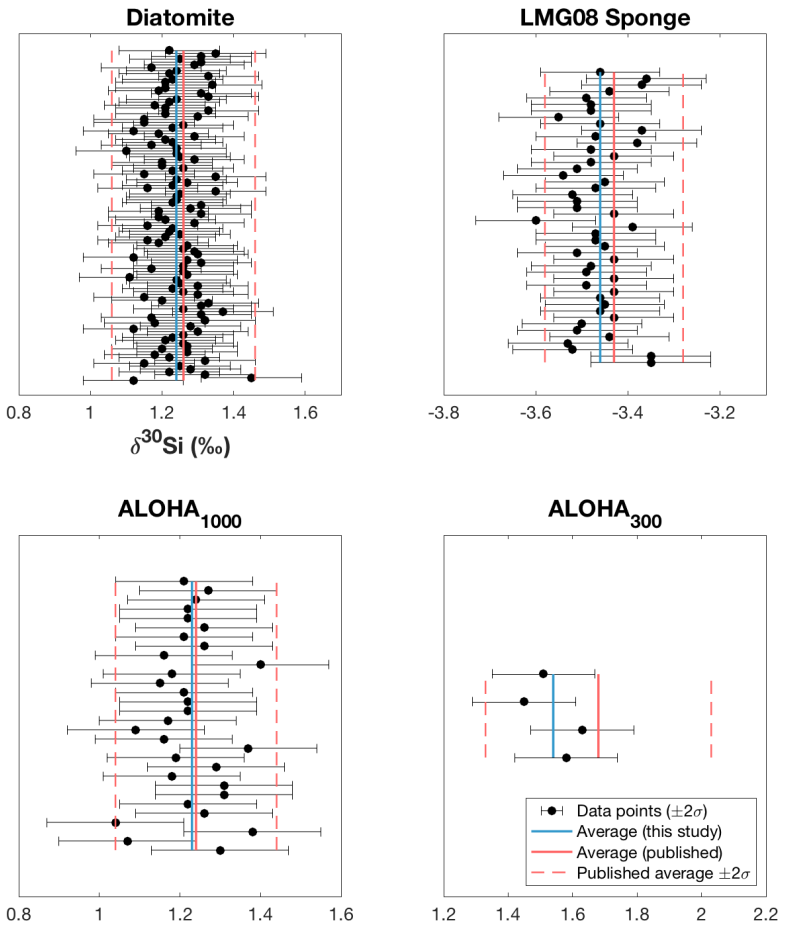

Figure 2.8: Long-term reproducibility of reference standards, including Diatomite, LMG08 sponge and GEOTRACES Station ALOHA seawater from 300 m and 1000 m depths. Blue lines represent the average value from this study, while the solid red lines depict the average published values. Error bars are ±2σ (Diatomite n=116, LMG08 n=46, $ALOHA_{1000}$ n=30, $ALOHA_{300}$ n=4), as are the dotted red lines, but from the respective publications (Diatomite from Reynolds et al. (2007); LMG08 from Hendry and Robinson (2012); $ALOHA_{1000}$ and $ALOHA_{300}$ from Grasse et al. (2017)).

that DSi was negligible in these rinses. This was carried out twice more for a total of three rinses. The 0.1 M HCl extraction phase is thought to remove authigenic products (metal oxide coatings and authigenic clay minerals), without activating the Na_2CO_3 pool (Michalopoulos and Aller, 2004; Pickering, 2020).

Immediately following the acid leach pretreatment, 5 mL of 10% H_2O_2 was pipetted into each sample tube, which were then sealed with parafilm, vortexed thoroughly and sonicated for 30 minutes. This step was removed when carrying out method tests to assess the need for sediment treatment with H_2O_2. An H_2O_2 pre-treatment is employed by Mortlock and Froelich (1989) to remove diluting organic phases, but is not carried out by Pickering et al. (2020). This stage is thought to expose surfaces of BSi to dissolution during the subsequent Na_2CO_3 leach phase.

Following a rinse of the remaining sediment samples (three times with Milli-Q), 25 mL of 0.1 M Na_2CO_3 (Sigma-Aldrich BioXtra, CAS: 497-19-8) was pipetted into each of the tubes, which were thoroughly vortexed. A procedural blank was prepared in duplicate. Sample tubes were then placed into a preheated water bath at 85^{o}C, with caps slightly loosened to allow for pressure release. After 20 minutes, tubes were removed from the water bath and the reaction was inhibited by the addition of 2.5 mL, 1 M HCl (in-house distilled). Samples were vortexed then centrifuged at 4000 rpm for 10 minutes. 25 mL of the supernatant was pipetted into new, acid cleaned 50 mL centrifuge tubes which were stored for isotopic analysis. 25 mL of fresh Na_2CO_3 was then added to the sample tubes, which were placed back in the water bath and the digestion was continued for a further 5 hours to allow for total removal of the biogenic phase (Pickering et al., 2020). After 5 hours, the sediment tubes were rinsed three times and frozen overnight. An additional digestion subset was carried out on the same sediment interval in triplicate, which were also pre-treated with 0.1 M and H_2O_2 to determine the BSi content. During this digestion, 0.5 mL aliquots were taken at 20 minutes, as well as 2, 3 and 5 hour intervals and acidified with 0.1 mL 1 M HCl following DeMaster (1981) and Pickering et al. (2020) for determination of the Si concentration by spectrophotometry.

This mild alkaline BSi extraction method is well established and consists of two distinct phases, relying on the difference between rapidly dissolving biogenic material and the slower dissolution of clay minerals (DeMaster, 1981). It is assumed that the majority of Si released in the initial non-linear portion of the experiment consists of biogenic material and the following linear increase in the Si concentration of subsequent aliquots is due to the dissolution of clay minerals (DeMaster, 1981). Therefore, the intercept of the linear regression should represent the sediment BSi content with no contamination from the lithogenic phase (Fig. 2.9). However, it has been shown that non-biogenic phases can also be released into the Na_2CO_3 solution within the first 2 hours of the digestion (Barão et al., 2015), including highly reactive glacially-derived amorphous silica (Hatton, 2019). Ragueneau and Tréguer (1994) estimate that this interference represents an average of 15%

of the BSi content calculated from the intercept of the linear regression. During this study, the 20 minute time interval sampled for isotopic analysis was within or well below the intercept of the linear regression and thus contamination from lithogenic phases is thought to be minimal (e.g. Fig. 2.9). However, for completeness, a correction of the sediment BSi concentrations, as well as their isotopic composition for lithogenic contamination was applied using sample Si and Al concentrations following Kamatani and Oku (2000) and Ragueneau et al. (2005).

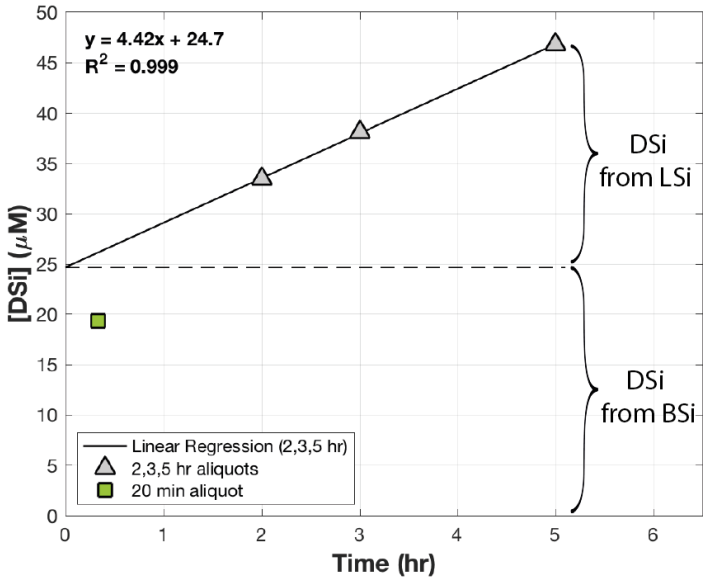

Figure 2.9: Example BSi extraction experiment from this study (B15 frozen, sample triplicate B, 2019). Intercept is extrapolated from the linear regression of the 2, 3 and 5 hour extractions (grey triangles). The green square depicts the [DSi] of the 20 minute extraction, which is below the regression intercept (used to calculate sample BSi content) and was used for Si isotopic analysis. Annotations illustrate the two stages of Si release. DSi released above the dashed line is sourced from the dissolution of clay minerals, while below is from BSi (DeMaster, 1981).

After being stored overnight, sediment tubes were again thawed to room temperature. 10 mL of 4 M NaOH (diluted from Honeywell Fluka 10 M NaOH) was added to the sample tubes, which were then placed into a preheated water bath at 85^{o}C for 2 hours. A procedural blank was prepared in triplicate. After 2 hours the leachate was neutralised with 4.2 mL 10 M HCl (in-house distilled) and vortexed. After centrifuging at 4000 rpm for 10 minutes, the supernatant (14.4 mL) was pipetted into acid-cleaned centrifuge tubes. The sediment was then rinsed once with 9 mL Milli-Q water, which was added to the 14.4 mL supernatant, after which the leached sediment was discarded. All supernatants analysed for Si isotopes were filtered (0.22 μm membrane) prior to column chemistry with acid-cleaned 25 mL syringes (HSW).

2.5 Inductively Coupled Plasma-Optical Emission Spectroscopy

The concentrations of a suite of metals (Al, Ti, Fe, Mn, Mg, V) were determined in the sediment extraction leachates (0.1 M HCl, 0.1 M Na_2CO_3, 4 M NaOH) by Inductively Coupled Plasma-Optical Emission Spectroscopy (ICP-OES) at the University of Bristol, using an Agilent Technologies 710. 0.1 M HCl samples were run in their concentrated form, whereas 0.1 M Na_2CO_3 and 4 M NaOH leachate samples were diluted by 10X and 100X respectively with in-house distilled 1% nitric acid to avoid issues of plasma interference by elevated Na concentrations. Blanks were also run between each sample during NaOH analyses. Where high salt content samples are delivered directly to the ICP-OES, plasma interference can range from simple disturbance through to extinction (∼500 ppm limit), which can potentially result in complications with measurement accuracy and precision (De Oliveira Souza et al., 2015).

After a test run to determine the approximate concentration of each element within the three leachates, ICP-OES calibration was carried out using a blank and five standards of known concentration to generate a calibration curve. The calibration curve was produced to derive a relationship between the intensity of light emitted at a given wavelength, with the concentration of the given element in solution. Multiple wavelengths were used for each run to increase the probability of successful element detection, although any measurement wavelengths that produced unacceptable lines were removed from the datasets.

Analytical performance was assessed throughout the four analytical sessions by periodic measurement of blanks and calibration standards. RSD (1σ) ranged from 0.25-12.75%, averaging 2.70% across repeat standard measurements (n=22) and all elements analysed. ICP-OES data was drift-corrected and corrected for the dilution factors employed to avoid Na interference. Values that were negative or outside the range of the calibration standard concentrations were removed from the dataset. Concentrations that could not be resolved against the blank solution were considered below the detection limit and thus undetectable, and were therefore also omitted. Limits of detection and quantification were calculated for the four analytical sessions, following equations 2.5 and 2.6 (Table 2.3):

$$LOD = [x]_{blank} + 3\sigma \tag{2.5}$$

$$LOQ = [x]_{blank} + 3\sigma \tag{2.6}$$

2.6 Spectrophotometry

DSi concentrations were measured colorimetrically by molybdate blue spectrophotometry (Heteropoly Blue Method, reagents from Hach Company) (Strickland and Parsons, 1972)

Table 2.3: ICP-OES limits of detection (LOD) and quantification (LOQ), calculated as an average across all acceptable wavelengths.

Element	LOD (ppb)	LOQ (ppb)
Al	6.0	16.1
Fe	3.1	8.2
Mg	0.9	2.3
Mn	0.6	1.8
V	0.6	1.4
Ti	0.3	0.8

Table 2.4: Heteropoly Blue Method protocol.

Step	Reagent	Volume	Time
1	Molybdate 3	14 drops	4 minutes
2	Citric Acid	1 powder pillow	1 minute
3	Amino Acid F	1 powder pillow	2 minutes

on a VWR V-1200 spectrophotometer at the University of Bristol (see protocol in Table 2.4). Prior to every analytical session, a Milli-Q (zero) and reagent blank (with no Amino Acid reagent) was analysed, as well as a series of 10 Si standard solutions of known concentrations (0, 1.25, 2.5, 3.75, 5, 10, 15, 20, 25 and 30, 33 and 35 μM) in order to obtain a calibration curve (absorbance *vs* DSi). Samples were diluted with Milli-Q in 15 mL PP centrifuge tubes (1 mL:10 mL) to ensure that absorbance values fell within range of those of the standard solutions. A Milli-Q blank (zero) remained in the spectrophotometer throughout each analytical session and was measured before each individual analysis. Molybdate 3 reagent was added to diluted samples, which reacts with phosphate and silicate under acidic conditions to form yellow phosphomolybdic and silicomolybdic acid complexes. The addition of Citric Acid Reagent then acts to remove the phosphomolybdic complexes, thereby removing interferences, while subsequent introduction of Amino Acid F reduces the yellow silicomolybdic complexes, which produces a blue color, the intensity of which is proportional to the DSi concentration (Hach, 2019).

2.7 Scanning Electron Microscopy

Imaging of the residue left on filter membranes after filtering certain sediment digestion leachates (see Chapter 3) was carried out using a Hitachi S-3500N Scanning Electron Microscope (SEM) at the University of Bristol. Energy Dispersive X-Ray Analysis (EDX) was also carried out using a ThermoNoran energy dispersive X-ray spectrometer to determine which elements were present within the samples to confirm the composition of the

Table 2.5: Goodness of fit measures between observational and simulated data. RMSE given in μM and ‰ for DSi and $\delta^{30}Si$ respectively. Normalised RMSE (NRMSE) is dimensionless, calculated by dividing RMSE by the difference between the maximum and minimum values.

	B13			**B14**			**B15**		
	RMSE	NRMSE	r^2	RMSE	NRMSE	r^2	RMSE	NRMSE	r^2
DSi	13.9	0.12	0.73	19.0	0.16	0.67	10.8	0.12	0.84
δ^{30}Si	0.16	0.12	0.83	0.30	0.13	0.87	0.21	0.11	0.60

residue. Filter membrane samples were mounted on a stub and sputtered with gold to avoid interference with C (Fig. 3.3A). Blank filter membranes were analysed to sample the background elemental composition. Filter membranes used were 0.22 and 0.02 μm PES syringe filters (Pall Acrodiscs) and Corning Costar Spin-X centrifuge tube filters, composed of hydrophilic polyethersulfone ($(C_{12}H_8O_3S)_n$) and cellulose acetate ($C_2H_4O_2{\cdot}x$) respectively.

2.8 Biogeochemical Reaction Network Simulator

2.8.1 Steady state model description

Reaction-transport models (RTMs) are used to simulate and disentangle the complex interplay of chemical reactions and transport processes in sediments. Through use of an array of boundary conditions, a virtual sediment core can be placed in a real world context and used to fit laboratory data, from which it becomes possible to discern further information from concentration and isotopic measurements. For the early diagenesis of Si, this can prove useful as RTMs allow for the quantification of precipitation and dissolution reaction pathways, which can be difficult to constrain otherwise. Data-model best-fits were obtained by minimising the root-mean-square error (RMSE) (equation 2.7) between the predicted and observed values (Table 2.5):

$$RMSE = \sqrt{\frac{1}{n}\sum_{i=1}^{n}(x_i - x_i)^2} \tag{2.7}$$

where i refers to variable i, n is the number of data points, x_i is the observational data and x_i represents the simulated data.

The Biogeochemical Reaction Network Simulator (BRNS) is an adaptive simulation environment suitable for large, mixed kinetic-equilibrium reaction networks (Aguilera et al., 2005; Regnier et al., 2003, 2002). A comprehensive list of boundary conditions and model parameters can be found in Table 2.6. This model assumes a steady state depositional dynamic and therefore cannot resolve seasonal or transient dynamics without modification. BRNS is based on the vertically-resolved mass conservation equation 2.8 (Boudreau,

1997), which simulates concentration changes for solid and dissolved species (i) in porous media at each depth interval and time step:

$$\frac{\delta\sigma C_i}{\delta t} = \frac{\delta}{\delta z}\left(D_{bio}\sigma\frac{\delta C_i}{\delta z} + D_i\sigma\frac{\delta C_i}{\delta z}\right) - \frac{\delta\sigma\omega C_i}{\delta z} + \alpha_i\sigma(C_i(0) - C_i) + \sum_j \lambda_i^j R_j, \qquad (2.8)$$

where ω, C_i, t and z represent the sedimentation rate, concentration of species i, time and depth respectively. The porosity term σ is given as $\sigma = (1 - \varphi)$ for solid species, whereas for dissolved species $\sigma = \varphi$, where φ is sediment porosity. This term ensures that the respective concentrations represent the amount or mass per unit volume of porewater or solids as required (Boudreau, 1997). Porosity is attenuated exponentially with depth to account for sediment compaction, following (Mogollón et al., 2012):

$$\varphi_z = \varphi_x + (\varphi_0 - \varphi_x)e^{-z\cdot\beta} \qquad (2.9)$$

where φ_z and φ_0 is the porosity at depth z and the surface respectively, φ_x refers to porosity at the base of the core and β is the attenuation coefficient. φ_0 and φ_x were determined for each core and depth interval of Barents Sea sediments alongside this study and values for β were established based on best-fits of equation 2.9 to that data. D_{bio} is the bioturbation coefficient, which is modelled as a diffusive process (cm^2 yr^{-1}) and was determined experimentally for ChAOS stations along with the maximum depth of mixing (4.9±1.4 cm at B13 and B14; 6.4±1.6 cm at B15) (Solan et al., 2020). D_i is the effective molecular diffusion coefficient ($D_i = 0$ for solids) for dissolved species i. D_i values for ^{28}Si and ^{30}Si measured in 2^oC seawater were taken from Rebreanu et al. (2008) and corrected for sediment tortuosity (θ^2) to produce D_{sed} (Boudreau, 1996). D_i varies with temperature (T) and viscosity (η), which was calculated with equation 2.10 (Rebreanu et al., 2008), using core top water temperatures measured at each station:

$$D_{sw} = 3.33 \times 10^{-12} \cdot (T \,/\, \eta) \qquad (2.10)$$

Sedimentation rate (ω) is relatively poorly constrained in the Barents Sea (Freitas et al., 2020), with estimates ranging from 0.04-2.1 mm yr^{-1} based on ^{14}C (10-50 cm), ^{210}Pb and ^{137}Cs ($\leq$20 cm below the seafloor) analysis (Carroll et al., 2008a; Elverhøi, 1984; Elverhøi and Solheim, 1983; Faust et al., 2020; Knies and Stein, 1998; Maiti et al., 2010; Smith et al., 1995; Zaborska et al., 2008). Given that measurements of DSi concentration and the isotopic compositions were determined only in the upper 30 cm of seafloor sediment, here we utilise ^{210}Pb sedimentation rate estimates from stations largely consistent with the localities of B13, B14 and B15.

Unlike for bioturbation, the bioirrigation rate (α_i, yr^{-1}) for dissolved species ($\alpha_i = 0$ for solid species) was not experimentally determined alongside this study. Instead we implement a global mean value for the coefficient itself and also for its attenuation depth

(x_{irr}) (Freitas et al., 2020; Thullner et al., 2009). We assume an attenuation depth of 3.5 cm, which typically irrigates sediment down to 15 cm depth (Thullner et al., 2009). The bioirrigation rate is determined from the coefficient applied at the surface (equation 2.11) and describes exchange between the sediment-water interface (SWI) and the pore water below, which is defined as a 'nonlocal' process, i.e. transport of material occurs between points that are not adjacent to one another (Boudreau, 1997). $\sum_j R_j$ represents the sum of the reactions (j) of reaction rate R_j within the implemented network that are either consuming or producing species i, while λ_i^j is the stoichiometric coefficient of species i for reaction j.

$$\alpha = \alpha_0 \cdot e^{\left(\frac{-z}{x_{irr}}\right)} \tag{2.11}$$

Mass conservation equation 2.8 is discretised spatially through use of a one dimensional finite-differencing mechanism (Thullner et al., 2009) over an irregular grid of 101 nodes (Boudreau, 1997), representing 50.4 cm of sampled core depth. Depth intervals are resolved at 0.1 cm to 3 cmbsf, 0.2 cm to 5 cmbsf, 0.4 cm to 10 cmbsf, 0.6 cm to 20 cmbsf and finally 1 cm intervals to 50 cmbsf.

To summarise, equation 2.8 simulates concentration changes for solid and dissolved species in porous media at each depth interval and time step, caused by multiple processes, including: sediment accumulation and compaction, molecular diffusion, macroinfaunal mixing (bioturbation and bioirrigation) and the consumption or production of species as defined by the user implemented reaction network.

2.8.2 Reaction network and isotopic fractionation

The version of Si-BRNS employed in this study is similar to that found in Cassarino et al. (2020), which largely follows the approach of Ehlert et al. (2016a). The model accounts for a pool of sediment pore water DSi (as DSi_{30} and DSi_{28}) and biogenic silica (as BSi_{30} and BSi_{28}). We assume that the total abundance of Si is accounted for by Si_{30} and Si_{28} (95.3%). In order to simulate the isotopic fractionation of Si due to early diagenetic processes, the model upper boundary conditions (at the SWI) require the concentration of the isotopes ^{28}Si and ^{30}Si in mol cm^{-3} of the implemented phases. Through the measured isotopic compositions of each phase and the abundance ratios of the NBS-28 reference standard ($[Si_{29}]/[Si_{28}] = 0.050745$ and $[Si_{30}]/[Si_{28}] = 0.034147$, Ding et al. (2005)), it is possible to calculate the same ratios of the analysed material through rearrangement of equation 2.12 (see equations 2.13 and 2.14). Subsequently, the concentration of each individual Si isotope was calculated through a series of mass balance equations (equations 2.15-2.18), which were used as upper boundary concentrations. A no-flux condition was imposed for all species at the lower boundary of the model environment ($\delta C_i/\delta z = 0$), thereby assuming that biogeochemical processes at greater depth do not influence the modelled

domain.

$$\delta^{30}Si = \left(\frac{(^{30}Si/^{28}Si)_{sample}}{(^{30}Si/^{28}Si)_{NBS-28}} - 1 \right) \cdot 1000 \tag{2.12}$$

$$\frac{[Si_{29}]}{[Si_{28}]}_{sample} = \left(\frac{\delta^{29}Si_{sample}}{1000} + 1 \right) \cdot \frac{[Si_{29}]}{[Si_{28}]}_{standard} \tag{2.13}$$

$$\frac{[Si_{30}]}{[Si_{28}]}_{sample} = \left(\frac{\delta^{30}Si_{sample}}{1000} + 1 \right) \cdot \frac{[Si_{30}]}{[Si_{28}]}_{standard} \tag{2.14}$$

$$\frac{[Si_{28}]}{[Si_{tot}]} + \frac{[Si_{29}]}{[Si_{tot}]} + \frac{[Si_{30}]}{[Si_{tot}]} = 1 \tag{2.15}$$

$$\frac{\frac{[Si_{28}]}{[Si_{tot}]} + \frac{[Si_{29}]}{[Si_{tot}]} + \frac{[Si_{30}]}{[Si_{tot}]}}{[Si_{28}]} = \frac{1}{[Si_{28}]} \tag{2.16}$$

$$\therefore [Si_{28}] = \frac{1}{\frac{1}{[Si_{tot}]} + \frac{1}{[Si_{tot}]} \cdot \left(\frac{[Si_{29}]}{[Si_{28}]} + \frac{[Si_{30}]}{[Si_{28}]} \right)} \tag{2.17}$$

$$\therefore [Si_{29}] = [Si_{tot}] - [Si_{28}] - \left([Si_{28}] \cdot \frac{[Si_{30}]}{[Si_{28}]} \right) \tag{2.18}$$

Following Ehlert et al. (2016a) and Cassarino et al. (2020), the model used in this study accounts for a pool of pore water DSi, sourced by a dissolving biogenic phase (BSi), from which Si can be incorporated into authigenic clay minerals as they precipitate ($AuSi_{30}$ and $AuSi_{28}$), thereby inducing a fractionation on the DSi phase. The Si isotopic fractionation factor ($^{30}\epsilon$) associated with clay mineral precipitation is relatively high (-1.8 to -2.2 ‰) (Hughes et al., 2013; Opfergelt and Delmelle, 2012; Ziegler et al., 2005a,b). The kinetic rate law for the dissolution of BSi follows equation 2.22 (Hurd, 1972), where k_{diss} is the reaction rate constant (yr^{-1}) and BSi_{sol} is the solubility of BSi (mol cm^{-3}), therefore stating that the rate is proportional to the saturation state of the DSi phase. The rate of BSi dissolution is allowed to decrease exponentially downcore following equation 2.21, where *ad* is the attenuation coefficient and *bd* is the minimum reaction rate, in order to account for a reduction in reactivity due to maturation and interaction with dissolved Aluminium (Al), as well as the preferential dissolution of more reactive material at shallower depths (Dixit et al., 2001; Rabouille et al., 1997; Rickert, 2000; Van Cappellen and Qiu, 1997b). While this study assumed that no isotopic fractionation occurs during BSi dissolution (α_d = 1.0) (Ehlert et al., 2016a; Wetzel et al., 2014), equations 2.23 and 2.24 allow for an equilibrium fractionation to be induced if required, through use of the fractionation factor α_d. Indeed, previous work has shown that BSi dissolution can sometimes induce a slight fractionation that enriches the DSi pool in the lighter isotope ($^{30}\epsilon$ of -0.55 ‰) (Demarest et al., 2009).

$$fb_{30} = \frac{BSi_{30}}{BSi_{30} + \alpha_d \cdot BSi_{28}} \tag{2.19}$$

$$fb_{28} = \frac{\alpha_d \cdot BSi_{28}}{BSi_{30} + \alpha_d \cdot BSi_{28}} \tag{2.20}$$

$$fb_z = e^{-ad \cdot x_{pos}} + bd \tag{2.21}$$

$$R_{db} = k_{diss} \cdot fb_z \cdot (BSi_{30} + BSi_{28}) \cdot \left(1.0 - \frac{(DSi_{30} + DSi_{28})}{BSi_{sol}}\right) \tag{2.22}$$

$$R_2 = fb_{30} \cdot R_{db} \tag{2.23}$$

$$R_3 = fb_{28} \cdot R_{db} \tag{2.24}$$

An additional two reaction pathways have been introduced into our model relative to those of Cassarino (2018) and Ehlert et al. (2016a): the dissolution of a lithogenic phase (LSi_{30} and LSi_{28}) and two reaction rates representing the release of DSi_{30} and DSi_{28} from solid phase Fe (oxyhydr)oxides. As for BSi, LSi dissolution is assumed to be dependent upon the degree of pore water DSi undersaturation and follows equation 2.27, where $k_{LSidiss}$ is the dissolution rate constant and LSi_{sol} represents the solubility of the lithogenic phase. Lerman et al. (1975) determined during a dissolution experiment of common silicate minerals that the reaction could be described by a first-order rate law, driven by the saturation state. The concentration of LSi (LSi_{28} and LSi_{30}) was determined based on sedimentary bulk Si contents measured by wavelength dispersive X-ray fluorescence (XRF) of the 0-0.25 cm sediment core depth interval: 26.1, 24.7 and 23.3 % Si at stations B13, B14 and B15 respectively. For XRF analyses, 700 mg sample splits were mixed with 4.2 g of di-lithiumtetraborate ($Li_2B_4O_7$, Spectromelt A10) and fused to form homogeneous glass beads, having been preoxidized at 500°C with 1 g of NH_4NO_3. Analysis of the homogeneous glass beads was carried out using a Philips PW-2400 WD-XRF spectrometer at the University of Oldenburg. The XRF spectrometer was calibrated with 53 geostandards. The accuracy and analytical precision of the XRF analysis was better than 5%, quantified using both in-house and international reference materials. Bulk sediment Si contents were then corrected for the BSi component, assuming that almost all of the solid phase is composed of terrigenous material. In Chapter 4, it was determined that approximately 96% of Barents Sea surface sediments are terrigenous in origin, calculated using equation 2.25 (Sayles et al., 2001):

$$\%Terrigenous = 100 - \%(BSi + \mathrm{CaCO_3} + TOC) \tag{2.25}$$

where TOC refers to total organic carbon content of the surface sediment interval.

The LSi dissolution rate is set to decrease exponentially with depth, following equation 2.26, where al is the attenuation coefficient, bl represents the minimum rate and x_{pos} is depth. This exponential reduction in rate is imposed because the uppermost sediment layers are thought to be where the majority of dissolved Al sourced from LSi dissolution is released in marine sediments (Ehlert et al., 2016a; Geilert et al., 2020a; Van Beusekom et al., 1997). We have assumed there is no isotopic fractionation during the dissolution of LSi.

$$fl_z = e^{-al \cdot x_{pos}} + bl \tag{2.26}$$

$$R_{dl} = k_{LSidiss} \cdot fl_z \cdot (LSi_{30} + LSi_{28}) \cdot \left(1.0 - \frac{(DSi_{30} + DSi_{28})}{LSi_{sol}}\right) \tag{2.27}$$

The desorption of DSi from solid phase Fe (oxyhydr)oxides as they reductively dissolve under hypoxic and anoxic conditions was modelled through two reaction rate constants, representing the release of DSi_{30} (k_{FeSi30}) and DSi_{28} (k_{FeSi28}) from the solid phase (equations 2.28-2.29). This parameter likely represents a significant simplification, however the exact process pertaining to the adsorption of Si onto Fe (oxyhydr)oxides is unclear and requires further study (Geilert et al., 2020a). Adsorption of Si onto Fe (oxyhydr)oxides preferentially takes up the lighter isotope, the degree to which is thought to increase with mineral crystallinity ($^{30}\epsilon$ of -1.06‰ for ferrihydrite and -1.59‰ for goethite) (Delstanche et al., 2009). Furthermore, Chapter 4 presents evidence for the presence of an isotopically light metal oxide phase, through analysis of weak acid leachates used to extract solid phase reactive Si pools (-2.88 ±0.17 ‰). The implemented ratio of k_{FeSi30} and k_{FeSi28} in the model reflects the composition of this reactive pool.

Step-functions (SW03 and SW04) were implemented in the FeSi reactions in the model to simulate the desorption of this phase at specific depth intervals, representing the Fe redox boundaries identified in Chapter 4. The step-functions act as a cut-off mechanism, either setting reaction rates to zero or activating them at specific depths. Release of the FeSi phase was ceased at a particular depth interval, determined based on the best-fit between the simulated and measured data.

$$R_7 = SW03 \cdot SW04 \cdot k_{FeSi28} \tag{2.28}$$

$$R_8 = SW03 \cdot SW04 \cdot k_{FeSi30} \tag{2.29}$$

The precipitation of authigenic clay minerals ($AuSi_{30}$ and $AuSi_{28}$) was modelled with equation 2.33, where k_{precip} represents the authigenic precipitation rate constant (Ehlert et al., 2016a). This rate law states, through use of a step-function ($SW02$), that the reac-

tion will proceed providing the concentration of DSi is greater than the solubility of the authigenic clay phase ($AuSi_{sol}$). The rate is thus proportional to the degree of pore water DSi oversaturation (Ehlert et al., 2016a). As with BSi dissolution, the rate of AuSi precipitation was allowed to decrease exponentially with depth through equation 2.32, where ap is the attenuation coefficient and bp is the minimum reaction rate. This reduction in reaction rate with depth accounts for the general consensus that the majority of authigenic clay mineral precipitation occurs in the upper portion of marine sediment cores. Here, DSi can more easily precipitate in the presence of dissolved Al, the concentration of which is typically higher in the upper reaches of shelf sediments, sourced from the dissolution of reactive LSi minerals (e.g. feldspar and gibbsite) contemporaneous to that of BSi (Aller, 2014; Ehlert et al., 2016a; Rabouille et al., 1997; Van Beusekom et al., 1997). Fractionation of the dissolved phase associated with clay mineral precipitation is accounted for by equations 2.34 and 2.35, through the fractionation factor α_p.

$$fp_{30} = \frac{DSi_{30}}{DSi_{30} + \alpha_p \cdot DSi_{28}} \tag{2.30}$$

$$fp_{28} = \frac{\alpha_p \cdot DSi_{28}}{DSi_{30} + \alpha_p \cdot DSi_{28}} \tag{2.31}$$

$$fp_z = e^{-ap \cdot x_{pos}} + bp \tag{2.32}$$

$$R_p = SW02 \cdot k_{precip} \cdot fp_z \cdot \left(\frac{(DSi_{30} + DSi_{28})}{AuSi_{sol} - 1.0} \right) \qquad \text{if [DSi]} > AuSi_{sol} \tag{2.33}$$

$$R_{10} = fp_{30} \cdot R_p \tag{2.34}$$

$$R_{11} = fp_{28} \cdot R_p \tag{2.35}$$

*Table 2.6: BRNS transport and reaction parameters and boundary conditions. Values are 'independent' (I) if based on laboratory or fieldwork measurements, 'constrained' (C) if potential values could be bracketed or calculated from an empirical relationship, or finally 'model-derived' (M). *Lerman et al. (1975) determined that glauconite, a common aluminosilicate reverse weathering product of BSi has a solubility of ∼50 μM in seawater at low temperatures. Hurd (1973) calculated that sepiolite, an authigenic clay mineral that forms on BSi could precipitate from sediment pore waters with a DSi as low as 30 μM. Zhu et al. (2016) observed fractionation factors ($^{30}\epsilon$) of -2.87 to +0.80 ‰, averaging -0.995 ±1.16 ‰ (1σ) during albite dissolution, with the DI water solution becoming enriched in the lighter isotope. However, the magnitude of $^{30}\epsilon$ was found to be dependent on pH and was much lower at pH 7 (averaging 0.11 ±0.98 ‰). References: [1] Thullner et al. (2009); [2] Zaborska et al. (2008); [3] Rebreanu et al. (2008); [4] Van Cappellen et al. (2002); [5] Lerman et al. (1975); [6] Hurd (1973); [7] Wetzel et al. (2014); [8] Opfergelt and Delmelle (2012); [9] Zhu et al. (2016).*

Parameter	**Unit**	**Type**	**B13**	**B14**	**B15**	**Source**
General						
L	cm	-	50.4	50.4	50.4	-
nNodes	-	-	101	101	101	-
Run time	yr	-	2600	3000	3000	-
T	^oC	I	1.78	1.9	-1.49	-
S	PSU	I	35.014	35.01	35.9	-
Depth	m	I	359	293	317	-
φ_0	-	I	0.83	0.89	0.90	-
φ_x	-	I	0.62	0.65	0.65	-
β	-	I	0.10	0.105	0.105	-
Transport						
D_{bio}	cm^2 yr^{-1}	I	6.1	3.9	1.9	-
x_{bio}	cm	I	2.0	2.0	2.0	-
α_0	yr^{-1}	C	10	10	10	[1]
x_{irr}	cm	C	3.5	3.5	3.5	[1]
ω	cm yr^{-1}	C	0.05	0.05	0.06	[2]
$D_{sed^{28}Si}$	cm^2 yr^{-1}	C	125	127	128	[3]
$D_{sed^{30}Si}$	cm^2 yr^{-1}	C	125	127	128	[3]
Reaction						
$[DSi_{28}]$	μmol Si cm^{-3}	I	0.00645	0.00829	0.00553	-
$[DSi_{30}]$	μmol Si cm^{-3}	I	0.00022	0.00028	0.00019	-
$[BSi_{28}]$	μmol Si cm^{-3} solid	I	$3.22{\cdot}10^2$	$4.27{\cdot}10^2$	$2.12{\cdot}10^2$	-
$[BSi_{30}]$	μmol Si cm^{-3} solid	I	$1.1{\cdot}10^1$	$1.46{\cdot}10^1$	7.23	-
$\delta^{30}Si_{DSi}$	‰	I	1.64	1.46	1.69	-

$\delta^{29}Si_{DSi}$	‰	I	0.84	0.8	0.89	-
$\delta^{30}Si_{BSi}$	‰	I	1.43	1.5	0.82	-
$\delta^{29}Si_{BSi}$	‰	I	0.71	0.76	0.39	-
$\delta^{30}Si_{LSi}$	‰	I	-0.89	-0.89	-0.89	-
$\delta^{29}Si_{LSi}$	‰	I	-0.49	-0.49	-0.49	-
$\delta^{30}Si_{FeSi}$	‰	I	-2.88	-2.88	-2.88	-
$\delta^{29}Si_{FeSi}$	‰	I	-1.46	-1.46	-1.46	-
BSi_{sol}	μM	C	800	800	800	[4]
LSi_{sol}	μM	C	95	100	95	Table 5.2
$AuSi_{sol}$	μM	C	50	50	50	[5,6]*
k_{diss}	yr^{-1}	M	$0.55{\cdot}10^{-2}$	$7.4{\cdot}10^{-2}$	$1.05{\cdot}10^{-2}$	-
$k_{LSidiss}$	yr^{-1}	M	$200{\cdot}10^{-4}$	$500{\cdot}10^{-5}$	$300{\cdot}10^{-5}$	-
k_{precip}	mol Si cm^{-3} yr^{-1}	M	$0.65{\cdot}10^{-4}$	$0.6{\cdot}10^{-5}$	$4.5{\cdot}10^{-5}$	-
$k_{FeSi_{28}}$	mol Si cm^{-3} yr^{-1}	M	$1.44{\cdot}10^{-6}$	$5.578{\cdot}10^{-8}$	$5.578{\cdot}10^{-8}$	-
$k_{FeSi_{30}}$	mol Si cm^{-3} yr^{-1}	M	$4.903{\cdot}10^{-8}$	$1.899{\cdot}10^{-9}$	$1.899{\cdot}10^{-9}$	-
α_d	-	C	1.0	1.0	1.0	[7]
α_p	-	C	1.0023	1.002	1.0023	[8]
α_l	-	C	1.0	1.0	1.0	[9]
ad	-	M	0.2	0.42	0.4	-
al	-	M	0.2	0.01	0.05	-
ap	-	M	0.65	0.85	0.35	-
bd	yr^{-1}	M	0.05	0.0	0.0	-
bl	yr^{-1}	M	6.0	1.5	6.0	-
bp	mol Si cm^{-3} yr^{-1}	M	0.05	0.0065	0.0001	-

Chapter 3

Using stable silicon isotopes and element ratios to study the characteristics of reactive Si pools in Barents Sea sediments

Sections 3.4.3 and 3.4.2 of this chapter reproduce the supplementary material of an article accepted for publication at Geochimica et Cosmochimica Acta, authored by J.P.J. Ward, K.R. Hendry, S. Arndt, J.C. Faust, F.S. Freitas, S.F. Henley, J.W. Krause, C. März, H.C. Ng, R.A. Pickering and A.C. Tessin (Chapter 4). The article is titled 'Stable Silicon Isotopes Uncover a Mineralogical Control on the Benthic Silicon Cycle in the Arctic Barents Sea' (ArXiv [preprint], https://doi.org/10.31223/X5F04Z). As lead author, I completed all laboratory analysis for Si isotopic compositions, as well as digestion experiences on solid phase samples, including measurement of element concentrations through spectrophotometry and ICP-OES (Si, Al, Fe, Mg, Mn, Ti, V). I led on writing the article, producing original figures and responding to reviewer comments.

3.1 Introduction

Marine sediment BSi content and its isotopic composition are commonly used to gain a better understanding of the early diagenetic cycling of Si, which can also be used as a paleoproxy for the uptake of DSi by diatoms. Historically, other pools of reactive Si have been neglected and so are relatively poorly understood. This lack of research and understanding has lead to a loss of valubale information on important early diagenetic processes, an underestimation of the mass of reactive Si in marine sediments and a potential biasing of measured BSi δ^{30}Si values (Pickering et al., 2020). Through use of a sequential alkaline digestion following a HCl pre-treatment, coupled to stable Si isotope analysis,

Pickering et al. (2020) observed a -5‰ difference in the δ^{30}Si of the mild acid and alkaline leachable pools, sampled from coastal river plume sediments. This observation highlights that previous studies have missed potentially important information, but also indicates that published isotopic compositions of BSi may incorporate a degree of contamination from the acid leachable phase, where an HCl pretreatment was not employed.

The reactive pools of Si studied here through a similar sequential digestion protocol are defined as follows: mild acid digestible (0.1 M HCl leachate, hereby referred to as Si-HCl); mild alkaline digestible (0.1 M Na_2CO_3 leachate, hereby referred to as Si-Alk); strong alkaline digestible (4 M NaOH leachate, hereby referred to as Si-NaOH) (DeMaster, 1981; Michalopoulos and Aller, 2004; Pickering, 2020; Pickering et al., 2020; Rahman et al., 2016). Here we also incorporate a H_2O_2 pre-treatment, carried out after the mild acid digestion and prior to the extraction of Si-Alk. Pickering et al. (2020) found that the 0.1 M HCl Si pool was very isotopically light for the marine environment (-2.89 ±0.45‰), and is thought to be associated with authigenic metal (Al, Fe and Mn) oxides that coat BSi particulates (Pickering et al. (2020) and references therein). The Si-Alk pool is associated with diagenetically altered and unaltered BSi, while the Si-NaOH pool is thought to liberate reactive LSi and residual, refractory BSi.

Many previous studies that analyse the isotopic composition of BSi in marine sediments do not report on additional reactive Si pools, as they follow a traditional alkaline digestion methodology (DeMaster, 1981), which omits an HCl pretreatment (Ehlert et al., 2016a; Frings et al., 2014; Ziegler et al., 2005a). Pickering et al. (2020) suggest that coastal environments where eutrophiciation has driven an increase in BSi deposition over the last century, could see a corresponding growth in authigenic product formation, resulting in greater Si and cation sequestration. It is therefore important to further study these operationally defined reactive pools for quantification in future global ocean element budgets. In the Barents Sea and wider Arctic Ocean context, characterisation of the isotopic composition of each of the reactive Si pools is critical for the future closure of the regional Si isotope budget (see section 5.4.5), as our current understanding is limited by a lack of sediment BSi δ^{30}Si observations (Brzezinski et al., 2021). A traditional alkaline digestion will not fully resolve the intricacies of the reactive components within seafloor sediments, resulting in minor changes to the estimated content of authigenic products, with potentially significant implications for the Si budget (DeMaster, 2002; Pickering et al., 2020). This study is the first of its kind in a non-estuarine or coastal setting and will allow for a comprehensive understanding of the composition of Si pools in Barents Sea sediments, which must be well characterised given the potential importance of BSi burial in balancing the regional isotope budget (Brzezinski et al., 2021).

For consistency, here I follow the sample preparation techniues employed by Pickering et al. (2020), however the methodologies commonly used to study marine sediment BSi pools are highly inconsistent across laboratories. Sample storage and preparation tech-

niques include: sediment pre-treatment with HCl and/or H_2O_2, freezing, freeze-drying, oven-drying and possible homogenisation through grinding. This lack of consistency results in uncertainty when compiling and comparing data on a global scale. In this thesis I also present the results of a set of sensitivity experiments, designed to determine the influence of different sediment pre-treatments on BSi content, as well as on the isotopic composition of the operationally defined pools of reactive Si sampled from a sequential digestion experiment protocol (Pickering et al., 2020), to assess whether the influence of these different sample preparation techniques can be traced isotopically. Recommendations are then made in an attempt to improve the consistency of interlaboratory analyses.

3.2 Materials and Methods

Operationally-defined reactive pools of Si were extracted from sediment samples following a sequential digestion protocol presented in Pickering et al. (2020). This sequential digestion separates the reactive pools based on the conditions, kinetics and sequence of the reaction (DeMaster, 1981; Michalopoulos and Aller, 2004; Pickering et al., 2020; Rahman et al., 2016). The following reagents were added in sequence to 50-70 mg of thawed surface sediment samples (0-0.5 cmbsf), collected during cruise JR16006 (2017) from stations B13, B14 and B15: 0.1 M HCl, 0.1 M Na_2CO_3, 4 M NaOH. These reagents are thought to activate authigenic products (metal oxides and AuSi), reactive BSi and LSi/recalcitrant BSi respectively (Pickering et al., 2020). A treatment with 10% H_2O_2 was also carried out on surface sediment samples to remove diluting organic carbon phases (see section 3.4.3). The concentration of DSi within the leachates (and thus the BSi content) was determined colorimetrically by molybdate blue spectrophotometry (Strickland and Parsons, 1972). The concentrations of a suite of metals (Al, Ti, Fe, Mn, Mg, V) was also determined in the leachates by ICP-OES to confirm the source of Si within each pool, and Si isotopes were measured using MC-ICP-MS (see section 2.3).

The traditional mild alkaline digestion method used to determine sediment BSi contents (DeMaster, 1981), whereby aliquots of Na_2CO_3 are extracted at 2, 3 and 5 hr intervals, requires the assumption that the Si released in a non-linear fashion over the first 1-2 hours is sourced from BSi (section 2.4) (Fig. 2.9). However, Barão et al. (2015) showed that non-biogenic phases can also be released into the Na_2CO_3 solution within the initial non-linear release phase. Ragueneau and Tréguer (1994) estimate that this interference represents ∼15% of the estimated BSi content. In order to minimise LSi contamination for isotopic analysis, digestion experiments were ceased at 20 minutes by neutralisation with in-house distilled HCl (Pickering et al., 2020). The [DSi] in the 20 minute Na_2CO_3 extractions were all below the linear regression intercept, thus contamination from LSi is thought to be minimal (Fig. 2.9). Corrections for LSi interference following Kamatani and Oku (2000) and Ragueneau et al. (2005) were carried out to confirm this assumption

(section 3.4.2).

An additional sensitivity study was also carried out to assess the influence of oven drying and grinding sediment samples prior to isotopic analysis. Oven-drying sediment samples can result in Si volatilisation (Conley, 1998) and fragmentation of diatom material (Flower, 1993), while grinding samples prior to digestion experiments can artificially increase reactivity by reducing surface crystallinity (Pickering, 2020). Previous work has found that a correction factor applied due to the effect of sample grinding/crushing can result in a reduction in the calculated sediment BSi content of 50% (DeMaster et al., 1983; Michalopoulos and Aller, 2004). Regardless, sediment drying and grinding remains a common method of sample preparation. Therefore, a method test was carried out in this study to assess the impact of drying and grinding of sediment on both the mass of silica released in and the isotopic composition of the leachates.

The 0-0.5 cmbsf core slice collected in 2019 from station B15 was selected at random for the method development study. BSi content, as well as δ^{30}Si and the concentration of a suite of metals was determined for all three leachates, in each sediment sample triplicate (50-70 mg dry weight) on three distinct groups, consisting of different preparation techniques: 1) thawed from frozen, 2) dried/in-tact and 3) dried/ground. Half of the B15 frozen sediment core slice was dried in a drying cabinet for 24 hours at 60^{o}C (for group 2), half of which was then thoroughly ground with a mortar and pestle (Cole-Parmer Agate) (for group 3). After grinding, the sample was allowed to re-equilibrate with the atmosphere for 24 hours before digestion.

A full description of the sediment digestion protocol (as well as methods to determine element concentrations and isotopic compositions) can be found in Chapter 4 and section 2.4.

3.3 Results

3.3.1 Isotopic Composition of reactive Si pools

Isotopic analysis of the sediment digestion leachates revealed highly variable compositions between the three reactive Si pools and a very isotopically light Si-HCl pool ($\delta^{30}Si_{HCl}$), which ranged from -3.0 to -2.7‰ with a mean of -2.88 ±0.17‰ (2σ, n=20). $\delta^{30}Si_{HCl}$ in Barents Sea surface sediments was within long term reproducibility at stations B13, B14 and B15. These observations are consistent with the findings of Pickering (2020), who measured a $\delta^{30}Si_{HCl}$ that ranged from -3.34 to -2.61‰, averaging -2.89 ±0.45‰ (2σ, n=48) in Mississippi River plume sediments.

In contrast to the Si-HCl pool, the isotopic composition of the Si-Alk pool ($\delta^{30}Si_{Alk}$) in Barents Sea sediments does vary spatially. The mean $\delta^{30}Si_{Alk}$ at stations B13 and B14 was +1.43 ±0.12‰ (2σ, n=8) and +1.50 ±0.19‰ (2σ, n=7) respectively, whereas the mean $\delta^{30}Si_{Alk}$ measured at station B15 in the northern, seasonally ice-covered region was

+0.82 ±0.16‰ (2σ, n=14). $\delta^{30}Si_{Alk}$ is therefore ~4‰ higher than $\delta^{30}Si_{HCl}$ in Barents Sea sediments. $\delta^{30}Si_{Alk}$ is within range of previously measured δ^{30}Si in BSi, which ranges from -0.7 to +3.5‰ (Sun et al., 2014; Sutton et al., 2018; Varela et al., 2016). The δ^{30}Si of marine diatoms is thought to average +1.1‰ (Sutton et al., 2018).

Consistent with Si-HCl, the isotopic composition of the Si-NaOH pool ($\delta^{30}Si_{NaOH}$), associated with LSi and residual BSi, showed very little variation between the three stations. $\delta^{30}Si_{NaOH}$ ranged from -1.02 to -0.79‰, averaging -0.89 ±0.16‰ (2σ, n=18). Barents Sea $\delta^{30}Si_{NaOH}$ values are therefore slightly isotopically lighter than those sampled from Mississippi River plume sediment digestions -0.54 ±0.15‰ (2σ, n=48) (ranging from -0.84 to -0.10‰) (Pickering, 2020). However, both the $\delta^{30}Si_{NaOH}$ measured in the Mississippi River plume and Barents Sea surface sediments is within range of the global average clay composition (-0.57 ±0.6‰) (Bayon et al., 2018).

Sample handling and preparation techniques (i.e. oven-drying and grinding) had a statistically significant impact on the isotopic composition of the Si-HCl and Si-Alk reactive Si pools. Station B15 surface sediment sub-samples that were oven-dried presented with δ^{30}Si values of +0.95 ±0.03‰, -2.85 ±0.05‰ and -0.89 ±0.12‰ in the Si-Alk, Si-HCl and Si-NaOH pools respectively. Sediment samples that were subsequently homogenised with a mortar and pestle prior to the sequential digestion, presented with δ^{30}Si values of +0.91 ±0.05‰, -2.55 ±0.03‰ and -0.89 ±0.02‰. Overall, oven-dried sediment sample leachates presented with an isotopically heavier Si-Alk pool, while the oven-dried and ground samples also had an isotopically heavier Si-HCl pool. $\delta^{30}Si_{NaOH}$ was consistent within long-term reproducibility across the three sample preparation techniques (frozen/thawed, oven-dried, oven-dried/ground) (Fig. 3.4).

3.3.2 Element concentrations in reactive Si pools

With regard to the mass of Si released into each leachate, the Si-HCl pool is the smallest, with an average of 90 ±11 μmol Si g^{-1} liberated from the surface sediment sample across the three Barents Sea stations (0-0.5 cm) (2σ, n=9, ranging from 81 to 97 μmol Si g^{-1}). The Si-Alk pool averaged 122 ±110 μmol Si g^{-1} (n=9, ranging from 55 to 195 μmol Si g^{-1}), while the Si-NaOH pool was the largest of the three, averaging 436 ±75 μmol Si g^{-1} (n=9, ranging from 381 to 482 μmol Si g^{-1}), approximately five and four-fold larger than the Si-HCl and Si-Alk pools respectively. In a similar study of Mississippi River plume sediments, Pickering (2020) also observed that the Si-NaOH pool (921 ±451 μmol Si g^{-1}) was the dominant of the three by mass, approximately five to 13-fold larger than the Si-HCl (99 ±42 μmol Si g^{-1}) and Si-Alk pools (89 ±45 μmol Si g^{-1}).

A suite of additional element concentrations (Al, Fe, Mg, Mn, Ti, V) were determined by ICP-OES in the three reactive Si pools (see section 2.5 for a description of the method). We observe a similar distribution in the data to Pickering (2020) in sediments that were thawed from frozen, with similar concentrations of Si across the Si-HCl and Si-Alk pools,

but two orders of magnitude lower concentrations of other elements in the Si-Alk pool relative to Si-HCl (Al, Fe, Mg, Mn) (Fig. 3.1). The only contrast with Pickering (2020) with regard to the concentration of these reactive elements, is that Al and Ti present with either similar, or larger concentrations in the Si-Alk leachates of Mississippi River plume sediments, relative to the Si-HCl samples. Leachates that had been in contact with sediment samples that were oven-dried overnight at 60^{o}C for the method sensitivity experiments, present with similar element concentrations to their frozen/thawed counterparts in the Si-HCl pool, but significantly elevated Mg and Mn concentrations in the Si-Alk pool (4 and 35-fold respectively), as well as slightly increased concentrations across all elements in the Si-NaOH phase (1.1 to 1.6-fold).

3.3.3 Sediment BSi contents

During the Si-Alk extraction step of the sequential digestion protocol, the BSi content of the surface sediment samples was estimated following the traditional method of DeMaster (1981). The DeMaster (1981) method uses a weak base (0.1 M Na_2CO_3) to encourage the dissolution of BSi, with minimal interference from silicate minerals. Aliquots of the Na_2CO_3 supernatant were sampled at the 2, 3 and 5 hr time intervals of the digestion for stations B13, B14 and B15, leading to estimated BSi contents of 0.39 $\pm$0.09, 0.52 $\pm$0.02, 0.26 $\pm$0.07 wt% (or 139 $\pm$33, 185 $\pm$7 and 92 $\pm$24 μmol g dry wt^{-1}) respectively. This BSi extraction method is based upon the assumption that most of the Si released from the sediment within the first two hours is from BSi, and the observation that primary and secondary silicate minerals release Si in a linear fashion over time. These assumptions allow for a separation of the two phases, therefore the 0 hr time intercept of a linear regression across the time course extractions is assumed to represent the BSi content, without interference from silicate minerals (Fig. 2.9) (DeMaster, 1981).

BSi contents of the Barents Sea stations are very low relative to the global seafloor average, estimated to be 14% (Mathewson, 2003), while values can exceed 80% in the Southern Ocean (Demaster, 1992; DeMaster et al., 1991). However, it is well established that Arctic Ocean sediment BSi contents rarely exceed 5 wt% (März et al. (2015) and references therein). BSi contents of the middle (14-15 cm) and deepest core slices (between 36 and 43 cm depth) were also determined, in addition to the surface sediment depth interval. At all three stations, the BSi content approaches a minima of $\sim$0.2 wt% by the mid-core (14-15 cm interval).

Sample handling and preparation techniques (i.e. oven drying and grinding) appeared to have an impact on the estimated BSi content. Experiments carried out on station B15 surface sediment indicate BSi contents of 0.12 $\pm$0.03 and 0.35 $\pm$0.05 wt% in the dried and dried/ground samples respectively (Fig. 3.4), representing a two-fold decrease and 1.3-fold increase relative to the frozen counterpart that had been thawed to room temperature prior to analysis.

3.4 Discussion and conclusions

3.4.1 What are the primary sources of Si in the reactive pools and the main controls on their formation?

The results of the sequential digestion experiment clearly demonstrate the presence of multiple operationally-defined reactive pools of Si within Barents Sea sediments, just as they have within coastal sediments globally (Krause et al., 2017; Michalopoulos and Aller, 2004; Pickering et al., 2020; Presti and Michalopoulos, 2008; Qin et al., 2012; Wang et al., 2015a). In order to infer the source of reactive Si within each reactive pool, the concentration of a suite of elements was measured by ICP-OES to calculate element ratios.

Molar Si/Fe ratios in the Si-HCl leach average 0.6 mol/mol across all Barents Sea surface sediments (Table 3.1), which is greater than that measured in marine Fe-Mn (oxyhydr)oxides, for example from the Atlantis II deep basin in the Red Sea (0.04-0.5 mol/mol, mainly composed of goethite and ferrihydrite) (Taitel-Goldman et al., 2009), and lower than the Si/Fe in modern Fe-Si (oxyhydr)oxide deposits sampled from a hydrothermal field of the Southwest Indian Ridge (0.67-0.72 mol/mol) (Sun et al., 2015). Pickering (2020) and Presti and Michalopoulos (2008) observed a similar trend, with Si-HCl molar Si/Fe ratios averaging 1.02 (range of 0.66-1.65) and 0.91 mol/mol respectively. Whereas, Mn/Fe ratios measured in the HCl leachate (0.16 mol/mol) are within range of Red Sea Fe (oxyhydr)oxides (0.1-0.25 mol/mol) (Taitel-Goldman et al., 2009), which is consistent with the suggestion that the acid-leachable Si fraction is in part sourced from authigenic metal oxides (Pickering et al., 2020). Molar Fe/Al ratios in the Barents Sea HCl leachate support this suggestion (2.5-5.2 mol/mol, averaging 3.2), which are much higher than the upper continental crust (0.21 mol/mol) (McLennan, 2001) and similar to Fe-rich hydrothermal plume sediments from the Gorda Ridge (2-6 mol/mol) (Feely et al., 1998). The Si/Fe ratios indicate the presence of elevated Si, relative to Fe, which could reinforce the suggestion that this pool can be associated with wider early diagenetic products, such as highly reactive, poorly formed authigenic clays (Pickering, 2020). This hypothesis would explain why Si/Fe in the Barents Sea sediment HCl leachate is greater than that measured in Red Sea Fe-Mn (oxyhydr)oxides, but lower than Red Sea Fe-Si (oxyhydr)oxides, as the latter measurement incorporates amorphous Si precipitates present on the Fe-filaments (Sun et al., 2015; Taitel-Goldman et al., 2009). Further, Al/Si ratios measured in the HCl leachate average 0.56 mol/mol (0.49-0.57), within range of common clay minerals (0.48-0.96 mol/mol) (Kim et al. (2004); Koning et al. (2002); Rahn (1976) and references therein). Therefore, the Si and Al present within the HCl leachate could be constituent of authigenic clay mineral precipitates incorporated within, or adhered to, the reactive metal oxides (Buffle et al., 1989).

It is widely accepted that weathering in marine sediments results in the transfer of terrestrially-derived elements (e.g. Al, Fe, Ti, Mn) and seawater cations (e.g. Mg, K)

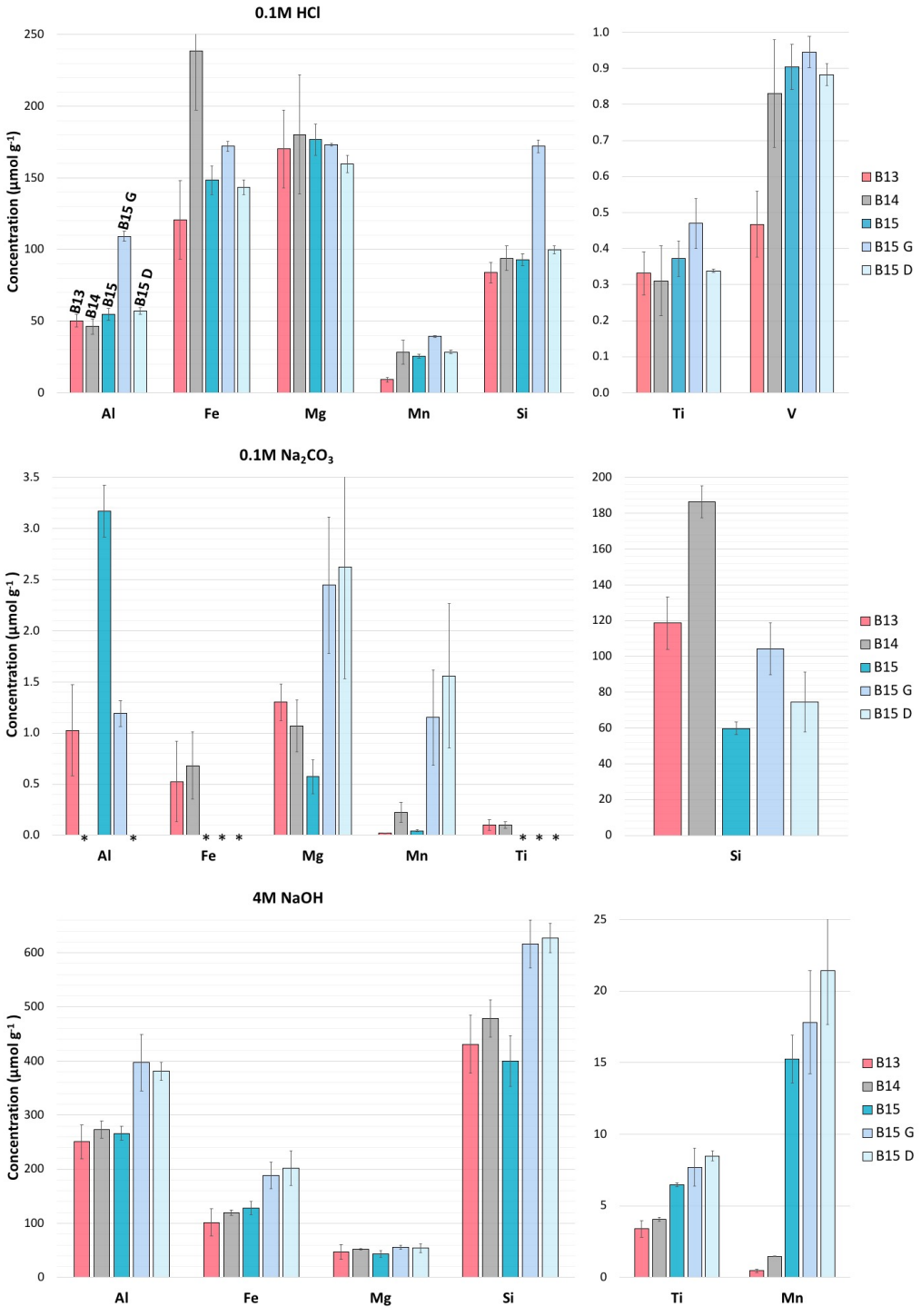

*Figure 3.1: Concentration of metals (µmol per dry weight g of sediment) measured by ICP-OES and Si by spectrophotometry in the sequential digestion experiment leachates for stations B13, B14 and B15, as well as in the B15 ground (B15 G) and dried (B15 D) samples. Top row: Si-HCl pool, middle row: Si-Alk, bottom row: Si-NaOH. Note the y axes scale changes. Error bars represent ±2σ of sample triplicates. * signifies a concentration below the limit of quantification (LOQ) (average blank concentration + 8σ).*

Table 3.1: Molar element ratios in the three operationally-defined reactive Si pools studied, averaged across the stations. Digested surface sediment samples (0-0.5 cm sediment core slice) were collected in 2019 (cruise JR18). Element concentrations were determine by ICP-OES (Al, Fe, Mg, Mn, Si, Ti, V) and spectrophotometry (Si). Research data can be found at doi.org/10.5285/8933af23-e051-4166-b63e-2155330a21d8.

Ratio	Si-HCl		Si-NaOH		Si-Alk	
	mol/mol	$\pm 2\sigma$	mol/mol	$\pm 2\sigma$	mol/mol	$\pm 2\sigma$
Mg/Si	1.86	0.37	0.10	0.02	0.009	0.005
Al/Si	0.56	0.10	0.61	0.09	0.024	0.05
Ti/Si	0.004	0.0007	0.012	0.01	0.0007	0.0004
Mn/Si	0.24	0.18	0.019	0.04	0.0007	0.001
Si/Fe	0.60	0.29	3.80	1.17	250	68
Mn/Fe	0.14	0.11	0.06	0.12	0.19	0.41
Fe/Al	3.20	2.65	0.46	0.11	0.51	-
Mg/Al	3.33	0.92	0.17	0.04	0.73	1.54

to authigenic oxide and aluminosilicate products that can coat BSi (Dixit et al., 2001; Loucaides et al., 2010), both of which appear to be forming in Barents Sea sediments. Ti/Si ratios presented here in the Si-HCl (0.004 $\pm$0.001 mol/mol) and Si-NaOH pools (0.012 $\pm$0.01 mol/mol) are not dissimilar to the upper continental crust (0.008 mol/mol) (McLennan, 2001), consistent with the observations of Pickering (2020) for sediments of the Mississippi River plume (0.006 mol/mol). This similarity could signify a contribution of Si to the Si-HCl and Si-NaOH reactive pools from terrestrially-derived LSi that dissolves into the leachate. Pickering et al. (2020) do hypothesise that the authigenic products extracted from their sediment samples are at least in part, sourced from the slow dissolution of LSi.

The Si-NaOH pool has a much higher Si/Fe (3.8 mol/mol) and lower Fe/Al (0.46 mol/mol) ratio than Si-HCl, consistent with the removal of metal oxides into the HCl leachate. However, Fe/Al ratios in the Si-NaOH pools are still higher than the typical range for marine sediments (0.15-0.42 mol/mol, averaging 0.27) (Clarkson et al. (2014); Raiswell et al. (2008) and references therein), and more than twice the upper continental crust value (0.21 mol/mol). The Fe/Al composition of the Si-NaOH pool is more akin to ratios observed in some clay minerals (0.3-0.6 mol/mol) (Song and Choi, 2009) and clay-rich horizons in marine sediments, within which it is typical for this metric to exceed the continental crustal average (Volz et al., 2020), for example in the southeastern Arabian Sea (0.21-0.78 mol/mol, average 0.42) (Pattan et al., 2012). This observation is consistent with Al/Si values (0.68 mol/mol), which are well within range of common clay minerals (0.48-0.96 mol/mol) (Kim et al. (2004); Koning et al. (2002); Wang et al. (2018); Rahn (1976) and references therein). Furthermore, Fe/Al measured in Fe-rich smectites (nontronite) can reach 8.9 mol/mol (Wang et al., 2018), which are found to dominate the expandable clay mineral content of western Laptev Sea sediments to the east of the Barents Sea (Vogt et al., 2002).

Table 3.2: Compilation of solid phase K/Al element ratios (mol/mol) of riverine suspended load, Arctic shelf and Central Arctic Ocean seafloor sediments, as well as of various material for context. Data collated from: Beeskow and Rachold (2003); Geilert et al. (2020a); Grotti et al. (2017); Krom et al. (1999); Michalopoulos and Aller (2004); Pokrovsky et al. (2010); Schoster et al. (2000); Shevchenko et al. (2010); Viers et al. (2009); Viscosi-Shirley et al. (2003); Wehausen and Brumsack (1999). CAO = Central Arctic Ocean, AuSi = authigenic clay minerals.

Suspended Load	Seafloor Sediments	Reference Values
Lena (0.23)	Laptev (0.22)	Upper crust (0.24)
Khatenga (0.10)	Kara (0.19)	Shale (0.24)
Yenisei (0.17)	Kongsfjord (0.23)	AuSi (0.22)
Pechora (0.21)	CAO (0.20)	$CaCO_3$ (0.17)
Global (0.13)	Barents (0.22)	

Barents Sea glacial trough sediments analysed in this study are indeed clay-rich (Orsi and Dunn, 1991; Vogt and Knies, 2009) and dominated by the clay/silt size fraction (Faust et al., 2020). These factors may explain why the average Al/Si in the Si-NaOH pool is greater than in the upper continental crust (0.27 mol/mol) (McLennan, 2001), given that clay minerals tend to be enriched in Al relative to primary silicates. These observations are consistent with the hypothesis that the harsh alkaline digestion activates the reactive LSi fraction (Pickering, 2020), which is why the NaOH liberates the most Ti and Al by mass of sample (Fig. 3.1), which are considered strong indicators of terrigenous material (Jia et al. (2013) and references therein).

Interestingly, element ratios derived from XRF measurements of the bulk solid phase (Si/Fe of 9.0-13.2, Fe/Al of 0.26-0.38 and Al/Si of 0.28-0.30 mol/mol) are similar to the upper continental crust (17.5, 0.21, 0.27 mol/mol respectively (McLennan, 2001)), but different to the Si-NaOH molar ratios determined by ICP-OES (Table 3.1). The K/Al ratios measured in suspended load delivered to the southern Barents Sea by the Pechora River, and surface sediments from Svalbard fjords (0.21-0.24 mol/mol, Grotti et al. (2017)) are consistent with Barents Sea surface sediment values (averaging 0.22 mol/mol) (Table 3.2), suggesting that the bulk seafloor sediment reflects the composition of allogenic terrestrial material. Some degree of the dissimilarity between Si-NaOH and the XRF element ratios will be accounted for by dilution of the LSi in the XRF signal by other sedimentary components, such as organic carbon, BSi and $CaCO_3$, estimated to account for $\sim$4% of the bulk sediment by mass (see section 4.5.2). Although given the relatively minor contribution of accessory components to the sediments studied here, it is probable that the majority of the disparity is due to a fractionation of the LSi pool into refractory and labile components, during sample digestion with NaOH. The more reactive of the terrigenous LSi components that are liberated into the leachate appear to be of a different chemical composition to the rest of the pool, likely composed of younger, less crystalline material.

XRF analysis of the solid phase indicates that station B15 surface sediments have the highest Fe content (5.1%) relative to B13 and B14 (3.9 and 4.8% respectively), while station B15 also presents with the highest Mn content (0.53% *vs* 0.07 and 0.10% at B13 and B14 respectively) (Fig. 4.12). Higher solid phase Fe contents at Barents Sea stations north of the oceanic polar front have previously been linked to physical glacial erosion on Svalbard, sea ice rafting and erosion of the shelf bedrock (Faust et al. (2020) and references therein). Intriguingly, station B14 presents with higher concentrations of both Fe and Mn in the Si-HCl pool per gram of sample, while the elevated solid phase Mn content observed at station B15 does not manifest until the harsher alkaline digestion (Fig. 3.1). This observation implies that, unlike for station B14, the Fe and Mn content at B15 is likely not associated with highly reactive authigenic metal oxides. Instead, the Fe and Mn content lies within the LSi sediment fraction, which is activated in the harsh alkaline extraction.

Leachate Al concentrations could only be determined in three of the five surface sediment Si-Alk pools studied (stations B13, B14, B15, B15 dried and B15 dried/ground), however the three molar Al/Si ratios measured are over an order of magnitude lower than those of the Si-HCl and Si-NaOH pools. Si-Alk molar Al/Si ranges from 0.009 to 0.053, with an average of 0.024 mol/mol, which is similar to BSi (including diatom, sponge and radiolarian-derived) collected from sediment traps, marine sediments and laboratory studies (2.1×10^{-5} to 0.165, averaging 0.029 mol/mol) (Hendry and Andersen (2013); Loucaides et al. (2010); Middag et al. (2009); van Bennekom et al. (1989); Ren et al. (2013) and references therein) (Fig. 3.1). Furthermore, Si-Alk molar Fe/Si (average 0.004 mol/mol) and Mg/Si ratios are similar to metal content ratios measured in diatom frustules sampled from Bering Sea sediments (Ren et al., 2013). The similarity between molar Al/Si and Fe/Si ratios in BSi and the Si-Alk pool indicates that the mild-alkaline extraction has predominantly activated the BSi pool, with minimal contamination from LSi phases, thus $\delta^{30}Si_{Alk}$ is likely representative of the true BSi isotopic composition. This suggestion is consistent with Si-Alk Si/Fe ratios (averaging 250 mol/mol), which are 2-3 orders of magnitude higher than in the other reactive pools. Similarly, Pickering (2020) observed that molar ratios of Al/Si and Fe/Si were much lower in the Si-Alk pool, than they were in the alkaline extraction of sediments where an acid pre-treatment was not included in the digestion protocol. The δ^{30}Si analysed in the former group were found to be 0.56‰ higher than in the latter. These coupled observations provide further evidence for the removal of authigenic products from BSi by the acid pre-leach, prior to the mild alkaline digestion.

Statistical analysis can be carried out on the isotopic composition of sediment leachates to determine the sources of the respective reactive pools (Pickering et al., 2020). The Si-HCl pool, which is sourced from the dissolution of authigenic products is very isotopically light for the marine environment. The Si-HCl pool within Barents Sea surface sediments is approximately 3.7 to 4.4‰ lower than the Si-Alk pool and 2.0‰ lower than the Si-NaOH

pool across the three stations. If early diagenetic authigenic products, such as metal oxides and AuSi are taking up DSi from the pore water phase, there could be a relationship between δ^{30}Si in the Si-HCl pool and the phases which source pore water DSi, most likely LSi (Si-NaOH) and BSi (Si-Alk). Statistical analysis indicates that there is a moderate and weak negative correlation between $\delta^{30}Si_{HCl}/\delta^{30}Si_{Alk}$ (Spearman's rank correlation: rho = -0.60, p-value = 0.09 (two-tailed)) and $\delta^{30}Si_{HCl}/\delta^{30}Si_{NaOH}$ (Spearman's rank correlation: rho = -0.15, p-value = 0.70 (two-tailed)) respectively, however neither relationship is statistically significant. This observation could empirically suggest that neither phase represents the Si source for the Si-HCl pool.

A -4‰ difference between the Si-Alk and Si-HCl pools is greater than the isotopic fractionation factor associated with adsorption of Si by metal oxides (-0.7 to -1.6‰ for Fe (oxyhydr)oxides, -1.8 to -3‰ for Al (oxyhydr)oxides) (Delstanche et al., 2009; Oelze et al., 2014), or precipitation of clay minerals (∼-2‰) (Geilert et al., 2014; Georg et al., 2007; Opfergelt and Delmelle, 2012; Ziegler et al., 2005a,b). It is considered that multiple cycles of dissolution-precipitation and adsorption-desorption can enhance the isotopic fractionation factor of both processes to -3‰ or greater (Opfergelt and Delmelle, 2012), which could resolve the majority of the difference between the two pools. Furthermore, there is some evidence for the preferential release of the lighter isotope during the dissolution of BSi (possible fractionation factor of -0.55 to -0.86‰)(Demarest et al., 2009; Sun et al., 2014), however other work has suggested that this process occurs in isotopic equilibrium, without fractionation (Wetzel et al., 2014).

In contrast to $\delta^{30}Si_{HCl}$ *vs* $\delta^{30}Si_{Alk}$, the difference between $\delta^{30}Si_{HCl}$ and $\delta^{30}Si_{NaOH}$ is just -2‰, similar to Si isotope fractionation factors associated with both Si adsorption onto metal oxides and clay formation. As a result, there are plausible mechanisms that could explain how both BSi and LSi represent a source to the Si-HCl pool, although the statistical analysis would suggest that there is no statistically significant relationship. The correlation coefficient between Si-HCl and Si-Alk (-0.60) is much greater than with Si-NaOH (-0.15), however one would expect the correlation to be positive, if either sourced the Si-HCl pool, whereby BSi and LSi of heavier and lighter isotopic compositions resulted in correspondingly heavier and lighter compositions of Si-HCl respectively. In a scenario where LSi dissolution is the source for Si-HCl, the latter pool inherits the already isotopically light composition of the LSi phase (-0.89‰), through one fractionation.

Following Pickering (2020), here we plot the mass of Si released into the Si-Alk pool against that in the Si-HCl phase, in order to determine whether the early diagenetic products released into the Si-HCl phase are forming as a product of the size of the Si-Alk pool. This characterisation is an important step towards understanding the early diagenetic processes involved in Si cycling within Barents Sea sediments. The global dataset suggests a positive correlation between Si-Alk and Si-HCl, indicating that the formation of authigenic products is a function of the availability of BSi, and thus that

BSi represents an important substrate for metal oxide and AuSi formation (Fig. 3.2). If the linear regression between the mass of these two reactive pools was 1:1, the implication would be that authigenic products are accumulating at the same rate as the BSi pool.

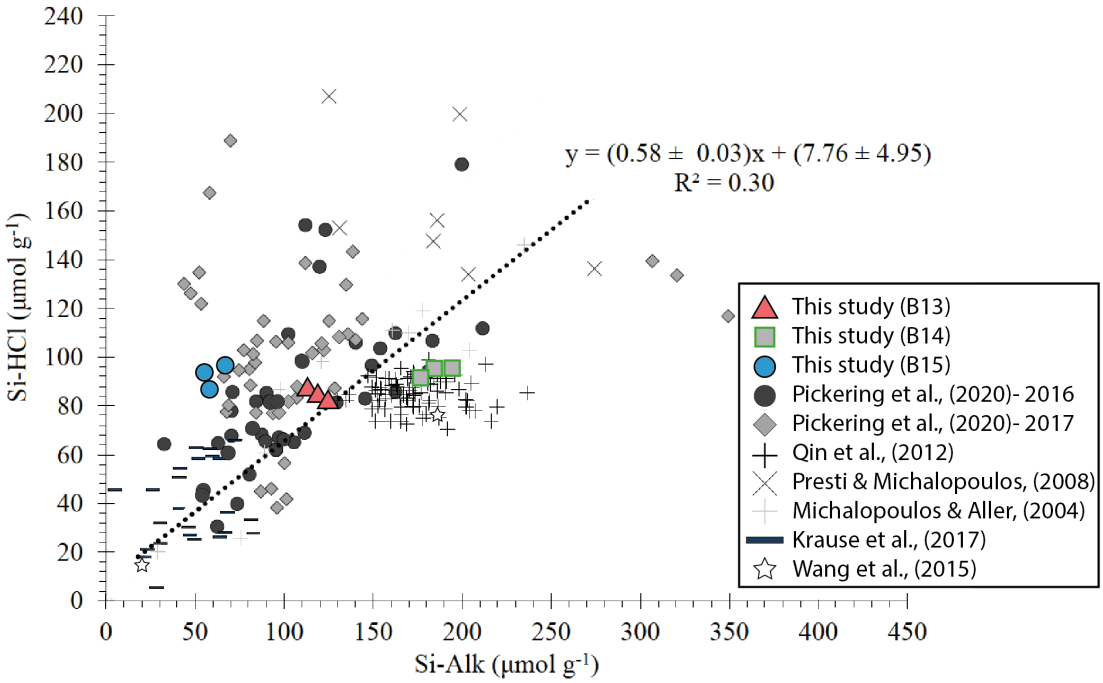

Figure 3.2: Global compilation of Si released in operationally-defined reactive pools of Si in µmol Si g^{-1} dry weight (Si-HCl and Si-Alk) (n=222), modified from Pickering (2020). Dotted line is a linear regression of the global dataset (Reduced Major Axis method) calculated by Pickering (2020). Samples plotted are from coastal sediments collected from the Mississippi River plume (Pickering et al., 2020), Mississippi Sound (Krause et al., 2017), Mississippi River Delta (Presti and Michalopoulos, 2008), Pearl River estuary (Qin et al., 2012), the Amazon Delta (Michalopoulos and Aller, 2004), end member values from the Yangtze Estuary (Wang et al., 2015a) and now the central Barents Sea (this study). Barents Sea data represents triplicate measurements of three sampling stations (B13, B14 and B15), which does not include dried and ground samples from the method development study, as heat treatment and sample grinding influences the mass of elements released into each reactive pool (Fig. 3.1).

Data collected from surface sediment intervals of three Barents Sea stations fall within range of the global data compilation (r^2 = 0.30, gradient = 0.58), which is composed of coastal samples (estuarine, deltaic, river plume). However, when considered in isolation, the relationship between Si-Alk and Si-HCl at stations B13, B14 and B15 exists in three distinct groups, which do not appear to lie on a linearly increasing trendline (r^2 = 0.02, gradient = 0.01, rho = 0.12). The observation that the size of the Si-HCl pool (authigenic products) does not scale with an increasing Si-Alk pool, could suggest that the formation of authigenic products in Barents Sea sediments is limited by the availability of critical terrestrially-derived elements (e.g. Al, Fe, Mn, Ti). However, this limitation is considered unlikely, as surface sediments in this study are estimated to be composed of an average of 96% terrigenous material (LSi), suggesting there could be ample stock of key elements.

The relationship between Si-Alk and Si-HCl in this study could also indicate that in contrast to coastal settings, BSi may not be the most important substrate for the formation of authigenic products, implying that the one-step isotopic fractionation scenario from a dissolving LSi pool (of Si-NaOH composition) is the most likely source for Si-HCl. Indeed, AuSi formation can occur on a wide range of possible substrates (clay minerals, quartz grains, glass beads (representing amorphous silica), fecal pellets, foram chambers, lithoclasts (Baldermann et al. (2022); Michalopoulos and Aller (1995) and references therein)), which could well be the case within the terrigenous-rich sediments of the Barents Sea. Previous studies have demonstrated that LSi can dissolve within seafloor surface sediments in undersaturated conditions (e.g. Geilert et al. (2020a)) and readily release Al, which can then facilitate the precipitation of poorly crystalline AuSi in detrital-rich sediments (Dixit et al., 2001).

Pickering (2020) was first to demonstrate the power of coupling a sequential sediment digestion protocol with measurement of stable Si isotopes, in gaining a better understanding of the early diagenesis of Si in marine sediments. Here we have built on this work by extending the global data compilation of operationally-defined reactive Si pools to a central continental shelf setting. Overall, the solid phase experiments carried out here lend support to the hypothesis of rapid authigenic product formation within the surface interval of Barents Sea sediments, as indicated by the element ratios and isotopic compositions of the Si-HCl leachates. However, here we have also shown that the Barents Sea stations have a much weaker relationship between Si-HCl and Si-Alk, relative to the global data compilation, which could indicate that BSi is not the primary substrate for the formation of these authigenic products. This hypothesis supports the suggestion that the source of the early diagenetic metal oxides and AuSi most likely lies within the Si-NaOH pool, rather than Si-Alk. Si isotopes reveal that a simpler one-step isotopic fractionation is required to explain the difference between $\delta^{30}Si_{HCl}$ and $\delta^{30}Si_{NaOH}$, the magnitude of which (-2‰) is similar to that observed in Si adsorption to metal oxides and during clay mineral precipitation, as opposed to inferring a Si-Alk source for Si-HCl, which would demand a multi-step isotopic fractionation amounting to ∼-4‰.

3.4.2 Correcting Si-Alk for LSi interference

Most previous studies analysing the Si-Alk component of marine sediments present raw data due to a lack of corresponding Al or Ti concentration data in the leachates. Following Kamatani and Oku (2000) and Ragueneau et al. (2005), here we present $\delta^{30}Si_{Alk}$ values corrected for LSi interference in the 20 minute Na_2CO_3 digestion leachate. Ragueneau and Tréguer (1994) estimate that this interference represents ∼15% of the BSi content calculated from the intercept of the linear regression, slightly higher than that calculated in Mississippi River plume sediments (7.4 ±4.5%) (Pickering et al., 2020).

The correction is calculated using equation 3.1 and makes the following assumptions:

1) the Al released into the Si-Alk pool is not sourced from BSi; 2) all the BSi is dissolved after the first (mild) alkaline digestion; 3) the LSi that dissolves during the second (harsh) alkaline digestion does so in a similar fashion to that which contaminates the Si-Alk pool (Ragueneau et al., 2005).

$$[Si_{Cor}]_{Na_2CO_3} = [Si]_{Na_2CO_3} - [Al]_{Na_2CO_3} \cdot \frac{1}{(Al:Si)_{LSi}} \tag{3.1}$$

where $[Si_{Cor}]_{Na_2CO_3}$ is the LSi-corrected Si concentration in the Na_2CO_3 leachate. $[Si]_{Na_2CO_3}$ is the total Si concentration initially measured in the 20 minute extraction, including the LSi and BSi components and $(Si:Al)_{LSi}$ is the inferred composition of the contaminating LSi phase.

Clearly there are some significant limitations associated with this methodology and thus LSi contamination calculations should be considered with caution. Firstly, previous work has shown that BSi dissolving in the presence of marine sediments during incubation experiments, drive elevated Al/Si and Fe/Si ratios in the dissolved phase relative to pure BSi counterparts (Loucaides et al., 2010). Furthermore, BSi is known to incorporate Al into its structure within seafloor sediments, causing a decrease in reactivity and increase in preservation potential (Van Cappellen et al., 2002). Secondly, as discussed by Pickering et al. (2020), it is possible for the harsh alkaline digestion can activate refractory BSi (such as sponge spicules and radiolarian tests). We might therefore anticipate some Al to be released alongside BSi during the mild alkaline digestion and possibly for refractory BSi to be liberated alongside the LSi phase, although element ratios in Barents Sea leachates support the hypothesis that Si-Alk and Si-NaOH is reflective of BSi and LSi respectively. Finally, through interpretation of element ratios we have determined that the harsh alkaline digestion could be preferentially dissolving the most reactive fractions of a multicomponent Barents Sea sediment matrix. We must then also assume that the dissolution behaviour of any contaminating phases within the Si-Alk pool was similar, thus releasing a similar Si/Al ratio into the dissolved phase.

To correct $\delta^{30}Si_{Alk}$ we used the following equation (Pickering, 2020):

$$\delta^{30}Si_{AlkCor} = \frac{(\delta^{30}Si_{Alk} \cdot [Si]_{Na_2CO_3}) - (\delta^{30}Si_{NaOH} \cdot [Si_{LSi}]_{Na_2CO_3})}{[Si_{Cor}]_{Na_2CO_3}} \tag{3.2}$$

where $[Si_{LSi}]_{Na_2CO_3}$ (LSi component in the Si-Alk pool) equates to $[Si]_{Na_2CO_3} - [Si_{Cor}]_{Na_2CO_3}$.

Unfortunately, due to a lack of corresponding [Al] data, we were only able to apply this correction to three samples (B13, B15 and B15 ground). All three of these present with relatively low LSi interferences, suggesting that the majority of Si released into this phase from sediments of both the Atlantic and Arctic regions is due to the incorporation of the BSi pool.

We used two different $(Al:Si)_{LSi}$ ratios to correct $\delta^{30}Si_{Alk}$. Our results demonstrate

Table 3.3: Summary of $\delta^{30}Si_{Alk}$ values corrected for LSi contamination using Al:Si ratios following Ragueneau et al. (2005) and Kamatani and Oku (2000). Comparison of calculated corrected $\delta^{30}Si_{Alk}$ values when using an $Al : Si_{LSi}$ of the average continental crust vs the second alkaline leach (Si-NaOH pool) carried out in this study. Units of $\delta^{30}Si_{Alk}$ are in ‰, numbers in brackets represent the difference between the corrected and measured values for B13, B15 and B15 ground.

	B13		B15 ground		B15	
	$\delta^{30}Si_{AlkCor}$	%LSi	$\delta^{30}Si_{AlkCor}$	%LSi	$\delta^{30}Si_{AlkCor}$	%LSi
Continental Crust	1.59 (+0.16)	6.6	1.08 (+0.17)	8.7	1.36 (+0.54)	39.6
NaOH supernatant	1.47 (+0.04)	1.5	0.94 (+0.03)	1.8	0.89 (+0.07)	7.7

that the magnitude of the correction varies greatly depending on this ratio. If we use a lower $(Al : Si)_{LSi}$, such as that of the mean continental crust (0.131), as has been applied in similar calculations of a previous study (Pickering et al., 2020), the inferred contamination from LSi is much greater, espcially at B15 (Table 3.3). However, an alternative method is to use the $(Al : Si)$ of a second alkaline leach carried out on the sediment samples. Ragueneau et al. (2005) digested particulates collected from filtering seawater twice with 0.2 M NaOH for 40 minutes at 100^{o}C and then assumed that the $(Al : Si)$ ratio measured in the supernatant of the second digestion (0.45) was reflective of the composition of the silicate minerals. Two alkaline leaches were carried out in this study, albeit using different reagents (0.1 M Na_2CO_3 followed by 4 M NaOH). After applying the method of Ragueneau et al. (2005), assuming that the $(Al : Si)$ measured in the NaOH leachate (0.57-0.67) is reflective of the Barents Sea sediment $(Al : Si)_{LSi}$, the corrections are significantly reduced and brought in-line with previous values and estimates (Pickering et al., 2020; Ragueneau and Tréguer, 1994) (Table 3.3).

3.4.3 How do different sediment reactive Si pool extraction and sample preparation methods affect BSi content and leachate δ^{30}Si?

Sediment organic matter removal

HCl is commonly used to clean sediments prior to analysis, acting to remove diluting carbonate phases, as well as to activate BSi by removing metal oxide coatings, thus enhancing dissolution rates in the subsequent weak alkaline extraction Michalopoulos and Aller (2004). Pickering (2020) showed that the Si-Alk pool is up to 10-fold larger than the BSi released into the alkaline digestion when an acid pre-treatment is not utilised, indicating that the pretreatment enhances the accessibility of authigenically altered BSi. Similarly, some research groups opt to pretreat sediment samples with H_2O_2 to remove protective organic coatings and aid in sediment disaggregation, which exposes opal surfaces (Mortlock and Froelich, 1989). In the traditional alkaline leach experiments, samples were not pre-treated with either H_2O_2 or a weak acid solution (DeMaster, 1981). However, Michalopoulos and Aller (2004) showed that without an HCl pretreatment, the rate

of Si release from the sediment during the weak alkaline digestion increased with reaction time, creating a concave-upward profile, not compatible with the assumed linear release on which the method is underpinned. In addition, Pickering et al. (2020) found that the weak alkaline leach of untreated samples was enriched in the lighter isotope (^{28}Si) relative to the treated counterparts, likely driven by contamination from Si adsorbed to metal oxide coatings that had not been removed. Most previous studies that analyse the isotopic composition of BSi in marine sediments have employed a traditional alklaine digestion without a HCl pretreatment (Ehlert et al., 2016a; Frings et al., 2014; Ziegler et al., 2005a). Some studies now utilise an HCl treatment, based on the observations of Michalopoulos and Aller (2004), but have lacked δ^{30}Si data until recently (Geilert et al., 2020a; Krause et al., 2017; Pickering et al., 2020; Presti and Michalopoulos, 2008; Qin et al., 2012; Wang et al., 2015b), which has limited understanding of the previously overlooked reactive pools. However, application of H_2O_2 is more inconsistent as its impact on estimated BSi contents is less well constrained.

Prior to designing the series of experiments that were carried out to study operationally-defined pools of reactive Si in Barents Sea sediments, a pilot test was completed to determine whether a hydrogen peroxide (H_2O_2) pre-treatment should be used. A pre-treatment such as this is recommended to remove diluting organic phases (Mortlock and Froelich, 1989), but is not always employed in sediment digestion experiments and is not specified within the novel reactive Si pool sequential digestion protocol of Pickering et al. (2020). Stations B13, B14 and B15 were studied by setting up two parallel experiments. ∼50 mg of dried and ground surface sediment samples (0-0.5 cm) collected on cruise JR16 (2017) were weighed out in duplicate. After the initial 0.1 M HCl leach, one sediment sub-sample was placed in a sonicator for 30 minutes with 10 mL of 10% H_2O_2 (Mortlock and Froelich, 1989), while a second was set aside. Both samples then underwent the same traditional alkaline digestion procedure to determine the BSi content, using extractions from the 2, 3 and 5 hour time intervals (DeMaster, 1981) (Fig. 2.9).

The estimated BSi contents across the three stations were 1.7 to 3.8-fold larger when the H_2O_2 pre-treatment was carried out prior to the alkaline digestion (0.18-0.38 wt% *vs* 0.05-0.22 wt% (Table 3.4). This finding is similar to those of Pickering (2020), who found that the mass of Si released by the Si-Alk leach stage was 2-9 times lower when a mild acid pre-treatment was not used. H_2O_2 acts to oxidise organic matter present in the sample, removing protective coatings on BSi, thus exposing fresher surfaces for the subsequent alkaline leach (Abramson et al., 2009). Whereas, a similar sensitivity study carried out on sediments from the Greenland shelf indicated no change in BSi content with or without an H_2O_2 pretreatment in the experiment protocol (Hong Chin Ng, pers. comm. 2019). This pretreatment step was included in the design of the wider experiments, given that the influence of H_2O_2 is potentially not consistent across all sediment types and can have a significant impact on the calculated BSi content. Wider application of a consistent H_2O_2

Table 3.4: Barents Sea surface sediment (0-0.5 cm interval) BSi contents (wt%) with and without a H_2O_2 pretreatment (5 mL, 10%, 30 minutes, sonicated).

Station	With H_2O_2 (wt%)	Without H_2O_2 (wt%)
B13	0.30	0.12
B14	0.38	0.22
B15	0.19	0.05

pretreatment would establish consistency across research laboratories and support data comparability, ensuring that BSi contents are not artificially enhanced or reduced due to the application of a H_2O_2 cleaning step or lack thereof.

Despite the fact that the H_2O_2 pre-treatment removed organics from Baents Sea sedients, exposing BSi, a yellow discolouration was found in the 0.1 M Na_2CO_3 and 4 M NaOH leachates after surface sediment samples from stations B13 and B14 (see Chapter 3). The equivalent supernatant collected from digestion of station B15 surface sediment showed no discolouration. Initial filtration through 0.22 and 0.02 μm (PES syringe filters (Pall Acrodiscs) and Corning Costar Spin-X centrifuge tube filters) had no effect on the colour of the solution. The leachates were acidified to pH 1 and the colouration was found to be resistant to acidification, indicating it was unlikely to be due to precipitation of Fe minerals. However, over a five day period, brown-coloured material flocculated and sank out of solution, leaving the supernatant colourless. Station B15 has the lowest total organic carbon content of the three stations (1.7 wt% compared to 2.2 and 2.5 wt% at stations B13 and B14 respectively, Freitas et al. (2020)), leading to the hypothesis that this material could be organic in nature, thus the Na_2CO_3 and NaOH was activating residual organics that were not removed by the H_2O_2 pre-treatment. After the colouration had aggregated and dropped out of the solution, the Na_2CO_3 samples were filtered through a 0.22 μm filter for a second time, leaving the brown-coloured material on the filter membrane.

The filter membranes that were used to remove the brown-coloured material were imaged using a Hitachi S-3500N Scanning Electron Microscope (SEM) at the University of Bristol. Energy Dispersive X-Ray Analysis (EDX) was also carried out using a ThermoNoran energy dispersive X-ray spectrometer to determine which elements were present within the samples to confirm the composition of the aggregates. Blank filter membrane was imaged and sampled by EDX first (Fig. 3.3). The Pall Acrodisc filters used consist of hydrophilic polyethersulfone (PES), which is composed of aromatic rings (phenyl and biphenyl groups) connected by ether or sulfone groups ($(C_{12}H_8O_3S)_n$), while the Corning Costar Spin-X centrifuge tube filter membranes are composed of cellulose acetate ($C_2H_4O_2{\cdot}x$). Hence, SEM-EDX spectra present with C and O peaks (Fig. 3.3). The filter membrane samples were mounted on stubs and subsequently sputter-coated with gold prior to imagine, hence, all samples present with SEM-EDX peaks at the Au X-ray wave-

length position. C-coating is typically preferred for SEM-EDX analysis, however as the flocculated material was hypothesised to be organic in origin, Au was selected as it does not interfere with the C peak. Imaging and SEM-EDX analysis of the brown aggregate-coated filter membrane demonstrated the presence of C, O, Au, Cl and Na as expected, given the chemical composition of the leachate (Na_2CO_3) that had been neutralised with in-house distilled HCl and the filter membrane ($(C_{12}H_8O_3S)_n$ / $C_2H_4O_2 \cdot x$) (Fig. 3.3). Minor peaks of Al, Fe, K, Ti, N and Si were also detected, although all of these elements were present in the leachate sample, as indicated by ICP-OES analysis (Fig. 3.1), which were likely detected as the Na_2CO_3 wet the hydrophilic filter membrane and subsequently dried. The inferred elemental composition of the aggregated material is not consistent with metal oxides or silicate minerals and more similar to organic compounds (Lybrand et al., 2019; Morata et al., 2008; Tobo et al., 2014).

Previous theoretical predictions and experiments have demonstrated that equilibrium fractionation factors between Si-bearing minerals and DSi can reach -10 to -19‰, the highest value observed thus far in Si isotope research (Stamm et al., 2020). Stamm et al. (2020) suggest that this phenomena could explain the substantial isotope fractionation associated with sponge spicule formation, caused by the presence of organic ligands during biomineralisation. It is unlikely, however, that this phenomena has influenced the isotopic composition of the residual Na_2CO_3 left behind after filtration. Firstly, the Si peak on the SEM-EDX spectra was minimal and was not detected at all in approximately half of the measurements. Secondly, isotopic measurements of the Na_2CO_3 leachate samples were highly reproducible across both sample and analytical replicates. Each sediment sample was digested in triplicate, of which each Na_2CO_3 leachate was analysed in duplicate or triplicate. The average reproducibility of the replicate Na_2CO_3 leachate sample measurements was ±0.11‰ (2σ n=48), which is lower than that for Diatomite (±0.14‰, n=116) and the seawater reference standard, ALOHA (±0.17‰, n=30). If the Si isotopes were being fractionated to such extremes by the aggregating organic material, it might be expected that the isotopic composition would differ between samples. Furthermore, the δ^{30}Si of the Si-Alk pool (Na_2CO_3 leachate) at stations B13 and B14 (+1.43 ±0.14 and +1.50 ±0.19‰ respectively) were similar to the composition of BSi measured in samples collected from sediment traps between 50-800 m water depth across the Arctic Ocean (+1.42 (Liguori et al., 2020) and +1.51‰ (Varela et al., 2016)). Furthermore, the DSi concentration within one of three triplicate leachate samples, for both station B13 and B14, was almost very similar before and after filtration, indicating minimal removal of Si from the reactive pool by the aggregating organic material.

Following confirmation that the colouration within the Na_2CO_3 leachate collected from digestions of stations B13 and B14 surface sediment was caused by organic material, a sensitivity test was conducted to assess whether the colouration could be avoided through alteration of the pre-treatment. The three tests consisted of systematic variation of either

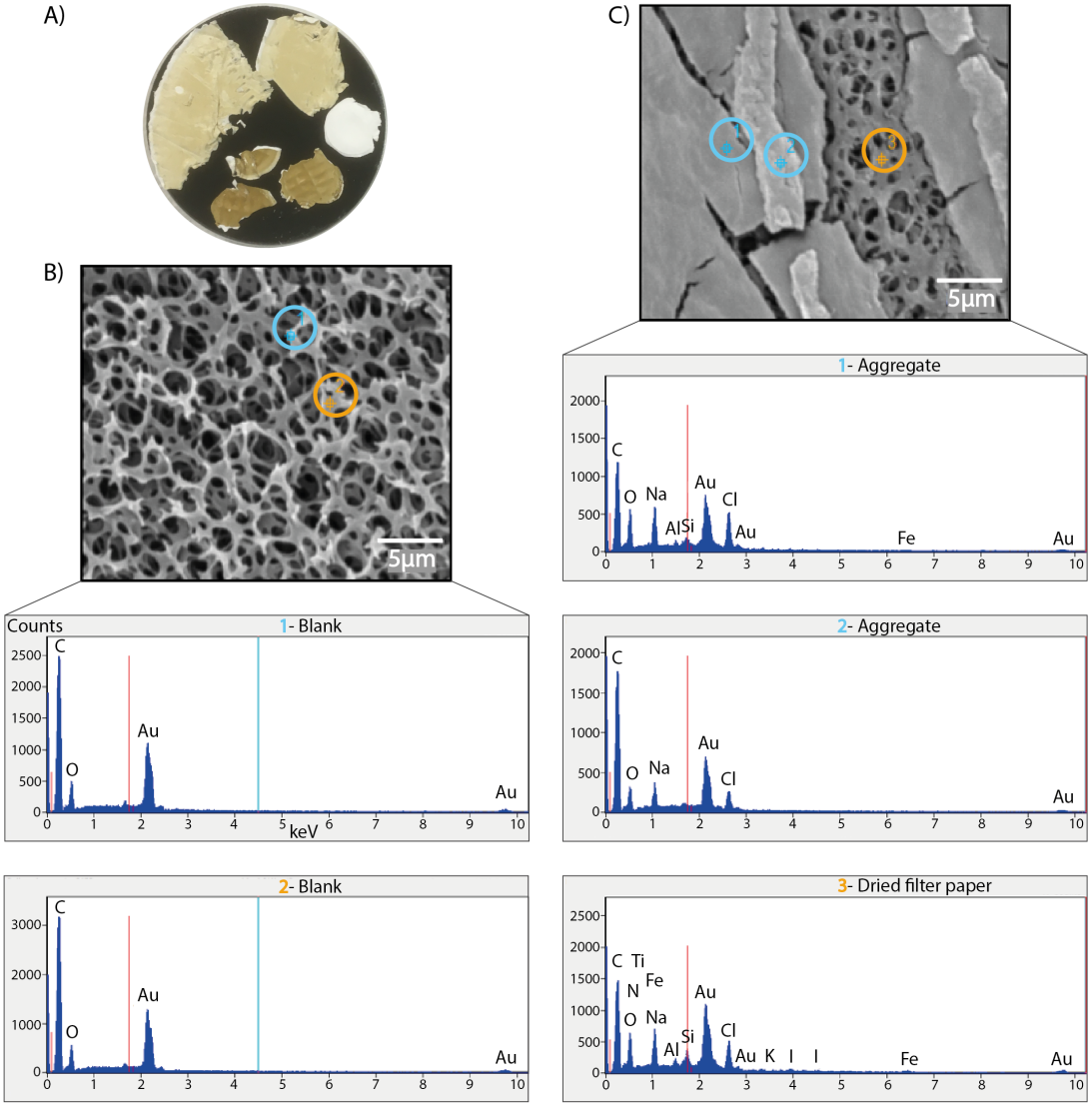

Figure 3.3: SEM imaging and EDX spectra of 0.1M Na_2CO_3 leachate filter membranes. A) Sample stub prior to Au sputtering, containing two different types of 0.22 µm filter membranes. Blank (white) Corning Costar Spin-X centrifuge tube filter membrane on the middle-right. B) SEM imaging and EDX spectra of the blank filter membrane. C) SEM imaging and EDX spectra of the filter membrane having been used to filter the brown aggregated material from the Na_2CO_3 leachate and left to dry. Note the formation of the brown-coloured crust and the visible filter membrane beneath. Vertical red line represents the Si wavelength.

the duration of the pre-treatment, or the strength of the H_2O_2, as follows:

- **Control**- 5 mL 10% H_2O_2, 30 mins
- **Test 1**- 20 mL 30% H_2O_2, 2 hrs
- **Test 2**- 20 mL 10% H_2O_2, 2 hrs
- **Test 3**- 20 mL 10% H_2O_2, 6 hrs

Green discolouration was found in the 0.1 M Na_2CO_3 and 4 M NaOH leachates sampled from each of the three tests, indicating that the changes made to volume, strength and duration of the H_2O_2 were insufficient to remove the material prior to digestion. Only two measurements were made of the isotopic composition of the 4 M NaOH leachate from the three tests, which averaged -0.82‰, similar to the average across the three stations (-0.89 ±0.16‰). Further work is therefore required to determine the composition of the organic material and a methodology for its removal from the sediment, however the similarity in δ^{30}Si of the prolonged pre-treatment NaOH samples to the three-station average provides support that the colouration is inconsequential to the isotopic composition. The sensitivity study carried out here is by no means exhaustive. 30 minute treatments with 10% H_2O_2 are commonly used to remove organic matter in sediments prior to accessing the BSi pool (Cassarino et al., 2020; Mortlock and Froelich, 1989; Sañé et al., 2013; Wang et al., 2015b; Welsby et al., 2016; Xu et al., 2020; Yang et al., 2016), although some researchers carry out harsher H_2O_2 treatments (up to 30% H_2O_2), which can involve leaving samples for much longer periods of time (12-72 hours) and at high temperatures (70-90^{o}C water bath) (Liu et al., 2019; Morley et al., 2004; Tyler et al., 2007; Wessels et al., 1999). In fact, some studies also opt for a subsequent treatment with nitric acid to remove any persistent organic material (Tyler et al., 2008).

Sediment sample preparation techniques: oven-drying and grinding

Contrasting sediment sample preparation techniques, for example oven drying and grinding, have been shown to significantly alter the estimated BSi content. Michalopoulos and Aller (2004) applied a correction factor of -50%, due to the effect of sample grinding/crushing, consistent with an artificial increase in sample reactivity through a decrease in surface crystallinity (Pickering, 2020). Regardless, sediment drying and grinding remains a commonly used method of sample preparation. In this study we carried out sensitivity tests on a sequential digestion experiment protocol designed to access operationally defined pools of reactive Si (Pickering et al., 2020), so as to determine if the influence of these different sample preparation techniques could be traced isotopically.

We found that grinding the sediment (group 3, dried/ground) increased the BSi content of surface sediment samples (0-0.5 cmbsf core slice) by 36.4% relative to the frozen sample (group 1), while drying the sediment (group 2, dried/in tact) decreased this value by 53.5%

(Fig. 3.4). The difference between the BSi content of groups 3 and 1 is within 2 standard deviations (2σ), although is outside of 2 standard error of the mean (2SEM) (equation 3.3) and is statistically signifciant (ANOVA p=0.024, group 1 n = 5, group 3 n = 4). The mechanical effect of grinding the sediment on the BSi content is consistent with the findings of Michalopoulos and Aller (2004), in that sample surface area was increased and fresh BSi surfaces exposed, resulting in greater Si release when placed in to contact with the Na_2CO_3 leachate.

$$2SEM = 2\sigma \,/\, \sqrt{n} \tag{3.3}$$

where σ is the standard deviation and n the number of sample measurements.

Throughout the sequential digestions, group 2 sediments were more difficult to homogenise within the leachate. This finding is consistent with Mortlock and Froelich (1989), who suggested that clay-rich samples, such as those collected in 2019 from the Barents Sea, should not be dried to hardness as this can inhibit disaggregation of the sediment during BSi extraction. This lack of disaggregation will likely have limited contact of the sample with the leachate, resulting in the reduced estimate of BSi content relative to the other preparation techniques (Fig. 3.4A).

The influence of drying and grinding sediment samples not only has an impact on the estimated BSi content, but there is also a perceptible imprint on the isotopic composition of the leachates. $\delta^{30}Si_{HCl}$ in group 3 (-2.56 ±0.14‰ (n=10)) was 0.28‰ heavier than that measured in groups 1 or 2 (-2.82 ±0.15‰ (n=9) and -2.85 ±0.14‰ (n=9) respectively), which is outside of both 2SEM and 2σ and is statistically significant (group 1 and 3 ANOVA p=$7.0E^{-8}$, group 1 n = 9, group 3 n = 10) (Fig. 3.4C). The Si-HCl operationally defined reactive pool of Si is associated with metal oxides (Pickering et al., 2020), however the increased surface area and reduced sediment grain size as a result of the grinding, in addition to the highly Si undersaturated nature of the pure HCl solution, could have allowed for the premature release/dissolution of an isotopically heavier phase from a different reactive pool (e.g. Si-NaOH or Si-Alk). This could explain why group 3 samples present with a ^{30}Si enriched $\delta^{30}Si_{HCl}$ relative to groups 1 and 2 and indicates that drying alone does not significantly influence the Si-HCl pool. This is supported by the ICP-OES metal concentration data, which indicates elevated Al and Ti in the Si-HCl of group 3 relative to groups 1 and 2 (Fig. 3.1). Al and Ti are typically considered to be lithogenic trace elements (Price et al., 1999), suggesting that grinding may have resulted in contamination of the Si-HCl pool from LSi minerals. It is possible that the difference in $\delta^{30}Si_{HCl}$ observed between group 3 and groups 1/2 is due to contamination of material from the agate mortar. However, there is no discernible influence of sample preparation techniques on $\delta^{30}Si_{NaOH}$ (Fig. 3.4D), nor between $\delta^{30}Si_{Alk}$ of groups 2 and 3 (Fig. 3.4B), which we would expect if there had been significant contamination of the sample from agate particulates.

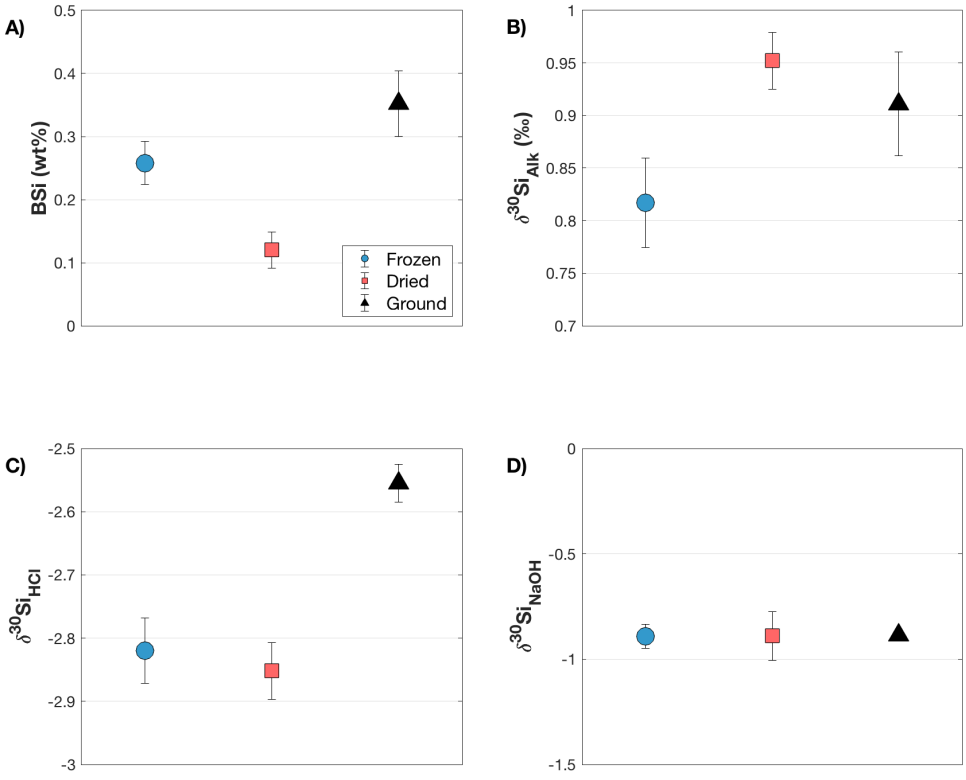

Figure 3.4: Sample preparation sensitivity experiment testing the influence of digesting thawed sediment (stored frozen), versus oven drying and subsequently grinding on the BSi content and Si isotopic compositions of the reactive pools. BSi content (wt%) (A), Si-Alk (B), Si-HCl (C) and Si-NaOH (D). Error bars are ±2SEM (equation 3.3).

We also observe a shift in $\delta^{30}Si_{Alk}$ induced by the distinct sample preparation methods. $\delta^{30}Si_{Alk}$ of group 1 (+0.82 ±0.16‰ (n=14)) is enriched in the lighter isotope, relative to groups 2 (+0.95 ±0.14‰ (n=9)) and 3 (+0.91 ±0.16‰ (n=10)) (Fig. 3.4B). Oven drying (as opposed to freeze drying) sediment samples has been found to cause fragmentation of diatom frustules (Conley, 1998), with Flower (1993) finding diatom breakage in 100% of samples oven dried at 50^{o}C overnight. This could explain why the Si-Alk pool of sediment samples exposed to elevated temperatures present with a slightly heavier isotopic composition, as frustule breakage and thus exposure of fresh BSi surfaces could increase the ratio of BSi:LSi release during the Na_2CO_3 digestion. This is supported by our contamination correction calculations (Table 3.3), which suggest that the B15 frozen 20 minute Na_2CO_3 leachate has a higher proportion of LSi within its Si pool than the dried and ground counterpart (see section 3.4.2).

As with the BSi content, the difference in $\delta^{30}Si_{Alk}$ across the sample preparation techniques is within 2σ, but outside of 2SEM and the difference between groups 1 and 3 is statistically significant (ANOVA p=0.009, group 1 n = 14, group 3 n = 10), as is that between groups 1 and 2 (ANOVA p=0.0001, group 1 n = 14 , group 2 n = 9).

There is very little influence of oven drying on $\delta^{30}Si_{NaOH}$, however this process does appear to enhance the release of Al, Fe, Si, Ti, Mg and Mn into the 4 M NaOH leachate, as well as Mg, Mn and Si in the Na_2CO_3 leachate, with the dried and ground samples presenting with higher concentrations of the aforementioned elements (Fig. 3.1). This suggests that heating may enable other phases to release into a given leachate which are not activated in the thawed group. This influence is thought to be detectable within $\delta^{30}Si_{Alk}$ due to the size of the Si pool, which is 7-10 times smaller in the Na_2CO_3 relative to the NaOH leachate (Fig. 3.1). The exact nature of the phase(s) is unclear, however isotopic analysis suggests that it is enriched in the ^{30}Si relative to $\delta^{30}Si_{Alk}$ at B15.

To conclude, given the impact of oven drying on the measured BSi content (group 2) and the contamination observed in the sequential leach extractions brought about by grinding (group 3), we recommend that sediment samples are frozen after core recovery and gently thawed to room temperature prior to any extraction procedure following the group 1 protocol.

Chapter 4

Investigating the behaviour of stable silicon isotopes in Barents Sea sediment pore and core top waters

This chapter reproduces an article accepted for publication at Geochimica et Cosmochimica Acta, authored by J.P.J. Ward, K.R. Hendry, S. Arndt, J.C. Faust, F.S. Freitas, S.F. Henley, J.W. Krause, C. März, H.C. Ng, R.A. Pickering and A.C. Tessin. The article is titled 'Stable Silicon Isotopes Uncover a Mineralogical Control on the Benthic Silicon Cycle in the Arctic Barents Sea' (ArXiv [preprint], https://doi.org/10.31223/X5F04Z). As lead author, I completed all laboratory analysis for Si isotopic compositions, as well as digestion experiences on solid phase samples, including measurement of element concentrations through spectrophotometry and ICP-OES (Si, Al, Fe, Mg, Mn, Ti, V). I led on writing the article, producing original figures and responding to reviewer comments. Co-author contributions: JF, FS, SH and AT helped in the sampling and processing of onboard samples. SH measured pore water and water column DSi concentrations. RP, JK and KH assisted JW with design of the sediment digestion experiments. JF, CM and AT measured pore water major and trace element concentrations. All authors contributed to manuscript assembly through comments on draft versions.

4.1 Abstract

Biogeochemical cycling of silicon (Si) in the Barents Sea is under considerable pressure from physical and chemical changes, including dramatic warming and sea ice retreat, together with a decline in dissolved silicic acid (DSi) concentrations of Atlantic inflow waters since 1990. Associated changes in the community composition of phytoplankton blooms

will alter the material comprising the depositional flux, which will subsequently influence recycling processes at and within the seafloor. In this study we assess the predominant controls on the early diagenetic cycling of Si, a key nutrient in marine ecosystems, by combining stable isotopic analysis (δ^{30}Si) of pore water DSi and of operationally defined reactive pools of the solid phase. We show that low biogenic silica (BSi) contents (0.26-0.52 wt% or 92-185 μmol g dry wt^{-1}) drive correspondingly low asymptotic concentrations of pore water DSi of ∼100 μM, relative to biosiliceous sediments (>20 wt% BSi) wherein DSi can reach ∼900 μM. While Barents Sea surface sediments appear almost devoid of BSi, we present evidence for the rapid recycling of bloom derived BSi that generates striking transient peaks in sediment pore water [DSi] of up to 300 μM, which is a feature that is subject to future shifts in phytoplankton community compositions. Using a simple isotopic mass balance calculation we show that at two of three stations the pore water DSi pool at 0.5 cm below the seafloor (+0.96 to +1.36 ‰) is sourced from the mixing of core top waters (+1.46 to +1.69 ‰) with the dissolution of BSi (+0.82 to +1.50 ‰), supplemented with a lithogenic Si source (LSi) (-0.89 ±0.16‰). Further, our sediment pore water δ^{30}Si profiles uncover a coupling of the Si cycle with the redox cycling of metal oxides associated with isotopically light Si (-2.88 ±0.17‰). We suggest that a high LSi:BSi ratio and apparent metal oxide influence could lead to a degree of stability in the annual background benthic flux of DSi, despite current pressures on pelagic phytoplankton communities. Coupled with supporting isotopic evidence for the precipitation of authigenic clays in Barents Sea sediment cores, our observations have implications for the regional Si budget.

4.2 Introduction

The Barents Sea represents a highly productive gateway that joins the Atlantic and Arctic Oceans. This shelf sea accounts for ∼40% of the total Arctic Ocean primary production, despite occupying just 10% of the areal extent (Oziel et al. (2016); Smedsrud et al. (2013) and references therein). However, the Barents Sea is at present subject to considerable climate-driven perturbations, including the highest rates of winter sea ice loss (47% in March from 1979-2018) (Årthun et al., 2012; Docquier et al., 2020; Smedsrud et al., 2013) and surface water warming (Lind et al., 2018) observed across the Arctic Ocean. Much of this sea ice melt and surface water warming is driven by an expansion of the southern Atlantic Water (AW) realm ('Atlantification'), which is separated from the Arctic Water mass (ArW) of the northern Barents Sea by the oceanic polar front (PF) (Årthun, 2011; Oziel et al., 2016) (Fig. 1.2). The consequences of these changes are predicted to have significant implications for CO_2 uptake in the surface ocean, long term carbon sequestration, deep water formation, nutrient cycling in the pelagic and benthic realms, as well as the balance of marine ecosystems and primary production in the Barents Sea (Faust et al., 2021; Freitas et al., 2020; Haug et al., 2017; Lind et al., 2018; Oziel et al., 2016).

At present, phytoplankton spring blooms of the Arctic Ocean are a cornerstone event that make up a significant proportion of annual primary productivity across the region (Krause et al., 2018). The community composition of spring and early summer blooms is typically dominated by diatoms, a group of photosynthesising microalgae that uses dissolved silicic acid (DSi) to build frustules of biogenic silica (BSi), commonly termed 'opal' (Giesbrecht and Varela (2021); Krause et al. (2018, 2019); Makarevich et al. (2022); Downes et al. (2021) and references therein). Seawater is undersaturated with respect to the solubility of BSi, which facilitates dissolution as diatoms and other silicifiers die and sink through the water column down to the seafloor following a bloom (Frings, 2017; Tréguer et al., 1995). Crucially, ∼30% of this dissolution globally occurs at or just below the sediment-water interface (SWI) during early diagenesis, creating strong concentration gradients between the upper sediment pore and ocean bottom waters (Tréguer et al., 2021). This recycling process drives DSi fluxes back to the water column (Frings, 2017), which are a major component of the ocean Si nutrient cycle and thus have significant implications for the global carbon cycle by sustaining subsequent diatom blooms locally (e.g. shallow systems) or non-locally (through nutrients advected or mixed into the euphotic zone) (Dixit and Van Cappellen, 2003; Loucaides et al., 2012a).

In addition to the recycling of diatom-derived BSi, other sources of DSi in marine sediment pore waters include the dissolution of siliceous sponge spicules (Ng et al., 2020), radiolarian tests (Maldonado et al., 2019) and lithogenic minerals (LSi) (Ehlert et al., 2016b; Fabre et al., 2019; Geilert et al., 2020a). The release of DSi from LSi phases has long been theorised in the North Atlantic to explain the magnitude of benthic recycling fluxes in sediments relatively devoid of BSi (Tréguer et al., 1995; Tréguer and De La Rocha, 2013). This dissolution is driven by low North Atlantic bottom water DSi concentrations ([DSi]) (∼10-40 μM), which are well below that of many LSi mineral solubilities (Tréguer et al., 1995) (130 μM, 70 μM and 100 μM for montmorillonite, kaolinite and quartz in seawater respectively (Lerman et al., 1975; Mackenzie et al., 1967; Schink et al., 1975)). Furthermore, Ng et al. (2020) suggested that an increase in pore water [DSi] in cores with the highest [Fe] from the Greenland shelf was driven by both DSi desorption from Fe (oxyhydr)oxides as they reductively dissolve and through an increase in the solubility of BSi due to the removal of protective metal oxide coatings. This supports the hypothesis that redox reactions can regulate pore water DSi by influencing BSi dissolution kinetics (Aller, 2014; Ng et al., 2020).

The build-up of pore water DSi from BSi, LSi and metal oxide sources is often curbed by uptake through the precipitation of authigenic clays (AuSi) (Ehlert et al., 2016a; Geilert et al., 2020a; Loucaides et al., 2010; Michalopoulos and Aller, 1995). The precipitation of AuSi can operate either through the dissolution of LSi and subsequent coprecipitation of DSi with the liberated dissolved Al, or through a typical reverse weathering pathway whereby BSi reacts with Al/Fe (oxyhydr)oxides and major cations present in pore waters

(Ehlert et al. (2016a) and references therein). Reverse weathering therefore results in the formation of cation-rich AuSi minerals at the expense of reactive Si phases, such as BSi and degraded clays (Aller, 2014; Frings et al., 2016), representing a significant global ocean sink for alkalinity and elements such as K, Mg, Li and Ge (Rahman et al., 2017; Sutton et al., 2018), taking the following general form:

$$ReactiveSi + Al(OH)_4^- + cations + HCO_3^- \rightarrow aluminosilicates + H_2O + CO_2 \quad (4.1)$$

The formation of AuSi minerals is recognised to occur across the marine environment, from the precipitation of 'green clay' (or glauconite) in continental shelf sediments, a product of BSi weathering, to smectite formation in the abyssal ocean (Aller, 2014; Cuadros et al., 2011; Ehlert et al., 2016a; Loucaides et al., 2010; Rahman et al., 2016). The formation of AuSi represents an important early diagenetic pathway for BSi that can greatly enhance the efficiency of its preservation (Aller, 2014; Dale et al., 2021; Frings et al., 2016; Rahman et al., 2017).

The balance of DSi release and uptake processes in marine sediments act to modulate the magnitude of benthic fluxes of DSi from Arctic shelf sediments (0.34 Tmol yr^{-1}), which are estimated to be as important for the regional Si budget as circum-Arctic rivers (∼0.4 Tmol yr^{-1}) (März et al., 2015). Globally, rivers are estimated to contribute ∼55% of the total Si input (including dissolved and amorphous Si) to the ocean Si budget (Tréguer et al., 2021). However, a 20% decrease in [DSi] has been observed in Barents Sea Atlantic inflow waters from 1990-2012 (Rey, 2012) and recent evidence suggests a kinetic limitation on diatom growth by surface water [DSi] in blooms off Svalbard (Krause et al., 2018), as well as in the Pacific and Canadian Arctic regions (Giesbrecht, 2019; Giesbrecht and Varela, 2021). This is compatible with the suggestion that a northward expansion of the AW realm will shift phytoplankton communities in favour of Atlantic flagellate species (e.g. *Emiliania huxleyi* and *Phaeocystis*), potentially leading to a reduction in the depositional flux of BSi to Arctic sediments (Neukermans et al., 2018; Orkney et al., 2020). It is therefore crucial to better understand how sensitive the benthic Si system is to further perturbations, given the pressures the Barents Sea and wider Arctic region face from anthropogenic warming and Atlantification. As a result, recent work has begun to develop a better mechanistic understanding of this subject through measurement of stable Si isotopes (Cassarino et al., 2020; Ehlert et al., 2016a; Geilert et al., 2020a; Ng et al., 2020).

The aim of this work is to further develop our understanding of the early diagenetic cycling of Si in Arctic marine sediments through stable Si isotopic analysis on pore water DSi and its solid phase sources. We address specific research questions, including: 'What is the magnitude of the benthic DSi flux?', 'What are the sources of pore water DSi near the SWI?', 'Is there evidence of AuSi precipitation or a redox control on the benthic Si system?' and 'What are the key geographic and temporal variations?'.

Table 4.1: Sampling station information averaged across the three cruises.

Station	Latitude (^{o}N)	Longitude (^{o}E)	Water Depth (m)	Bottom Water Temp (^{o}C)
B03	72.6342	17.9224	367	3.9
B13	74.4331	29.9532	359	1.8
B14	76.5019	30.5012	295	1.9
B15	78.2192	29.9574	317	-1.5
B16	80.0982	30.0257	286	-1.5
B17	81.2825	29.6153	337	1.8

4.3 Materials and methods

4.3.1 Field methods

During the Changing Arctic Ocean Seafloor (ChAOS) sampling campaign sediment cores were collected from the Barents Sea Opening (B03) and from five stations along a 30^{o}E transect between 74 and 81^{o}N in the central Barents Sea (B13-B17) over three consecutive years (2017-2019). This sampling was carried out to assess the temporal and spatial dynamics of the benthic Si system (Fig. 1.2, Table 4.1). Samples were collected between late June and early August aboard the RRS *James Clark Ross* (JR16006, JR17007 and JR18006), with sampling targeted at sites of similar water depth (286-367 m) (Table 4.1). Cruise reports are available, which include all accompanying details and complementary data (Barnes, 2019; Hopkins, 2018; Solan, 2018).

Sampling for sediment and pore water analysis was carried out with a Multicorer from UK National Marine Facilities. This device allowed for sampling of the upper 30-40 cm of sediment including the overlying core top water and intact SWI. For solid phase sampling, the core tubes were placed onto a manual core extruder and slices were taken with a Perspex plate (sampling resolution of 0.5 cm intervals from 0-2 cm below seafloor (cmbsf), 1 cm from 2 cmbsf), which were then stored at -20^{o}C. For the dissolved phase, the overlying core top water was collected first, after which pore water samples were extracted with Rhizon filters attached to 30 mL plastic syringes, using spacers to create a vacuum (sampling resolution of 1 cm from 0.5-2.5 cmbsf, 2 cm to 20.5 cmbsf, 5 cm to 35.5 cmbsf). Pore water extractions were carried out at 4^{o}C and were stored at the same temperature having been acidified with Romil UpA HCl. At stations B15 and B16 the in-situ temperature was 5.5^{o}C colder than the sampling temperature, however pore water extractions were performed immediately after core recovery. Hendry et al. (2019) found that temperature change resulted in a deviation of measured sediment pore water [DSi] from original values, only when sediment cores had been standing at ambient temperature for more than 10 hours prior to pore water extraction.

For sediment pore water element concentration analysis, pore waters were collected

from three separate Multicorer deployments at each station and year. One of the replicate deployments for each year at B13, B14 and B15 were also sampled for Si isotopic analysis. These three stations span the three main hydrographic domains of the Barents Sea (AW, PF and ArW) (Fig. 1.2).

Sediment core incubations were carried out on-board in 2019 at a fixed temperature of 4^oC to quantify benthic DSi fluxes. Shortly after retrieval, an air-tight cap was sealed over the top of a core tube containing an undisturbed sediment surface and overlying core top water. The cap incorporated a plastic tube where a 60 mL plastic syringe could be connected for sample collection and a magnetic stirrer attached to the base to gently homogenise the core top water (Fig. 4.1). The incubations were run over a 24 hour period, with 50 mL samples extracted through an Acrodisc filter (0.2 μm) at 3 hour intervals. Sediment core incubations are commonly used to measure DSi benthic flux magnitudes (Berelson et al., 2003; Gehlen et al., 1995; Hou et al., 2019; Ragueneau et al., 2002; Srithongouthai et al., 2003) and are considered a more practical solution to in-situ benthic flux chambers (Hammond et al., 2004). Experiments of this nature cannot replicate the in-situ physical conditions, such as bottom water currents, however they are thought to be a better representation of the DSi benthic flux than estimates based on concentration gradient calculations, as processes such as bioturbation and bioirrigation are typically better represented (Cermelj et al., 1997).

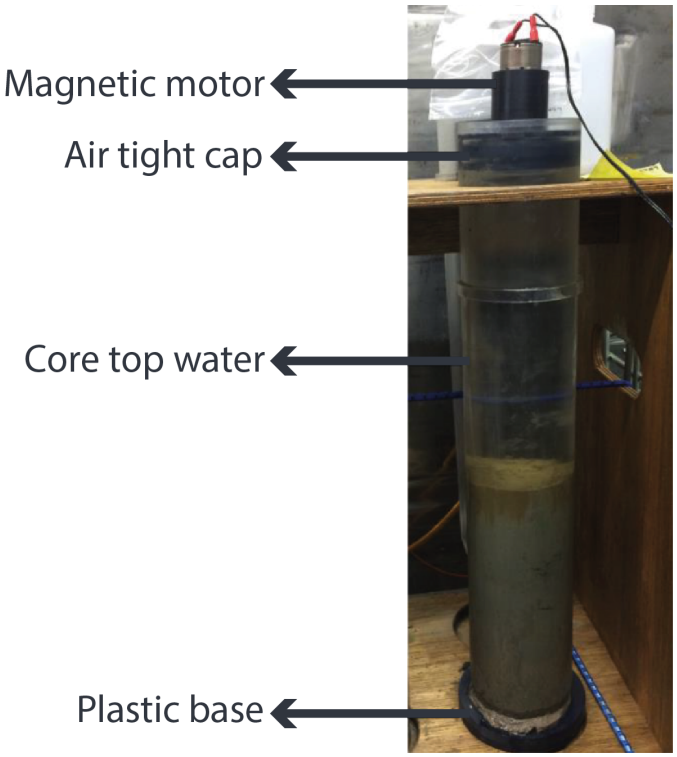

Figure 4.1: On-board (JR18006, 2019) core incubation experiment set-up.

4.3.2 DSi concentration analysis of pore waters and seawater

[DSi] analysis of pore water samples, as well as the incubation samples from 2019 (see section 4.5.1) were carried out on-board using a Lachat QuikChem 8500 flow injection autoanalyser. Internationally certified reference materials for seawater nutrients (KANSO Ltd., Japan) were used to define the accuracy associated with this method, which averaged 2.8% across the three cruises (1.5-5%).

4.3.3 Solid phase extraction and DSi concentration analysis

Operationally defined reactive pools of Si were extracted from the solid phase following Pickering et al. (2020). An additional study was also carried out here to assess the influence of oven drying and grinding sediment samples prior to isotopic analysis (see section 3.4.3). In summary, oven drying and grinding can significantly alter the isotopic composition of the sediment leachates and measured BSi content. We therefore present data sourced from samples that were frozen after core recovery and gently thawed to room temperature prior to digestion.

This sequential digestion procedure separates Si into operational pools based on the conditions, kinetics (time dependent) and sequence of the reaction (DeMaster, 1981; Michalopoulos and Aller, 2004; Pickering et al., 2020; Rahman et al., 2016). Reagents were added to 50-70 mg of thawed (dry weight) or dried sediment in the following sequence: 36 mL 0.1 M HCl (in-house distilled) for 18 hours at room temperature (Si-HCl pool); 25 mL 0.1 M Na_2CO_3 (Sigma-Aldrich BioXtra) for 5 hours in an 85^{o}C water bath (Si-Alk pool); 10 mL 4 M NaOH (Honeywell Fluka Trace SELECT) for 2 hours at 85^{o}C (Si-NaOH pool). Predominantly, these sequential extractions are thought to remove authigenic metal oxide coatings, BSi and LSi phases respectively (Michalopoulos and Aller, 2004; Pickering et al., 2020). In addition to the digestion sequence applied by Pickering et al. (2020), here 5 mL of 10% H_2O_2 (Fisher Chemical Extra Pure SLR) was added to the sediment samples for 30 minutes after the 0.1 M HCl leach to remove diluting organic phases (Mortlock and Froelich, 1989). After each digestion the supernatants were extracted after centrifugation and filtered through 0.22 μm PES syringe filters (Pall Acrodisc). The residual sediment was rinsed three times with Milli-Q water (18.2 MΩ) to remove any remaining reagent.

The use of Na_2CO_3 to remove BSi relies on the difference between rapid, nonlinear dissolution of BSi and the slower, linear dissolution of LSi (DeMaster, 1981). The traditional intercept method was employed for BSi concentration analysis, whereby aliquots of Na_2CO_3 are extracted at 2, 3 and 5 hr intervals over the course of the digestion. The [DSi] of the aliquots were plotted as a function of time and the extrapolated intercept of a linear regression was taken as the sediment sample BSi content (DeMaster, 1981) (Fig. 2.9). It is known that the intercept method encapsulates some degree of contamination from LSi dissolution. For example, Barão et al. (2015) have shown that non-biogenic phases can

be released into the Na_2CO_3 solution within the initial non-linear phase of the digestion. Ragueneau and Tréguer (1994) estimate that this interference represents ∼15% of the BSi content calculated from the intercept of the linear regression. In order to minimise LSi contamination for isotopic analysis of the BSi phase, digestion experiments were ceased at 20 minutes by neutralisation with in-house distilled HCl (Pickering et al., 2020). The [DSi] in the 20 minute Na_2CO_3 extractions were all found to be below the linear regression intercept, thus contamination from LSi is thought to be minimal (Fig. 2.9). Corrections for LSi interference following Kamatani and Oku (2000) and Ragueneau et al. (2005) were carried out to confirm this assumption (see section 3.4.2). These calculations were found to depend strongly on the inferred Si/Al ratio of the LSi phase, however the results suggest a low degree of LSi interference in the 20 minute extraction (1.5-8%) (Table 3.3).

After neutralising and separating the 20 minute Na_2CO_3 supernatant from the sediment sample centrifuge tubes, 25 mL of fresh Na_2CO_3 was added and the digestion resumed for a further 5 hours according to the traditional approach (DeMaster, 1981), prior to the NaOH digestion (Pickering et al., 2020).

[DSi] in the leachate samples collected from the sequential digestion experiments were measured colorimetrically by molybdate blue spectrophotometry (Heteropoly Blue Method) (Strickland and Parsons, 1972) on a VWR V-1200 spectrophotometer at the University of Bristol. This method has an analytical precision of 2-3% (RSD), with a slightly higher average reproducibility of triplicate samples normalised to sediment dry weight of 5.5% (range 0.09 to 16.4%). This external reproducibility is higher as it captures environmental factors, including spatial heterogeneity.

4.3.4 Isotopic analysis

Sample preparation (DSi co-precipitation and column chemistry)

Sample preparation was carried out at the University of Bristol's Bristol Isotope Group (BIG) clean laboratories. Core top and pore water samples were pre-concentrated prior to isotopic analysis by the Mg-induced co-precipitation (MAGIC) method following Karl and Tien (1992) and de Souza et al. (2012). This method involves the adsorption of Si to brucite ($Mg(OH)_2$) as it precipitates from seawater, which concentrates the Si and reduces the cation and anion matrix by up to two orders of magnitude, allowing for the effective use of cation exchange resin columns (de Souza et al., 2012). Brucite precipitation is induced by the addition of 1 M NaOH (Titripur) to pH-neutral samples in two steps. After both 1 M NaOH additions the samples were centrifuged and the supernatant removed. Precipitates were rinsed with 0.001 M NaOH solution to remove excess ions (Na^+, Cl^-, $SO_4{}^{2-}$, Ca^{2+}, K^+) after the second precipitation cycle (Ng et al., 2020). Samples were dissolved for column chemistry by the addition of 60-200 μL in-house distilled HCl (depending on sample size) and diluted with Milli-Q.

The pre-concentrated sea and pore water samples, solid phase leachates and reference standards were all passed through cation exchange columns, following Georg et al. (2006). Here, a resin (Bio-Rad AG50W-X12) was used for the chromatographic separation of Si from seawater matrix (de Souza et al., 2012). Each sample was loaded onto the columns and eluted with the required volume of Milli-Q to produce a 2 ppm solution. This method retains ambient cations (e.g. Na^+, Mg^{2+}, Fe^{2+}) and does not attract DSi as non-ionic orthosilicic acid (H_4SiO_4) or the negatively charged species $H_3SiO_4^-$, which are in equilibrium at pH 2-8 (Georg et al., 2006). Samples were collected with acid-cleaned Nalgene LDPE bottles and the Si isotopic composition was analysed within 48 hours of column chemistry.

Mass spectrometry

Stable Si isotopic compositions were measured on a Finnigan Neptune Plus High Resolution MC-ICP-MS by Thermo Fisher Scientific in the BIG laboratory. Data acquisition was carried out through numerous sessions over two years. Si solutions were transferred from the autosampler via a PFA Savillex C-flow nebuliser (100 μl min^{-1}) connected either to a PFA Teflon barrel spray chamber or an Apex IR Desolvating Nebulizer.

Most samples analysed for their Si isotopic composition were measured in duplicate or triplicate (80 of 123 pore and core top water samples and 39 of 45 sediment leachates) using a standard-sample bracketing technique (De La Rocha, 2002) and were blank corrected. The intensity of ^{28}Si in the 0.1 M HCl blank was <1% of the sample intensity in every analytical session. Each standard and sample was doped with Mg (10 ppm Inorganic Ventures) to further address mass bias and instrumental drift through internal standard normalisation (Cardinal et al., 2003), as well as with 0.001 M H_2SO_4 (ROMIL-UpA) and 1 M HCl to counteract anionic matrix effects (SO_4^{2-} and Cl^-) (Hughes et al., 2011; Van Den Boorn et al., 2009).

Stable Si isotopic compositions are reported in δ^nSi notation in units of per mille (‰), which represents a deviation of the ^{30}Si/^{28}Si or ^{29}Si/^{28}Si ratio of the sample relative to the international standard NBS-28:

$$\delta^n Si = \left(\frac{(^n Si/^{28} Si)_{sample}}{(^n Si/^{28} Si)_{standard}} - 1 \right) \cdot 1000 \tag{4.2}$$

Data quality was assessed through the correlation between δ^{29}Si and δ^{30}Si (R^2 = 0.997). Isotopic data presented here falls on a mass dependent fractionation line of gradient 0.5119 (Fig. 2.7), which is in between that expected of mass dependent kinetic (0.5092) and equilibrium (0.518) Si isotope fractionation (Cardinal et al., 2003; Reynolds et al., 2007). Regular analysis of reference standards was carried out in each analytical session to quantify the long-term external reproducibility of sample measurements to 2 standard deviations (2σ). The mean values of standards measured in this study (Diatomite +1.24

±0.14‰ (n=116); LMG08 -3.47 ±0.13‰ (n=46); $ALOHA_{1000}$ +1.23 ±0.17‰ (n=30)) agree well with published values (+1.26 ±0.2‰ (Reynolds et al., 2007); -3.43 ±0.15‰ (Hendry et al., 2011; Hendry and Robinson, 2012); +1.24 ±0.2‰ (Grasse et al., 2017) respectively) (Fig. 2.8). Measurement replicate reproducibility (2σ) ranges from 0.01 to 0.30‰ for pore waters, 0.10 to 0.19‰ for core top waters and 0.01 to 0.23‰ for sediment leachates, averaging 0.11‰.

4.3.5 Metal concentrations

The concentrations of a suite of metals (Al, Ti, Fe, Mn, Mg, V) were determined in the sediment extraction leachates (0.1 M HCl, 0.1 M Na_2CO_3, 4 M NaOH) by Inductively Coupled Plasma-Optical Emission Spectroscopy (ICP-OES) at the University of Bristol, using an Agilent Technologies 710 (Fig. 3.1). Analytical performance was assessed throughout the four sessions by periodic measurement of blanks and calibration standards. RSD (1σ) ranged from 0.25-12.75%, averaging 2.70% across repeat standard measurements (n=22) and all elements analysed.

4.3.6 Benthic flux calculations

The core top water [DSi] (μM) of each sample extraction from the incubation experiments was plotted as a function of the ratio of time:core top water height (day m^{-1}). The gradient of the linear regression represents the flux magnitude (mmol m^{-2} day^{-1}) and the total benthic flux (J_{tot}), as it takes into account molecular diffusion, bioturbation and bioirrigation and potentially advection, driven by the continuous stirring of core top waters throughout incubation experiments (Janssen et al., 2005; Ng et al., 2020). This method corrects the rate of DSi release over time for the influence of sample removal at each time interval following Hammond et al. (2004) and Ng et al. (2020). The flux magnitude uncertainties were obtained from the error on the gradient of the linear regression.

Molecular diffusive fluxes (J_{diff}) were also calculated using Fick's first law of diffusion while assuming a linear [DSi] gradient across the SWI:

$$\theta = 1 - \ln(\phi^2) \tag{4.3}$$

$$D_{sed} = D_{sw} \,/\, \theta \tag{4.4}$$

$$J_{diff} = -\phi \cdot D_{sed} \cdot (d[DSi] \,/\, dz) \tag{4.5}$$

where θ represents sediment tortuosity, ϕ is porosity in the surface sediment, D_{sed} is the is the diffusion coefficient of DSi in seawater (D_{sw}) corrected for tortuosity (Boudreau, 1996) and $d[DSi]/dz$ is the [DSi] gradient across the SWI. D_{sw}, which is dependent on

temperature (T) and viscosity (η), was determined based on an empirical relationship derived from an experimental study (Rebreanu et al., 2008) (equation 4.6), using bottom water temperatures measured at each station in 2017 (Table 4.1):

$$D_{sw} = 3.33 \times 10^{-12} \cdot (T \,/\, \eta) \tag{4.6}$$

where D_{sw} is in $cm^2\ s^{-1}$, T in kelvin and η in poises (g $cm^{-1}\ s^{-1}$).

A linear concentration gradient assumption uses the [DSi] at ∼0 cmbsf (core top water) and the uppermost sediment porewater (0.5 cmbsf). Previous studies have also employed an exponential curve fitting methodology to determine DSi flux magnitudes (Frings, 2017; McManus et al., 1995; Ng et al., 2020). Both methods were compared here (Table 4.2) and it was deemed that the linear assumption was more appropriate for the Barents Sea stations (please see section 4.6 for the discussion).

4.4 Results

4.4.1 Pore water

DSi concentration profiles

Overall, pore water asymptotic and quasi-asymptotic DSi concentrations of the Barents Sea range from ∼95-105 μM, similar to those of the nearby Norwegian Sea (∼100 μM) and North Atlantic Ocean (99-230 μM) (Ragueneau et al., 2001; Rickert, 2000; Sayles et al., 1996; Schlüter and Sauter, 2000). In general the northern, ArW sites (B15, B16, B17) (Fig. 1.2) exhibit typical [DSi] asymptotic profiles and are more alike between both the coring events within one cruise and between the three cruise years when compared with the AW stations (B03, B13, B14) (Fig. 4.2). The AW stations exhibit quasi-asymptotic profiles, generally showing gradual increases in [DSi] towards the base of the sediment cores, as well as greater variability in the surface sediment intervals relative to the northern stations. Station B15 exhibits a typical downcore logarithmic increase in DSi to an asymptotic value of approximately 100 μM at 3 cmbsf (Fig. 4.2), while station B13 also displays a rapid increase in [DSi] in the upper pore waters to a similar concentration as B15, but continues to gradually increase with depth. Station B14 [DSi] profiles are more variable, presenting with striking peaks in 2017 and 2019 of up to 300 μM at 2.5-3 cmbsf, also showing a gradual increase in DSi towards the base of the sediment cores (Fig. 4.2).

Benthic DSi flux magnitudes

Diffusive flux (J_{diff}) magnitudes calculated for the triplicate [DSi] profiles of stations B13, B14 and B15 for each cruise year (Fig. 4.2), using a two-point linear assumption of the concentration gradient at the SWI, range from +0.05 to +0.44 mmol m^{-2} day^{-1} (mean +0.21 ±0.23 mmol m^{-2} day^{-1} (2σ, n=27)) (see Table 4.5 and a summary in Table

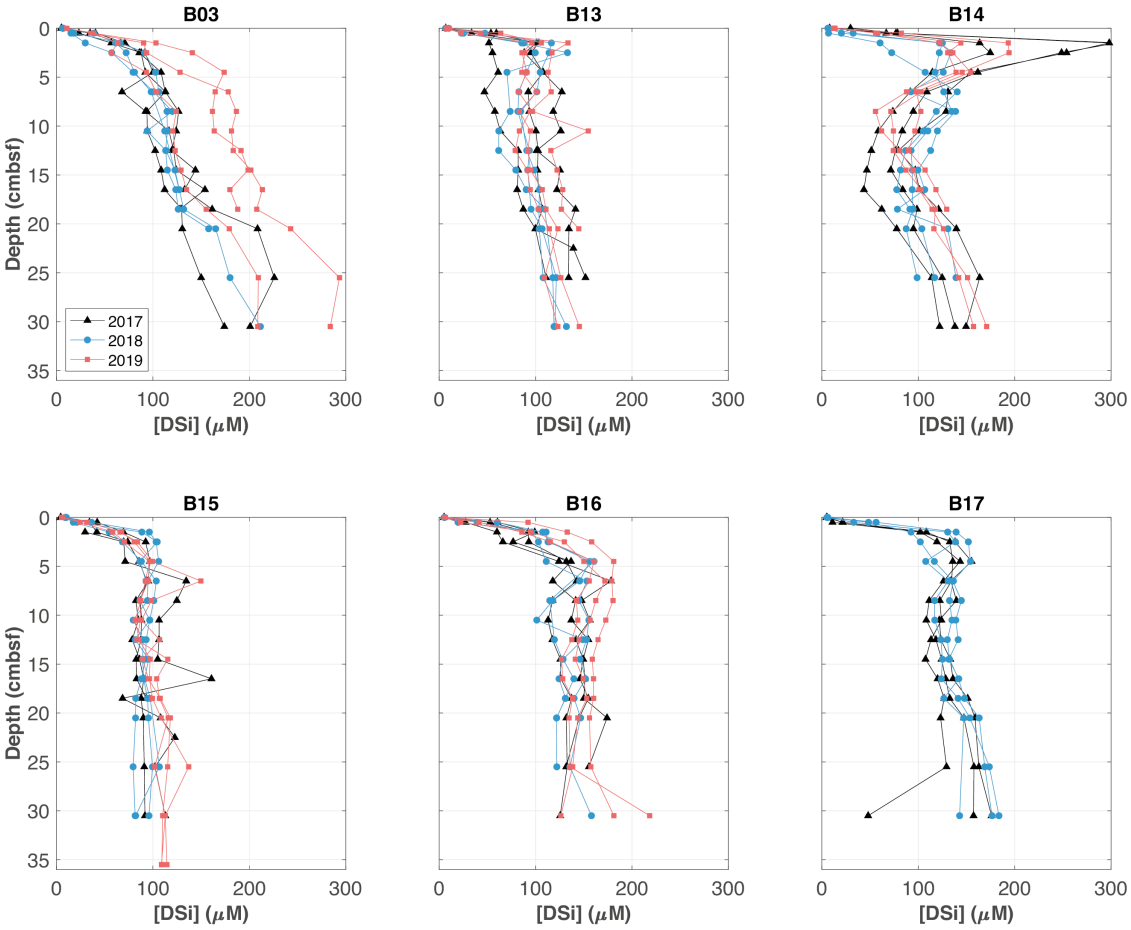

Figure 4.2: Compilation of all [DSi] depth profiles analysed on board the three ChAOS cruises. Top row: southern, Atlantic water stations (B03, B13, B14 (PF)). Bottom row: northern, Arctic water stations (B15, B16, B17). Includes all three Multicorer deployments per station for each cruise year.

4.2). J_{tot} values derived from the 2019 on-board incubation experiments range from +0.08 ±0.06 to +0.19 ±0.13 mmol m^{-2} day^{-1} (Fig. 4.3, Table 4.2). However, the core incubation temperature (4^{o}C) differed slightly from that in-situ at most stations. For stations B13 and B14, incubations were 2^{o}C too warm and 5.5^{o}C too warm at B15 and B16. Temperature change over the course of an incubation can induce a shift in the calculated DSi benthic flux of 6.0%^{o}C^{-1} due to the additive effects of temperature on molecular diffusion rates and pore water DSi concentrations (Hammond et al., 2004; Li and Gregory, 1974). This observation indicates that core incubation-derived J_{tot} estimates presented in Table 4.2 and Fig. 4.3 could be overestimated by 12-30%.

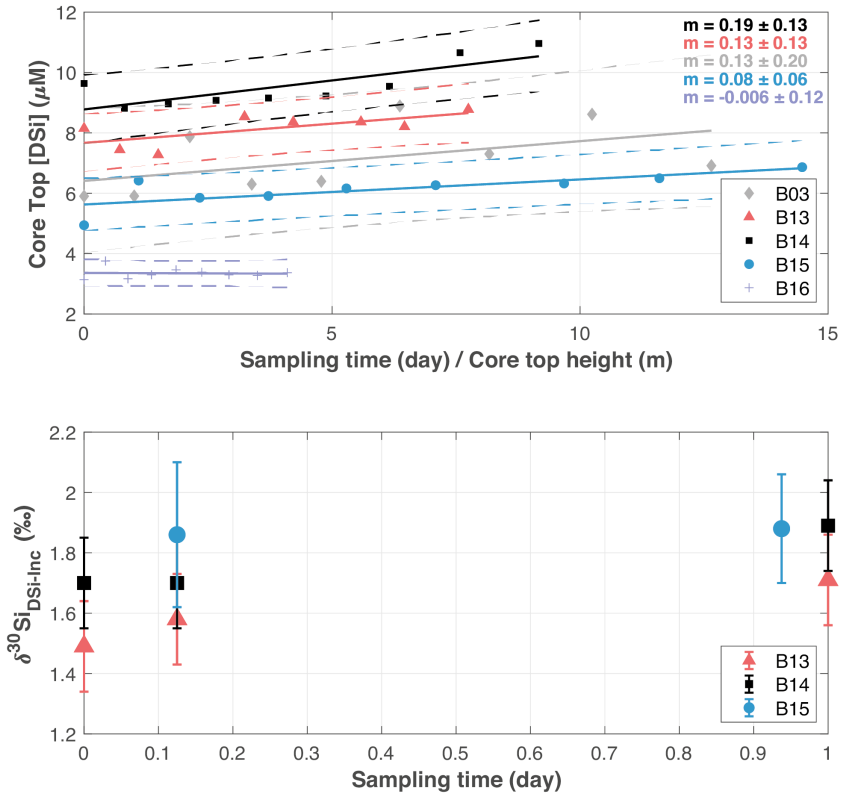

Figure 4.3: On-board sediment core incubation experiment from 2019 (JR18006). Sampling was carried out every 3 hours over a 24 hour period. Top row: Core top water [DSi] against the ratio of sampling time (hours) to core top height (cm). Gradient ('m') of the linear regressions represent the magnitude of the DSi benthic flux (mmol m^{-2} day^{-1}, where μM is equivalent to mmol m^{-3}). Gradient uncertainty is represented by 95% confidence limits, dashed lines depict 95% prediction bands. Bottom row: Si isotopic composition of the core top water ($\delta^{30}Si_{DSi-Inc}$). Error bars represent long term reproducibility of Si standards (2σ ±0.14), unless 2σ of measurement replicates was greater.

Both the raw and temperature corrected J_{tot} values lie within uncertainty of equivalent Fick's first law derived J_{diff} magnitudes and within range of a pan-Arctic review of shelf sediment DSi fluxes (J_{tot}) (-0.03 to +6.2 mmol m^{-2} day^{-1}, mean +0.6 ±1.3 mmol m^{-2}

day^{-1}, where a negative flux indicates DSi diffusion from bottom waters into the sediment) (Fig. 1.1) (Bourgeois et al., 2017).

Isotopic composition of DSi

$\delta^{30}Si_{DSi-PW}$ values fall within range of those previously analysed in terrestrial (Frings et al. (2016); Opfergelt and Delmelle (2012); Sutton et al. (2018) and references therein) and marine (Cassarino et al., 2020; Ehlert et al., 2016a; Geilert et al., 2020a; Ng et al., 2020) sediment pore waters, ranging from -0.51 to +1.69 (±0.14‰ 2σ) (Fig. 4.4). Station B13 $\delta^{30}Si_{DSi-PW}$ ranges from +0.30 to +1.36‰, B14 is the most variable ranging from -0.51 to +1.69‰ and B15 from +0.53 to +1.63‰. Only two of nine cores were found to have a $\delta^{30}Si_{DSi-PW}$ composition at the base within error of that at 0.5 cmbsf (B14 and B15 2019), most tend towards isotopically lighter compositions with depth (Fig. 4.4). The composition of core top waters from 2017 ($\delta^{30}Si_{DSi-CT}$) are similar across the three sites (B13 +1.64 ±0.19‰ (n=5), B14 +1.46 ±0.15‰ (n=3), B15 +1.69 ±0.18‰ (n=6)). $\delta^{30}Si_{DSi-CT}$ at B13 is within long term reproducibility of the composition of North Atlantic Waters at 300-400 m depth (+1.55‰) and B15 presents with a similar composition to that of Arctic deep waters of the Beaufort shelf (+1.84 ±0.10‰ at the halocline (125-200 m)) and Canada Basin (+1.88 ±0.12‰ below 2000 m) (de Souza et al., 2012; Varela et al., 2016).

4.4.2 Solid phase

BSi content

BSi contents were measured in three sediment depth intervals across the three sites for samples collected in 2019. Values ranged from 0.26-0.52 wt% (92-185 μmol g dry wt^{-1}) in the surface sediment interval (0-0.5 cmbsf), highest at B14 underneath the PF (Fig. 4.5A), consistent with observations of total organic carbon (Fig. 4.14). However, these values appear to be highly susceptible to sample preparation technique, with sediment grinding found to artificially increase BSi content by more than one-third (see section 3.4.3 for discussion). The BSi contents analysed here are low relative to the Southern Ocean (∼40%), but consistent with the North Atlantic mean (<1%) (Khalil et al., 2007) and neighbouring Kara (<1 wt%) and Norwegian (<2 wt%) Seas (Kulikov, 2004; Rickert, 2000). All three cores show a decrease in BSi content with depth to ∼0.20 wt% in the mid-core (Fig. 4.5A). Analyses have only been carried out on samples from 2019, but it is assumed that sediment composition does not vary considerably on an interannual scale due to the generally low sedimentation rates observed in the Barents Sea since the last glacial period (0.04-2.1 mm yr^{-1}) (Faust et al., 2020).

*Table 4.2: Parameters used to calculate the benthic fluxes of DSi through the two-point linear and exponential curve-fitting techniques. Please see section 4.6 for a discussion on the curve fitting methodology. All values for the diffusive fluxes (J_{diff}) represent a mean of triplicate coring events for each station and cruise year. Porosity (ϕ) was determined in the surface interval for JR16 (2017) samples, which was then used as the assumed value for the following years. Uncertainty on J_{diff} represents 2σ of the triplicate cores for each cruise year. For J_{tot} uncertainty is derived from the error on the gradient. * due to a shortage of sample volume, B15 $\delta^{30}Si_{DSi-Inc}$ values represent mixtures of the 0/6 hr and 21/24 hr extractions.*

Cruise	2017			2018			2019		
Station	B13	B14	B15	B13	B14	B15	B13	B14	B15
Sampling Date	17/07	30/07	20/07	14/07	25/07	17/07	07/07	13/07	10/07
Fick's First Law									
ϕ	0.90	0.91	0.92	-	-	-	-	-	-
θ^2	1.21	1.19	1.17	-	-	-	-	-	-
D_{sw} $\times 10^2$ (m^2 yr^{-1})	1.51	1.51	1.49	-	-	-	-	-	-
D_{sed} $\times 10^2$ (m^2 yr^{-1})	1.25	1.27	1.28	-	-	-	-	-	-
Linear									
$\frac{d[DSi]}{dz}$ (mmol m^{-3} m^{-1})	8400	12000	5100	4800	3900	3100	6900	11000	4300
J_{diff} (mmol m^{-2} day^{-1})	0.26	0.37	0.16	0.15	0.12	0.10	0.21	0.33	0.14
$\pm 2\sigma$	0.17	0.13	0.20	0.14	0.08	0.12	0.24	0.19	0.05
Exponential									
C_{SWI} (μM)	6.9	15.4	4.4	7.8	6.5	9.4	8.8	13.0	6.1
C_{asymp} (μM)	92	123	98	90	102	91	101	162	103
β (m^{-1})	130	175	65	78	57	57	115	93	52
$\frac{d[DSi]}{dz}$ (mmol m^{-3} m^{-1})	9600	17000	5700	6600	5400	4700	10000	14000	5100
J_{diff} (mmol m^{-2} day^{-1})	0.30	0.54	0.18	0.20	0.17	0.15	0.31	0.44	0.16
$\pm 2\sigma$	0.17	0.09	0.20	0.21	0.11	0.13	0.35	0.23	0.06
Incubation (J_{tot})									
$\frac{d(\mu MDSi)}{d(t/h)}$	-	-	-	-	-	-	0.13	0.19	0.08
$\pm$ (mmol m^{-2} day^{-1})	-	-	-	-	-	-	0.13	0.13	0.06
$\delta^{30}Si_{DSi-Inc\ 0hr}$ (‰)	-	-	-	-	-	-	1.49	1.70	-
$\delta^{30}Si_{DSi-Inc\ 3hr}$ (‰)	-	-	-	-	-	-	1.58	1.69	1.86*
$\delta^{30}Si_{DSi-Inc\ 24hr}$ (‰)	-	-	-	-	-	-	1.71	1.89	1.88*

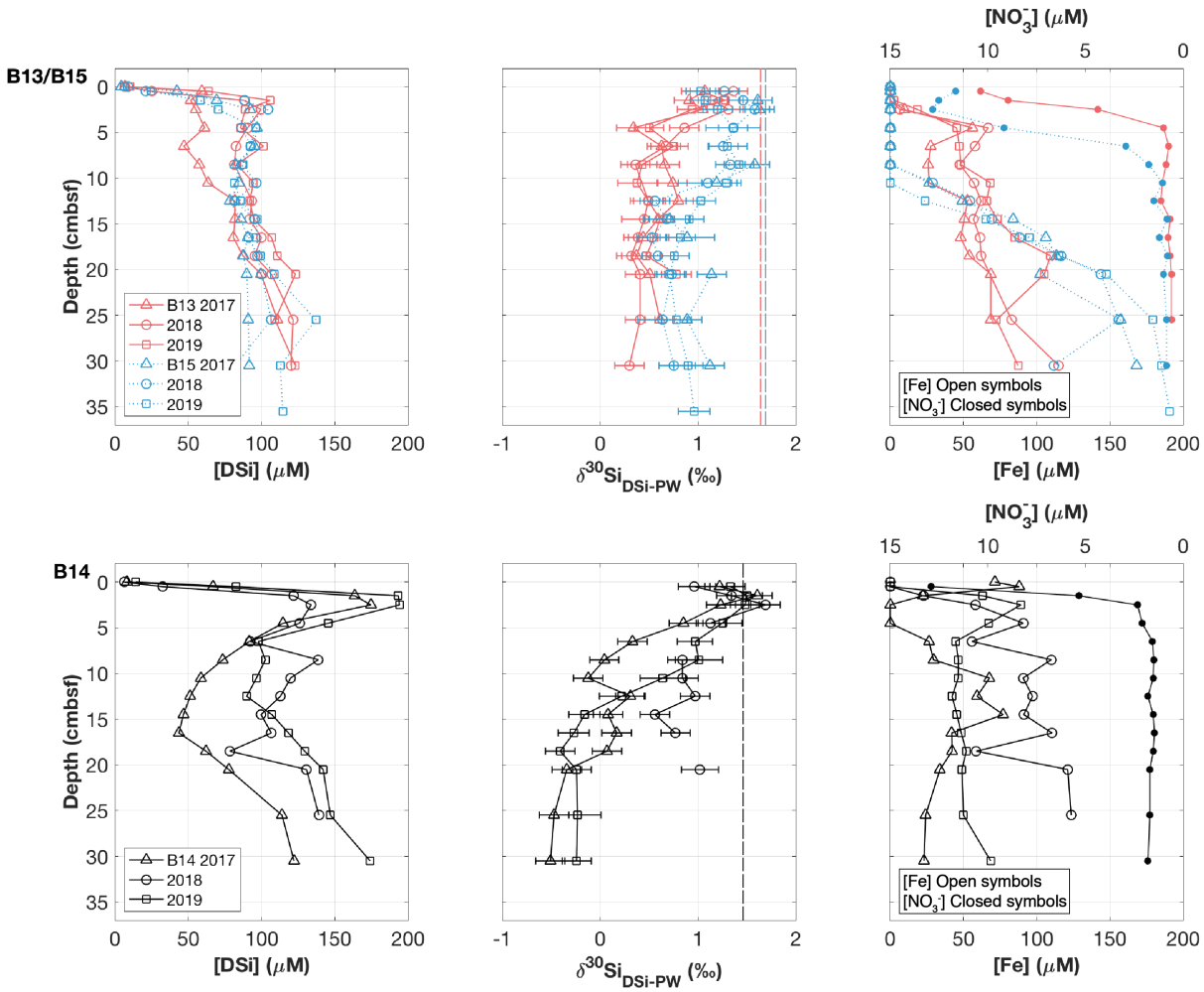

Figure 4.4: Stations B13, B14 and B15 pore water $\delta^{30}Si_{DSi-PW}$ and [DSi] depth profiles for the three ChAOS cruises, as well as representative pore water [Fe] (open symbols) (Faust et al., 2021) and NO_3^- (closed symbols) concentrations (Freitas et al., 2020). The decrease in NO_3^- concentration with depth from the SWI reflects the shift from oxic to anoxic conditions in the pore waters, driving the increase in pore water Fe. The NO_3^- concentration axis has been reversed for clarity. Top row: B13 (black) and B15 (grey), bottom row: B14. Error bars represent ±2σ of the long term reproducibility of Diatomite standard, unless the same value for measurement replicates was greater. Vertical dashed lines show the core top water composition ($\delta^{30}Si_{DSi-CT}$) for the three stations from 2017. Water column CTD samples were also analysed in 100 m intervals from the seafloor to the euphotic zone at station B14. $\delta^{30}Si_{DSi}$ was found to increase towards the surface ocean: +1.46 ±0.15‰ (~295 m depth, core top water), +1.51 ±0.14‰ (279 m), +1.75 ±0.14‰ (179 m), +2.11 ±0.30‰ (74 m).

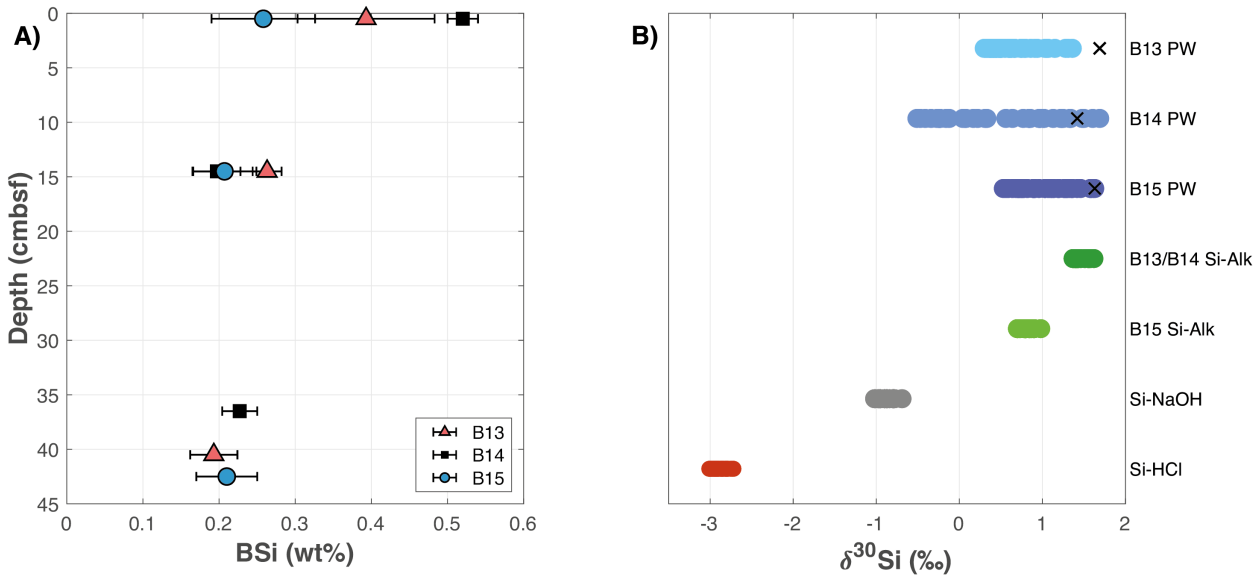

Figure 4.5: A) BSi wt% for B13, B14 and B15 samples from the 2019 cruise. Error bars denote ±2σ of sample triplicates. B) $\delta^{30}Si$ compilation from this study, including all pore water and solid phase leachate measurements. $\delta^{30}Si_{NaOH}$ and $\delta^{30}Si_{HCl}$ values are grouped for the three stations (B13, B14, B15), as they are indistinguishable within long term reproducibility. 'X' denotes the isotopic composition of the core top water from 2017 ($\delta^{30}Si_{DSi-CT}$).

Isotopic composition of the operational pools

The composition of the 0.1 M HCl leach (Si-HCl pool) was isotopically very light for the marine environment, averaging -2.88 ±0.17‰ (n=20), almost identical to the mean value analysed in the same leach phase of Mississippi River plume sediments (-2.89 ±0.45‰) (Pickering et al., 2020). The values presented in this study are within long term reproducibility and so indistinguishable across the stations. The 0.1 M Na_2CO_3 leach (Si-Alk) composition ($\delta^{30}Si_{Alk}$) was geographically distinct, presenting with values of +1.43 ±0.14‰ (n=8) and +1.50 ±0.19‰ (n=7) at B13 and B14 respectively, but +0.82 ±0.16‰ (n=14) under ArW conditions at B15 (Fig. 4.5B). $\delta^{30}Si_{BSi}$ of suspended particulates collected from the Beaufort Shelf and Canada Basin are higher than this and amongst the highest values recorded for surface pelagic diatoms (+2.03 to +3.51 ±0.10‰), thought to be driven by the incorporation of sea-ice species into the assemblages (Varela et al., 2016). However, Varela et al. (2016) observed a decrease in $\delta^{30}Si_{BSi}$ with water depth, with a value of +1.51‰ (n=1) measured at 800 m. Furthermore, an average $\delta^{30}Si_{BSi}$ of +1.42 ±0.95‰ (n=26) was analysed in samples collected from surface and intermediate water depths (50 to 500 m) across the Central Arctic Ocean (CAO) by Liguori et al. (2020). These compositions are consistent with $\delta^{30}Si_{Alk}$ at stations B13 and B14.

The isotopic composition of surface sample NaOH leachates ($\delta^{30}Si_{NaOH}$), a harsh alkaline digestion thought to activate the LSi pool (Pickering et al., 2020), was found to be within uncertainty across the three stations, averaging -0.89 ±0.16‰ (n=18) and did

not vary with sample preparation techniques (section 3.4.3). $\delta^{30}Si_{NaOH}$ in this study is lower than that measured by Pickering et al. (2020) in the same leachate of coastal Mississippi River plume sediments (-0.54 ±0.15‰) but is within range of the mean weathered continental crust and global average clay composition (-0.57 ±0.6‰, Bayon et al. (2018)).

4.5 Discussion

4.5.1 Quantifying the benthic flux of DSi in the Barents Sea

A recent compilation estimated that the global benthic flux of DSi (comprising both J_{diff} calculations and J_{tot} from incubation experiments) ranges from -0.03 to +24.2 mmol m^{-2} day^{-1} (Ng et al., 2020). Benthic fluxes of DSi emanating from CAO basin sediments are within the lower end of this range (+0.002 to +0.035 mmol m^{-2} day^{-1}) (März et al., 2015) and an order of magnitude lower than J_{tot} measurements from Arctic shelf sediments (-0.03 to +6.2 mmol m^{-2} day^{-1}) (Bourgeois et al., 2017), but are similar to flux magnitudes estimated for Norwegian Sea sediments (+0.06 mmol m^{-2} day^{-1} (Rickert, 2000)) and the deep Northwest and Northeast Atlantic (+0.057 and +0.16 mmol m^{-2} day^{-1} respectively) (Ragueneau et al., 2001; Sayles et al., 1996). In this study of the Barents Sea, the J_{diff} (+0.05 to +0.44 mmol m^{-2} day^{-1}) and J_{tot} (+0.08 ±0.06 to +0.19 ±0.13 mmol m^{-2} day^{-1}) approximations of the benthic DSi flux are consistent within uncertainty (Table 4.2) and are in the range of previously published values for pan-Arctic shelf and nearby Svalbard sediments (Bourgeois et al., 2017). Despite the importance of benthic remineralisation for water column nutrient replenishment, the spatial coverage of DSi flux magnitudes is particularly sparse in the European sector of the Arctic Ocean (Fig. 1.1) (Bourgeois et al., 2017), which is improved by our new estimates.

Previous studies have found no systematic relationship between DSi benthic flux magnitudes and seafloor depth, latitude or temperature, although significant differences were observed with sediment lithology (Bourgeois et al., 2017; Frings, 2017). While there are substantial spatial gaps in available observational data, 88% of the Arctic seafloor is estimated to be dominated by clay and siliceous mud (Fig. 4.6) (lithological data from Dutkiewicz et al. (2015)), including the Barents Sea. These lithological groups present with similar global DSi benthic flux magnitudes (+0.36 (+0.11 to +1.29) and +0.52 (+0.08 to +4.66) mmol m^{-2} day^{-1} respectively) (Frings, 2017). Therefore, following März et al. (2015), a multiplication of the calculated flux magnitude by total Arctic shelf area could be deemed a reasonable estimate for the regional contribution of Arctic shelf sediments to the DSi budget.

Our shelf sediment fluxes are an order of magnitude greater than those observed in CAO basins, consistent with the findings of März et al. (2015). If we assume a total Arctic shelf area of 5.03×10^6 km^2 (Jakobsson et al., 2003) we can build upon previous estimates for the regional delivery of DSi from Arctic shelf sediments. With a conservative shelf

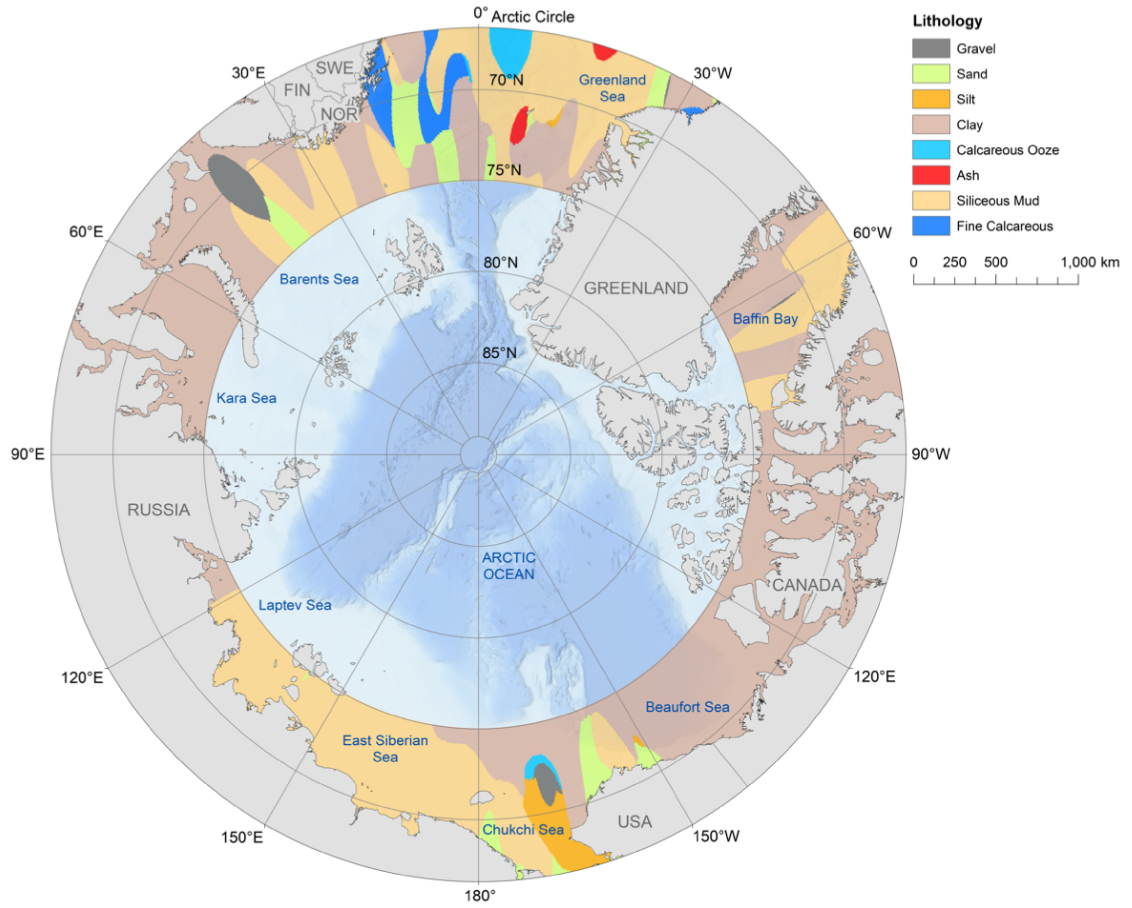

Figure 4.6: Seafloor lithological data for the Arctic Ocean taken from the Dutkiewicz et al. (2015) digital map. There is a paucity of data for the Central Arctic Ocean, but of the area with available data within the Arctic Circle (coastal and shelf sea regions) 52% is dominated by clay and 36% by siliceous mud. SWE- Sweden, FIN- Finland, NOR- Norway.

flux of +0.05 mmol m^{-2} day^{-1}, the lowest Barents Sea J_{diff} among the three stations, a regional contribution of 0.10 Tmol yr^{-1} is estimated. This represents 25% of the contribution from major Arctic rivers (0.4 Tmol yr^{-1}) (Holmes et al., 2012). However, if we use the mean diffusive Barents Sea flux of +0.21 ±0.23 mmol m^{-2} day^{-1} (2σ), representing an average of the linear diffusive flux estimates (Table 4.5), we calculate a regional value of 0.39 Tmol yr^{-1}. This is comparable to März et al. (2015) and represents 98% of the riverine DSi flux, potentially 111% if the pan-Arctic riverine flux calculated by Hawkings et al. (2017) is used (0.35 Tmol yr^{-1}), providing further support for the relative importance of the DSi flux from early diagenetic cycling in Arctic shelf sediments. Furthermore, this regional estimate errs on the side of caution, given that benthic fluxes an order of magnitude greater than those observed in this study can be found in the Canadian Archipelago and Beaufort Sea (Fig. 1.1) (Bourgeois et al., 2017; März et al., 2015).

4.5.2 What are the sources of pore water DSi near the SWI?

Indications from sediment core incubation experiments

Isotopic analysis of incubation core top water samples ($\delta^{30}Si_{DSi-Inc}$) was carried out to determine the source material fuelling the measured fluxes (Fig. 4.3). The temporal evolution of $\delta^{30}Si_{DSi-Inc}$ across the incubation experiment should reflect the composition of phases dissolving in the sediment and released into the overlying water (Ng et al., 2020). Here we briefly summarise the low temperature kinetic isotope fractionations associated with phases that are important in modulating benthic DSi fluxes, to assist in the interpretation of $\delta^{30}Si_{DSi-Inc}$.

The main process that removes DSi from the water column is uptake by diatoms for the formation of BSi, which discriminates against the heavier isotope (^{30}Si) (Varela et al., 2016), the degree to which is potentially species dependant (De La Rocha et al., 1997; Milligan et al., 2004; Sun et al., 2014; Sutton et al., 2013). However, dissolution of BSi is thought to either occur without isotopic fractionation, or invoke a slight enrichment in the lighter isotope in the dissolved phase (Demarest et al., 2009; Sun et al., 2014; Wetzel et al., 2014). The formation of clay minerals through kinetic precipitation reactions and sorption of Si onto metal oxides (specifically Fe (oxyhydr)oxides) on the other hand, preferentially uptake the lighter isotope to a similar degree, leaving the residual DSi relatively isotopically heavy in composition (Delstanche et al., 2009; Hughes et al., 2013; Opfergelt and Delmelle, 2012; Zheng et al., 2016). An enrichment in the heavier isotope was observed in surface sediments of the Peruvian margin, where reaction transport modelling revealed that DSi was reprecipitating with a fractionation factor ($^{30}\epsilon$) of -2‰, attributed to AuSi precipitation (Ehlert et al., 2016a).

At stations B13 and B14 we observe an increase in $\delta^{30}Si_{DSi-Inc}$ between the initial ($\delta^{30}Si_{DSi-Inc\ 0hr}$ of +1.49 and +1.70 ±0.14‰ respectively) and final ($\delta^{30}Si_{DSi-Inc\ 24hr}$

of +1.71 and +1.89 ±0.14‰ respectively) sample measurements, albeit just within long term reproducibility of Diatomite standard measurements (2σ ±0.14‰ (n=116)) (Fig. 4.3, Table 4.2). There is little change in $\delta^{30}Si_{DSi-Inc}$ across the incubation at B15, although the two samples analysed are mixtures of 0/6 hr and 21/24 hr due to inadequate sample volume and so any variation over the time period could be suppressed (Fig. 4.3, Table 4.2). Isotopic variation over the course of the incubation should reflect the composition of the material dissolving into the pore waters and subsequently being released into the core top water. Therefore, as [DSi] increases, the composition of the core top water should tend closer to the average $\delta^{30}Si_{DSi-PW}$ measured in the 0.5 cmbsf interval (1.16 ±0.3‰), which likely reflects the isotopic composition of the benthic DSi flux. Here we use a simple mass balance calculation to determine whether the evolution of $\delta^{30}Si_{DSi-Inc}$ over the course of the core incubation experiments can be explained by the dissolution of BSi or LSi:

$$\delta^{30}Si_{24hr} = \delta^{30}Si_{0hr} \cdot f_{0hr} + \delta^{30}Si_{BSi} \cdot (1 - f_{0hr}) \tag{4.7}$$

where f_{0hr} represents the fraction of the initial incubation core top water ($\delta^{30}Si_{0hr}$) present in the mixture at the end of the core incubation experiment ($\delta^{30}Si_{24hr}$).

The results of the mass balance calculations show that the observed increases in $\delta^{30}Si_{DSi-Inc}$ cannot solely be driven by the dissolution of BSi or LSi, which is supported by the composition of the solid phase reactive pools, as $\delta^{30}Si_{DSi-Inc\ 24hr}$ is higher than $\delta^{30}Si_{Alk}$ and $\delta^{30}Si_{NaOH}$ at all stations (Table 4.2; Table 4.3). This discrepancy is most apparent at B15 where the difference between $\delta^{30}Si_{Alk}$ and $\delta^{30}Si_{DSi-Inc}$ is >1.0 ‰.

The observed increase in [DSi] across all incubations is not significant enough to have driven the concomitant increase in $\delta^{30}Si_{DSi-Inc}$, without the presence of a BSi phase isotopically much heavier than $\delta^{30}Si_{Alk}$ measured here. Assuming $\delta^{30}Si_{DSi-Inc\ 24hr}$ represents a mixture of $\delta^{30}Si_{DSi-Inc\ 0hr}$ and the dissolving BSi (or LSi) ($\delta^{30}Si_{BSi}$), we can use the increases in [DSi] across the incubation period to determine the theoretical composition of BSi (equation 4.7). We find that the dissolving phase would require a composition of +4.5 ±0.20, +2.7 ±0.20 and +1.9 ±0.30‰ at B13, B14 and B15 respectively. These theoretical compositions are heavier than many $\delta^{30}Si$ values previously measured in BSi (-0.75 to +3.0‰, mean +1.11‰ (Egan et al., 2012; Frings et al., 2016; Sutton et al., 2018)) and $\delta^{30}Si_{Alk}$ in this study (+0.82 to +1.50‰).

Both J_{diff} and J_{tot} observed here are up to two orders of magnitude lower than those of Greenland margin incubation experiments (+0.31 to +3.1 mmol m^{-2} day^{-1}) (Ng et al., 2020), therefore the relatively slow rate of DSi release from Barents Sea sediments could allow for the expression of uptake processes (precipitation or adsorption) within the core top water composition on short timescales through the incubation, rather than solely representing the composition of the dissolving phase(s). However, the gradual increase in DSi in the core top waters over the incubation period indicates that the release rate of DSi from dissolution exceeds that of the uptake processes, while the contemporaneous

increase in $\delta^{30}Si_{DSi-Inc}$ implies that the latter impose a stronger isotopic fractionation on the dissolved phase than the former.

Indications from an endmember mixing model

Given the difficulties in determining the sources of the pore water DSi pool through isotopic analysis of the incubation experiment samples, an assessment into the complexity of the processes controlling the δ^{30}Si of Barents Sea pore waters ($\delta^{30}Si_{PW-DSi}$) was carried out. If $\delta^{30}Si_{PW-DSi}$ values are a consequence of a simple two endmember mixing system, whereby a fluid of core top water composition (+1.46 to +1.69‰, 4-27 μM) mixes with a pure phase derived from the dissolution of BSi (~900 μM solubility (Loucaides et al., 2012a; Van Cappellen and Qiu, 1997a) and +0.82 to +1.50‰ $\delta^{30}Si_{Alk}$) or LSi (~100 μM solubility (Fanning and Schink, 1969; Jones et al., 2012; Lerman et al., 1975; Mackenzie et al., 1967; Willey, 1978) and -0.89‰ $\delta^{30}Si_{NaOH}$), the data points should lie along a mixing line. The mixing lines were calculated using the following equation (Geilert et al., 2020a), which assumes steady state:

$$\delta^{30}Si_{mix} = \frac{(\delta^{30}Si_{DSi-CT} \cdot [DSi]_{CT} \cdot f) + (\delta^{30}Si_{BSi} \cdot [DSi]_{BSisol} \cdot (1-f))}{([DSi]_{CT} \cdot f) + ([DSi]_{BSisol} \cdot (1-f))} \tag{4.8}$$

where CT refers to the core top water and f represents the mixing fraction between the two phases. $\delta^{30}Si_{mix}$ was calculated across a range of f values.

$\delta^{30}Si_{B(L)Si}$ and $[DSi]_{B(L)Sisol}$ represent the isotopic composition of the BSi/LSi phase and the dissolution equilibrium DSi concentrations respectively. $\delta^{30}Si_{Alk}$ and $\delta^{30}Si_{NaOH}$ were assumed to represent $\delta^{30}Si_{BSi}$ and $\delta^{30}Si_{LSi}$. The harsh alkaline digestion can activate recalcitrant BSi (Pickering et al., 2020), however molar Al/Si ratios (0.57-0.67) analysed in the NaOH leachates of stations B13, B14 and B15, while being higher than the Al/Si of the continental crust (0.22-0.29 (Rahn (1976) and references therein)), are within range of common clay minerals (0.48-0.96 (Kim et al. (2004); Koning et al. (2002); Rahn (1976) and references therein) (Fig. 3.1). Furthermore, molar Al/Si ratios of 0.57-0.67 are much higher than that measured in BSi (diatom, sponge and radiolarian-derived) in sediment traps, marine sediments and laboratory studies, which ranges from 2.1×10^{-5} to 0.165 (averaging 0.029) (Hendry and Andersen (2013); Middag et al. (2009); van Bennekom et al. (1989); Ren et al. (2013) and references therein). Instead, these values are more consistent with the average Al/Si measured in the Na_2CO_3 leachates (0.024) (Fig. 3.1), indicating that $\delta^{30}Si_{Alk}$ likely reflects the true composition of the BSi pool.

The Barents Sea pore water isotopic data presented here do not fall on the calculated mixing lines plotted in Fig. 4.7, indicating that Si cycling within the Barents Sea seafloor is not conservative and is influenced by processes that fractionate $\delta^{30}Si_{PW-DSi}$ to higher (heavier) and lower (lighter) values. To further elucidate the specific sources and sinks

that combine to produce the observed [DSi] profiles, we can examine the downcore trends in [DSi] and $\delta^{30}Si_{PW-DSi}$.

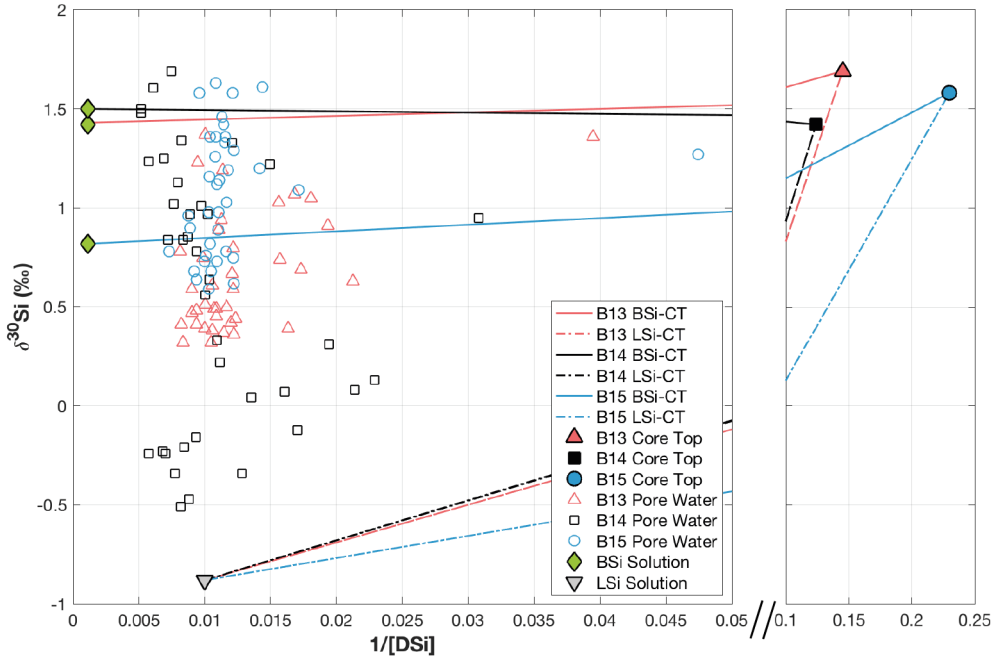

Figure 4.7: Pore water $\delta^{30}Si_{DSi-PW}$ plotted against the inverse of the DSi concentration (1/[DSi]). The mixing line was calculated following equation 4.8, from Geilert et al. (2020a). The $\delta^{30}Si$ of the BSi and LSi solution for each station is equivalent to $\delta^{30}Si_{Alk}$ and $\delta^{30}Si_{NaOH}$ respectively.

Barents Sea asymptotic and quasi-asymptotic sediment pore water DSi concentrations are much lower than the theoretical solubility of pure BSi in seawater (600-1000 μM at 0-2^{o}C, 1600-1900 μM at 25^{o}C (Dixit et al., 2001; Hurd, 1983; Lawson et al., 1978; Rickert, 2000; Rickert et al., 2002; Van Cappellen and Qiu, 1997a)). Multiple hypotheses have been used to explain the magnitude of pore water DSi asymptotes, including a true equilbirium (Dixit et al. (2001) and references therein), however numerous studies have since shown that the apparent solubility of BSi is inversely correlated to the ratio of lithogenic to biogenic components. This ratio is widely accepted to be, or correlate with, the main factor controlling the accumulation of DSi in marine sediments (Dixit et al., 2001; Gallinari et al., 2002; Loucaides et al., 2010; Rickert, 2000; Van Cappellen and Qiu, 1997a). The term apparent solubility is used as the value represents a weighted average of all the silicate phases present within the matrix (Rickert, 2000; Van Cappellen and Qiu, 1997a). The apparent solubility tends to be very similar in magnitude to the measured in-situ pore water asymptotic DSi concentration, therefore solubility represents an important control on the pore water DSi pool (Dixit et al., 2001; Gallinari et al., 2002; Rickert, 2000; Sarmiento and Gruber, 2006; Van Cappellen and Qiu, 1997a).

Stations B13, B14 and B15 have surface level (0-0.5 cmbsf interval) BSi contents of 0.39 $\pm$0.09 (2σ), 0.52 $\pm$0.02 and 0.26 $\pm$0.07 wt% respectively (or 139 $\pm$33, 185 $\pm$7, 92 $\pm$24

μmol g dry wt^{-1}) and an estimated LSi fraction of 96%, calculated using the following equation (Sayles et al., 2001)):

$$\%LSi = 100 - \%(BSi + \mathrm{CaCO_3} + TOC) \tag{4.9}$$

where TOC refers to the total organic carbon content.

This LSi fraction is similar to those of the Greenland and Norwegian Seas (37-98%, mean 86%) (Pirrung et al., 2008) and Kara Sea to the east (84-98%, mean 88%) (Fahl et al., 2003; Rickert, 2000). The presence of silicate minerals (LSi or AuSi) reduces the solubility of the bulk sediment as these minerals have a much lower solubility than fresh BSi (Rickert, 2000). However, the sediment detrital component also actively influences the BSi solubility in multiple ways. LSi dissolution releases Al into the pore water dissolved phase, which can be incorporated into BSi, thereby introducing interferences in the dissolution properties (Van Bennekom et al., 1991). Further, reverse weathering produces cation-rich aluminosilicates that directly replaces BSi with a less soluble clay phase (Dixit et al., 2001; Van Cappellen and Qiu, 1997a) (equation 4.1), although this process can also occur at the expense of other reactive Si phases, such as degraded terrigenous clays (Aller, 2014; Frings et al., 2016).

The pore water asymptotic DSi concentration thus represents a dynamic balance between dissolution and reprecipitation of Si phases, that reflects the average solubility of each constituent phase in the assemblage. Given our estimate that clay rich Barents Sea surface sediments are composed of approximately 96% detrital content and very low surface BSi contents of just 0.26-0.52 wt%, it is then not surprising that the asymptotic concentrations measured here are similar to the solubility of many silicate minerals. Indeed, a previous study of neighbouring Norwegian Sea sediments that are almost devoid of BSi (<1 wt%) show low apparent solubilities (140 μM) and corresponding asymptotic pore water DSi concentrations (110 μM) (Rickert, 2000) not dissimilar to those observed here, as do sediments of the CAO (70-100 μM) (März et al., 2015). These values are much lower than pore water [DSi] found in BSi rich sediments (>20 wt%) of the subarctic North Pacific or Southern Ocean, which can exhibit asymptotic DSi concentrations of 500-900 μM (Aller, 2014; Dixit et al., 2001; King et al., 2000; Rabouille et al., 1997).

Indications from δ^{30}Si measured in sediment pore waters and solid phase reactive pools

Relative to the respective core top waters, stations B13, B14 and B15 have isotopically lighter upper pore waters and higher [DSi], indicating an isotopically lighter phase is being released into the DSi pool (Fig. 4.4). Through a simple mass balance, akin to equation 4.7, we calculate the theoretical isotopic composition of the 0.5 cmbsf pore water interval, with the assumption that the increase in [DSi] between the core top water and this depth is

Table 4.3: Mean values of the parameters used in the upper pore water mass balance calculations (equation 4.7) for the three cruise years. $\delta^{30}Si_{DSi-PW}$ at 0.5 cmbsf was predicted based on two calculations simulating the sole dissolution of BSi and LSi respectively. The proportion of LSi dissolution contributing to the 0.5 cmbsf DSi pool was calculated assuming a known fraction of core top water ($[DSi]_{CT}/[DSi]_{0.5cmbsf}$) and no influence of AuSi precipitation at this depth interval. For B15, calculations were only carried out for 2018 and 2019 as the 0.5 cmbsf $\delta^{30}Si_{DSi-PW}$ value was not available. $\delta^{30}Si_{DSi-CT}$ could only be determined for 2017 due to a lack of sufficient sample volume in subsequent years.

Parameter	B13	B14	B15
$[DSi]_{CT}$ (μM)	8.0	9.2	7.7
$\delta^{30}Si_{DSi-CT}$ (‰)	1.64	1.46	1.69
$[DSi]_{0.5cmbsf}$ (μM)	49.6	60.6	22.8
f_{CT}	0.18	0.16	0.34
$\delta^{30}Si_{Alk}$ (‰)	1.43	1.50	0.82
$\delta^{30}Si_{NaOH}$ (‰)	-0.89	-0.89	-0.89
$\delta^{30}Si_{DSi-PW}$ predicted (BSi release) (‰)	1.47	1.49	1.12
$\delta^{30}Si_{DSi-PW}$ predicted (LSi release) (‰)	-0.43	-0.52	0.0
$\delta^{30}Si_{DSi-PW}$ 0.5 cmbsf measured (‰)	1.15	1.17	1.15
LSi contribution to 0.5 cmbsf [DSi] (%)	14	13	-

driven solely by the dissolution of either the BSi or LSi phase (of $\delta^{30}Si_{Alk}$ and $\delta^{30}Si_{NaOH}$ composition respectively). Below 0.5 cmbsf, the predicted $\delta^{30}Si_{DSi-PW}$ is much lower than that analysed, likely reflecting the precipitation of AuSi as the pore water [DSi] surpasses the solubility concentration of the AuSi (see section 4.5.3). In summary, while the composition of the 0.5 cmbsf pore water intervals at B15 across the three cruises can be reproduced by the discrete dissolution of the BSi phase, at B13 and B14 neither phase is able to reproduce the analysed composition alone (Table 4.3). This finding points to the contemporaneous release of BSi and LSi into the pore water DSi pool, which has implications for the Barents Sea Si bud get, as BSi dissolution represents a recycling of oceanic Si, while LSi constitutes a source of new Si discharging from the seafloor.

The importance of LSi as a DSi source for the pore water pool was inferred in a similar study of Guaymas basin sediment cores (Geilert et al., 2020a), as well as for diagenetic products in Mississipi River plume sediment (Pickering et al., 2020). Furthermore, Tréguer et al. (1995) posited that LSi could be significant for Atlantic sediments, given that [DSi] in bottom waters is well below the solubility of many terrigenous minerals. These observations are consistent with the hypothesis that non-siliceous oceanic sediments (i.e. clays and calcareous sediment) contribute an estimated 64% of the global benthic Si flux (Frings, 2017) and with numerous experiments that demonstrate the release of Si from silicate minerals within days of being placed in low [DSi] seawater at ArW temperatures (Fanning and Schink (1969); Lerman et al. (1975); Mackenzie and Garrels (1965); Mackenzie et al. (1967); Siever (1968); Tréguer et al. (2021) and references therein). Additionally, LSi dissolution has been shown to represent a significant yet previously overlooked source of DSi

to beach and ocean margin sediments (Ehlert et al., 2016b; Fabre et al., 2019; Jeandel et al., 2011).

Digestion experiments carried out in this study show that the Si-NaOH pool, associated with soluble LSi and residual, less reactive BSi (e.g. sponge spicules and radiolarians) (Pickering et al., 2020) is isotopically light and indistinguishable in composition across the three stations ($\delta^{30}Si_{NaOH}$ of -0.89 ±0.16‰). Thus, dissolution of the Si-NaOH pool could account for the shift towards lower $\delta^{30}Si_{PW-DSi}$ observed across the SWI at the three stations.

In order to explain the regionally distinct $\delta^{30}Si_{Alk}$ compositions, we simulate the uptake of DSi and production of BSi by diatoms assuming a Rayleigh model of isotope fractionation following De La Rocha et al. (1997). With an initial surface water composition of +2.0‰ (Liguori et al. (2020); Varela et al. (2016) and the 74 m water column $\delta^{30}Si_{DSi}$ from this study (Fig. 4.4)), a $^{30}\epsilon$ of -1.18‰ represents the minimum fractionation factor that is able to reproduce a δ^{30}Si in the accumulated BSi pool of +0.82‰ and therefore the fraction of DSi remaining in the surface water (f) is equal to 1 (Fig. 4.8). A $^{30}\epsilon$ of -1.18‰ is within range of previously measured values for the uptake of DSi by diatoms (-0.42 to -2.21‰, averaging -1.1 ±0.4‰) (De La Rocha et al., 1997; Sutton et al., 2013). If we then assume instead that the diatoms take up DSi with a more substantial $^{30}\epsilon$ of -2‰, the accumulating BSi pool has a composition of +0.82‰ when f is equal to 0.4. Under either modelled $^{30}\epsilon$ scenario, a δ^{30}Si of +1.5‰ in the accumulated BSi can also be accounted for (f equal to 0.1-0.2), equivalent to the $\delta^{30}Si_{Alk}$ measured at station B14 (Fig. 4.8). This observation illustrates that in a scenario wherein the diatom community composition of the spring blooms both north and south of the PF are identical, the discrepancy in $\delta^{30}Si_{Alk}$ can be explained by a contrast in the stage of bloom development from which the sampled BSi phases were deposited. Regional differences in the cycling of Si are the most likely driver of the observed disparity in $\delta^{30}Si_{Alk}$ across the Barents Sea stations, although regional and species-specific variability in $^{30}\epsilon$ have been observed (De La Rocha et al., 1997; Fripiat et al., 2012; Sutton et al., 2013), which could also represent contributing factors. Indeed, a range of diatom species have been identified across the three hydrographic domains of the Barents Sea (e.g. *Chaetoceros*/*Thalassiosira* at the PF/marginal ice zone (MIZ) and *Fragilariopsis*/*Chaetoceros*/*Melosira arctica* in the ArW region) (Oziel et al., 2017; Wassmann et al., 1999, 2006a).

To summarise, the benthic Si cycle of the Barents Sea cannot be characterised as a conservative system comprised of mixing between two endmember solutions, one of core top water composition and the other derived from the dissolution of BSi. We conclude there is strong evidence for the dissolution of both BSi and LSi, as well as the uptake of DSi by processes within the sediment cores. We also observe evidence for uptake processes active within the incubation experiments, potentially demonstrating that the uptake of DSi can occur on both shorter (daily) and longer (thousands of years) timescales.

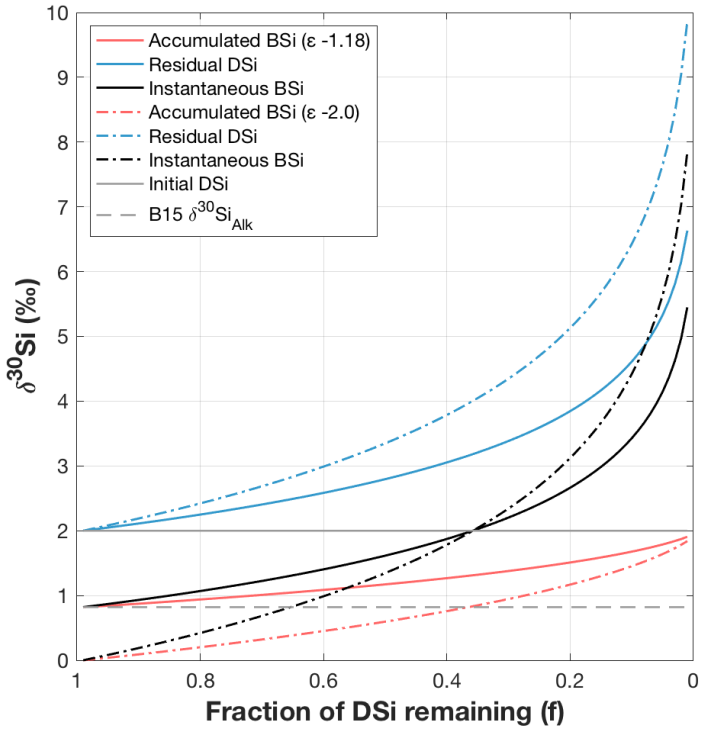

Figure 4.8: Simulating Rayleigh fractionation during the uptake of DSi by diatoms from seawater (De La Rocha et al., 1997). Lines depict changes in $\delta^{30}Si$ of the DSi pool (blue) and the compositions of the instantaneously formed BSi (black) and accumulated BSi (red). A fractionation factor ($^{30}\epsilon$) of -1.18‰ (solid lines) represents the maximum value $^{30}\epsilon$ can be, in order to generate an accumulated BSi composition of +0.82‰, when assuming an initial surface water composition of +2.0‰ (Liguori et al., 2020). We also model DSi uptake assuming a $^{30}\epsilon$ of -2.0‰ (dashed lines), representing the upper range of measured $^{30}\epsilon$ values (Sutton et al., 2013).

4.5.3 Is there evidence of AuSi precipitation or a redox control on the benthic Si system?

Evidence of AuSi precipitation

The composition and trends of $\delta^{30}Si_{DSi-PW}$ values in the upper 3 cmbsf are similar at B14 and B15 and across the three cruises (Fig. 4.4), characterised by an enrichment in the heavier isotope below 0.5 cmbsf, which drives the $\delta^{30}Si_{DSi-PW}$ back towards the core top water compositions. This shift is likely to be caused by the precipitation of AuSi in Barents Sea sediments, which preferentially removes the lighter isotope. At B13 we see a deviation towards a heavier composition at the same depth interval (Fig. 4.4) that is consistent with AuSi formation, although the shift is within analytical uncertainty. Similar shifts have been observed in $\delta^{30}Si_{DSi-PW}$ profiles of previous studies of both temperate and high latitude systems (Ehlert et al., 2016a; Geilert et al., 2020a; Ng et al., 2020). This increase in the $\delta^{30}Si_{DSi-PW}$ is unlikely to be caused by the dissolution of a solid phase, as the $\delta^{30}Si_{DSi-PW}$ at 3.5 cmbsf at the three stations increases to higher values than that measured in the operationally-defined reactive Si pools of the solid phase, especially at B15 (Fig. 4.5B). Additionally, dissolution would not resolve the relative shift from 0.5 cmbsf to 3.5 cmbsf observed at stations B14 and B15 (Fig. 4.4), which requires enrichment in the heavier isotope downcore.

It is possible that the enrichment in the heavier isotope towards the 3 cmbsf maxima is driven by adsorption of Si onto Fe (oxyhydr)oxides, which has been inferred as an important pathway for the early diagenesis of Si in modern marine sediments and throughout geological history (Ehlert et al., 2016a; Fischer and Knoll, 2009; Geilert et al., 2020a; Kennedy et al., 2003; Li et al., 2014; Ng et al., 2020). However, pore water dissolved oxygen concentrations decrease rapidly downcore from the SWI (Fig. 4.9), reaching hypoxic conditions (62.5-94 μM or 2-3 mg L^{-1}) by 0.5 cmbsf and between 0-0.25 cmbsf at stations B13 and B14 respectively. Sediment pore waters at these two stations become almost completely devoid of oxygen within the upper 1-1.5 cmbsf, while dissolved Fe concentrations begin to increase from the depths at which hypoxia is reached, reflecting reductive dissolution of solid phase Fe minerals (Fig. 4.4 and Fig. 4.10). Adsorption and desorption of Si onto Fe (oxyhydr)oxides is poorly understood relative to other elements (e.g. P), however it is generally assumed that this process is dependent upon the degree of oxygenation (Niemistö et al. (2018) and references therein). A previous modelling study found better agreement between measured and simulated sediment DSi fluxes when a dependency on oxygenation was imposed, with DSi desorption occurring below a threshold oxygen concentration of 62.5 μM (Testa et al., 2013). Furthermore, this assumption is supported by batch laboratory experiments, which showed that sediments released increased amounts of DSi under hypoxic conditions, a significant portion of which was potentially sourced from adsorbed Si (Lehtimäki et al., 2016).

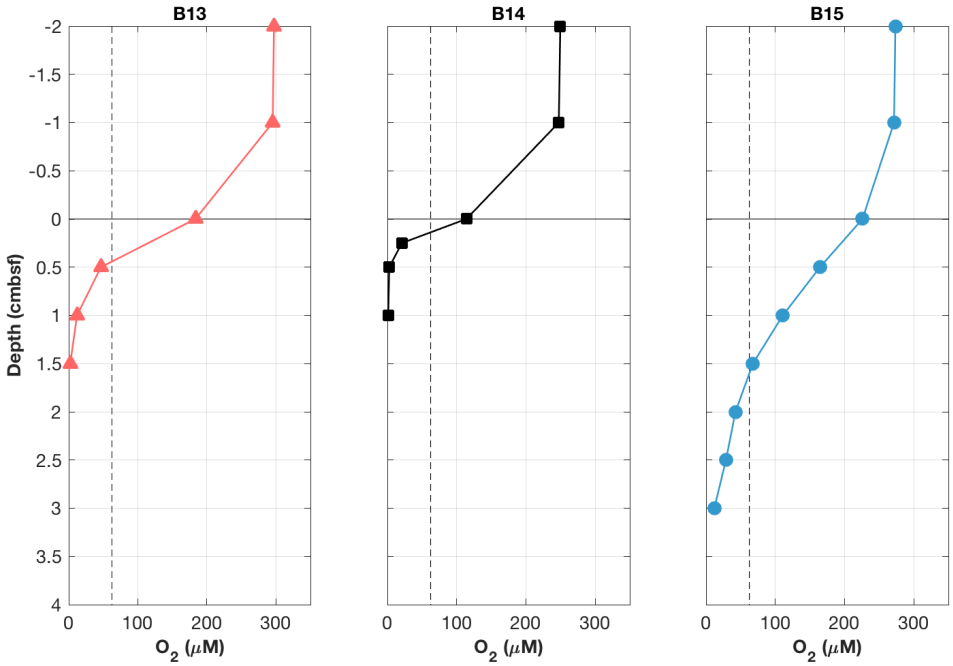

Figure 4.9: Pore water dissolved oxygen profiles measured on cruise JR18006 (2019) for stations B13, B14 and B15 with a FireStingO2-Mini (PyroScience). Vertical dashed black lines depict hypoxic conditions (62.5 μM), thicker solid horizontal black line represents the SWI. Data can be found in the supplementatry material of Freitas et al. (2020).

Hypoxic conditions are attained at very shallow depths within the seafloor of the Barents Sea shelf, which could suggest that it is unlikely that the downcore enrichment in the heavier Si isotope between the SWI and 3 cmbsf is driven by Si adsorption onto Fe (oxyhydr)oxides. However, adsorption cannot be completely ruled out given the lack of complete mechanistic understanding of this process and the relationship with oxygenation, especially at station B15 where dissolved oxygen persists below 4 cmbsf.

Sediment pore water solutes are incorporated into authigenic clay minerals during reverse weathering, following a reaction scheme similar to equation 4.1. Therefore, pore water elemental concentrations can be analysed alongside $\delta^{30}Si_{DSi-PW}$ to provide a further indication as to whether AuSi precipitation is active within the sediments (Aller, 2014). Most pore water Mg concentration profiles measured in this study show a gradual negative trend downcore at stations B13, B14 and B15, potentially indicating their uptake into AuSi. This observation suggests that authigenic clay formation is not necessarily limited to the upper 3 cmbsf, wherein we observe the shift towards higher $\delta^{30}Si_{DSi-PW}$ (Fig. 4.11). While AuSi precipitation is generally thought to be concentrated within the upper ~5 cmbsf of hemipelagic sediments (Mackin and Aller, 1984; Van Cappellen and Qiu, 1997a), this process has been inferred at greater depth (Ehlert et al., 2016a; Geilert et al., 2020a; Rude and Aller, 1994) and below ~30-50 cmbsf in CAO sediments (März et al., 2015).

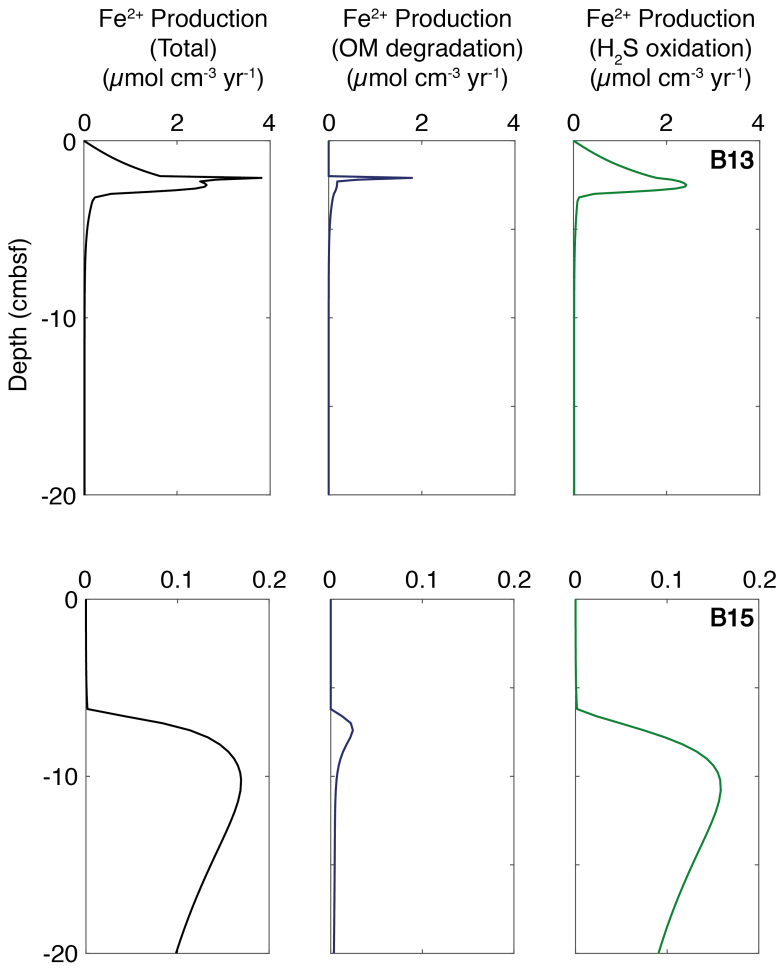

Figure 4.10: Simulated rates of dissolved Fe production in Barents Sea sediment cores, derived from steady state reaction-transport model simulations (Freitas et al., 2020). Note the change in x axis scale across the top (B13) and bottom (B15) rows. OM = organic matter.

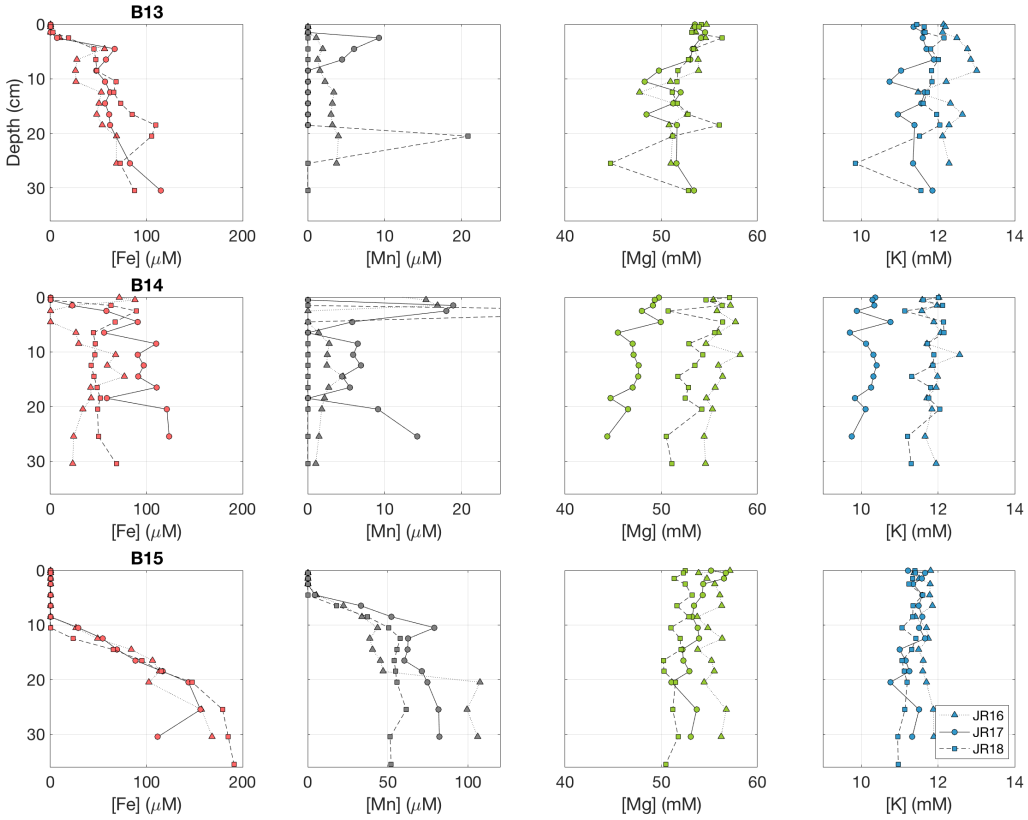

Figure 4.11: Pore water major (Mg, K) and trace element (Fe, Mn) concentrations for the three cruise years analysed by ICP-OES (top row station B13, middle row B14, bottom roe B15). Data presented correspond to the same coring events from which samples were collected for pore water Si isotope analysis. Note the change in scale of Mn concentrations between stations. Pore water trace and major element concentrations (Fe, Mn, Mg and K) were analysed at the University of Leeds using a Thermo Scientic iCAP 7400 Radial ICP-OES, uncertainty was ±3.5% (Faust et al., 2021). Fe and Mn data are provided in the supplementary to Faust et al. (2021), Mg and K data can be found in Table 4.4.

Fewer of the K concentration profiles show a similar decline, with most presenting with little to no downcore change (Fig. 4.11). However, a lack of concomitant dissolved K uptake does not necessarily preclude the interpretation that reverse weathering is occuring within the seafloor. Ng et al. (2020) observed a similar decline in Mg with no decrease in K in sediments from the Greenland margin, which they interpret as reflecting the precipitation of an AuSi clay phase that has a different stoichiometry than might be expected under a typical reverse weathering regime. Geilert et al. (2020a) determined that AuSi is precipitating within oxygen minimum zone sediments of the Guaymas Basin, which exhibit an increasing pore water dissolved K concentration downcore. Furthermore, our hypothesis that LSi is dissolving in Barents Sea sediments complicates the interpretation of pore water elemental indicators that are typically associated with reverse weathering. Dissolution of terrigenous clays from the LSi pool would release solutes into the pore water phase, potentially mitigating some of the K uptake that corresponds to AuSi precipitation.

Previous assumptions as to the solubility of AuSi minerals (220-330 μM) would preclude precipitation of AuSi in Barents Sea and many North Atlantic sediments, as [DSi] remains undersaturated with respect to these minerals (Cassarino et al., 2020; Dixit et al., 2001; Ehlert et al., 2016a; Krissansen-Totton and Catling, 2020; Loucaides et al., 2010). However, dissolution experiments carried out over 8.5 years suggest that glauconite, an aluminosilicate and common weathering product of BSi (Odin and Fröhlich, 1988), has a solubility of $\sim$50 μM in seawater (Lerman et al., 1975). In addition, Wollast (1974) calculated that sepiolite, an authigenic clay mineral found to form on BSi surfaces in deep ocean sediments (Hurd, 1973), could theoretically precipitate from seawater with a [DSi] as low as 30 μM. Subsurface formation of low solubility AuSi minerals such as these could explain why we see an initial decrease in $\delta^{30}Si_{DSi-PW}$ as LSi dissolves, then an increase to the 3.5 cmbsf $\delta^{30}Si_{DSi-PW}$ maxima, as DSi increases past the solubility of the precipitating phase. This hypothesis is consistent with previous work evidencing the precipitation of AuSi in LSi-dominated high latitude sediments (März et al., 2015). This is an important observation, as approximately one-third of the global seafloor is occupied by sediments relatively devoid of BSi (<1 wt%) (Tréguer and De La Rocha, 2013).

Coupling the evidence for benthic LSi dissolution near the SWI with that for AuSi precipitation has implications for the regional ocean Si budget. If LSi sourced from a terrestrial environment is dissolving in shallow seafloor sediments, contributing to the benthic DSi flux, these minerals represent a new source of ocean DSi. If this LSi-sourced DSi is subsequently reprecipitated as AuSi, the AuSi term represents a true sink, as that benthic DSi can no longer interact with the bottom water DSi pool. It is for this reason that the early diagenetic conversion of BSi to AuSi is generally also considered a significant sink of ocean Si (Laruelle et al., 2009; Rahman et al., 2016, 2017). It has been argued that the BSi to AuSi reaction pathway does not represent a significant sink for ocean Si, instead reflecting an early diagenetic conversion between solid phases at depth that

enhances the preservation of BSi (DeMaster, 2019; Frings et al., 2016). However, here we have shown that both LSi and BSi are dissolving in the uppermost sediments of the Barents Sea and thus contribute to the benthic DSi flux. Therefore, AuSi precipitation likely represents a true sink of Si in the context of the shallow sediment cores studied here, as the exchange of sediment pore water DSi with the overlying bottom water is impeded by their precipitation.

Evidence for a redox influence on the benthic Si cycle

Below 3.5 cmbsf at B13 and B14 and below 10.5 cmbsf at B15, we see an enrichment in the lighter isotope downcore across all cruise years (Fig. 4.4) in addition to a general trend towards increased [DSi] towards the base of the cores at B13 and B14 (Fig. 4.2), albeit at a much slower rate than beneath the SWI. These observations point to the release of an isotopically light Si source. The downcore increase in [DSi] is unlikely to be driven by the dissolution of BSi, given that corresponding BSi contents have reached or are approaching their minima of ∼0.2 wt% by the mid-core (∼15 cmbsf) (Fig. 4.5A). Furthermore, we have presented evidence supporting the dissolution of LSi in the upper reaches of the sediment, below the SWI. However, below this depth the rate of LSi dissolution is likely to slow, given that pore water [DSi] at all Barents Sea stations approaches ∼100-150 μM within the upper 5 cmbsf, which is similar to or above the apparent Si solubility of many silicate minerals (Lerman et al., 1975; Mackenzie et al., 1967) and low BSi bulk sediment in seawater at low temperatures (Fanning and Schink, 1969; Jones et al., 2012; Willey, 1978).

Potential sources for this isotopically light pool of Si at depth are: i) the desorption of Si adsorbed onto metal oxides, or ii) sponge derived BSi dissolution. The affinity of the lighter Si isotope for metal oxides, specifically Fe (oxyhydr)oxides, is well documented. Adsorption of DSi onto Fe (oxyhydr)oxides has a $^{30}\epsilon$ of -1.1 to -3.2‰, enriching the residual dissolved phase in the heavier isotope (Delstanche et al., 2009; Zheng et al., 2016). Following Pickering et al. (2020) we are able to demonstrate the presence of such a reactive pool in all three sediment cores. The δ^{30}Si of the Si-HCl pool ($\delta^{30}Si_{HCl}$), which is thought to remove metal oxide coatings from BSi (Pickering et al., 2020), averaged -2.88 ±0.17‰ and was indistinguishable within long term reproducibility across the three sites. $\delta^{30}Si_{HCl}$ did however appear susceptible to contrasting sample preparation techniques, presenting with much higher $\delta^{30}Si_{HCl}$ values in ground sediment samples (-2.56 ±0.14‰), likely as a result of LSi contamination (see section 3.4.3 for discussion). The ubiquitous presence and desorption of Si from this metal oxide phase at the three stations could explain the ^{28}Si enrichment we observe across the oxic-anoxic boundaries, as well as the gradual increase in [DSi] observed below ∼3.5 cmbsf most clearly at B13. It is possible that the adsorption of ^{28}Si onto metal oxides may also contribute to the increasing $\delta^{30}Si_{DSi-PW}$ we observe downcore from the SWI to a maxima at ∼3 cmbsf, however sediment pore waters at

stations B13 and B14 become hypoxic (dissolved oxygen concentrations of <62.5 μM) by 0.5 cmbsf and between 0-0.25 cmbsf respectively. Such conditions have previously been reported to stimulate desorption of Si from Fe (oxyhydr)oxides, rather than adsorption (Lehtimäki et al., 2016; Testa et al., 2013). Coupled with our observations of downcore decreasing pore water Mg concentrations, it is probable that the trends in $\delta^{30}Si_{DSi-PW}$ observed in the surface sediment intervals of the Barents Sea stations are a result of AuSi precipitation, although adsorption cannot be completely ruled out as the relationship between this process and oxygenation requires further investigation. Adsorption of Si onto Fe (oxyhydr)oxides within the oxygenated water column and subsequent desorption within surface sediment intervals has been inferred through analysis of stable Si isotopes in sediment cores of the Guaymas Basin (Geilert et al., 2020a).

Examination of the [Fe] pore water profiles of the same sampling stations indicates that the light isotope enrichment occurs at a similar depth interval to where Fe appears and NO_3^- is diminishing in the pore water phase (Fig. 4.4). This observation is consistent with a change in redox state to anoxic conditions, which drives the reductive dissolution of solid Fe (oxyhdr)oxides. Furthermore, reaction-transport model output derived from baseline steady-state simulations of B13 and B15 (Freitas et al., 2020) indicate that the release of Fe into the dissolved phase across the redox boundaries is driven by a combination of organic matter degradation and the reoxidation of reduced species (H_2S) diffusing upwards towards the SWI (Fig. 4.10). The disparity in $\delta^{30}Si_{DSi-PW}$ profiles between 3.5 and 10.5 cmbsf at B13 and B15 (which reaches a peak at 8.5 cmbsf with B15 an average of +0.96‰ higher), are consistent with the different depths of the redox boundaries found at the two sites, which is shallower at B13 than at B15 (Fig. 4.4).

In addition to the reductive dissolution of Fe (oxyhydr)oxides observed across Barents Sea sediment redox boundaries, reductive dissolution of Mn (oxyhydr)oxides is indicated by a decrease in the solid phase Mn content and concomitant increase in dissolved Mn across distinct depth intervals (Fig. 4.12 and 4.11). The cycling of Mn metal oxides could also influence $\delta^{30}Si_{DSi-PW}$, however the release of dissolved Mn occurs at slightly shallower depth intervals than Fe. At station B15 for example, pore water Fe concentrations increase from 10.5 cmbsf compared with 4.5 cmbsf for Mn, the latter being approximately 5 cm shallower than where the shift in $\delta^{30}Si_{DSi-PW}$ begins (Fig. 4.4). The interpretation that Fe (oxyhydr)oxides are driving the observed shifts in pore water δ^{30}Si across the redox boundaries is therefore favourable, however both metal oxides could be contributing.

It has previously been suggested for sediments of the Greenland Shelf that the reductive dissolution of protective solid phase Fe coatings on BSi increased pore water DSi, by enhancing the reactivity of the BSi, although there appeared to be no influence on $\delta^{30}Si_{DSi-PW}$ (Ng et al., 2020). Higher $\delta^{30}Si_{DSi-PW}$ values at one station in the Peruvian Upwelling Zone were interpreted to be due to the adsorption of Si onto reactive Fe (Ehlert et al., 2016a) and a heavy $\delta^{30}Si_{DSi-PW}$ in pore fluids of elevated [Fe] (190 μM) in the

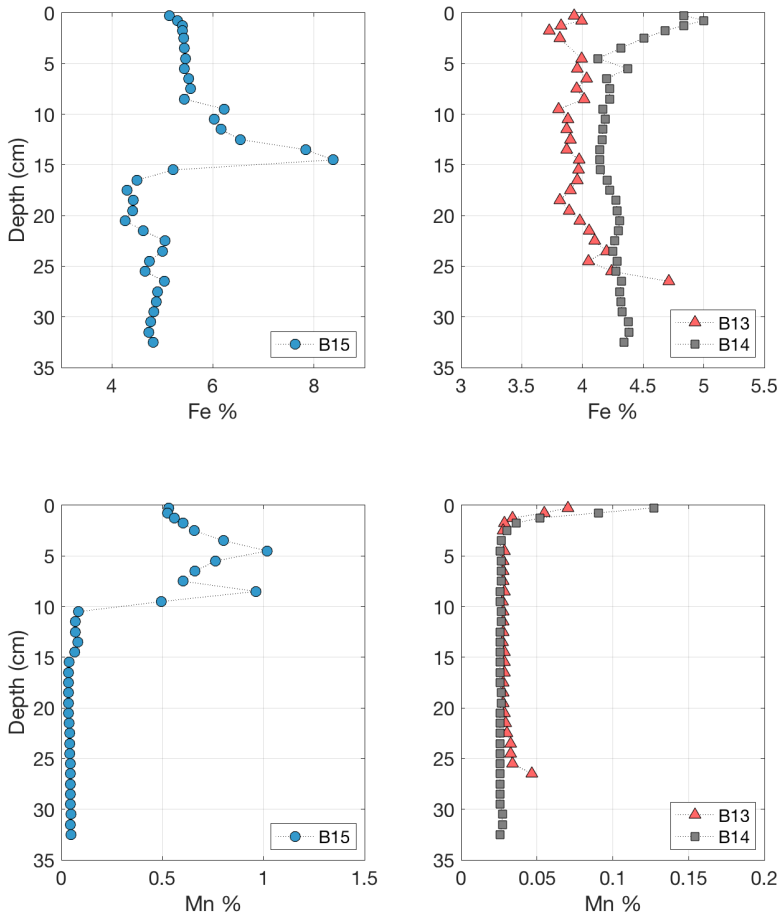

Figure 4.12: Solid phase Mn and Fe content measured by XRF. Note the scale change between the stations and elements. The increased Fe content between 12-15 cm at station B15 represents a pink, Fe-rich sediment band, hosting an increased content of crystalline Fe phases relative to the surrounding sediment layers. The sediments deposited within this pink band are thought to originate from Devonian sandstones in central Svalbard (Faust et al., 2021). XRF analysis was carried out using a Philips PW-2400 WD-X-ray fluorescence spectrometer at the University of Oldenburg. Analytical precision and accuracy were better than 5%. Solid phase Fe and Mn data can be found in the main text and supplementary information respectively of Faust et al. (2021).

Guaymas Basin was interpreted to be driven by the precipitation of Fe-Si silicates (Geilert et al., 2020a). Our finding supports this previous work by identifying a redox-driven shift in $\delta^{30}Si_{DSi-PW}$ in marine sediment cores. It is likely that the low asymptotic and quasi-asymptotic [DSi] in the sediments studied here allows for the detection of this process, which is masked by a much larger DSi pool in other shelf seas.

Dissolution of sponge spicule derived BSi, which has been observed in core incubation experiments of Greenland shelf sediments (Ng et al., 2020), is another potential DSi source enriched in the lighter isotope ($\delta^{30}Si_{sponge}$ values range from -5.72 to +0.87‰, mean -2.1‰ (Sutton et al. (2018) and references therein)). While the release of DSi from sponge BSi cannot be ruled out for the Barents Sea stations, the corresponding depths of negative shifts in $\delta^{30}Si_{DSi-PW}$ profiles with increasing (decreasing) pore water [Fe] ($[NO_3^-]$) indicate a redox driven coupling between metal oxides and Si. In addition, the $\delta^{30}Si_{HCl}$ values at all three stations provide strong evidence for the presence of an isotopically light metal oxide phase in the sediment, as this digestion is highly unlikely to dissolve sponge spicules and instead thought to predominantly remove authigenic metal oxide coatings from BSi (Pickering et al., 2020). As a result, desorption of Si from the metal oxide phase is thought to be the most likely cause of the observed downcore shift towards lighter compositions at the three Barents Sea stations (Fig. 4.4). Coupled with the observations supporting the release of LSi in the surface sediment layers, this evidence suggests that there is a ^{28}Si enriched, mineralogical control on the DSi released into Barents Sea cores below the SWI.

4.5.4 What are the key geographic and temporal variations?

[DSi] profiles of the ArW stations (B15, B16, B17) (Fig. 1.2) show striking similarities both spatially (within sediment core replicates of one cruise) and temporally (between cruises) (Fig. 4.2). This characteristic is not as evident in the cores of the AW dominated region (B03, B13, B14), which is most apparent at B14 where there is evidence for non-steady state, transient dynamics in the upper 5 cmbsf. Here, we see strong peaks in [DSi] and consequently the benthic flux magnitudes in 2017 and 2019, which is in contrast to 2018, where the [DSi] profile presents with a more typical, asymptotic form (Fig. 4.4, Table 4.2).

Oceanic frontal zones are highly dynamic and the PF (B14, Fig. 1.2) of the Barents Sea is no exception, where the interleaving of multiple water masses enhances physical mixing (Barton et al. (2018) and references therein). Wassmann and Olli (2004) attributed this feature to the observed increase in particulate organic carbon export efficiency at depth underneath the Barents Sea PF, relative to stations on the adjacent sides (Fig. 4.14).

In addition to the physical mixing, studying of sea ice conditions from the respective cruise years indicates that the MIZ was influencing B14 much later in 2017 and 2019 than prior to the 2018 cruise (Fig. 4.13). In 2018 the MIZ in the Barents Sea retreated more

rapidly and earlier in the season, receding north of the polar front almost three months prior to sampling, unlike in 2017 and 2019 when the retreat was just six weeks prior to sediment coring. The most distinct phytoplankton blooms observed in the Barents Sea are found beneath the MIZ, supported by stratification of the nutrient rich photic zone in late spring and summer as sea ice melts (Olli et al., 2002a; Reigstad et al., 2002; Wassmann et al., 2006b). Phytoplankton community compositions of Barents Sea MIZ blooms are initially dominated by diatoms (Makarevich et al., 2022; Olli et al., 2002a) and observations from the Fram Strait indicate that BSi export fluxes increase with sea ice cover (Lalande et al., 2013a). We therefore suggest that the sediment pore water [DSi] peaks at station B14 are transient features, sourced from the dissolution of fresher, more reactive BSi relative to the background material, which is deposited under MIZ bloom conditions and results in stronger [DSi] gradients across the SWI. The resulting enhanced rate of molecular diffusion would then begin to dissipate the peak. We suggest that the increased time under ice free conditions in 2018 prior to sampling relative to the other cruise years allowed for sufficient recovery of the DSi profile towards steady state conditions, such that the peak was not observed after pore water extraction.

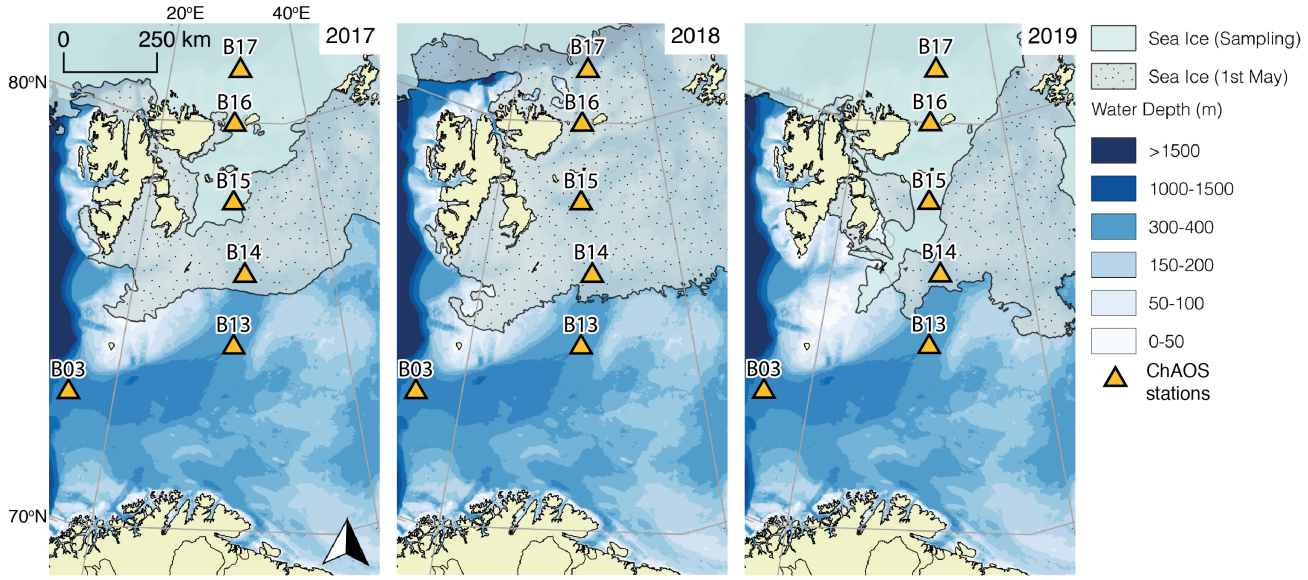

Figure 4.13: Comparison of sea ice conditions on the day of sampling at station B14 (30th July 2017, 25th July 2018, 13th July 2019) compared to the sea ice extent on the 1st May of each cruise to demonstrate the disparity in ice melt across the three years. Left to right: JR16006 (summer 2017), JR17007 (2018), JR18006 (2019). Daily sea ice extent data from the U.S. National Ice Center and National Snow and Ice Data Center (NSIDC) (Fetterer et al., 2010).

The hypothesis that fresh, bloom derived BSi dissolution is driving the sediment pore water [DSi] peaks observed at B14 is also evidenced in a comparison of the $\delta^{30}Si_{DSi-PW}$ values at 0.5 cmbsf across the cruise years. In 2017 and 2019 where the peaks in pore water DSi are observed, the 0.5 cmbsf pore water samples have heavier isotopic compositions (+1.22 and +1.33 ±0.14‰ respectively) than that sampled in 2018 (+0.96 ±0.16‰).

This disparity is likely to be a result of the dissolution of fresh BSi with a δ^{30}Si similar to that measured in the Si-Alk reactive pool of the 2019 surface sediment interval (+1.50 ±0.19‰). In all three cruise years, the $\delta^{30}Si_{DSi-PW}$ then increases to a maxima within the 1.5 and 2.5 cmbsf depth intervals. The average $\delta^{30}Si_{DSi-PW}$ within these two pore water intervals in 2018 was +1.52‰ (+1.34 to +1.69‰), indicating that the dissolution of fresh BSi in 2017 and 2019 would be indistinguishable from the $\delta^{30}Si_{DSi-PW}$ background signal.

We estimate that the bloom derived fresh BSi contributes an additional 0.23 mmol m^{-2} d^{-1} to the B14 background (2018) DSi flux of 0.12 mmol m^{-2} d^{-1} (43.8 mmol m^{-2} yr^{-1}) (Table 4.2), representing an increase of 192%. If we assume this elevated flux endures across the three months required to dissipate the DSi peak, which is likely an overestimation, this would equate to an additional 20.9 mmol m^{-2} to the total annual DSi flux at B14 of 64.7 mmol m^{-2} (background plus the contribution from the bloom material).

The superposition of non-steady state seasonal dynamics driven by tight benthic-pelagic coupling under bloom conditions onto a background steady state benthic Si system can also elucidate the intricate downcore structures observed in the DSi profiles at station B14 (Fig. 4.2). The gradual increase in DSi observed downcore from 10-15 cmbsf across the cruise years is consistent with the other AW stations (B03 and B13). Therefore the addition of a transient DSi peak onto the DSi profiles of stations B03 or B13 within the upper 5 cmbsf would result in a DSi profile not dissimilar to that observed at B14 in 2017 and 2019. The linear increases in DSi towards the base of the AW station sediment cores is unlikely to be driven by the dissolution of BSi, given that measurements of the solid phase show that a BSi minima of ∼0.2 wt% is reached in the mid core (Fig. 4.5A). This increase could instead be fuelled by the continued dissolution of LSi or desorption of Si from metal oxides, consistent with $\delta^{30}Si_{DSi-PW}$ observations that evidence the continued release of an isotopically light source of Si at depth (Fig. 4.4).

Previously it was thought that dissolution rates of BSi were very slow relative to the residence time of BSi in upper seafloor sediments, leading to the assumption that the benthos represented a stable repository, unaffected by seasonal variability in surface processes and the export efficiency of phytodetritus (Ragueneau et al., 2001). This stability was interpreted to be due to the fact that the residence time of BSi in surface sediments (decades to centuries) is much longer than that of seasonal and interannual variation in fluxes to the seafloor (Sayles et al., 1996; Schlüter and Sauter, 2000), which is in agreement with similar findings regarding the early diagenetic remineralisation of organic matter (Martin and Bender, 1988; Sayles et al., 1994). In direct contrast to these findings, research into the Si cycle of the Porcupine Abyssal Plain uncovered strong evidence for non-steady state, transient responses in the pore water DSi stock driven by deposition of fresh BSi phytodetritus on a seasonal timescale (Ragueneau et al., 2001). Ragueneau et al. (2001)

noted an increase in the sediment pore water DSi inventory of +19% from early spring to summer, resulting in an enhanced DSi benthic flux of +54% across the same time interval. These increases were coeval with a significant rise in the deposition flux of BSi at the SWI. Typically these peaks in DSi inventory were found within the upper 5.5 cmbsf, however they were observed as deep as 10-20 cmbsf. Ragueneau et al. (2001) conclude that the delivery of fresh BSi to depth by megafaunal mixing allowed for the expression of seasonal dynamics well below the SWI.

Bioturbation coefficients were determined experimentally for stations B13, B14 and B15, which range from 2-6 cm^2 yr^{-1} to a maximum depth of 6.5 cmbsf (Solan et al., 2020). These observations illustrate that fresh BSi deposited at the SWI could influence the sediment column at the depth intervals wherein we observe peaks in DSi (1.5-4.5 cmbsf), despite the low rates of sediment accumulation (Faust et al., 2020; Zaborska et al., 2008) that would preclude burial to such a depth on a seasonal timescale if advective processes were acting alone (Fig. 4.2).

As with organic matter (Sayles et al., 1994), in order for variations in BSi deposition fluxes to influence pore water DSi on a seasonal time frame, the mean lifetime of the deposited material must be less than one seasonal period (1 year) (Burdige, 2006). Therefore, BSi undergoing dissolution must *a priori* have a reactivity constant (k_{diss}) of >1 yr^{-1}, as the lifetime of material undergoing first-order dissolution is equivalent to $1/k_{diss}$ (Burdige, 2006). k_{diss} of fresh diatoms in the surface ocean range from 3 to 70 yr^{-1} (Ragueneau et al., 2000). Typically, k_{diss} values of this magnitude are not found in sediment cores, however a k_{diss} of 1.38 yr^{-1} (mean lifetime of 9 months) was measured as deep as 19 cmbsf at 4850 m depth at the Porcupine Abyssal Plain, attributed to bioturbation by megafauna (Ragueneau et al., 2001). A bloom derived BSi k_{diss} of 1.38 yr^{-1} corresponds to a half life of six months, implying that just 25% of the material would be preserved beyond one year. It is therefore plausible that the periodic deposition of fresh phytodetritus associated with the Arctic spring bloom in the much shallower Barents Sea (∼300 m) could readily influence sediment pore water chemistry, especially given the effect of frontal mixing on export efficiency observed in proximity to station B14 (Wassmann and Olli, 2004).

4.5.5 Conclusions

This work highlights the highly dynamic nature of the Arctic benthic Si system, which involves the cycling of Si from BSi, LSi and Si adsorbed onto metal oxides to the DSi phase, some of which is then taken up, most likely during the formation of AuSi. These findings provide important implications for the Arctic Ocean Si budget, as the dissolution of LSi represents a source of new Si and the subsequent reprecipitation of DSi as AuSi constitutes a potentially important isotopically light sink.

We show that fresh BSi derived from pelagic phytoplankton blooms is rapidly recycled in the upper reaches of the Barents Sea seafloor. This recycling process presents as dis-

tinctive, transient increases in pore water [DSi] immediately beneath the SWI, consistent with lower latitude systems (e.g. the Porcupine Abyssal Plain (Ragueneau et al., 2001)). These [DSi] peaks appear to dissipate within six weeks to three months, as evidenced by the contrasting sea ice conditions relative to the sampling time across the three cruises.

This strong benthic-pelagic coupling for Si in the spring bloom period will probably be subject to change as the community composition of phytoplankton blooms tend towards that of the Atlantic system and the MIZ retreats northwards (Dybwad et al., 2021). The impacts of Atlantification and sea ice loss that bring about these changes in community composition are also amplified by the observed reduction in [DSi] across the subpolar North Atlantic Ocean (Hátún et al., 2017) and consequently in Barents Sea Atlantic inflow waters over the last three decades (Rey, 2012). These pressures will likely result in less favourable conditions for diatom growth, potentially exacerbating the Si-limitation observed in diatom blooms off Svalbard (Krause et al., 2018), which has also been detected across the Arctic Ocean and in the North Atlantic subpolar region (Giesbrecht, 2019; Giesbrecht and Varela, 2021; Krause et al., 2019).

These changes would significantly influence the transient dynamics observed in this study. At present, the magnitude of the benthic DSi fluxes driven by seasonal dynamics in primary productivity (2017 and 2019) at B14 represent an estimated 192% increase relative to the apparent background flux magnitude (2018). The anticipated adjustment in the composition of pelagic primary producers that will be deposited at the SWI may hinder this recycling process in the future, thereby reducing the estimated contribution of the bloom derived material to the annual DSi benthic flux. However, here we have inferred a significant influence of Si derived from or associated with minerals (LSi and metal oxides) on the background Barents Sea benthic Si system, which is almost devoid of BSi. This mineralogical control may afford an element of stability to the magnitude of the annual benthic flux of DSi. Whether this benthic-derived DSi directly influences pelagic primary production in the Barents Sea photic zone or is transported off-shelf is unclear and is the subject of ongoing research.

Appendix: Supplementary Material

4.6 Quantifying the benthic flux magnitude by curve-fitting

In addition to using a linear assumption of the DSi concentration gradient at the SWI (i.e. [DSi] in the core top water and at 0.5 cmbsf) for the flux calculations, here we also utilise an exponential function (Frings, 2017; McManus et al., 1995) to reproduce the sediment pore water [DSi] profiles, in order to determine which method is appropriate for the Barents Sea:

$$[DSi]_z = C_{asymp} - (C_{asymp} - C_{SWI}) \times e^{-\beta z} \tag{4.10}$$

$$(d[DSi] \,/\, dz)_{z=0cm} = \beta \times (C_{asymp} - C_{SWI}) \tag{4.11}$$

Calculated fits of the profiles were obtained through adjustment of the asymptotic concentration (C_{asymp}) and exponential constant (β). Differentiation of equation 4.10 at the SWI (depth (z) = 0) (equation 4.11) was carried out to determine the concentration gradient for Fick's first law of diffusion. Previous studies have employed both the linear assumption (Cassarino, 2018; März et al., 2015) and the full profile exponential fit methods (Frings, 2017; Ng et al., 2020).

Flux estimates for B15 are consistent across the two methodologies, indicating that a two point linear assumption of the gradient is adequate for estimating benthic flux magnitudes at this station (see Table 4.2). However, for B13 and B14 the flux magnitudes derived from the exponential fit method are significantly higher than the linear counterparts (see Table 4.2). An adequate representation of the asymptotic concentration at depth and the [DSi] gradient at the SWI are the two main sources of uncertainty in the curve fitting method (Rickert, 2000). The disparities observed across the two methods at B13 and B14 is therefore thought to be due to the deviations in the [DSi] profiles from a typical asymptotic increase (Cassarino et al., 2020) (Fig. 4.2), which precludes an accurate replication of the observational data in the modelled profiles. Unsurprisingly, this is reflected in the normalised RMSE between the calculated and measured [DSi] values, which are lowest for B15 profiles, indicating a better prediction of the measured data by the model at B15 relative to B13 and B14.

Research Data

Research data associated with this article are available in the UK Polar Data Centre (UK PDC), British Antarctic Survey and can be accessed with https://doi.org/10.5285/8933AF23-E051-4166-B63E-2155330A21D8.

Table 4.4: Sediment pore water Mg and K concentrations for stations B13, B14 and B15 across the three cruise years. Data corresponds to the same coring events from which samples were collected for pore water Si isotope analysis.

	JR16		JR17		JR18	
Depth (cmbsf)	Mg (mM)	K (mM)	Mg (mM)	K (mM)	Mg (mM)	K (mM)
B13						
0.0	54.7	12.1	53.5	11.4	54.2	11.5
0.5	53.3	12.2	53.5	11.4	53.9	11.6
1.5	53.6	12.1	54.6	11.6	53.2	11.7
2.5	54.6	12.5	54.1	11.6	56.3	12.2
4.5	53.5	12.8	53.2	11.7	53.3	11.8
6.5	53.8	12.9	53.0	11.9	52.8	12.0
8.5	53.9	13.0	49.8	11.0	51.7	11.8
10.5	51.0	12.2	48.3	10.7	51.6	11.8
12.5	47.7	11.5	52.0	11.7	51.2	11.7
14.5	51.3	12.3	51.2	11.6	51.7	11.6
16.5	52.7	12.6	48.5	11.0	52.8	12.0
18.5	50.8	12.3	51.7	11.4	56.1	12.0
20.5	51.2	12.1			51.2	11.5
25.5	51.0	12.3	51.6	11.3	44.7	9.8
30.5			53.4	11.9	52.8	11.6
B14						
0.0	57.2	12.0	49.8	10.4	57.1	12.0
0.5	55.4	11.6	49.3	10.3	54.6	11.6
1.5	57.2	12.0	49.1	10.3	56.3	12.1
2.5	55.8	11.6	48.0	9.9	50.7	11.1
4.5	57.7	11.9	50.0	10.8	56.4	12.1
6.5	56.0	12.1	45.5	9.7	55.6	12.2
8.5	54.6	11.7	47.0	10.1	52.9	11.7
10.5	58.2	12.6	47.1	10.3	54.3	11.9
12.5	56.0	11.9	47.6	10.4	53.5	11.9
14.5	56.4	12.0	47.6	10.3	51.7	11.3
16.5	55.6	12.0	47.0	10.3	52.8	11.8
18.5	54.7	11.7	44.7	9.8	52.5	11.8
20.5	55.3	11.8	46.5	10.1	54.2	12.0
25.5	54.4	11.7	44.4	9.7	50.5	11.2
30.5	54.6	12.0			51.1	11.3
B15						

0.0	57.2	11.8	55.2	11.2	52.5	11.4
0.5	53.9	11.4	56.7	11.7	52.3	11.4
1.5	54.8	11.5	56.5	11.6	51.3	11.3
2.5	55.6	11.8	54.3	11.4	52.5	11.2
4.5	56.1	11.8	54.3	11.6	53.2	11.6
6.5	56.3	11.9	53.4	11.5	51.7	11.4
8.5	53.8	11.4	53.2	11.6	52.9	11.3
10.5	54.8	11.7	53.8	11.5	51.0	11.1
12.5	56.3	11.7	54.0	11.7	52.0	11.4
14.5	53.8	11.5	52.2	11.0	52.0	11.3
16.5	55.2	11.6	52.3	11.2	50.2	11.1
18.5	55.5	11.6	52.9	11.3	50.3	11.1
20.5	54.5	11.7	51.1	10.8	51.5	11.2
25.5	56.8	11.9	53.7	11.5	51.2	11.1
30.5	56.2	11.9	53.1	11.3	51.8	10.9
35.5					50.5	11.0

Table 4.5: Triplicate DSi benthic flux estimates for all Multicorer deployments and cruise years (Fig. 4.2), as summarised in Table 4.2.

Cruise	2017			2018			2019		
Station	B13	B14	B15	B13	B14	B15	B13	B14	B15
Sampling Date	17/07	30/07	20/07	14/07	25/07	17/07	07/07	13/07	10/07
Linear									
J_{diff}	0.32	0.37	0.24	0.11	0.09	0.08	0.09	0.44	0.17
(mmol m^{-2} day^{-1})	0.17	0.44	0.19	0.23	0.17	0.17	0.21	0.27	0.12
	0.29	0.31	0.05	0.10	0.11	0.06	0.33	0.29	0.13
Exponential									
J_{diff}	0.31	0.29	0.28	0.17	0.11	0.14	0.16	0.58	0.18
(mmol m^{-2} day^{-1})	0.21	0.56	0.20	0.32	0.22	0.22	0.28	0.36	0.13
	0.37	0.58	0.08	0.12	0.19	0.09	0.50	0.39	0.19

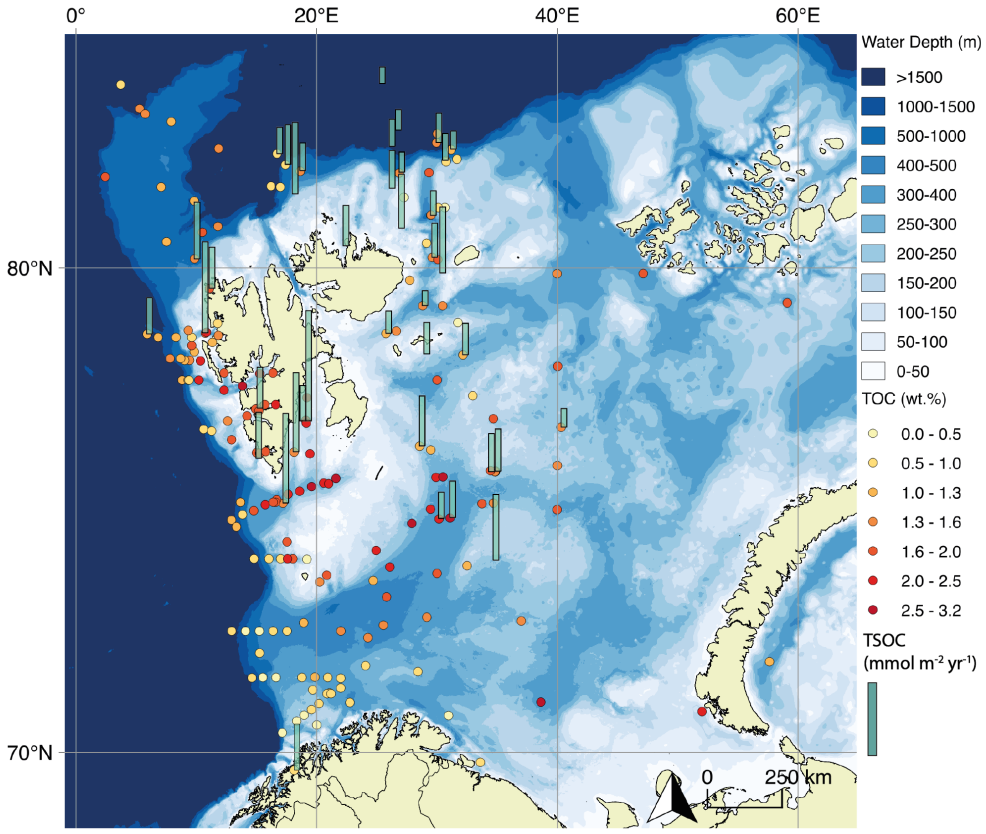

Figure 4.14: Total organic carbon content (TOC) compilation (wt%), represented by circular symbols graduated with a yellow-red colour ramp. Transparent green bars represent total sediment oxygen consumption (TSOC), a proxy for organic carbon remineralisation rate. Note how the higher TOC values trace the approximate location of the polar front (Fig. 1.2). TOC and TSOC data: Glud et al. (1998); Hulth et al. (1994); Kostka et al. (1999); Lein et al. (2008); Nickel et al. (2008); Vandieken et al. (2006a,b). TSOC only: (Morata et al., 2013; Pfannkuche and Thiel, 1987). TOC only: Carroll et al. (2008b); Knies and Martinez (2009); Lein et al. (2008); Piepenburg et al. (1995) and ChAOS data (Faust et al., 2020).

Chapter 5

Using a reaction-transport model to further disentangle and quantify key processes involved in Barents Sea benthic silicon cycling

This chapter reproduces an article in revision at Biogeosciences, authored by J.P.J. Ward, K.R. Hendry, S. Arndt, J.C. Faust, F.S. Freitas, S.F. Henley, J.W. Krause, C. März, A.C. Tessin and R.L. Airs. The article is titled 'Benthic Silicon Cycling in the Arctic Barents Sea: a Reaction-Transport Model Study' (BGD [preprint], https://doi.org/10.5194/bg-2022-51). As lead author, I completed the laboratory work to compile the isotopic composition dataset as per Chapter 4. I co-developed the steady state and transient model code, alongside SA and FS and performed all simulations to attain model-data best-fits. Additional co-author contributions include: JF, FS, SH and AT helped in the sampling and processing of onboard samples. SH measured Si concentrations in sediment pore water and water column samples. KH and JK assisted JW with sediment digestion experiment design. JF, CM and AT measured pore water major and trace element concentrations and RA conducted surface sediment pigment analysis. All authors contributed to manuscript improvement through commenting on draft versions.

5.1 Abstract

Over recent decades the highest rates of water column warming and sea ice loss across the Arctic Ocean have been observed in the Barents Sea. These physical changes have resulted in rapid ecosystem adjustments, manifesting as a northward migration of temperate phytoplankton species at the expense of silica-based diatoms. These changes will potentially alter the composition of phytodetritus deposited at the seafloor, which acts

as a biogeochemical reactor, pivotal in the recycling of key nutrients, such as silicon (Si). To appreciate the sensitivity of the Barents Sea benthic system to the observed changes in surface primary production, there is a need to better understand this benthic-pelagic coupling. Stable Si isotopic compositions of sediment pore waters and the solid phase from three stations in the Barents Sea reveal a coupling of the iron (Fe) and Si cycles, the contemporaneous dissolution of lithogenic silicate minerals (LSi) alongside biogenic silica (BSi) and the potential for the reprecipitation of dissolved silicic acid (DSi) as authigenic clay minerals (AuSi). However, as reaction rates cannot be quantified from observational data alone, a mechanistic understanding of which factors control these processes is missing. Here, we employ reaction-transport modelling together with observational data to disentangle the reaction pathways controlling the cycling of Si within the seafloor. Processes such as the dissolution of BSi are active on multiple timescales, ranging from weeks to hundreds of years, which we are able to examine through steady state and transient model runs.

Steady state simulations show that 60 to 98% of the sediment pore water DSi pool may be sourced from the dissolution of LSi, while the isotopic composition is also strongly influenced by the desorption of Si from metal oxides, most likely Fe (oxyhydr)oxides (FeSi), as they reductively dissolve. Further, our model simulations indicate that between 2.9 and 37% of the DSi released into sediment pore waters is taken up with a fractionation factor of approximately -2 ‰, most likely representing reprecipitation as AuSi. These observations are significant, as the dissolution of LSi represents a source of new Si to the ocean DSi pool and precipitation of AuSi an additional sink, which could address imbalances in the current regional ocean Si budget. Lastly, transient modelling suggests that at least one-third of the total annual benthic DSi flux could be sourced from the dissolution of more reactive, diatom-derived BSi deposited after the surface water bloom at the marginal ice zone. This benthic-pelagic coupling will be subject to change with the continued northward migration of Atlantic phytoplankton species, northward retreat of the marginal ice zone and the observed decline in DSi inventory of the subpolar North Atlantic Ocean over the last three decades.

5.2 Introduction

The Barents Sea is one of seven shelf seas encircling the central Arctic Ocean and lies on the main inflow route for Atlantic Water. Oceanic circulation is driven by regional cyclonic atmospheric circulation and constrained by areas of prominent bathymetry (Fig. 1.2) (Smedsrud et al., 2013). Atlantic Water is fed in to the Barents Sea through the Barents Sea opening between mainland Norway and Bear Island. This water mass then flows northwards through the Barents Sea basin, where it is met by colder, fresher Arctic Water, infiltrating the Barents Sea from the northern openings (Oziel et al., 2016). The

oceanic polar front delineates these two water masses, the geographic position of which is tightly constrained in the western Barents Sea by the bathymetry, but is less well defined in the east (Barton et al., 2018; Oziel et al., 2016). The heat content of the Atlantic Water-dominated region south of the polar front maintains a sea ice free state year-round, whereas the northern Arctic Water realm is seasonally sea ice covered, with a September minimum and a March/April maximum (Årthun et al., 2012; Faust et al., 2021).

The Barents Sea winter sea ice extent has been in decline since circa 1850 (Shapiro et al., 2003), but from 1998 the rate of retreat has become the most rapid observed on any Arctic shelf (Årthun et al., 2012; Oziel et al., 2016). Current forecasts suggest the Barents Sea will become the first year-round, sea ice free Arctic shelf by 2075 ($\pm$28 years) (Onarheim and Årthun, 2017). The atmospheric and water column warming driving this sea ice retreat is both a result of anthropogenic and natural processes, with recent 'Atlantification' arising from a northward expansion of the Atlantic Water realm (Årthun et al., 2012) and a reduction in sea ice import to the northern Barents Sea. The impact of these changes is an increase in upward heat fluxes, which inhibits sea ice formation (Lind et al., 2018).

The dynamic nature of the Barents Sea with respect to the physical oceanographic characteristics is reflected biologically in the ecosystems of the two main hydrographic realms. Annual primary production in the Barents Sea is estimated to range from 70 to 200 gC m^{-2}, with lower values found in the northern Arctic Water realm, where a deep meltwater-formed pycnocline limits nutrient replenishment through wind-induced mixing (Sakshaug, 1997; Wassmann et al., 1999). However, the most distinct peaks in the rates of primary production are found in the marginal ice zone (MIZ) (reaching 1.5-2.5 gC m^{-2} d^{-1}, Hodal and Kristiansen (2008); Titov (1995)) (Fig. 5.1), which forms in spring/early summer as sea ice melts and retreats northwards, stratifying the water column and stabilising the nutrient-rich photic zone (Krause et al., 2018; Olli et al., 2002a; Reigstad et al., 2002; Vernet et al., 1998; Wassmann et al., 1999; Wassmann and Reigstad, 2011; Wassmann et al., 2006b). The phytoplankton communities of the Barents Sea in proximity to the polar front and MIZ tend to be dominated by pelagic and ice-associated diatom species, as well as the prymnesiophyte *Phaeocystis pouchetii* (Degerlund and Eilertsen (2010); Downes et al. (2021); Makarevich et al. (2022); Syvertsen (1991); Wassmann et al. (1999) and references therein).

Temperate flagellate species are becoming more dominant in the Eurasian Basin of the Arctic Ocean and are expected to become the resident bloom formers in the region, with further expansion of the Atlantic Water realm and as sea surface temperatures continue to rise (Ingvaldsen et al., 2021; Neukermans et al., 2018; Orkney et al., 2020; Oziel et al., 2020). Nutrient concentrations in Atlantic Waters flowing into the Barents Sea have declined over the last three decades and are forecast to do so throughout the 21st century (Neukermans et al. (2018) and references therein). Crucially, a much more sig-

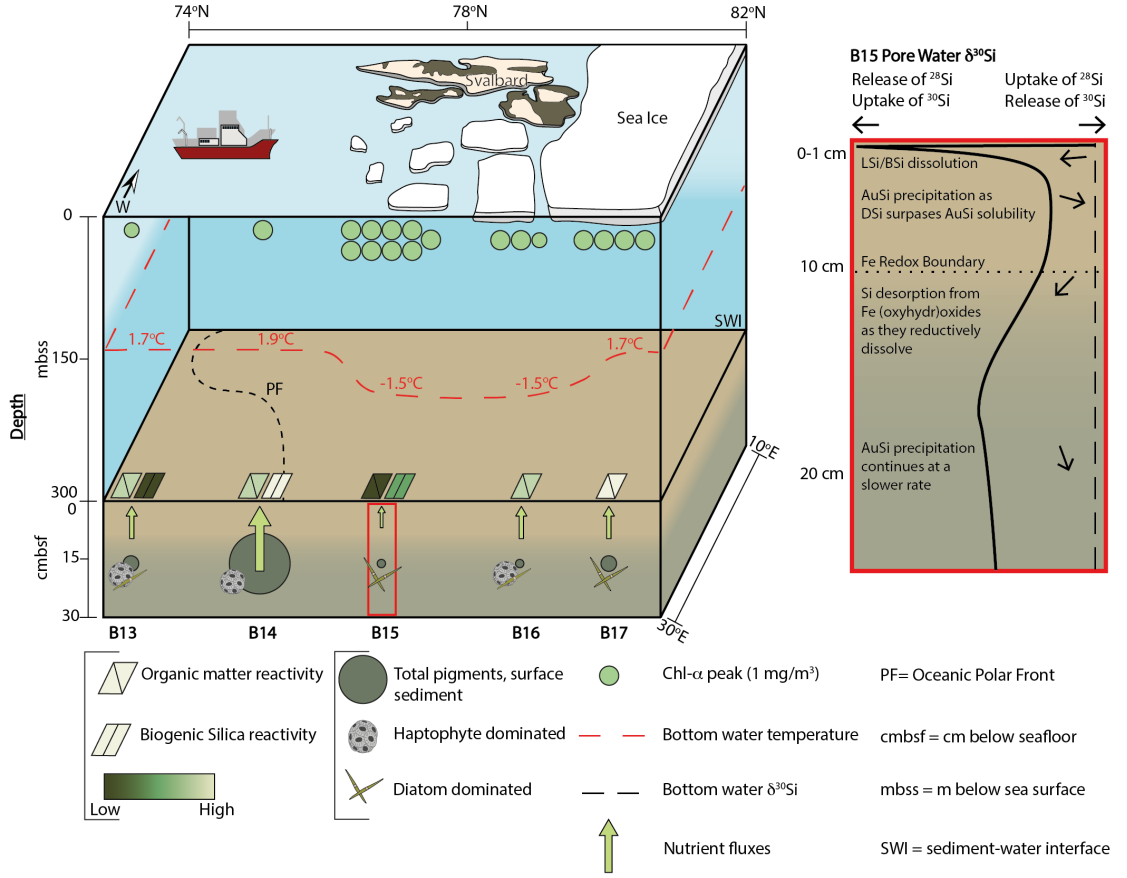

Figure 5.1: Changing Arctic Ocean Seafloor (ChAOS) project summary. Chlorophyll-α represents the peak value measured at each station during JR16006 CTD casts, data available at doi:10.5285/89a3a6b8-7223-0b9c-e053-6c86abc0f15d. Benthic nutrient flux magnitudes are for DSi measured in this study, as well as PO_4^{3-} and NH_4^+ from Freitas et al. (2020). The red box is a schematic summary of the main processes involved in the early diagenetic cycling of Si in the Barents Sea, derived from the results of the steady state model simulations. Sea ice extent represents an approximation of the conditions at the time of sampling in 2017 and 2019. BSi reactivities were determined by the steady state model simulations. Please see section 5.6.2 for a description of sediment pigment extraction methods. BSi- biogenic silica, LSi- lithogenic silica, AuSi- authigenic clay minerals, DSi- dissolved silicic acid.

nificant drop in dissolved silicic acid (DSi) concentrations has been observed relative to nitrate (Rey, 2012), creating less favourable conditions for diatom growth (Neukermans et al., 2018). This shift in phytoplankton community composition is predicted to reduce the export efficiency of organic material, with significant implications for pelagic-benthic coupling (Fadeev et al., 2021; Wiedmann et al., 2020). Observations from long-term sediment trap data show that carbon export and aggregate sinking rates are two-fold higher underneath diatom-rich blooms in seasonally sea ice covered areas of the Fram Strait, compared with that in *P. pouchetii* dominated blooms in the ice free region (Fadeev et al., 2021). A similar contrast was observed in carbon export fluxes measured using short-term sediment trap deployments north of Svalbard (Dybwad et al., 2021). It is estimated that 40-96% of surface ocean primary production is exported to the seafloor in the Barents Sea (Cochrane et al. (2009) and references therein), while the export efficiency of net primary production out of the euphotic zone in the central gyres is typically <10% (Turner (2015) and references therein).

Diatoms take up DSi from seawater to build silica-based frustules (termed 'biogenic silica' (BSi) or 'opal'), which is then recycled or reworked in transition to and within the seafloor. The seafloor acts as a biogeochemical reactor, generating a benthic return flux of DSi across the pan-Arctic region that is estimated to equal the input from all Arctic rivers (März et al., 2015). These recycling and reworking processes are therefore important for the regional Si budget and for fuelling subsequent blooms, where seafloor-derived nutrients are able to be advected into the photic zone. We can then anticipate that the changes observed in the predominant spring/MIZ bloom phytoplankton species and the efficiency with which phytodetritus is delivered to the seafloor will impact the regional Si cycle, exacerbated by an observed decrease in the DSi concentration of the Atlantic Water inflow over the last three decades (Hátún et al., 2017; Rey, 2012).

Given the changes forecast in the pelagic-benthic coupling of Si in the Arctic, it is important to understand the baseline benthic biogeochemical system in order to anticipate the implications of further perturbations. Based on Si isotopic data from various reactive sedimentary pools and the sediment pore water dissolved phase from the Barents Sea seafloor in Chapter 4, it was hypothesised that the Si cycle is isotopically coupled to the redox cycling of metal oxides, most likely solid phase Fe (oxyhydr)oxides. The reductive dissolution of Fe (oxyhydr)oxides and release of adsorbed Si (FeSi) is thought to drive marked shifts in the isotopic composition of the Barents Sea sediment pore water DSi pool towards lighter compositions. Further, in Chapter 4 it was proposed that sediment pore water undersaturation drives the contemporaneous dissolution of lithogenic silicate minerals (LSi) alongside BSi, some of which is reprecipitated as authigenic clay minerals (AuSi), representing a sink of isotopically light Si to the regional Si budget. Finally, it was suggested in Chapter 4 that seasonal pelagic phytoplankton blooms generate stark peaks in pore water DSi that dissipate on the order of weeks-months. However, to fully understand

the early diagenetic cycling of Si within the seafloor of the Barents Sea we must be able to quantify the relative contribution of LSi and BSi to the DSi pool, as well as establish whether AuSi precipitation removes a significant portion of that pool. Here we employ steady state reaction-transport modelling to reconstruct the benthic cycling of Si in the Barents Sea, informed by our dataset of solid and dissolved phase Si isotopic compositions (Chapter 4) to test these hypotheses. Such techniques allow for the disentangling and quantification of the aforementioned early diagenetic reactions (Cassarino et al., 2020; Ehlert et al., 2016a; Geilert et al., 2020a), as well as the return benthic flux of DSi to the overlying bottom water. Furthermore, reaction-transport modelling allows for the quantification of processes on much shorter timescales, thus we use transient model runs to validate the hypothesis that the pulsed deposition of bloom-derived BSi can perturb the benthic Si cycle. We then quantify the bloom-derived BSi contribution to the total annual benthic DSi flux, the deposition of which is subject to the anticipated shifts in community compositions of pelagic primary producers across the Arctic Ocean.

Understanding the key aims presented here is not only important for anticipating the biogeochemical reponse of the Barents Sea seafloor to physical, chemical and biological changes in the surface ocean, but also has implications for the pan-Arctic Si budget. Currently there are disparities in the isotopic and mass balances of the Arctic Ocean Si budget, with Torres-Valdés et al. (2013) concluding that the Arctic Ocean is a slight net exporter of Si. Furthermore, a recent isotopic assessment identified the need for an additional benthic sink of light Si to close the Si budget (Brzezinski et al., 2021). However, current understanding is limited by a lack of direct observations from major gateways, including the Barents Sea (Brzezinski et al., 2021). By coupling observational data with reaction-transport modelling we are able to construct a balanced Si-budget for the Barents Sea (section 5.4.5), contributing to the data gaps that currently limit our understanding of pan-Arctic Ocean Si cycling.

5.3 Methods

5.3.1 Reaction-transport modelling

General approach

We use the Biogeochemical Reaction Network Simulator (BRNS) to disentangle the interplay of chemical and physical processes involved in the early diagenetic cycling of Si at stations B13, B14 and B15 of the Changing Arctic Ocean Seafloor (ChAOS) project in the Barents Sea (Fig. 1.2 and 5.1, Table 4.1). These stations span the main hydrographic features (Polar Front) and realms (Atlantic and Arctic Water) of the Barents Sea. BRNS is an adaptive simulation environment suitable for large, mixed kinetic-equilibrium reaction networks (Aguilera et al., 2005; Regnier et al., 2002), which is based on a vertically-resolved

mass conservation equation (equation 5.1) (Boudreau, 1997), simulating concentration changes for solid and dissolved species (i) in porous media at each depth interval and time step.

$$\frac{\delta\sigma C_i}{\delta t} = \frac{\delta}{\delta z}\left(D_{bio}\sigma\frac{\delta C_i}{\delta z} + D_i\sigma\frac{\delta C_i}{\delta z}\right) - \frac{\delta\sigma\omega C_i}{\delta z} + \alpha_i\sigma(C_i(0) - C_i) + \sum_j \lambda_i^j R_j, \qquad (5.1)$$

where ω, C_i, t and z represent the sedimentation rate, concentration of species i, time and depth respectively. The porosity term σ is given as $\sigma = (1-\varphi)$ for solid species and $\sigma = \varphi$ for dissolved species, where φ is sediment porosity (Table 2.6). This term ensures that the respective concentrations represent the amount or mass per unit volume of sediment pore water or solids as required (Boudreau, 1997). A full description of the model can be found in section 2.8.

Steady state reaction-transport modelling

Steady state modelling was employed to reproduce Si isotopic observational data, in order to quantify the reaction rates of key processes involved in the cycling of Si within the seafloor. The version of the Si BRNS model employed here is adapted from Cassarino et al. (2020), which largely follows the approach of Ehlert et al. (2016a) and assumes steady state. To ensure steady state was achieved in the baseline simulations, the applied run time was dependent upon the sedimentation rate (0.05-0.06 cm yr^{-1}, Zaborska et al. (2008), Faust et al. (2020)) and core length, so as to allow for at least two full deposition cycles (~2500 years for a 50 cm Barents Sea core). The implemented reaction network accounts for a pool of pore water DSi, sourced by a dissolving BSi phase, from which Si can be incorporated into authigenic clay minerals (AuSi) as they precipitate. The kinetic rate law for the dissolution of BSi follows equation 5.2 (Hurd, 1972), where k_{diss} is the reaction rate constant (yr^{-1}) and BSi_{sol} is the solubility of BSi (mol cm^{-3}), implying that the rate of dissolution is proportional to the saturation state. The rate of BSi dissolution is allowed to decrease exponentially downcore, in order to account for a reduction in reactivity due to BSi maturation and interaction with dissolved Al, as well as the preferential dissolution of more reactive material at shallower depths (Dixit et al., 2001; Rabouille et al., 1997; Rickert, 2000; Van Cappellen and Qiu, 1997b). The rate constants for BSi dissolution (k_{diss}, equation 5.2) were constrained using the solid phase BSi content measurements (Fig. 5.2 and Fig. 5.3).

Equation 5.2 represents a simplification of the reaction rate law, which in reality is influenced by processes not incorporated into the model, such as surface area, temperature, pH, pressure and salinity. It is possible in some circumstances for the dissolution rate to deviate from the linear rate law (Van Cappellen et al., 2002), however, it is generally accepted that the dissolution of BSi is predominantly driven thermodynamically by the degree of undersaturation, leading to the linear rate law implemented in this study (Lou-

caides et al., 2012b; Rimstidt and Barnes, 1980; Van Cappellen et al., 2002; Van Cappellen and Qiu, 1997b).

$$R_{db} = k_{diss} \cdot [BSi] \cdot \left(1.0 - \frac{[DSi]}{BSi_{sol}}\right) \tag{5.2}$$

The precipitation of AuSi was modelled through equation 5.3, where k_{precip} is the precipitation rate constant (Ehlert et al., 2016a). This rate law assumes that the reaction will proceed, providing the concentration of DSi is greater than the solubility of the AuSi ($AuSi_{sol}$). The rate is thus proportional to the degree of pore water DSi oversaturation (Ehlert et al., 2016a). We assume a value of 50 μM for $AuSi_{sol}$ at all three stations (Hurd, 1973; Lerman et al., 1975) (Table 2.6). As with BSi dissolution, the rate of AuSi precipitation was allowed to decrease exponentially with depth, compatible with the hypothesis that the majority of AuSi precipitation occurs in the upper portion of marine sediment cores. Here, DSi can more easily precipitate in the presence of more readily available dissolved Al, the concentration of which is typically higher in the upper reaches of shelf sediments, sourced from the dissolution of reactive LSi (e.g. feldspar and gibbsite) contemporaneous to that of BSi (Aller, 2014; Ehlert et al., 2016a; Rabouille et al., 1997; Van Beusekom et al., 1997).

$$R_p = k_{precip} \cdot \left(\frac{[DSi]}{AuSi_{sol} - 1.0}\right) \qquad \text{if [DSi]} > AuSi_{sol} \tag{5.3}$$

In addition to the dissolution of BSi and precipitation of AuSi accounted for in previous early diagenetic modelling studies of the benthic Si cycle (Cassarino et al., 2020; Ehlert et al., 2016a), we incorporate the dissolution of LSi which is thought to be an important oceanic source of numerous elements, including Si (Ehlert et al., 2016b; Fabre et al., 2019; Geilert et al., 2020a; Jeandel and Oelkers, 2015; Jeandel et al., 2011; Morin et al., 2015; Pickering et al., 2020; Tréguer et al., 1995). Here we assume that the dissolution of LSi is predominantly driven by the degree of undersaturation (equation 5.4), although as with the dissolution of BSi, LSi dissolution is a complex reaction and sensitive to processes that are not included in the model, including the potential for being catalysed by microbes (Liu et al., 2017a; Vandevivere et al., 1994; Vorhies and Gaines, 2009). The undersaturation of Si minerals is known to include most primary and secondary silicates, thus dissolution extends beyond BSi in marine sediments (Isson and Planavsky (2018) and references therein). Indeed, a suite of experiments have shown that primary silicates and clay minerals can rapidly release Si when placed in DSi undersaturated seawater and take up Si in DSi enriched waters (Fanning and Schink, 1969; Gruber et al., 2019; Hurd et al., 1979; Lerman et al., 1975; Mackenzie and Garrels, 1965; Mackenzie et al., 1967; Pickering, 2020; Siever, 1968). Lerman et al. (1975) determined in one such experiment that the dissolution of eight clay minerals could be described by a first-order reaction rate law driven by the saturation state, consistent with that applied here. Further, our

assumption that LSi dissolution is driven by the degree of undersaturation is consistent with the suggestion that low bottom water DSi concentrations of the North Atlantic Ocean could allow for the dissolution of silicate minerals and thus account for high benthic DSi flux magnitudes in areas almost devoid of BSi (<1 wt%) (Tréguer et al., 1995). A value of ∼100 μM was used for the solubility of LSi (LSi_{sol}) at all three stations, consistent with observations during multiple dissolution experiments of common silicate minerals in seawater (Table 5.2), as well as the estimated solubility of amorphous silica in high detrital component estuarine sediments (Kemp et al., 2021).

$$R_{dl} = k_{LSidiss} \cdot [LSi] \cdot \left(1.0 - \frac{[DSi]}{LSi_{sol}}\right) \tag{5.4}$$

The desorption of Si from solid Fe (oxyhydr)oxide phases under anoxic conditions was simulated using a simple reaction rate constant (k_{FeSi}), representing the rate of desorption. The value assigned to k_{FeSi} was calculated during the modelling exercise and no assumed amount of FeSi was included in the upper boundary conditions. This parameter likely represents a significant simplification, however the exact process pertaining to the adsorption of Si onto Fe (oxyhydr)oxides is unclear and requires further study (Geilert et al., 2020a). Step-functions were included in the FeSi reactions in the model to simulate the desorption of this phase at specific depth intervals, representing the Fe redox boundaries identified (see Chapter 4). The step-functions act as a cut-off mechanism, either setting reaction rates to zero or activating them at specific depths. A full description of the model, including all boundary conditions and how isotopic fractionation was imposed in the AuSi precipitation and FeSi desorption reactions can be found in section 2.8.

Our estimates for all reaction rate constants in the steady state simulations (k_{diss}, k_{precip}, $k_{LSidiss}$ and k_{FeSi}) were not based on published values and were model-derived (Table 2.6). These values were constrained by ensuring best-fit of the observational data with the simulated solid phase BSi content and pore water DSi concentration and isotopic compositions, which were obtained by minimising the root-mean-square error (RMSE) between simulated and measured values (Table 2.5). Despite being model-derived, k_{diss} values (0.0055-0.074 yr^{-1}) are found to lie within the published range for marine sediment BSi (section 5.4.2). After the best-fit scenarios were established for each station, a sensitivity experiment was carried out by sequentially setting each reaction rate constant to zero, in order to assess the importance of each process to the model fit (Fig. 5.2).

Processing the simulated data

Depth-integrated rates (R) of a given reaction (j) were calculated across the model domain using equation 5.5, for the best-fit simulation data of each station.

$$R_j(x) = \sum_j \int_{x=0}^{x=L} R_j dx \tag{5.5}$$

where L is the model domain length and dx denotes the given depth interval.

The deposition flux of BSi at the sediment-water interface (SWI) ($J_{BSi,in}$) was then calculated based on equation 5.6, which states that $J_{BSi,In}$ equates to the sum of the flux of BSi out of the sediment (assumed to equate to the integrated rate of BSi dissolution, R_{db}) and the BSi burial flux ($J_{BSi,bur}$) (Burdige, 2006; Freitas et al., 2021). $J_{BSi,bur}$ was estimated at the base of the model domain (50.4 cm), following the mass accumulation equation 5.7 (Varkouhi and Wells (2020) and references therein), which is controlled solely by advection. The sedimentation rate at depth (ω_z) was corrected for compaction following equation 5.8 (Berner, 1980). $J_{BSi,bur}$ calculations assume a sediment wet bulk density of 1.7 g cm^{-3}, consistent with previously assumed values for the Arctic seabed (Backman et al., 2004; Brzezinski et al., 2021) and that measured in clay-rich sediments of the Barents Sea (Orsi and Dunn, 1991).

$$J_{BSi,in} = R_{db} + J_{BSi,bur} \tag{5.6}$$

$$J_{BSi,bur} = (1 - \varphi_z) \cdot \omega_z \cdot [BSi]_z \cdot \rho_z \tag{5.7}$$

$$\omega_z = \omega_0 \cdot (1 - \varphi_0)/(1 - \varphi_z) \tag{5.8}$$

We are also able to use the model simulation output to determine the total benthic flux of DSi at the SWI (J_{tot}), which has multiple constituent parts that contribute to the benthic flux magnitude. Following equation 5.9 (Freitas et al., 2020), we calculate J_{tot} and thus the relative contributions from bioturbation ($J_{bioturb}$), bioirrigation (J_{bioirr}), advection (J_{adv}) and molecular diffusion (J_{diff}), to complement the calculated J_{diff} estimates and core incubation-derived J_{tot} from Chapter 4.

$$J_{tot} = J_{bioturb} + J_{bioirr} + J_{adv} + J_{diff} \tag{5.9}$$

The calculation of J_{diff} for the model-derived benthic DSi flux is calculated using a second-order approximation of the gradient at the SWI. This assumption uses three simulated grid points to describe the gradient, as opposed to two data points in the previously described methods in Chapter 4 (equation 5.10) (Boudreau, 1997). It is thought that a second-order approximation provides a better representation of the concentration gradient, although here we find very similar flux magnitudes when using a simpler first-order (two data point) approximation. Use of the reaction-transport model to estimate benthic fluxes allows for comparison of an assumed steady-state profile with that of core incubations, which can be enhanced by transient processes, such as the dissolution of fresh BSi lying on the SWI (Conley, 1987; Ragueneau et al., 2001).

$$\left.\frac{d[DSi]}{dz}\right|_{z=0cm} = \frac{-3C_0 + 4C_1 - C_2}{2\Delta x} \tag{5.10}$$

where C_1 and C_2 represent the simulated pore water DSi concentration at the first and second grid point respectively

Transient reaction-transport modelling

The influence of seasonality in pelagic primary production on the benthic Si cycle of the Barents Sea has been inferred through interpretation of pore water DSi depth profiles at station B14 (Chapter 4). However, BRNS assumes steady state and therefore cannot resolve seasonal biogeochemical dynamics without modification to allow certain boundary conditions to become time dependent, enabling their activation and deactivation on a temporal scale. Here we use transient model runs to test the hypothesis that the pulsed deposition of bloom-derived BSi can rapidly perturb the benthic DSi pool, which is then able to recover on the order of weeks to months.

The steady state baseline simulations at station B14 represent a data-model best-fit of the 2018 observational data, wherein we do not observe transient peaks in sediment pore water DSi concentrations. This steady state scenario was used as the initial conditions for the transient simulations, which were run for one simulation year, producing output data at weekly time intervals. We simulate the phytoplankton spring bloom event by incorporating an additional, more reactive BSi phase into the model, coupled with a similar mechanism to the depth step-functions employed in the steady state reaction network, in order to initiate the deposition of the bloom-derived BSi pool in late spring and terminate it after one to three weeks. This time period is thought to represent the typical length of a Barents Sea MIZ and spring bloom respectively (Dalpadado et al., 2020; Sakshaug, 1997). All boundary conditions were kept constant, with the exception of those related to the bloom-derived BSi pool.

During the one to three week time interval the bloom-derived material was deposited at a rate equivalent to an increase in the steady state BSi deposition flux of eight to 26-fold. The background BSi deposition flux magnitude at station B14 is a model-derived parameter, constrained in the steady state simulations with the measured sediment BSi content and pore water DSi depth profiles. A 26-fold increase on the background deposition flux is consistent with observations of a 10 day post-bloom diatom mass sinking event in the sub-polar North Atlantic down to 750 m depth (Rynearson et al., 2013). The Barents Sea covers a relatively shallow continental shelf (average depth 230 m) and intense physical mixing at the polar front has been shown to enhance rates of vertical organic carbon flux at depth, close to station B14 (Wassmann and Olli, 2004). We could therefore aniticpate an even greater increase in BSi depositional flux under bloom conditions than the maximum value assumed here. The reactivity of the bloom-derived material ($k_{dissbloom}$) ranged from

5 to 35 yr^{-1}, which is within the reactivity range of fresh pelagic BSi (3 to 100 yr^{-1}, Nelson and Brzezinski (1997); Ragueneau et al. (2000)). Each of these three boundary conditions (length of the bloom period, $k_{dissbloom}$ and the deposition flux) was varied across multiple simulations within the constraints of published values to assess the influence of each parameter on the size and longevity of the sediment pore water DSi peak.

5.3.2 Observational data

As many reactions responsible for the biogeochemical cycling of Si between the solid and dissolved phases fractionate the isotopes of Si (^{28}Si, ^{29}Si, ^{30}Si) relative to each other, we are able to use stable Si isotopes as a tool to trace these pathways. All solid phase, core top and sediment pore water samples collected for Si isotopic analysis were collected over three summers in the Barents Sea (30^{o}E transect spanning 74 to 81^{o}N) aboard the *RRS James Clark Ross* (2017, 2018, 2019). Dissolved phase pore and core top water DSi concentration measurements were determined on-board using a Lachat QuikChem 8500 flow injection analyser with an accuracy of 2.8%, defined using CRMs (KANSO Co., Ltd.). Stable Si isotopic compositions of the samples were determined at the University of Bristol in the Bristol Isotope Group laboratory. Isotopic compositions are expressed in δ^{30}Si notation (per mille ‰), relative to the international Si standard NBS-28 (equation 5.11). A full description of field methods, as well as Si isotopic and concentration data of the solid and dissolved phase reconstructed using BRNS are provided in in Chapter 2 (doi.org/10.5285/8933AF23-E051-4166-B63E-2155330A21D8).

$$\delta^{30}Si = \left(\frac{(^{30}Si/^{28}Si)_{sample}}{(^{30}Si/^{28}Si)_{NBS-28}} - 1 \right) \cdot 1000 \tag{5.11}$$

One early diagenetic process that fractionates isotopes of Si is the formation of AuSi clay minerals, which preferentially takes up the lighter isotope from the dissolved phase, leaving sediment pore and core top waters relatively isotopically heavy in composition. A Si isotopic fractionation factor ($^{30}\epsilon$) associated with AuSi formation has yet to be thoroughly established, however Ehlert et al. (2016a) and Geilert et al. (2020a) modelled a $^{30}\epsilon$ of -2‰ for marine AuSi formation. A $^{30}\epsilon$ of this magnitude is consistent with the formation of clay minerals in riverine and terrestrial settings (-1.8 to -2.2 ‰) (Hughes et al., 2013; Opfergelt and Delmelle, 2012; Ziegler et al., 2005a,b) and similar to that observed in the adsorption of Si onto Fe (oxyhydr)oxide minerals ($^{30}\epsilon$ of -0.7 to -1.6 ‰) (Delstanche et al., 2009; Opfergelt et al., 2009; Wang et al., 2019; Zheng et al., 2016). However, the magnitude of $^{30}\epsilon$ associated with AuSi precipitation can reach up to -3‰ in deep-sea settings (Geilert et al., 2020b), likely depending on pore water properties (pH, temperature, salinity, saturation states). This relatively high $^{30}\epsilon$ is also consistent with repetitive clay mineral dissolution-reprecipitation cycles (Opfergelt and Delmelle, 2012). Similarly, $^{30}\epsilon$ during Si adsorption onto Fe (oxyhydr)oxides is thought to increase with

mineral crystallinity ($^{30}\epsilon$ of -1.06 ‰ for ferrihydrite and -1.59 ‰ for goethite) (Delstanche et al., 2009). This characteristic is in contrast to the dissolution of BSi and LSi, which is assumed to occur without isotopic fractionation (Ehlert et al., 2016a; Wetzel et al., 2014), although previous work has shown that BSi dissolution could induce a slight fractionation that enriches the DSi pool in the lighter isotope ($^{30}\epsilon$ of -0.55 ‰) (Demarest et al., 2009).

Model upper boundary conditions for the dissolved phase were based on the DSi concentration and Si isotopic composition of the core top waters (+1.64 ±0.19 (n=5), +1.46 ±0.15 (n=3) and +1.69 ±0.18 ‰ (n=6) at stations B13, B14 and B15 respectively). The Si isotopic compositions of the solid phases (BSi, LSi, FeSi) implemented in the model were determined based on a series of sequential digestion experiments carried out on surface sediment samples of the three aforementioned stations (Chapter 3). The digestion sequence (0.1 M HCl, 0.1 M Na_2CO_3, 4 M NaOH) activates operationally defined reactive pools of Si, including: Si-HCl (Si associated with metal oxide coatings on BSi, assumed here to represent the FeSi pool), Si-Alk (authigenically altered and unaltered BSi) and Si-NaOH (LSi and refractory BSi) (Pickering et al., 2020). The composition of the FeSi (-2.88 ±0.17 ‰, n=20) and LSi (-0.89 ±0.16 ‰, n=18) pools in Barents Sea sediment leachates were within long term reproducibility of Diatomite standard measurements (2σ ±0.14 ‰, n=116) across the three stations, whereas the BSi phase was found to vary spatially, with an isotopic composition of +0.82 ±0.16 ‰ (n=14) at station B15 and +1.43 ±0.14 ‰ (n=8) and +1.50 ±0.19 ‰ (n=7) at stations B13 and B14 respectively (Chapter 4).

5.4 Results and discussion

5.4.1 What can reaction-transport modelling reveal about the controls on the background, steady state benthic Si cycle?

LSi dissolution and AuSi precipitation

An inverse modelling approach is applied here to reconstruct the benthic Si cycle of the Barents Sea to further investigate and disentangle the interplay of processes that combined to produce our observational dataset. Model results show that the sediment pore water DSi profiles cannot be reproduced by the dissolution of BSi alone at all three stations (B13, B14 and B15) (dashed blue lines, Fig. 5.2). At station B13 the simulations suggest that while there is sufficient DSi released to reproduce the asymptotic DSi concentration due to the higher BSi content at depth compared to B15, the rate of release in the upper sediment layers is not consistent with that in the pore water DSi concentration profiles downcore from the SWI in the observational data (Fig. 5.2). This observation is in contrast to B15, where the simulated asymptotic DSi concentration is just 23 μM when BSi is the only source of DSi, consistent with the measured BSi content profiles that suggest a cessation

in BSi dissolution by the middle of the sediment cores (∼15 cm, asymptotic BSi content of ∼0.2 wt%) (Fig. 5.2). Because of the continued increase in DSi with depth at station B13 (solid grey line), partly driven by the elevated BSi content in the mid-core relative to B15, a relatively slow rate of AuSi precipitation is required at depth to take up the excess DSi and reproduce the observed asymptotic DSi value. Generally it is assumed that AuSi precipitation is concentrated in near-SWI sediments (0-5 cm), where the concentration of other essential solutes (Al, Fe, Mg^{2+}, K^{+}, Li^{+}, F^{-}) are generally highest, sourced from Fe and Al (oxyhydr)oxides and reactive LSi (Aller, 2014; Ehlert et al., 2016a; Mackin and Aller, 1984; Van Cappellen and Qiu, 1997a). However, the uptake of DSi through AuSi precipitation has previously been inferred in terrigenous-dominated shelf sediments of the Arctic Ocean at >50 cm depth (März et al., 2015).

Due to the discrepancies between observational and simulated DSi pore water concentration data, we incorporated a LSi phase into our model, which dissolves according to the presumed degree of undersaturation. Without this additional phase (when $k_{LSidiss}$ is set to zero), model simulations show that the rate of DSi release is insufficient to reconstruct the observational DSi data (Fig. 5.2). Implementing LSi dissolution in conjunction with BSi produced the best data-model fit (red dashed lines). The dissolution of LSi has been inferred in a similar study of marine sediment pore waters of the Guaymas Basin (Geilert et al., 2020a), as well as in beach and ocean margin sediments (Ehlert et al., 2016b; Fabre et al., 2019). Indeed, Morin et al. (2015) report Si dissolution rates for basaltic glass particles in seawater that exceed that of diatoms (Pickering et al. (2020) and references therein).

The inference based on the pore water DSi concentration profiles that an additional phase, most likely LSi, is dissolving into Barents Sea pore waters is supported by the simulated isotopic composition of the pore water phase at stations B13 and B15. Without the dissolution of the LSi phase, the δ^{30}Si of the pore waters represents a mixture of the composition of the core top water and the BSi phase composition (+1.44 and +1.04 ‰ at B13 (solid grey line) and B15 (dashed blue line) respectively) (Fig. 5.2). In this simulation scenario at station B15, the integrated rate of AuSi precipitation is zero as the concentration of pore water DSi has not surpassed the imposed AuSi solubility so cannot influence the sediment pore water δ^{30}Si. Therefore, the model set up without LSi dissolution cannot reproduce the intricacies of the downcore isotopic profile, as the lack of DSi released results in an insufficient concentration to allow for the precipitation of AuSi, thus the relative shift from isotopically lighter to heavier compositions between 0.5 and 2.5 cm cannot be resolved. The downcore shift to heavier isotopic compositions between 0.5 and 2.5 cm is thought to be caused by AuSi formation as the pore water DSi concentration crosses the saturation of the AuSi phase, facilitating its precipitation.

These model observations are consistent with a mass balance calculation using the isotopic compositions of the 0.5 cm pore water sample, as well as the BSi and LSi leachate

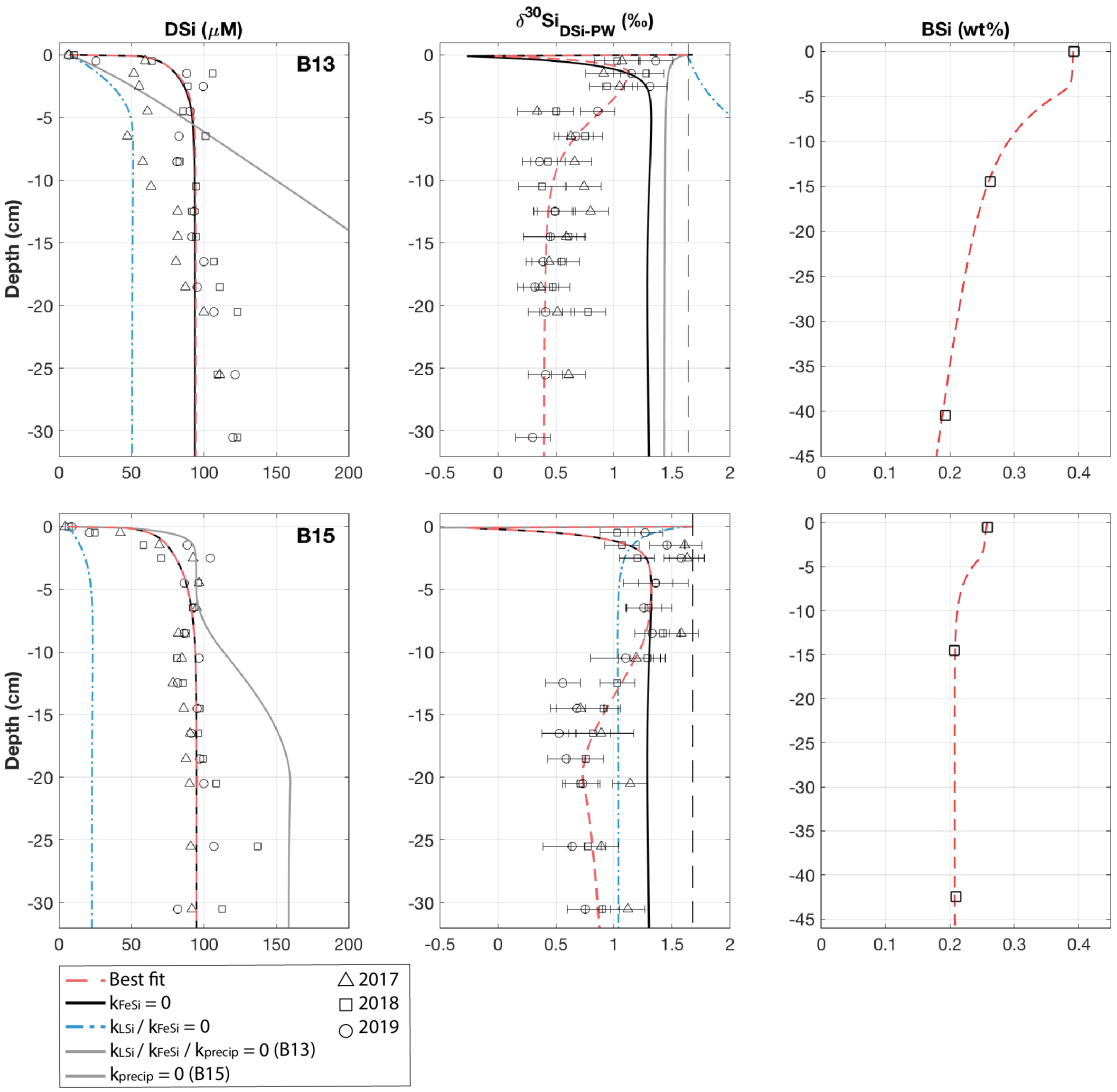

Figure 5.2: Dashed red lines show best-fit steady state model simulations for stations B13 (top row) and B15 (bottom row), as well as additional fits based on a series of sensitivity experiments carried out to assess the importance of each reaction pathway. For station B14, see Fig. 5.3. From left to right: sediment pore water DSi concentration, sediment pore water DSi stable Si isotopic composition, solid phase BSi content. Vertical dashed black line represents the Si isotopic composition of the core top water from 2017 and open shapes show observational pore water data (Chapter 4). Error bars on the Si isotopic data are based on long-term reproducibility, derived from repeat measurements of Diatomite Si standard (2σ ±0.14, n=116), unless that from analytical replicates was greater.

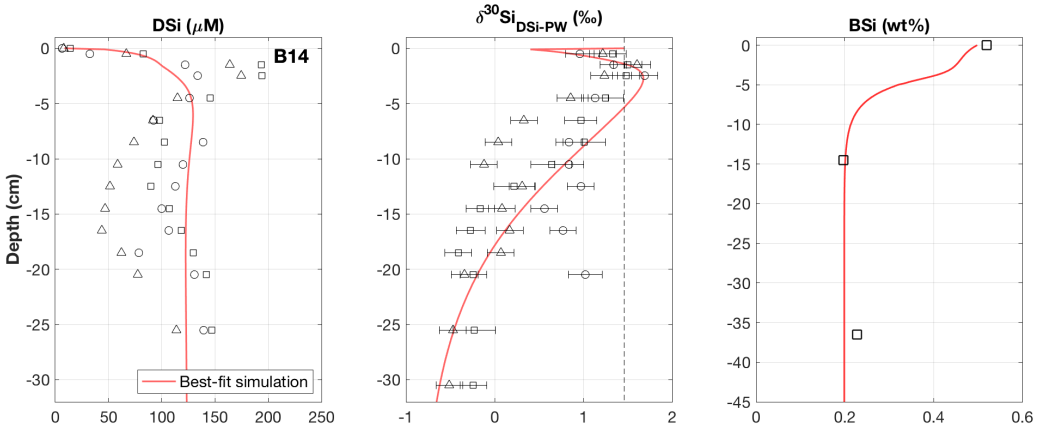

Figure 5.3: Best-fit model simulation for station B14 (red line). Vertical dashed black line represents the isotopic composition of the core top water from 2017. BSi content was measured from samples collected in 2019. Model output was fit to the sediment pore water DSi concentrations from 2018 (open circles), as this profile is closer to the background steady state system than 2017 or 2019.

samples at stations B13 and B14, which indicate a contemporaneous release of both phases. Our model findings therefore support the hypotheses presented in Chapter 4 that LSi minerals are likely to be dissolving in the upper few cm of the Barents Sea seafloor. The depth-integrated reaction rates of the best-fit steady state simulations suggest that between 60 and 98% of the DSi released into the sediment pore water from the solid phase is sourced from the dissolution of LSi (Table 5.1). This range was determined by calculating the depth-integrated rate of LSi dissolution across the model domain and three stations as a proportion of the total integrated rate of DSi input from the three simulated sources (BSi dissolution, LSi dissolution and desorption from metal oxides). The predominance of LSi over BSi dissolution is consistent with the observation that Barents Sea sediments consists of ∼96% terrigenous material (Chapter 4), which is compatible with previous work showing that clay mineral assemblages in the Barents Sea are dominated by terrestrial signals from Svalbard and northern Scandinavia (Vogt and Knies, 2009). The Si isotopic composition of the LSi phase in surface sediments of stations B13, B14 and B15 (-0.89 ±0.16 ‰, Chapter 4) is also more consistent with that of dissolving secondary clay minerals (-2.95 to -0.16 ‰, Opfergelt and Delmelle (2012) and references therein) than primary silicates of the crust and mantle (∼0 and -0.34 ‰ respectively, Opfergelt and Delmelle (2012) and references therein). This isotopic composition is not surprising, given the predominance of the clay and silt size fraction in these sediment cores (87% <63μm) (Faust et al., 2020).

However, while previous mass balance calculations and the model-derived integrated reaction rates presented here agree that both LSi and BSi dissolution contribute to the sediment pore water DSi pool, the magnitudes of the LSi dissolution contribution vary significantly. In Chapter 4, it is suggested that just 14 and 13% of the DSi pool in the 0.5 cm pore water interval is sourced from the dissolution of LSi at stations B13

and B14 respectively, while at station B15 it is inferred that the δ^{30}Si can be resolved through BSi dissolution alone. This is in contrast to the 84, 60 and 98% contributions calculated here (Table 5.1). There are multiple contributing factors to this discrepency. Firstly, previous mass balance calculations are based on one depth interval, whereas the estimates presented here are derived from depth-integrated dissolution rates of the entire 50.4 cm model domain. Furthermore, reaction-transport modelling has revealed that this contradiction is likely born of the assumption that the BSi pool at all three stations is sufficient to fuel the pore water DSi stock. Dissolution dynamics were not taken into account in the simple mass balance calculation of Chapter 4, however here we have shown that the composition of Barents Sea surface sediments, which are almost devoid of BSi (0.26-0.52 wt%, or 92-185 μmol g dry wt^{-1}), cannot reproduce the rate of pore water DSi build-up with depth from the SWI and can only support an asymptotic DSi concentration of 23 μM at station B15 (dashed blue line, Fig. 5.2). This observation implies that the additional assumption made in Chapter 4 that the 0.5 cm pore water δ^{30}Si value is not impacted by AuSi precipitation could be invalid. If the 0.5 cm pore water interval was directly or indirectly influenced by AuSi precipitation, such an assumption would lead to an underestimation of the LSi contribution, as the δ^{30}Si value would be isotopically heavier than if it were derived solely from dissolving solid phases mixing with trapped core top water.

Previously it has been suggested that the quantification of AuSi precipitation rates in marine sediments is not critical in order to fully understand the early diagenetic cycling of Si, as reverse weathering typically represents a diagenetic solid phase conversion from BSi to AuSi, via the dissolved phase (DeMaster, 2019). Model simulations reveal that 37, 2.9 and 13.8% of the DSi released across the 50 cm model domain at stations B13, B14 and B15 respectively is taken out of solution in the formation of AuSi. This observation is consistent with a similar previous study of the Peruvian margin upwelling region, which determined that 24% of DSi released from the dissolution of BSi was reprecipitated as AuSi at a rate of 1.53 mmol Si m^{-2} d^{-1} (Ehlert et al., 2016a). AuSi precipitation rates in sediments of the Amazon Delta on the other hand can reach 7.7 mmol Si m^{-2} d^{-1} (Michalopoulos and Aller, 2004). Reprecipitation of the DSi pool within the relatively shallow cores studied here will inhibit its exchange with overlying bottom waters. Therefore, in this context, AuSi precipitation can be considered a sink term for the regional Si budget. In a setting where AuSi precipitation occurs at such a depth where pore water DSi exchange with bottom waters is not possible, this reaction pathway could instead be considered an early diagenetic solid phase conversion (from BSi/LSi to AuSi), as opposed to a true sink term (DeMaster, 2019; Frings et al., 2016).

Table 5.1: Depth-integrated reaction rates of the steady state best-fit simulations across the upper 50 cm of sediment (Fig. 5.2), as well as calculated BSi deposition rates and model-derived DSi benthic fluxes. All magnitudes are given in units of mmol Si m^{-2} d^{-1}.

	Station		
Parameter	B13	B14	B15
AuSi precipitation (R_p)	5.31	0.13	1.88
LSi dissolution (R_{dl})	12.07	2.66	13.45
Si desorption (R_{FeSi})	1.99	0.08	0.02
BSi dissolution (R_{db})	0.29	1.69	0.15
BSi deposition ($J_{BSi,in}$)	0.32	1.71	0.17
BSi burial ($J_{BSi,bur}$)	0.027	0.025	0.021
Total benthic flux (J_{tot})	0.14	0.34	0.25
Diffusive benthic flux (J_{diff})	0.11	0.27	0.21
% DSi sourced from LSi	84	60	98
% DSi reprecipitated	37	2.9	13.8
% BSi buried	8.6	1.4	12.2

Evidence for coupling of the benthic Fe and Si cycles in the Barents Sea

It is suggested in Chapter 4 that the benthic Fe and Si cycles are coupled in the Barents Sea, evidenced by a contemporaneous increase in pore water Fe concentrations with an enrichment in the lighter Si isotope of the DSi pool at all three stations. Model simulations support this hypothesis by demonstrating that the Barents Sea DSi pore water profiles can be reconstructed when applying the dissolution of both a BSi and LSi phase, however under the model scenario where the desorption of FeSi is inhibited ($k_{FeSi} = 0$), the δ^{30}Si pore water profiles are inconsistent with the observational data (solid black lines, Fig. 5.2). With the dissolution of the LSi phase implemented at both stations B13 and B15, it is possible to resolve the δ^{30}Si pore water profiles in the upper 2.5 cm and 8.5 cm respectively. However, below these depths the simulated profiles have isotopically heavier compositions than the observational data. Release of an isotopically light phase at specific depth intervals (beginning at 1.5 cm at B13, 10 cm at B15) results in a simulated δ^{30}Si profile within range of the observational data (Fig. 5.2). This isotopic shift to lower pore water δ^{30}Si is interpreted to represent the desorption of Si from solid Fe (oxyhydr)oxide phases, wherein the depth intervals of the same isotopic shifts correspond to the depths at which Fe is released into the pore waters (Faust et al., 2021; Ward et al., 2022). This increase in pore water Fe also occurs at similar depth intervals to decreases in pore water dissolved O_2 and NO_3^- concentrations, consistent with a transition from oxic to anoxic conditions (Freitas et al. (2020); Ward et al. (2022) (in press)).

As discussed above, the Si-HCl reactive Si pool is isotopically light and thought to be associated with metal oxide coatings on BSi (Pickering et al., 2020). The δ^{30}Si composition of the Si-HCl phase is assumed here to represent the composition of the phase desorbing

across the Fe redox boundaries. When using a composition of -2.88 ‰ for the FeSi phase, simulation scenarios have identical DSi concentration profiles whether k_{FeSi} is active or set to zero (dashed red and solid black lines, Fig. 5.2). This similarity is in contrast to the δ^{30}Si pore water profiles, which cannot be reproduced without release of this isotopically light phase at the redox boundaries of all three modelled stations.

This discrepancy between the sediment pore water DSi and δ^{30}Si profiles when the FeSi desorption is active and inactive may explain why the influence of FeSi desorption is so apparent in Barents Sea sediment cores and more ambiguous in similar, previous studies of the Si cycle in lower latitude marine sediments. The preferential adsorption of ^{28}Si onto Fe (oxyhydr)oxides and the subsequent dissolution or formation of these minerals has been used to interpret both heavy and light δ^{30}Si marine sediment pore water signals in previous work (Ehlert et al., 2016a; Geilert et al., 2020a). In addition, while not inducing a clear signal in the δ^{30}Si, redox cycling of Fe was highlighted as a potential regulating factor in the release of DSi into pore waters of the Greenland margin (Ng et al., 2020). Ng et al. (2020) hypothesised that the reductive dissolution of Fe mineral coatings increased the reactivity of the BSi pool, hence the elevated DSi concentrations found in cores with increased pore water Fe (Ng et al., 2020). In the Barents Sea, FeSi desorption across sedimentary redox boundaries is thought to be so prominent in the δ^{30}Si data because the asymptotic concentration of pore water DSi (∼100 μM) is much lower than that in the aforementioned studies (∼350-900 μM). The low sediment pore water DSi concentration allows for the direct detection of this process, whereas in previous studies the influence of Fe on the benthic Si cycle is either inferred through elevated DSi and Fe concentrations (Ng et al., 2020), or by depositional context, for example in cores sampled from systems with an abundance of reactive Fe (e.g. hydrothermal vent systems (Fe sulfides) (Geilert et al., 2020a) or the Peruvian oxygen minimum zone (Ehlert et al., 2016a)).

At stations B13 and B14, and to a lesser extent at B15, there is an increase in the sediment pore water DSi concentration downcore from the middle to the base of the profiles. This feature can be reproduced in the model simulations with the desorption of FeSi from the respective redox boundary depths (Fig. 5.4), however the required ratio of k_{FeSi} for ^{28}Si and ^{30}Si suggests an isotopic composition of the FeSi phase of just -1.0 to -1.5 ‰. This isotopic composition is heavier than that measured in the Si-HCl pool (-2.88 ‰), likely reflecting a complexity in the desorption process not captured by the model. Nevertheless, both scenarios support the release of an isotopically light phase at depth, most likely sourced from the Fe redox cycle.

In summary, model simulations somewhat support the hypothesis, based on observational data, that the Barents Sea benthic Si cycle is influenced by the Fe-redox system. Model results suggest that the influence of the Fe redox cycle is relatively unimportant for the magnitude of the pore water DSi pool, which appears to be controlled by release from the BSi and LSi phases. However, the coupling of these element cycles is evidenced in the

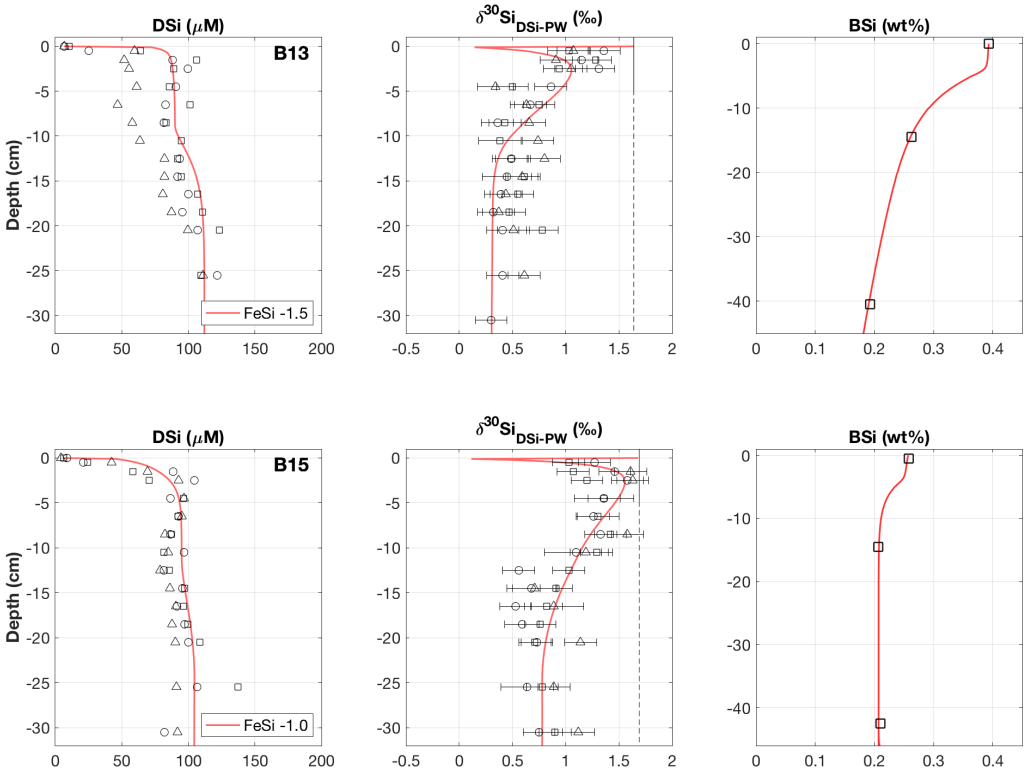

Figure 5.4: Best-fit model simulations (red line) with heavier FeSi compositions of -1.5 and -1.0 ‰ implemented at stations B13 and B15 respectively. The heavier composition of the desorbing phase allows for sufficient DSi release to resolve the slight increase in pore water DSi concentration from the mid-core to depth. Vertical dashed black lines represents the isotopic compositions of the core top waters from 2017.

pore water δ^{30}Si data, indicating that the Fe cycle is important for the isotopic budget within the seafloor. We suggest the influence of FeSi desorption is detectable in the Barents Sea pore water δ^{30}Si data, due to the relatively low pore water DSi concentrations and the distinctly isotopically light nature of the FeSi phase. These findings indicate that FeSi desorption should be considered when interpreting downcore δ^{30}Si trends, especially in low DSi concentration settings.

5.4.2 Can seasonal phytoplankton blooms drive transient, non-steady state dynamics in the benthic Si cycle?

Observational pore water DSi concentration data from station B14 suggest that a pulsed increase in the deposition of reactive phytodetritus to the seafloor, derived from phytoplankton blooms, can drive transient peaks in pore water DSi of up to ∼300 μM (Chapter 4). This non-steady state dynamic is evidenced in the three consecutive years of pore water DSi concentration data collected during the summers of 2017 to 2019, which show that in 2017 and 2019, when the MIZ was above station B14 just one and a half months prior to sediment coring, a sediment pore water DSi peak is present. This characteristic is in contrast to 2018 when station B14 had been sea ice free for three months prior to sampling (Downes et al., 2021) and no peak in DSi concentration was observed in the pore water nutrient data (Fig. 4.13). This observation may indicate that the sediment pore water DSi peaks form under the MIZ, which supports the formation of phytoplankton blooms in late spring/early summer, supplying fresher BSi to the benthos relative to the background BSi pool. Dissolution of this fresher BSi could then fuel peaks in DSi concentration that dissipate between one and a half and three months after formation, driven by the enhanced rate of molecular diffusion. Additional model simulations were carried out on the baseline, steady state best-fit model scenario of station B14 to assess this hypothesis.

Results of the transient simulations show that it is possible for the deposition of fresh, bloom-derived BSi to reproduce the observed peaks in pore water DSi concentration in 2017 and 2019 (Fig. 5.5). Calculated rates of background BSi deposition across the three stations (0.17 to 1.71 mmol Si m^{-2} d^{-1}, Table 5.1) are similar to BSi export rates measured in short-term and moored sediment traps in Kongsfjorden, Svalbard at 100 m depth and the eastern Fram Strait at 180-280 m depth (0.2-1.3 mmol Si m^{-2} d^{-1}) (Lalande et al., 2013b, 2016). A simulated three week, 10-fold increase of this BSi depositional flux at a much higher reactivity ($k_{dissbloom}$ 20 yr^{-1}) than the background value (k_{diss} 0.074 yr^{-1}) derived from the 2018 baseline simulation, results in a DSi peak consistent with the magnitude of that in the observational data after one and a half months (dashed red lines, Fig. 5.5). This simulated peak in DSi concentration is then able to dissipate by three months after bloom initiation (Fig. 5.5). Similarly, with a shorter bloom (one week), compatible with the typical length of an ice edge bloom in the Barents Sea (Dalpadado et al., 2020) and a 30-fold increase in BSi depositional flux of $k_{dissbloom}$ 15 yr^{-1}, the DSi

peak is able to form and dissipate on a timeframe similar to that of the former scenario (solid black lines, Fig. 5.5). The generated peak in DSi concentration must be able to disperse after three months if the timing of core sampling relative to MIZ retreat is valid as the explanation for the lack of pore water DSi peak observed in the 2018 data.

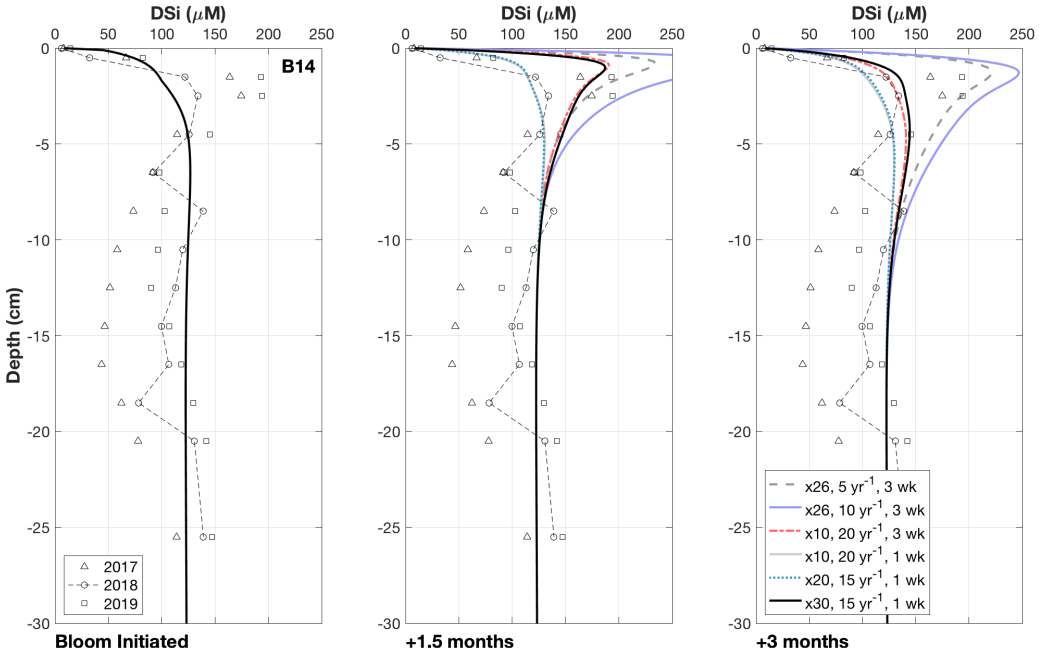

Figure 5.5: Results of the transient simulations under different conditions. Multiplier refers to the increase in the deposition flux ($J_{BSi,in}$) of the bloom-derived BSi, which was assigned a reactivity ($k_{dissbloom}$ in yr^{-1}) and deposited over either one or three weeks. Note that the 'Bloom Initiated' panel represents the first day of the simulated bloom, therefore all the modelled scenarios overlap and reflect the background steady state simulation.

The implemented $k_{dissbloom}$ values fall within the reactivity expected of fresh diatoms, which is thought to range from 3 to 70 yr^{-1} (Ragueneau et al., 2000). Dissolution rate constants of 0.98-1.38 yr^{-1} have been observed in sediment cores collected from the Porcupine Abyssal Plain (mean water depth of 4850 m), considered high for BSi in deep marine sediments (Ragueneau et al., 2001), while values of up to 6.8 yr^{-1} have been measured in much shallower sediments of Jiaozhou Bay in the Yellow Sea (Wu et al., 2015). These published values are lower than those employed in the transient simulations and typically BSi material with dissolution rate constants of this magnitude are not observed in marine sediments. However, station B14 is located beneath the polar front, which is a location of intense physical mixing due to the interleaving of multiple water masses (Barton et al., 2018). This physical mixing was interpreted to be the driving force behind an enhanced particulate organic carbon depositional flux at ~150 m water depth, relative to that measured in sediment traps both north and south of the frontal zone (Wassmann and Olli, 2004). Furthermore, data collected from sediment traps deployed to the north and

north-west of Svalbard has uncovered an approximately two-fold higher vertical carbon export flux from diatomaceous aggregates formed in seasonally sea ice covered regions, compared with aggregates from *P. pouchetii* blooms (Dybwad et al., 2021; Fadeev et al., 2021). Therefore, it is considered here that given the shallow depth of the Barents Sea seafloor and the location of station B14 beneath the polar front, that fresh and reactive BSi formed in MIZ blooms could be efficiently ferried to the seafloor. It is likely that the production of BSi and its export from the surface ocean is highest on the shelves of the Arctic Ocean (Macdonald et al., 2010). This observation, coupled with reduced BSi dissolution rates in the cold regional waters (Kamatani, 1982), results in more of the BSi recycling being transferred towards the seafloor (Brzezinski et al., 2021).

The $k_{dissbloom}$ of the bloom-derived BSi is much higher than that required to reproduce the solid phase BSi content profiles of the background system (k_{diss}) (Fig. 5.2). At stations B13, B14 and B15, the implemented k_{diss} values in the steady state simulations were 0.0055, 0.074 and 0.0105 yr^{-1} respectively (Table 2.6, Fig. 5.1), which are not dissimilar to those estimated for deep sea sediments from DSi pore water profile fitting procedures and flow-through reactor experiments (0.006-0.44 yr^{-1}) (McManus et al., 1995; Rabouille et al., 1997; Ragueneau et al., 2001; Rickert, 2000). The inverse of the dissolution rate constant provides an estimate of the residence time or mean lifetime of the given pool of BSi (McManus et al., 1995), which suggests that the less reactive pool of BSi has a mean lifetime of 182, 13.5 and 95 years at stations B13, B14 and B15 respectively. These mean lifetimes are too long to influence the Si cycle on a seasonal scale, which must be <1 yr^{-1} to do so, as is the case for organic matter (Burdige, 2006). The model-derived estimates of $k_{dissbloom}$ on the other hand would suggest a mean lifetime of approximately 20 days for the fresh BSi.

Therefore, this work suggests that there are at least two types of BSi in Barents Sea sediments, one less reactive pool that dissolves at a slower rate and one fresher, bloom-derived pool that is able to perturb the sediment pore water DSi stock on a seasonal timescale. This conclusion is compatible with findings from a study of the equatorial Pacific region (McManus et al., 1995) and observations from the Arabian Sea, indicating that the bulk sediment BSi content should not be treated as a single pool of uniform reactivity, but should instead be separated into reactive and unreactive fractions (Rickert, 2000; Schink et al., 1975). Consistent with these conclusions, Boutorh et al. (2016) observed up to an order of magnitude fall in k_{diss} over the course of a three week batch dissolution experiment. This result indicates the presence of two phases of BSi within diatom frustules, one protecting the other, denoting a potential physiological basis for the differentiation in reactivity of seafloor BSi.

5.4.3 What is the simulated benthic DSi flux and how important is the contribution of bloom-derived BSi dissolution to the annual flux?

The simulated J_{diff} magnitudes (0.11-0.27 mmol Si m^{-2} d^{-1}) that contribute to J_{tot} (Table 5.1) are within error of previously calculated J_{diff} values (0.10-0.37 mmol Si m^{-2} d^{-1}) for these Barents Sea sediment cores (Chapter 4). Thus, our model-derived benthic DSi fluxes are well within range of a compilation of pan-Arctic shelf benthic DSi fluxes (-0.03 to +6.2 mmol Si m^{-2} d^{-1}) (Bourgeois et al., 2017). Based on previous calculations and the simulation results presented here, we estimate that the mean DSi J_{diff} benthic flux magnitude for the Barents Sea is +0.23 ($\pm$0.11 1σ) mmol Si m^{-2} d^{-1}, ranging from +0.08 to +0.54 mmol Si m^{-2} d^{-1}.

J_{tot} at all stations is dominated by the molecular diffusive component (J_{diff}) (76-85%), in agreement with simulated estimates of phosphate fluxes at the same stations (Freitas et al., 2020) (Fig. 5.6). J_{tot} at station B13 has the highest contribution from bioturbation (6%), consistent with the highest experimentally determined bioturbation diffusion coefficient of the Barents Sea stations (Solan et al., 2020). The advective component of J_{tot} is negligible at all stations, while the bioirrigation element represents the greatest source of uncertainty in the simulated flux magnitudes, as this parameter was not constrained in parallel to this work, thus a global value was assumed (Thullner et al., 2009). At station B15, the model-derived J_{tot} (+0.25 mmol Si m^{-2} d^{-1}) is greater than $J_{BSi,in}$ (0.17 mmol Si m^{-2} d^{-1}) (Table 5.1). This observation points to the release of an additional source of DSi to the dissolving BSi, which is compatible with the hypothesis that LSi is being released into the pore water dissolved phase.

DSi benthic flux magnitudes were also calculated for the transient simulations carried out on station B14 to quantify the influence of fresh bloom-derived BSi. Dissolution of the fresher BSi has an immediate and significant effect on the benthic flux, doubling the steady state background value of +0.34 mmol Si m^{-2} d^{-1} to +0.66 mmol Si m^{-2} d^{-1} within one week, which peaks two weeks after bloom material deposition at +1.84 mmol Si m^{-2} d^{-1}, representing a five-fold increase (an additional +1.5 mmol Si m^{-2} d^{-1}) on the background steady state benthic flux magnitude. The prominent DSi peak then dissipates and becomes largely undetectable after three months (Fig. 5.5). The average DSi benthic flux at the SWI over the twelve week period is +1.07 mmol Si m^{-2} d^{-1}, indicating that the bloom-derived BSi releases an additional +0.73 mmol Si m^{-2} d^{-1} to the overlying bottom water. The steady state and transient model simulations therefore suggest that the background benthic flux of Si from the benthos is +124 mmol Si m^{-2} yr^{-1} at station B14, while the additional contribution over the twelve week period sourced from fresh BSi dissolution is +61.3 mmol Si m^{-2} (based on a rate of +0.73 mmol Si m^{-2} d^{-1}). This estimate suggests that a minimum of 33% of the total annual benthic flux of Si discharging from the seafloor at station B14 is sourced from the deposition of fresh BSi during the one week MIZ bloom.

The contribution of bloom-derived BSi dissolution to the annual benthic DSi flux magnitude reported here (an additional +0.73 mmol Si m^{-2} d^{-1} over the three months) for station B14 is greater than that in Chapter 4 (an additional +0.23 mmol Si m^{-2} day^{-1} over the same time interval), although the proportion is consistent across the two estimates (approximately one-third of the total annual benthic DSi flux). In part, this is due to the simulated fluxes incorporating the contribution from bioirrigation and bioturbation (J_{tot}). When using only the simulated J_{diff} component, an additional +0.46 mmol Si m^{-2} d^{-1} is estimated to be sourced from the bloom-derived BSi, which is more consistent with the observational data calculations. However, this disparity is also due to the nature of the simulated flux calculation. The model-derived benthic flux magnitudes are calculated at the SWI, whereas previous J_{diff} estimates are based on observational data of a much lower resolution, with the concentration gradient determined based on the DSi concentration in the core top water and in the sediment pore water at 0.5 cm depth. Furthermore, the simulated benthic flux estimates are based on a mean value derived from a weekly temporal resolution, which is not accessible in the observational data. However, both estimates can be used to draw a range of possible contributions from the bloom-derived BSi and although there is a disparity in the benthic flux magnitude, both methodologies suggest that at least one-third of the annual DSi benthic flux at station B14 is sourced from the dissolution of BSi deposited after a short MIZ bloom.

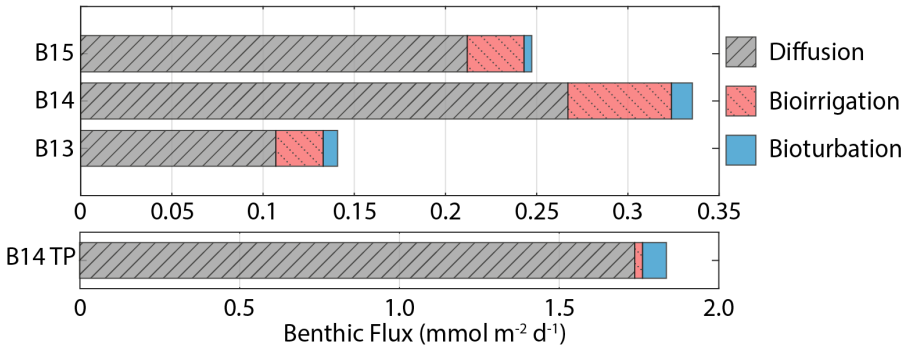

Figure 5.6: Benthic DSi flux magnitudes at the SWI calculated from steady state simulations. Includes contributions from molecular diffusion, bioirrigation and bioturbation. B14 TP refers to the B14 DSi flux magnitude at the peak of the transient simulations (x30 BSi depositional flux, 15 yr^{-1} $k_{dissbloom}$, 1 week bloom duration).

5.4.4 How much BSi is buried long-term in the Barents Sea?

Traditionally, burial efficiencies of BSi were not included within Si budgets of the Arctic Ocean, due in part to a low mean BSi content (<5 wt%), as well as a low estimated sedimentation rate (a few mm kyr^{-1}) (Brzezinski et al., 2021; März et al., 2015). However, more recently Arctic Ocean seafloor BSi burial efficiencies are being re-evaluated due to revised models of sediment accumulation rates (Brzezinski et al., 2021). Asymptotic BSi

content profiles approach 0.2 wt% at 14.5 cm below the SWI and remain constant with depth at all three Barents Sea stations (Fig. 5.2, Fig. 5.3), suggesting that some BSi is buried and able to accumulate in the seabed. Assuming a sedimentation rate of 0.05-0.06 cm yr^{-1} (Zaborska et al., 2008), BSi particulates deposited at the SWI would approach 14.5 cm depth within approximately 240-300 years due to sediment accumulation, where BSi dissolution appears to cease. This timescale is a similar magnitude to the calculated mean lifetime based on k_{diss} from the model simulations at station B13 (182 years), indicating that some BSi from this pool could accumulate at depth. However, the steady state BSi pools at stations B14 and B15 have mean lifetimes of just 95 and 13.5 years respectively, theoretically precluding burial of this pool below 14.5 cm depth. The observation that BSi is present at ∼40 cm depth at all three stations with a concentration of ∼0.2 wt% indicates that there may be three fractions of BSi constituting the bulk BSi phase: fresh bloom-derived BSi represented by $k_{dissbloom}$, the less reactive background BSi (k_{diss}), and a non-reactive pool that contributes to the 0.2 wt% BSi at depth alongside any surviving component from the background pool. A mean BSi burial rate of 0.024 mmol Si m^{-2} d^{-1} is estimated here for the Barents Sea (equation 5.7, Table 5.1), corresponding to 0.012 Tmol Si yr^{-1} for the whole shelf, assuming an area of 1.4 million km^{-2}.

Global seafloor BSi burial efficiencies (calculated as the BSi burial flux divided by the deposition rate) range from 1 to 97% (DeMaster, 2001; DeMaster et al., 1996; Frings, 2017; Liu et al., 2005; Ragueneau et al., 2001, 2009; Westacott et al., 2021), averaging ∼11% (Frings, 2017; Tréguer et al., 2021). Typically, BSi burial efficiencies are much higher in coastal and shelf settings and underneath polar fronts, due in part to higher rates of sedimentation (DeMaster, 2001). Indeed, studies of the Southern Ocean (Indian sector and the Ross Sea) and the Peruvian margin uncovered a four to 30-fold increase in BSi burial efficiency at the continental shelf stations (22-58%), relative to the open ocean counterparts (2-17%) (Dale et al., 2021; DeMaster, 2001; Ragueneau et al., 2001). BSi burial efficiencies estimated here for three Barents Sea stations (1.4-12%, Table 5.1) are within range of published values and similar to the global mean at stations B13 and B15, but low relative to other continental shelves. Our estimated BSi burial efficiencies are based on the same sedimentation rates employed in the model (Table 2.6), which are similar to the Barents Sea mean of 0.07 cm yr^{-1} (Zaborska et al., 2008). However, Barents Sea sedimentation rates of up to 0.21 cm yr^{-1} have been estimated since the last glacial period (Faust et al., 2021), which would significantly increase the estimated BSi burial efficiencies (5-33%) (equation 5.7).

While the BSi burial efficiency calculated at station B14 is also within previously published values, it is much lower than the Barents Sea stations to the north and south. Solid phase BSi contents in the surface intervals were determined from samples collected during the third cruise in summer 2019. As discussed, the pore water DSi profiles at B14 from this cruise are thought to be influenced by the dissolution of bloom-derived

BSi, which would account for the elevated BSi content in the surface sediment relative to that at stations B13 and B15. The higher BSi content has likely resulted in an elevated estimation of $J_{BSi,in}$ and thus a reduced burial efficiency, which would also explain why the model-derived estimate of the contribution of LSi dissolution to the DSi released from the solid phase is lower at station B14 (60%), due to an elevated R_{db}, enhanced by the deposition of fresher BSi. In addition, this would also explain why the estimated mean lifetime of the BSi from the steady state simulations at station B14 is much shorter than for the other two sites (13.5 years *vs* 95-182 years). If the measured surface BSi content at station B14 is indeed influenced by residual bloom-derived BSi, this would result in an overestimate of the background BSi reactivity in the model.

Relatively low burial efficiencies of BSi in sediments underneath oxygen depleted bottom waters (7-12%), similar in magnitude to those calculated here for the Barents Sea, have previously been attributed to low rates of bioturbation, resulting in less efficient export of BSi towards more saturated pore waters (Dale et al., 2021). Bioturbation coefficients were determined experimentally for the Barents Sea stations (2-6 cm^{-2} yr^{-1}) (Table 2.6) and are much lower than might be expected, based on an empirical global relationship with water depth ($\sim$24 cm^{-2} yr^{-1}) (Middelburg et al., 1997). Furthermore, the impacts of the low rates of macrofaunal mixing on BSi burial efficiency is likely exacerbated by slow rates of sediment accumulation in the Barents Sea. High rates of BSi burial in the Bohai (60%) and Yellow Seas (42%) are thought to be driven by high sediment accumulation rates (Liu et al., 2002), which as with bioturbation is much lower in the Barents Sea than might be expected based on an empirical global relationship with water depth (0.55 cm yr^{-1}) (Middelburg et al., 1997). The combination of low rates of macrofaunal mixing and sediment accumulation may therefore be the cause of the lower BSi burial efficiencies observed here relative to the global ocean mean.

5.4.5 What are the implications of this work for the Arctic Ocean Si budget?

Brzezinski et al. (2021) uncovered an imbalance in the Arctic Ocean Si budget after carrying out an assessment using Si isotopes. The δ^{30}Si values measured in the main Arctic Ocean water mass inflow and outflows are similar ($\sim$+1.70 ‰, Brzezinski et al. (2021); Giesbrecht (2019); Liguori et al. (2020)), suggesting that the cycling of Si within the Arctic Ocean has little net effect on δ^{30}Si. Brzezinski et al. (2021) conclude that given the relatively isotopically light input from fluvial sources (+1.30 ±0.3 ‰, Sun et al. (2018)), as well as that emerging from seafloor sediments (+1.16 ±0.11 ‰), balance must be maintained through the burial of isotopically light Si by BSi. However, a mass balance showed that the isotopically light inputs to the system are only partially offset by the burial of BSi (0.16-0.30 Tmol Si yr^{-1}), assumed to have a δ^{30}Si of +1.16 ±0.10 ‰ (Brzezinski et al., 2021). There must therefore be an additional sink of isotopically light Si if the Arctic

Ocean Si isotope budget is to maintain balance (Fig. 5.7). The absence of direct isotopic observations from some of the major gateways, including the Barents Sea shelf over which most of the DSi sourced from the Atlantic Ocean flows (Torres-Valdés et al., 2013), as well as a lack of data for the isotopic composition of BSi in Arctic Ocean sediments must be addressed to confirm the mechanisms proposed by Brzezinski et al. (2021). Si isotopes measured in the weak alkaline leachate (0.1 M Na_2CO_3, $\delta^{30}Si_{Alk}$) extracted from surface sediment sequential digestion experiments and measurements of $\delta^{30}Si$ in core top waters (Chapter 3), coupled with reaction-transport modelling (this study) for stations B13, B14 and B15 contribute to the Arctic Ocean Si isotope dataset and help to fill these knowledge gaps.

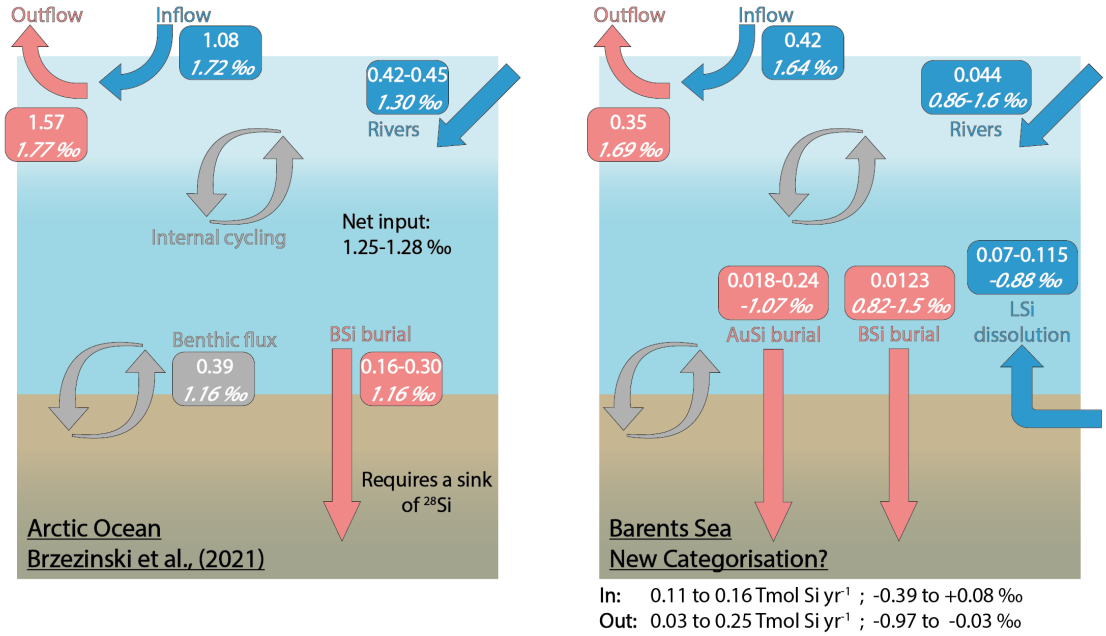

Figure 5.7: The Arctic Ocean Si budget (Brzezinski et al., 2021) (left) and a proposed Si budget for the Barents Sea (right), including a benthic flux recategorisation (i.e. contributions from BSi and LSi) and AuSi burial. Boxes include flux magnitudes given in Tmol Si yr^{-1} (top values) and the flux $\delta^{30}Si$ in ‰ (italicised bottom values). 'In' and 'Out' refer to the Si fluxes, discounting the water mass inflow and outflow (i.e. In (blue) = Rivers + LSi; Out (red) = AuSi + BSi). Grey boxes and arrows represent internal cycling. See section 5.6.1 for further information on how the Barents Sea Si budget was calculated.

$\delta^{30}Si_{Alk}$ in the Barents Sea ranges from +0.82 ±0.16 ‰ at station B15 to +1.50 ±0.19 ‰ at B14 (Chapter 3). The Na_2CO_3 leachate activates an operationally defined reactive pool of Si, thought to be associated with authigenically altered and unaltered BSi (Pickering et al., 2020). Molar Al/Si ratios of the Na_2CO_3 support this concept, which fall within range of that expected of BSi (Chapter 3). $\delta^{30}Si$ measured in the core top waters at the Atlantic (B13, +1.64 ±0.19 ‰) and Arctic Water stations (B15, +1.69 ±0.18 ‰) are similar to the composition of the main Arctic Ocean inflow and outflow water masses (~1.7 ‰) (Brzezinski et al., 2021; Giesbrecht, 2019; Liguori et al., 2020) and heavier than

that measured in the BSi deposited at the seafloor. Therefore, assuming the composition of the BSi below the BSi dissolution zone within the seafloor is similar to that at the SWI, Barents Sea sediments represent a sink of ^{28}Si, relative to the composition of the inflow waters. However, $\delta^{30}Si_{Alk}$ at stations B13 and B14 is still isotopically heavier than the Arctic Ocean riverine input (+1.30 ±0.3 ‰), as well as the assumed composition of the BSi buried across the Arctic seabed (+1.16 ±0.10 ‰) in the Si budget (Brzezinski et al., 2021) (Fig. 5.7). Through reaction-transport modelling we have estimated that between 2 and 40% of the sediment pore water DSi pool is sourced from the dissolution of BSi. Moreover, 2.9-37% of the total amount of DSi released is reprecipitated as AuSi (Table 5.1). AuSi preferentially takes up the lighter isotope in the Barents Sea with a $^{30}\epsilon$ of -2.0 to -2.3 ‰ (Table 2.6), thereby enhancing the preservation of BSi and further enriching the solid phase in the lighter isotope. Clays formed during weathering have a δ^{30}Si composition ranging from -2.95 to -0.16 ‰ (Opfergelt and Delmelle, 2012). The burial of AuSi alongside BSi could therefore account for some of the isotopic imbalance.

Our reaction-transport model study has also highlighted the important contribution of LSi dissolution to the sediment pore water DSi pool (60-98%). If our findings on the dissolution of LSi are consistent across other Arctic shelves, a portion of the benthic DSi flux cannot be defined as internal cycling of Si and should be recategorised as an additional input to that from the major ocean gateways and discharge from rivers. It is currently estimated that the benthic flux of DSi across the whole Arctic Ocean seafloor is ∼0.39 Tmol Si yr^{-1} (März et al., 2015), therefore between 0.23 and 0.38 Tmol Si yr^{-1} may represent an input of Si rather than a recycling term. This recategorisation could account for the additional Si inputs required to close the Si budget, as currently 32-47% (or 0.21-0.38 Tmol Si yr^{-1}) of the estimated net Si output is unaccounted for (Brzezinski et al., 2021). The addition of AuSi as an output to resolve the isotopic imbalance would offset to some extent the release of DSi from LSi, while the LSi input compounds the isotopic imbalance identified by Brzezinski et al. (2021). However, here we show that through AuSi precipitation acting as an additional sink for ^{28}Si, both mass and isotopic balance can be attained in our proposed Si budget for the Barents Sea (Fig. 5.7, section 5.6.1). Future work should look to assess whether similar relationships exist between the dissolution of LSi and precipitation of AuSi on other Arctic Ocean shelves, if we are to use these mechanisms to balance the pan-Arctic Si budget.

5.5 Conclusions

In this study we quantify and disentangle the processes involved in the early diagenetic cycling of Si in the Arctic Barents Sea seafloor by reproducing Si isotopic and DSi concentration data from the solid and dissolved phase in a reaction-transport model. Baseline simulations are able to reproduce the observational data well, however we have also shown

that the benthic Si cycle is responsive on the order of days to the delivery of fresh BSi. Therefore, while the transient disturbances appear to be short-lived, future work should look to incorporate these processes into the baseline simulations.

Baseline model simulations also reveal that a significant proportion of the Si released from the solid phase within Barents Sea surface sediments is sourced from the dissolution of LSi (60-98%) on account of the low BSi contents (0.26-0.52 wt%). Furthermore, we demonstrate that without the influence of the Fe-redox cycle, which results in the release of Si adsorbed onto solid Fe (oxyhydr)oxides under anoxic conditions, the observed isotopic composition of the pore water DSi pool cannot be reconciled. Both the LSi and FeSi sources are depleted in the heavier isotope (-0.89 and -2.88 ‰ respectively), as demonstrated in a sequential digestion experiment (Chapter 3), consistent with the observation that sediments of the Barents Sea represent a source of light DSi to the overlying bottom waters (Brzezinski et al., 2021). Of the DSi sourced from BSi, LSi and FeSi, we show that between 2.9 and 37% is reprecipitated as AuSi. Coupled with the observation that a significant proportion of the sediment pore water DSi pool is sourced from the dissolution of LSi, this hypothesis is significant for the regional Si budget. The dissolution of LSi represents a source of 'new' Si to the ocean DSi pool and the precipitation of AuSi inhibits exchange of pore water DSi with overlying bottom waters and therefore represents a sink term. These observations could require a recategorisation of a portion of the benthic flux in the Arctic Ocean Si budget, which is currently defined as a recycling term, as well as the inclusion of an additional Si sink. If LSi dissolution and AuSi precipitation is not exclusive to the Barents Sea shelf, the additional input and isotopically light output could account for both the isotopic imbalance and the remaining proportion of net Si outflow that is currently unaccounted for (Brzezinski et al., 2021).

Model simulations also highlight a dichotomy in the cycling of Si in the Barents Sea seafloor, which is hypothesised to occur on at least two timescales. Observational data at stations B13 and B15 can be reproduced by assuming a steady state dynamic, thus representing a background system, which is controlled by the release of Si into the DSi pool from LSi and the reprecipitation of DSi as AuSi. However, sampling across three years at station B14 has uncovered Si cycling on a much shorter timescale, controlled by the deposition of fresh phytodetritus. In this transient dynamic, the release of DSi is controlled by the dissolution of more reactive BSi. The processes occurring on the former steady state time frame will likely remain largely unaltered with further Atlantification of the Barents Sea, due to the mineralogical control on DSi release. Whereas the latter, transient system is reliant upon the seasonal delivery of fresh BSi, which is subject to change as the community compositions of the MIZ and spring phytoplankton blooms shift to favour temperate Atlantic flagellate species (Neukermans et al., 2018; Orkney et al., 2020), or diatoms with lower silica content than polar species (Lomas et al., 2019). Furthermore, we have shown that the benthic DSi flux magnitude can increase five-fold

after a simulated one week bloom, which is calculated here to contribute a minimum of one-third of the total annual flux of DSi from the seafloor at station B14. Any perturbation in the delivery of bloom-derived, relatively reactive BSi to the seafloor could therefore be detrimental to the total annual supply of Si from Barents Sea sediments.

Research data

Research data associated with this article can be accessed with https://doi.org/10.5285/8933AF23-E051-4166-B63E-2155330A21D8. Reaction-Transport Model code (Si BRNS) can be accessed with https://doi.org/10.5281/zenodo.6023767.

5.6 Supplementary Material

5.6.1 A proposed Si budget for the Barents Sea

An isotopic assessment of the Arctic Ocean Si budget has highlighted the requirement for an additional sink of light Si, if isotopic balance is to be attained (Brzezinski et al., 2021). Here we build on this work by combining isotopic analysis of the water column and the dissolved and solid phases of the sediment, with reaction-transport modelling carried out in this study, to present an isotopically balanced Si budget for the Barents Sea that may help to inform the pan-Arctic Ocean equivalent.

The Si inflow rate from Atlantic Waters crossing the Barents Sea Opening is 0.42 $\pm$0.07 Tmol Si yr^{-1} (Torres-Valdés et al., 2013), while the outflow rate through the northern openings (the Barents Sea Exit between Novaya Zemlya and Franz Josef Land, as well as the Franz Victoria Trough (Fig. 1.2) estimated here is 0.35 Tmol Si yr^{-1}. This outflow was calculated by integrating the water column DSi depth profiles of the northernmost ChAOS stations (B16 and B17) and similar profiles measured during the ARK IX/4 cruise on the Barents Sea side of the shelf break (PS27/006-1, PS27/026-1 and PS27/027-1, Luchetta et al. (2021)). All water column nutrient data for JR16006 (doi:10.5285/b4c1537e-c729-6463-e053-6c86abc0c7de), JR17006 (doi:10.5285/b62f2d5d-1f40-0c2c-e053-6c86abc0265d) and JR18006 (doi:10.5285/cc1dec98-40b5-5c51-e053-6c86abc01a6d) is available at the British Oceanographic Data Centre (BODC). The average depth-integrated DSi concentration (4.8 μM) was then multiplied by the Barents Sea volumetric outflow rate (2.3 Sv) (Smedsrud et al., 2013). Unlike the Arctic Ocean as a whole, which is a slight net exporter of Si with respect to the main inflow and outflow water masses (Brzezinski et al., 2021), the Barents Sea appears to be a slight net importer. However, our calculations are based on DSi water column profiles sampled from the lesser of two Barents Sea outflow locations. The main outflow gateway, between Novaya Zemlya and Franz Josef Land, is also north of the oceanic polar front and dominated by the Arctic Water mass (Fig. 1.2), therefore we would not expect a significant difference in DSi water column profiles between the two

localities. Nevertheless we cannot be certain of the Barents Sea Si outflow rate without concentration data from the eastern side of the shelf. Consistent with the wider Arctic Ocean Si budget, the δ^{30}Si of the core top water from the Arctic (B15) and Atlantic Water (B13) stations, range from +1.64 to +1.69 ‰ (Chapter 4), assumed here to represent the main outflow and inflow water masses respectively.

The riverine DSi influx presented in Fig. 5.7 (2580×10^3 $tSiO_2$ yr^{-1}, or 0.044 Tmol Si yr^{-1}), represents the sum of the four main rivers draining into the Barents and White Seas, including the Onega, Northern Dvina, Mezen and the Pechora (Gordeev et al., 1996). The estimated average δ^{30}Si of the fluvial flux to the Arctic Ocean is 1.3 ±0.3 ‰, but varies temporally by season and spatially from +0.86 ±0.3 ‰ in the Lena to +1.6 ±0.25 ‰ in the Yenisey River, which flow into the Laptev and Kara Seas respectively (Sun et al., 2018).

The benthic flux of DSi has been recategorised in our budget of the Barents Sea, relative to that of Brzezinski et al. (2021), reflecting the conclusions drawn from our reaction-transport model study. Here we assume that between 60 and 98% of the benthic DSi flux is sourced from the dissolution of LSi, which represents an input of new Si into the Barents Sea Si budget, while the remainder constitutes an internal recycling flux (i.e. the dissolution of BSi). Therefore, the contribution of LSi to the influx of Si to the Barents Sea, assuming an average benthic flux of +0.23 ±0.11 mmol Si m^{-2} d^{-1} and a shelf seafloor area of 1.4 million km^{-2}, ranges from 0.07 to 0.115 Tmol Si yr^{-1}. A δ^{30}Si of -0.89 ‰ for the dissolving LSi phase is based on a series of sequential digestion experiments carried out on the surface sediment interval collected from stations B13, B14 and B15 (Chapter 3), but can range from -0.90 to +0.73 ‰ across primary silicates (felsic crustal and mafic mantle source rocks) and -2.9 to 0 ‰ for secondary clay minerals (Opfergelt and Delmelle, 2012) (mean -1.07 ‰, Sutton et al. (2018)).

The two outputs in the biogeochemical cycle of Si in the Barents Sea seafloor, outside of the main water mass outflow, are the burial of AuSi and BSi. The burial of BSi (0.0123 Tmol Si yr^{-1}) is calculated in section 5.4.4 of the main text, based on an asymptotic BSi content of 0.2 wt% below the mid-core at all three stations, assumed to be controlled solely by advection due to sediment accumulation (corrected for compaction). The same equation was used to calculate the burial rate of AuSi across the shelf (0.018-0.24 Tmol Si yr^{-1}), based on the simulated concentration at the base of the model domain at stations B14 and B15 (0.32 and 4.8 wt% respectively). The AuSi concentration at depth in the model for station B13 (12 wt%) is much higher than that at B14 and B15, consistent with the increased depth-integrated reaction rate (Table 5.1), corresponding to a burial rate of 0.87 Tmol Si yr^{-1}. This AuSi burial rate far outweighs the sum of the inputs to the Barents Sea, which would lead to a significant imbalance in the Si budget if it were considered a reasonable value with which to scale up our calculations. We therefore employ the values at stations B14 and B15 as conservative estimates for AuSi burial in the Barents Sea in

our calculations, as B13 likely represents a site of localised, elevated AuSi precipitation. Alternatively, there could be a complexity that our model does not adequately capture for this station, leading to an overestimated AuSi precipitation rate. The δ^{30}Si of the buried BSi phase is assumed to be the same as the composition measured in the surface sediments, determined from sequential digestion experiments (+0.82 to +1.50 ‰, Chapter 3). For the mass balance calculations, the composition of the AuSi phase was assumed to be -1.07 ‰, based on the average composition of secondary minerals (Sutton et al., 2018), however this can range from -2.9 to ∼0 ‰ (Opfergelt and Delmelle, 2012).

Disregarding the main water mass in and outflows, our Si budget suggests an influx to the Barents Sea of 0.11-0.16 Tmol Si yr^{-1} at -0.39 to +0.08 ‰ and an outflux of 0.03-0.25 Tmol Si yr^{-1} at -0.97 to -0.03 ‰, with the potential for the higher outflux to account for the slight mass imbalance between the water mass inflow and outflow (0.12 Tmol Si yr^{-1}). Our Si budget of the Barents Sea therefore demonstrates that through the re-categorisation of the benthic flux term and the introduction of AuSi burial, we are able to achieve isotopic and mass balance.

5.6.2 Sediment pigment extraction methodology

Surface sediment samples (2–3 g) were thawed and centrifuged at 4000 rpm for 5 minutes at 4^{o}C to remove excess water. 3 mL of 100% acetone was then added to the sediment samples after transferring to extraction tubes. Throughout the extraction, samples were kept in the dark and on ice. Samples were then sonicated for 40 seconds, left on ice for 1 hour and centrifuged at 4000 rpm for 5 minutes at 4^{o}C. The supernatants were decanted after centrifugation and the protocol was repeated until colourless extracts were observed. Prior to high performance liquid chromatography (HPLC) analysis, samples were filtered through a 0.2 μm filter membrane (17 mm Teflon syringe filters, DHI, Denmark). An HPLC method for sediment pigment analysis (Airs et al. (2001), Method C) was carried out using an Agilent 1200 HPLC system. In the autosampler (G1376B thermostated), 80 μL pigment extracts were mixed with 8 μL of Milli-Q water and injected onto the HPLC column (two 150 x 4.6 mm Waters Spherisorb ODS2 cartridges coupled together, 3 μm particle size). The autosampler was kept in the dark at 4 ^{o}C and extract analysis was carried out within one day of extraction. Prior to sample extract analysis, a pigment resolution check was carried out using a mixed standard (DHI). Chlorophyll and its various products of degradation were quantified by calculating response factors, based on the injection of standards (DHI). Due to a lack of available standards and because the UV/visible absorbance spectra are similar, the response factor for pheophorbide-a was used for measurement of hydroxychlorophyllone (Airs et al., 2001). LC/MS^n analysis was also carried out at Plymouth Marine Laboratory on selected samples to assign components following Airs et al. (2001), using a 6330 Series Ion Trap Liquid Chromatography-Mass Spectrometer (LC/MS) coupled with an atmospheric pressure chemical ionisation (APCI)

source. LC/MS operating conditions were as follows: positive ionisation mode, 350 ^{o}C and 450 ^{o}C drying and vaporiser temperature respectively, 60 PSI nebuliser pressure, 5 L min^{-1} drying gas flow rate. Following Airs and Keely (2000), acid was added to samples after column chemistry to assist in the ionisation of metallated components. Relative retention times, on-line UV/visible spectra and protonated molecule/fragmentation data was used to assign components (Airs et al., 2001).

For schematic Fig. 5.1 of the main text, we have assumed that a shift from fucoxanthin (fuco)-dominated surface sediments to those containing both fuco and hexanoyoxyfucoxanthin (hex-fuco) represents a switch from diatom to haptophyte-dominated (e.g. *E. huxleyi* or *Phaeocystis*) material. Fuco is the more common of the two and the dominant pigment of diatoms, while hex-fuco is typical of *Phaeocystis* (Antajan et al., 2004). Therefore, the abundance of hex-fuco relative to fuco, can be used as a proxy to determine *Phaeocystis* prevalence (Antajan et al. (2004) and references therein).

Table 5.2: Solubility of primary and secondary silicates in seawater (SW). The Siever (1968) experiment was carried out in distilled water (DW).

Mineral	**Solubility (μM)**	**Source**	**Conditions**
Kaolinite	67	Siever (1968)	25 days, 25^{o}C, DW
	64;83	Mackenzie et al. (1967)	375 days, room temp, SW
	50	Lerman et al. (1975)	8.5 years, Bermuda SW
	10-300	Hurd et al. (1979)	12 weeks, 1-2^{o}C, SW
Montmorillonite	130; 183	Mackenzie et al. (1967)	
	100	Fanning and Schink (1969)	10 months, room temp, SW
	130;166	Lerman et al. (1975)	
	80-250	Hurd et al. (1979)	
Chlorite	33	Mackenzie and Garrels (1965)	10 months, room temp, SW
	70	Mackenzie et al. (1967)	
	30	Fanning and Schink (1969)	
	40-80	Hurd et al. (1979)	
Illite	95	Mackenzie et al. (1967)	
	100	Lerman et al. (1975)	
	40-70	Hurd et al. (1979)	
Muscovite	127	Mackenzie et al. (1967)	
	125	Lerman et al. (1975)	
Glauconite	60	Mackenzie et al. (1967)	
	50	Lerman et al. (1975)	
Bentonite	433		
	115-340	Hurd et al. (1979)	
Quartz	100	Lerman et al. (1975)	
Phillipsite	150		
Analcite	100		
Prehnite	92		
Albite	55-110		
Hornblende	50-120		
Nepheline	35-75		
Biotite	60-120		
Hypersthene	200-275		
Epidote	150-200		
Tremolite	200-275		
Olivine	300-700		

Bulk sediment			
Congo fan	48	Loucaides et al. (2010)	22 months, ocean mooring
Mississippi delta	46;52		
Basalt			
River bedload	103	Jones et al. (2012)	9 months, 5^{o}C, SW
Estuary sediment	129		
Volcanic glass	90	Staudigel et al. (1998)	314 days, room temp, SW

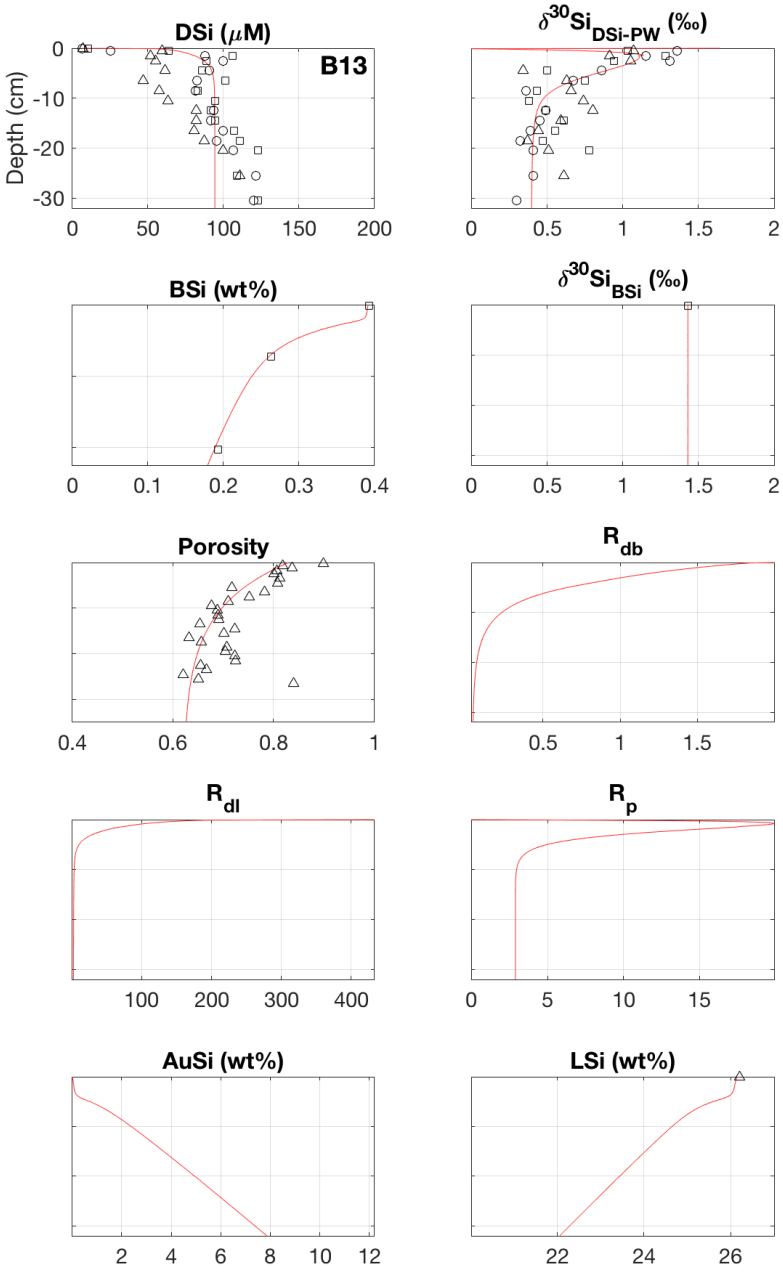

Figure 5.8: Model output summary (red lines) vs data (open shapes) from the best-fit simulation at station B13. R_{db}- rate of BSi dissolution, R_{dl}- rate of LSi dissolution, R_p- rate of AuSi precipitation. All reaction rates are given in $\mu mol\ cm^{-3}\ yr^{-1}$.

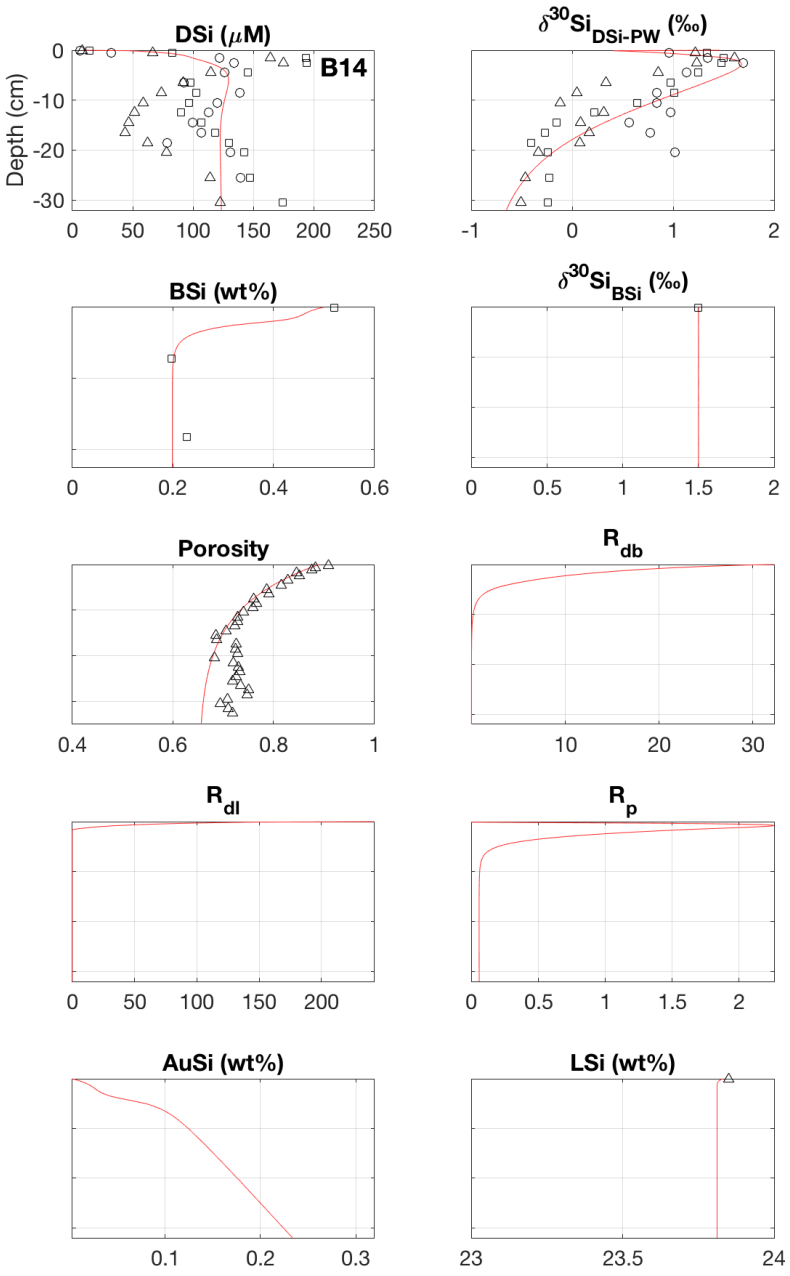

Figure 5.9: Model output summary (red lines) vs data (open shapes) from the best-fit simulation at station B14. All reaction rates are given in μmol cm^{-3} yr^{-1}.

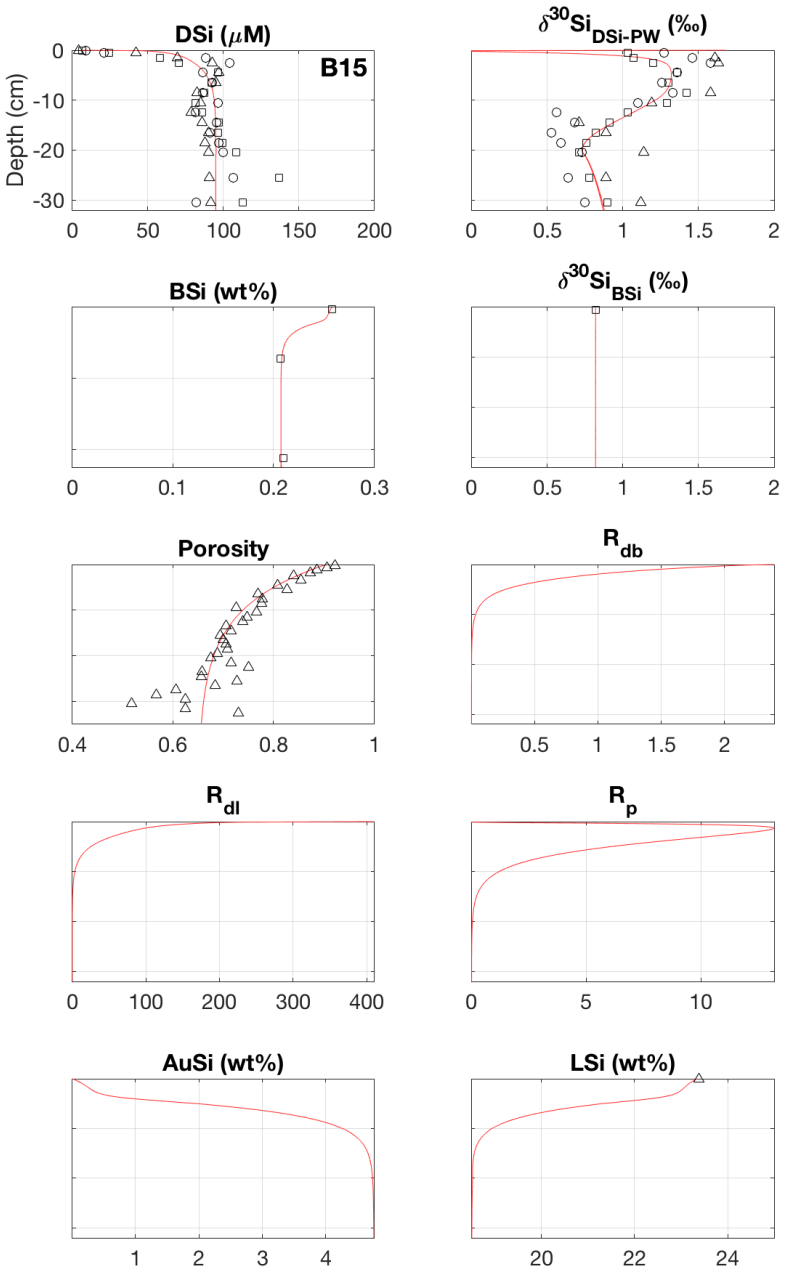

Figure 5.10: Model output summary (red lines) vs data (open shapes) from the best-fit simulation at station B15. All reaction rates are given in μmol cm^{-3} yr^{-1}.

Chapter 6

Overall summary and conclusions

This thesis represents the first isotopic study of benthic Si cycling within the Arctic circle, as well as the first time that the isotopic composition of solid phase reactive Si pools has been studied in a non-coastal setting. In addition, this study represents the first attempt to couple isotopic measurements of the dissolved pore water phase and multiple reactive pools of the solid phase, with a reaction-transport model. This research therefore provides a key insight into Si cycling in the Arctic Ocean, which is under considerable pressure from anthropogenic and natural forcings. Specifically, this work fills a crucial area of data paucity in our understanding of the pan-Arctic Ocean Si budget (Brzezinski et al., 2021), by providing isotopic compositions of water column samples of the Barents Sea, an important gateway for Atlantic Water, as well as of BSi within Arctic Ocean seafloor sediments. In this section, I present a summary of the key findings from each chapter and how each aim has been addressed, as well as suggestions for future research to build on this work and further advance our understanding of benthic Si cycling.

6.1 Main Conclusions

6.1.1 Summary of Chapter 3 findings (Aim 1)

Aim 1: Produce a δ^{30}Si dataset of operationally-defined reactive Si pools in Barents Sea sediments and investigate the effect of differing sample preparation techniques on those compositions.

This thesis builds on previous research on the magnitude of operationally-defined reactive Si pools (Krause et al., 2017; Michalopoulos and Aller, 2004; Presti and Michalopoulos, 2008; Qin et al., 2012; Wang et al., 2015a) by expanding the global dataset into a non-coastal setting. In addition, the dataset presented here represents the second time isotopic compositions have been measured in the reactive Si pools following Pickering et al. (2020), providing a novel insight into early diagenetic processes on a continental shelf.

Chapter 3 uncovers the presence of a reactive Si phase that is very isotopically light

for the marine environment (Si-HCl) and a reactive LSi pool (Si-NaOH), both of which show minimal spatial heterogeneity. The dataset in Chapter 3 also demonstrates the presence of a Si-Alk (BSi) phase, which differs in isotopic composition across the Atlantic and Arctic Water realms, likely representing disparities in Si cycling (i.e. the stage of bloom development from which the BSi was deposited), but are within range of pan-Arctic $\delta^{30}Si_{BSi}$ measured at 50-800 m in the water column (as stated in hypothesis 1). Furthermore, estimated BSi contents are low relative to the global average, but similar to the neighbouring Norwegian and Kara seas, although are elevated underneath the oceanic polar front, likely due to enhanced physical mixing (as stated in hypothesis 2).

Unlike previous studies of reactive Si pools, Barents Sea samples are not consistent with the global trend, whereby the size of the Si-HCl pool typically increases linearly with the size of the Si-Alk pool (Pickering, 2020). This observation indicates that BSi may not be the primary substrate for authigenic products in Barents Sea sediments, which may in fact be sourced from LSi phases.

Chapter 3 also summarises the use of stable Si isotopic analysis to evaluate the influence of different sample preparation techniques on the mass and source of Si liberated during sediment digestion experiments. I show that grinding sediment samples significantly increases the estimated BSi content and introduces contamination into the Si-HCl pool from an isotopically heavier source, most likely LSi. Furthermore, as stated in hypothesis 3, Chapter 3 shows that oven-drying sediment activates additional phases that are released into the Si-Alk and Si-NaOH pools that are not liberated during digestions of thawed sample counterparts. This hypothesis is evidenced by elevated metal concentrations in both phases and a shift in the isotopic composition of Si-Alk in leachates from dried and dried/ground samples. Based on these findings, I advocate for a standardised methodology for the investigation of operationally-defined reactive Si pools, in order to improve the interlaboratory comparability of data. This is particularly pertinent as the number of studies using stable Si isotopes to examine reactive Si pools increase in number.

6.1.2 Summary of Chapter 4 findings (Aim 2)

Aim 2: Produce a δ^{30}Si dataset of Barents Sea sediment core top waters and pore water depth profiles to determine the processes responsible for pore water DSi build-up.

To compliment the solid phase analysis in Chapter 3, Chapter 4 presents a comprehensive dataset of δ^{30}Si and DSi concentration measurements in core top and sediment pore waters. This dataset provides an insight into the spatial and temporal variability of Barents Sea benthic Si cycling, spanning three sampling stations and cruise years.

As stated in hypothesis 1, sediment pore water DSi concentrations are consistent with neighbouring Norwegian and Kara Seas, as well as the wider North Atlantic and Arctic

Ocean, where LSi to BSi ratios are generally high and sediments are often devoid of BSi (<1 wt%).

Measurements of δ^{30}Si in sediment pore waters show very little interannual variability at a given station, exhibiting similar downcore trends across the cruise years, especially at stations B13 and B15. Mass balance calculations in Chapter 4 present strong evidence for the contemporaneous dissolution of BSi and LSi at all three stations. In addition, we build on previous work that evidences AuSi precipitation in CAO sediments (März et al., 2015), with measurements of stable Si isotopes. δ^{30}Si increases between the SWI and a maxima at 3 cmbsf at stations B14 and B15, indicating uptake of the lighter isotope, likely during AuSi precipitation, which is coupled with supporting evidence from cation concentration profiles (hypothesis 2). This observation has potentially significant implications for the regional Si budget, which currently lacks an isotopically light sink of Si (Brzezinski et al., 2021).

While there is little apparent interannual variability in benthic Si cycling at a given station, the dataset presented in Chapter 4 uncovers significant regional differences. The contrast in downcore sediment pore water δ^{30}Si profiles at stations B13 and B15 reveals an influence of redox cycling of metal oxides. Stark shifts towards lighter isotopic compositions are observed across different depth horizons at the three stations, corresponding to depths where dissolved Fe begins to accumulate and NO_3^- and O_2 concentrations diminish. These coupled observations point to the reductive dissolution of metal (most likely Fe) (oxyhydr)oxides under hypoxic and anoxic conditions, resulting in the desorption and release of ^{28}Si-enriched DSi. The dissolved phase pore water evidence for a redox influence compliments isotopic analysis of the Si-HCl reactive Si pool in Chapter 3, which is thought to remove metal oxides from the sediment sample.

Chapter 4 therefore clearly demonstrates that the early diagenetic cycling of Si on the Barents Sea shelf cannot be characterised by a simple endmember mixing dynamic. Downcore trends in pore water δ^{30}Si do not only tend towards the isotopic composition of the principle dissolving phases (i.e. BSi and LSi), as stated in hypothesis 3, as they are altered by AuSi precipitation and redox cycling.

6.1.3 Summary of Chapter 5 findings (Aim 3)

Aim 3: Simulate the early diagenetic cycling of Si to quantify rates of reaction to inform a Barents Sea Si budget and explore whether seasonal deposition of fresh BSi can perturb the pore water DSi pool.

Chapter 5 brings together and reproduces the datasets presented in Chapters 3 and 4, enabling the respective hypotheses to be tested and for the processes inferred to be quantified.

As suggested in hypothesis 1, the steady state simulations were unable to reproduce the

sediment pore water DSi concentration profiles at the three stations with the dissolution of BSi alone. The best data-model fits were attained when the dissolution of a LSi phase was imposed, driven by the degree of undersaturation. Simulations suggest that up to 96% of the steady state DSi pool is derived from the dissolution of LSi, which has important implications for the regional Si budget, as LSi represents an input of 'new' Si, whereas BSi dissolution constitutes an internal recycling term.

Furthermore, as suggested in hypothesis 2, Chapter 5 demonstrates that the measured δ^{30}Si pore water profiles cannot be reproduced by the steady state simulations without imposing the uptake of isotopically light Si in the upper 3 cmbsf (most likely through AuSi precipitation), as well as the release of an isotopically light phase across the respective redox boundaries. These model observations therefore support the conclusions drawn in Chapter 4.

Pore water DSi concentration profiles presented in Chapter 4 exhibit distinct interannual variability, with strong peaks detected in the upper 3 cmbsf of 2017 and 2019 samples. Transient reaction-transport modelling was employed in Chapter 5 to determine whether tight benthic-pelagic coupling could be driving this variability (hypothesis 3). This is a key question, as the community composition of the Barents Sea spring bloom is shifting in favour of Atlantic flagellate species, which could significantly alter the composition of the phytodetritus deposited at the seafloor. Results of the transient modelling indicate that seasonal variability in the flux of BSi to the seafloor can be expressed in the pore water DSi concentration signal, which disperses on the order of weeks. Furthermore, Chapter 5 indicates that approximately 33% of the total annual flux of DSi emanating from Barents Sea sediments is potentially sourced from the dissolution of material deposited from a short spring bloom of just 2-3 weeks.

Coupling the datasets compiled across Chapters 3 and 4 with the reaction-transport modelling techniques employed in Chapter 5, allows for a comprehensive, systematic and quantitative assessment of the Barents Sea benthic Si cycle. Chapter 5 therefore presents a Si budget for the Barents Sea, based on the simulations with the best data-model fits across the three stations. Crucially, the Si budget constructed here is isotopically balanced. This research product has potentially significant implications, as current understanding in the most recent pan-Arctic Ocean Si budget (Brzezinski et al., 2021) is limited by a lack of direct stable Si isotopic observations of the Barents Sea water column and BSi within the seafloor. These knowledge gaps are contributing factors to the isotopic imbalance of the current regional Si budget, which is missing an isotopically light sink of Si. The findings in Chapter 5 indicate that the burial of AuSi could potentially resolve this discrepancy.

6.2 Limitations and suggestions for future work

This thesis provides important insights into high latitude benthic Si cycling and has begun the process of addressing significant areas of data paucity that limit our present understanding of the Arctic Ocean Si budget. However, this work has highlighted a number of research questions and areas where a mechanistic understanding of important processes are lacking. This section therefore suggests potential avenues that future work could take to address these outstanding issues and expand upon this study.

Investigate AuSi precipitation on other Arctic Ocean shelf seas

This thesis has presented evidence supporting the precipitation of AuSi in Barents Sea sediments, contributing an important isotopically light sink of Si that balances the Barents Sea Si budget. However, this process has not been widely studied in Arctic Ocean sediments, with previous evidence based upon pore water DSi concentration profiles alone (März et al., 2015). Future work should look to analyse pore water isotope ratios (e.g. Si, Ge, Li, Be) (Baronas et al., 2019; Bernhardt et al., 2020; Xu et al., 2022) and element concentrations (e.g. K, Mg, F) (Aller, 2014; Geilert et al., 2020a; Ng et al., 2020) from sediment cores collected on other Arctic Ocean shelves, to determine whether this process could resolve the isotopic imbalance in the latest pan-Arctic Ocean Si budget (Brzezinski et al., 2021). This work could be expanded to include imaging of sediment samples, to look for direct optical evidence of the formation of authigenic products and alteration of BSi or detrital precursor clay minerals (Loucaides et al., 2010; Michalopoulos and Aller, 2004; Presti and Michalopoulos, 2008).

Investigate LSi dissolution on other Arctic Ocean shelf seas

Mass balance calculations in Chapter 4 and reaction-transport modelling in Chapter 5 point to the contemporaneous dissolution of BSi and LSi. However, estimates of the relative contribution of LSi are wide-ranging across the two methods, potentially due to interference from AuSi precipitation. The dissolution of LSi in marine sediments is important to quantify, as LSi represents a source of new Si to the ocean budget. Future work should look to establish whether LSi dissolution is occurring in other undersaturated Arctic shelf sediments and ascertain the relative contribution to the pore water DSi pool. Additional geochemical proxies could be measured that were not employed here, such as pore water dissolved Al concentrations, rare earth element abundances and solid phase K/Al ratios (Abbott et al., 2019; Geilert et al., 2020a).

Develop a better mechanistic understanding of Si adsorption/desorption of Si onto/from metal oxides and the relationship with the degree of oxygenation

This thesis presents strong geochemical and reaction-transport model evidence for a coupling of the Si and Fe-redox cycles. However, we lack a clear mechanistic understanding of the adsorption and desorption of Si onto and from metal oxides, especially in comparison to other elements (e.g. P) (Geilert et al., 2020a; Niemistö et al., 2018). Crucially for Barents Sea sediments, the relationship between adsorption/desorption and the degree of pore water oxygenation is poorly constrained. Future work should look to better constrain the threshold between adsorption and desorption and develop a better mechanistic understanding to improve the way in which we model this process. Our reaction transport model is able to demonstrate that a source of isotopically light Si must be released across the redox boundaries at all three stations to reproduce the pore water δ^{30}Si profiles, but the rate of release is not dependent on any other variable.

Develop a better understanding of the impact of Atlantification on BSi deposition fluxes and determine whether benthic DSi recycling fluxes are mixed into the photic zone

An increasing body of evidence is pointing to the evolution of Arctic Ocean spring bloom phytoplankton community compositions towards more temperate flagellate species, as Atlantification of the Barents Sea progresses, sea-ice retreats northwards and pre-bloom DSi concentrations continue to decline (Neukermans et al., 2018; Orkney et al., 2020). However, the impact of these factors on the flux of BSi from the surface ocean to the seafloor has yet to be quantified, which could be modelled or studied through time-series monitoring of phytodetritus deposition with sediment traps. This work would also allow for the validation of model-derived BSi reactivities and BSi deposition flux magnitudes through direct measurements. Furthermore, the transient reaction-transport model study in Chapter 5 indicates that a significant portion (approximately one-third) of the annual benthic flux of DSi from Barents Sea sediments is sourced from the dissolution of the freshly deposited BSi, derived from the spring bloom. However, it is currently unclear as to whether the benthic DSi flux is admixed into shallower Barents Sea waters and used to fuel subsequent phytoplankton blooms, or if it is transported off-shelf. These avenues for further research would advance our understanding of the impacts of continued environmental perturbations on the Barents Sea Si cycle.

Development and use of standardised sediment sample digestion protocols

The dataset presented in Chapter 3 highlights that using different sediment sample handling and preparation techniques can lead to marked differences in the isotopic composition of sample digestion leachates, and/or the concentration of particular elements released per

unit mass over the digestion. Currently, a wide range of techniques are used, including oven drying, freeze drying, grinding and use of frozen and thawed sediment. Future research on reactive Si pools should look to further develop and use a consistent, standardised approach for sample handling and preparation to ensure comparability of data across laboratories. A framework for the analysis of operationally-defined reactive Si pools could follow the example of GEOTRACES protocols, published to advise on sampling and sample handling for the measurement of trace metals and isotope ratios (Cutter et al., 2017).

6.3 Closing remarks

This study has produced a wide range of laboratory and simulated data that expands the global dataset of Si isotope measurements in sediment pore waters into the Arctic Circle and analysis of operationally-defined reactive Si pools away from an exclusively coastal setting. In this thesis I have uncovered the major controls on the early diagenetic cycling of Si through an extensive observational dataset and used a reaction-transport model to quantify the rates of reaction, which could have significant implications for our understanding of the pan-Arctic Ocean Si budget. This research therefore demonstrates the importance of using a wide range of analytical tools in both dissolved and solid sediment phases to gain a comprehensive and holistic understanding of benthic Si cycling. Furthermore, I have outlined the crucial need to develop a standardised protocol for the handling and preparation of sediment samples when studying operationally-defined reactive pools of Si, especially where analysis of stable Si isotopes is being considered. Overall, this work has established a baseline understanding of Barents Sea benthic Si cycling, helping to better anticipate the impacts of continued natural and anthropogenically-driven physical, chemical and biological changes across the Arctic Ocean.

Appendix A

Barents Sea literature review paper

This review paper was written in 2018 during the scoping phase of this research project and is unpublished.

Acronym glossary.

Acronym	Units	Definition
IPCC	-	Intergovernmental Panel on Climate Change
ROMS	-	Regional Ocean Model System
SST	^{o}C	Surface Sea Temperature
SAT	^{o}C	Surface Air Temperature
AO	Phase (+/-)	Arctic Oscillation
NAO	Phase (+/-)	North Atlantic Oscillation
AMO	Phase (+/-)	Atlantic Multi-Decadal Oscillation
AW	^{o}C & psu	Atlantic Water
ArW	^{o}C & psu	Arctic Water
BSW	^{o}C & psu	Barents Sea Water
NCCW	^{o}C & psu	Norwegian Coastal Current Water
MW	^{o}C & psu	Meltwater
NADW	-	North Atlantic Deep Water
ArIW	-	Arctic Intermediate Water
BSB	-	Barents Sea Basin
BSO	-	Barents Sea Opening
BSX	-	Barents Sea Exit
PF	-	Polar Front
MIZ	-	Marginal Ice Zone
DIC	MtC yr^{-1} (flux)	Dissolved Inorganic Carbon (<0.45μm)
POC(M)	mgC m^{-2} d^{-1} (flux)	Particulate Organic Carbon (Matter)

DOC	gC m^{-2} yr^{-1}	Dissolved Organic Carbon (<0.45μm)
TOC	wt.%	Total Organic Carbon
TOM	wt.%	Terrestrial Organic Matter
MOM	wt.%	Marine Organic Matter
HNLC	-	High Nutrient Low Chlorophyll
SWI	-	Sediment-Water Interface
TSOC	mmol m^{-2} d^{-1}	Total Sediment Oxygen Uptake
DOU	mmol m^{-2} d^{-1}	Diffusive Oxygen Uptake
SR	mmol m^{-2} d^{-1}	Sulphate Reduction
DIR	-	Dissimilatory Iron Reduction
DMR	-	Dissimilatory Manganese Reduction

A.1 Introduction

The Barents sea is one of seven shelf seas encircling the Arctic Ocean. It has an area of 1.4×10^6 km^2 and borders the Norwegian Sea to the south, Kara Sea to the east and the central Arctic Ocean to the north. Its mean depth is 230 m, however the bathymetry of the Barents Sea Shelf is highly irregular, characterised by the juxtaposition of banks as shallow as 50 m (including Central Bank, Spitsbergen Bank and Great Bank) and deep troughs, such Bear Island at the western inlet (maximum depth of 470 m) (Fig. 1.2). The Barents Sea is a region of intense feedback cycles and especially strong coupling (Smedsrud et al., 2013) between the air-ice-ocean systems, on account of its shallow floor, resulting in a highly dynamic ecosystem that marks a frontier 'buffer' between the Arctic and the rest of Earths oceans. The Barents Sea has been described as exhibiting the most powerful ocean-air exchange in the Arctic (Serreze et al., 2007). This efficient mixing and resulting cooling and densification of inflowing waters ventilates the intermediate depths of the Arctic Ocean and sequesters CO_2. Therefore, despite occupying just 10% of the total area (Smedsrud et al., 2013), the Barents Sea is disproportionately influential for the Arctic Ocean. Not only does this cooling ventilate the Arctic Ocean, but it also influences regional climate directly and indirectly through heat exchange and local circulation irregularities (Smedsrud et al., 2013).

Global warming is amplified across the whole Arctic region, which is experiencing the most severe and rapid changes on earth (IPCC, 2021). However, within the Arctic the Barents Sea is at present subject to the highest rates of sea ice retreat, the consequences of which could have significant and widespread implications (Docquier et al., 2020; Lind et al., 2018). These changes will likely affect carbon sequestration, primary productivity and deep water formation, having far-field implications such as triggering colder winters across much of Europe (Smedsrud et al., 2013; Yang and Christensen, 2012). The influence of the Barents Sea over a wide latitudinal gradient along with its unique features and

a comprehensive observational history spanning over 500 years (Smedsrud et al., 2013), makes for an excellent natural laboratory in which to study the effects of a changing climate on shelf sea ecosystems. I will begin with a top-down description of the Barents Sea by surveying the available literature on the air-ice-ocean and ecological systems, followed by a detailed description of sediment biogeochmical dynamics and a discussion. I will also discuss the potential impacts of climate change on the ecosystem as a whole, with a specific interest in how the sensitivity of processes in the pelagic and atmospheric realm could impact processes in the basin sediments, including benthic fluxes and reaction rates of biologically relevant solutes.

A.2 Atmosphere-ocean interactions

The Barents Sea is highly influential in driving climate variability via coupled feedback mechanisms within the Arctic air-ice-ocean system, given that it lies on the main thoroughfare for Atlantic Water (AW) entering the Arctic Ocean (Smedsrud et al., 2013). As a result, variability in the Barents Sea system will have important implications for downstream climates. Barents Sea climate variability occurs on timescales ranging from weeks to multiple decades. Variability in Barents Sea climate consists of a complex interplay of these timescales, with general patterns of variability occurring on a high frequency timescale (3-10 year) superimposed upon a lower frequency (multidecadal) timescale. Lower frequency variability is correlated to the Atlantic Multi-decadal Oscillation (AMO) (Levitus et al., 2009; Oziel et al., 2016), the mechanism for which is not considered in this review.

Multi-decadal variability has presented itself in three distinct terms across the last century, including the 'Early Warming' (1930-1950), followed by the 'Cool 70s' and finally a tendency toward warming over the past three decades (Bengtsson et al., 2004; Levitus et al., 2009; Loeng, 1991). The mechanisms and causal factors for these longer-term oscillations have not yet been fully defined, however it is clear these processes are coupled to localised mechanisms of the Barents Sea system (Smedsrud et al., 2013). In contrast, higher frequency climate variability (7-10 years) is strongly correlated to AW inflow (which cycles at a similar temporal rate ((Bengtsson et al., 2004; Oziel et al., 2016))) and also to regional heat fluxes (Loeng, 1991; Smedsrud et al., 2013). This cycling is driven by feedback mechanisms (Fig. A.1), which stimulate an alternating pattern of warm and cold periods. The transition between these phases is likely driven by larger modes of climate variability, for example: the Arctic Oscillation (AO) (also known as Northern Hemisphere Annular Mode) or North Atlantic Oscillation (NAO) (Oziel et al., 2016). These anomalies are close relatives and often share phases, which have been shown to impact atmospheric circulation regionally in the Arctic and more locally above the Barents Sea, with the AO having been described as the primary pattern of Arctic atmospheric variability on interannual and decadal timescales (Oziel et al., 2016; Smedsrud et al., 2013; Thompson

and Wallace, 1998).

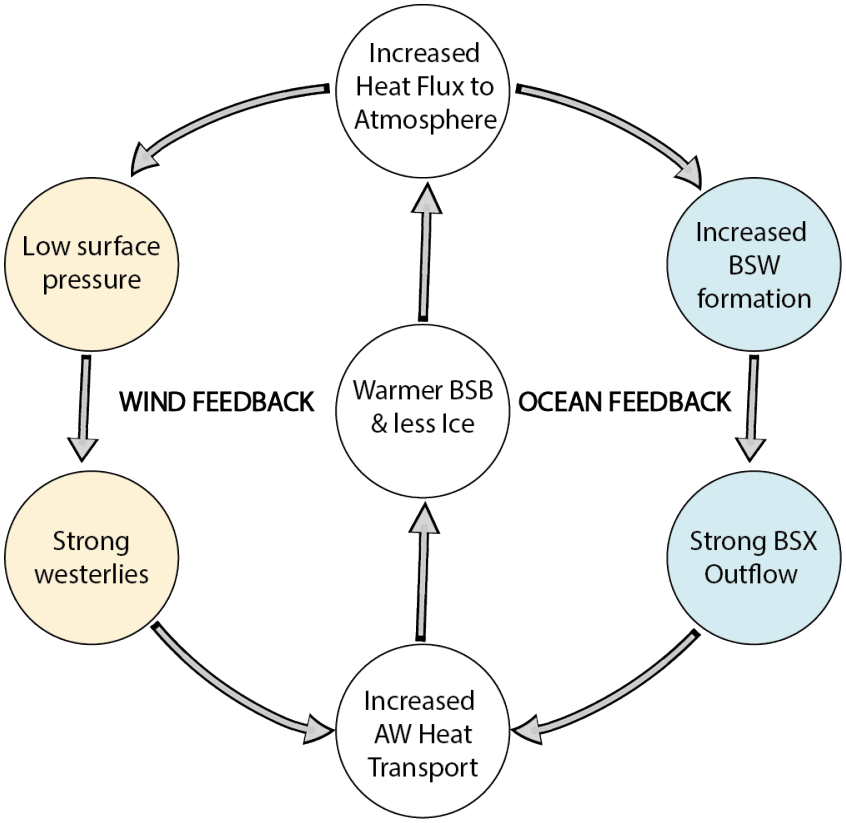

Figure A.1: Hypothesised feedback loops that connect the Barents Sea ocean, ice and atmospheric systems. The ocean and wind loops from (Smedsrud et al., 2013) share a common axis, originally hypothesised by (Ikeda, 1990), comprising increased inflow through the BSO. The two loops are complementary to each other and negative cycles can occur within these loops. This mechanism of positive feedback has been suggested as the mechanism maintaining decadal variation in the Barents Sea climate, such as 'the Cool 70s' or the 'Early Warming' from 1925-1940. It is suggested that these cycles are self maintaining, however the initial perturbation is likely a result of the discussed large scale modes of atmospheric or oceanic circulation (Smedsrud et al., 2013). The Barents Sea influences atmospheric circulation and climate over a much larger geographical area, however it is as yet unclear as to what proportion of the change is response or forcing.

The AO index has two phases: positive and negative. In a negative phase, the semi-permanent band of low pressure circumnavigating the subpolar region ('subpolar lows') presents with a relatively higher pressure, while the highs across the horse latitudes ('subtropical highs') are characterised by lower than average pressures. This shift drives a more anticyclonic circulation regime over the Barents Sea, decreasing air temperatures, thereby increasing heat exchange across the ocean-air interface. Due to the reduced gradient between the two pressure belts, the westerly winds decrease in strength, resulting in reduced advection of AW across the Barents Sea opening (BSO). Importantly, sea ice maxima are significantly correlated (correlation coefficient of -0.33) to this AO phase (Oziel et al., 2016), likely via perturbations in climatic variables. Observations support this conclusion, which indicate that surface air temperature (SAT) and sea surface temperatures (SST)

fluctuate concurrently (Ozhigin et al., 2011), both of which shift in-phase with sea ice cover (Ozhigin et al., 2011; Smedsrud et al., 2013). During a positive index phase, the poles present with lower atmospheric pressures, bolstering the regional cyclonic circulation and strengthening the prevailing westerlies. Stronger westerlies inflate the rate of advection of AW from the Norwegian Sea, increasing the proportion of warm AW residing in the Barents Sea Basin (BSB) relative to Arctic Water (ArW) (Ingvaldsen et al., 2002). As a result of this increased oceanic heat content, sea ice coverage is reduced and heat fluxes to the atmosphere increase accordingly (Oziel et al., 2016). The effect of this phenomena is a positive feedback loop, whereby the heightened heat flux from the ocean surface bolsters the AO-enhanced atmospheric cyclonic circulation, further increasing AW inflow through the BSO (Fig. A.1).

The 3-10 year periodicity of alternating cold and warm periods that span observational datasets of Barents Sea climate are associated with the more anticyclonic (negative) or cyclonic (positive) circulation patterns respectively (Ikeda, 1990; Smedsrud et al., 2013). For example, during the winter of 1998 the AO was in a negative phase, during which time sea ice coverage capped $>750\times10^3$ km^2 of the BSB. In contrast, the conditions in the winter of 2000 were antithetical, as the AO switched to a positive phase, culminating in a rapid decrease in sea-ice cover to less than half of its extent two years prior ($>300\times10^3$ km^2) and SAT to rise by 6^{o}C to 0^{o}C. Observational and simulated data support the theory of feedback mechanisms (Fig. A.1) in the Barents Sea (Otterå et al., 2009; Oziel et al., 2016). Observational data indicate that concurrent to the warming through this time period, westerly winds drove the AW proportion to increase from 25% to 30% (Oziel et al., 2016), while a 600 year Bergen Climate Model (BCM) study simulated a consistent positive correlation between the strength of the Westerlies and BSO inflow (Otterå et al., 2009; Smedsrud et al., 2013).

The Barents Sea region is also affected by atmospheric variation on a much shorter 1-2 week timescale. The atmospheric polar front traverses the planet at $\sim$60^{o}N, separating warmer subtropical air from colder polar air. This front can meander and regularly forms low pressure centres, known as 'polar lows'. Polar lows are mesoscale cyclonic weather features, which can separate from the atmospheric front and travel with the prevailing wind towards the Barents Sea, thereby replicating the symptoms of a positive AO phase. Anomalous heat fluxes from the Barents Sea surface can feed these mesoscale cyclones. This is one of many unique features of the Barents Sea, given that typical spatial scales of atmospheric processes are much larger than those in the ocean (Smedsrud et al., 2013).

Given their reliance on energy provided by surface ocean heat fluxes, polar lows become more frequent as a result of increased AW content and corresponding sea ice reduction in the BSB, associated with global warming and Atlantification (Alexeev et al., 2017; Smedsrud et al., 2013). A consequence of this increased polar low frequency would be similar to a positive AO phase, as heightened cyclonic conditions in the Barents Sea system

Table A.2: Water mass attributes (Barents Sea). Modified from (Lind and Ingvaldsen, 2012) and (Oziel et al., 2016).

Water Mass	Salinity (psu)	Temperature (^{o}C)
Atlantic Water (AW)	S>34.8	T>3^{o}C
Arctic Water (ArW)	S<34.7	T<0^{o}C
Barents Sea Water (BSW)	S>34.75	T≤0^{o}C
Norwegian Coastal Current Water (NCCW)	S<34.4	T>3^{o}C
Meltwater (MW)	S<34	-1.9<T<4^{o}C

would increase advection across the BSO, driving the oceanic positive feedback mechanism (Fig. A.1). However, it has been suggested that the atmospheric response to sea ice reduction and increased heat flux could be non-linear, whereby sea ice concentrations within a certain range (similar to present values) may cause strong anticyclonic circulation over the Barents Sea (Petoukhov and Semenov, 2010; Smedsrud et al., 2013). This scenario would result in easterly flow over Europe, presenting as a negative AO phase, implying a potential (albeit temporary) mechanism for mitigating the effects of regional warming and the initiated positive feedback mechanisms. It is evident then that both large scale modes of climate variability and shorter temporal scale pressure features significantly influence Barents Sea dynamics. It will therefore prove critical to understand how the potential effects of anthropogenically-driven change will superimpose itself upon these prominent natural cycles (Fig. A.1).

A.3 Pelagic processes

A.3.1 Oceanic circulation

Oceanic circulation within the BSB is driven by (general) regional cyclonic atmospheric circulation (Smedsrud et al., 2013) and constrained by areas of prominent bathymetry, such as between the Spitsbergen Bank and the Bear Island Trough. The BSO (470 m at its deepest) spans the 550 km distance between mainland Norway and the southern tip of Spitsbergen Bank. This inlet feeds the Barents Sea from the south-west with an eastward inflow of AW from the Norwegian Sea at a rate of 2 Sv (1 sverdrup = 1×10^6 m^3 s^{-1}) (Table A.2). A further 1.1 Sv of Norwegian Coastal Current Water (NCCW) flows through the BSO (Årthun et al., 2012; Loeng, 1991; Oziel et al., 2016), however the strength of both inflows at any given time is largely dependent upon prevailing wind conditions. It is estimated that the average residence time for a water mass based on Barents Sea volume and flow rate across the BSO is 2 years (Smedsrud et al., 2010).

Upon entry to the BSB, the AW inflow bifurcates. One branch tracks the Norwegian coastline towards Novaya Zemlya and the other flows through the Hopen Trench and across the northern side of Central Bank (Fig. 1.2). The third major water mass in the region

is cold and fresh ArW (Table A.2), which infiltrates the Barents Sea from the north-east. ArW is present at 1200 m depth in the Norwegian Sea and inflow is therefore halted by bathymetry at the BSO. However, north of 80^oN in the Nansen Basin, ArW is present from the surface to a depth of 100 m, thus the leading entry point for ArW is through the northern openings (Oziel et al., 2016). Instead, the BSO is the predominant inlet for AW (and therefore heat) in the BSB, experiencing a flow that is an order of magnitude greater than all other gateways (Aksenov et al., 2010; Årthun et al., 2012; Smedsrud et al., 2013).

As is the case for the Arctic Ocean as a whole, fluvial fluxes are the largest input of freshwater to the Barents Sea system (Bowling et al., 2000). River water from the Baltic Sea is entrained in the brackish NCCW, alongside input from northern european watersheds, which supply the Barents Sea with a total of >650 km^3 yr^{-1} of freshwater. Given that Arctic watersheds are driven by cryospheric processes, it is assumed they are highly sensitive to climate change. Dankers and Middelkoop (2008) use a hydrological model to predict changes in the Barents Sea fresh water balance under an Intergovernmental Panel on Climate Change (IPCC) B2 scenario (Nakicenovic and Swart, 2000), representing a modest increase in temperature of 1.5-2^oC by 2100. A 24% increase in riverine run-off to the BSB is predicted (to >810 km^3 yr^{-1}) by the end of the century under these conditions, which could have significant and wide ranging implications for biogeochemical cycling, but also for the density structure of the Barents Sea and therefore the Arctic Ocean as a whole. This is an exceptionally conservative estimate given that the IPCC project 3-4^oC warming (of SAT) in the central Arctic by 2050 (Schoolmeester et al., 2019), which is also reflected in a 2050 forecast for the Barents Sea climate specifically (Smedsrud et al., 2013).

Given their pervasive hydrological dissimilarities (Table A.2), all water masses are subject to significant transformations as they travel through the BSB. Warm, saline AW mixes along the Norwegian coast with brackish NCCW and fresh ArW, while extensive heat loss to the atmosphere coupled with brine rejection through sea-ice formation on shallow banks (e.g Central and Novaya Zemlya) compiles denser Barents Sea Water (BSW). BSW is then able to sink below the well-mixed surface layer, cascading to greater depths (Smedsrud et al., 2013) in a northeasterly direction, eventually draining into the Arctic Ocean through the Barents Sea exit (BSX) positioned in the aperture between Novaya Zemlya and Franz Josef Land (Fig. 1.2). Subsequent to its transport across the BSX, BSW flows north through the St Anna Trough before retroflecting and flowing southwards along the margins of the Nansen Basin and eventually through the Fram Strait towards the Greenland-Iceland-Scotland Ridge. Here, BSW feeds North Atlantic Deep Water (NADW) with its densest fraction (Mauritzen, 1996; Smedsrud et al., 2013). Therefore, not only is the Barents Sea influential on a much larger geographical area than itself from an atmospheric perspective, but it also has a significant impact on oceanic circulation across the entire Atlantic Ocean.

The oceanic polar front (PF) delineates these Barents Sea water masses, predominantly

dividing ArW to the north and east from AW in the southern and central regions. The PF is sometimes referred to as the 'marginal ice zone' (MIZ), as on a decadal scale the boundary between the two water masses demarcates the ice-margin. Most modelling studies will use the PF as the sea-ice extent, however in reality the margin (MIZ) can vary interannually and between seasons (Slagstad, 1984). The eastern branch of the PF presents with significant spatial variation on both seasonal and interannual timescales (Smedsrud et al., 2013) (Fig. A.2). This is in contrast to the western PF in proximity to the BSO, where its position is constrained by topography, consistently navigating around the walls of Spitsbergen and Great Bank (Oziel et al., 2016). Given the PFs propensity to wander, it is accepted that the eastern PF is highly susceptible to changes in the relative proportions of water masses in the BSB, which has important implications for sea ice dynamics as evidenced by the enhanced sea ice retreat in the eastern and central Barents Sea relative to the west (Årthun et al., 2012). This is further evidenced by water mass occurrence analysis for summers spanning 1980-2011 at 50-100 m depth in the BSB, which suggests that AW is present 100% of the time in the south-west over Spitsbergen Bank, penetrating the Barents Sea through the Bear Island Trough, which extends to the foot of Great Bank (Fig. 1.2) (Oziel et al., 2016). In just 20-30% of the period studied did pre-mixed AW expand as distally from the BSO as Central Basin (Oziel et al., 2016).

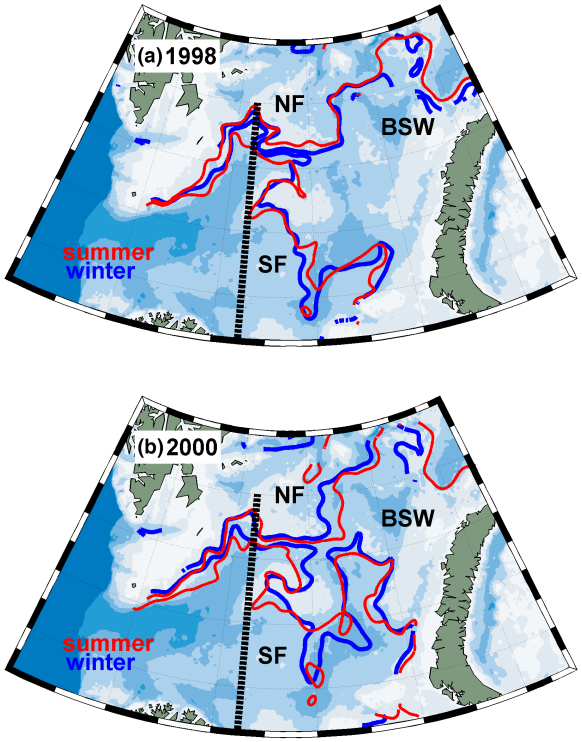

Figure A.2: Interannual and seasonal variations in the position of the oceanic PF (including southern and northern branches) for 1998 (a) and 2000 (b). The observed shift in PF positions was used as an analogue to discuss the impacts of Atlantification in the BS. SF = Southern Front, NF = Northern Front. From (Oziel et al., 2016).

BSW predominantly forms locally on Central Bank in winter, with some formation in the eastern Barents Sea over Novaya Zemlya Bank where sea-ice formation drives density up in surface waters through brine rejection. As would be expected, no dominant water mass was observed in the eastern BSB, which implies that significant mixing also occurs here (Oziel et al., 2016). The eastern BSB is shallower (<300 m depth) and has a much smoother bathymetry (Parsons et al., 1996) compared with the stark depth contrasts found in the west (Fig. 1.2), therefore the limits of water mass position imposed by the isobaths are less extreme.

Extensive study of the BSB inflow and mixing dynamics has been undertaken over the last decade (Årthun et al., 2012; Barton et al., 2018; Oziel et al., 2016; Smedsrud et al., 2013), to observe and better predict how conditions in the BSB may change and what impacts these changes may have, given the observed sensitivity of the eastern PF to changes in water mass proportions and the ingredient balance required to form BSW. This need is on account of the importance of BSW on a regional scale and the potential for significant changes to water mass inflows and mixing processes in various climate change scenarios (see section A.3.1). Currently, BSW is critical for the ventilation of the Arctic Ocean proper, as it forms Intermediate Arctic Water (ArIW) at ∼1200 m depth. The Barents Sea has an increased riverine input and shallower seafloor depth compared to the other six shelf seas, which increases the volume and decreases the irregularity of dense water outflow relative to the other shelves (Rudels et al., 1994; Smedsrud et al., 2013).

Not only is this process important for ventilating the deep Arctic Ocean, but it is also crucial for carbon uptake. Approximately 25% of anthropogenic carbon release (∼10 PgC yr^{-1}, Zeebe et al. (2016)) is taken up by the oceans globally, although sequestration occurs only in specific regions, such as the Nordic Seas, Arctic Ocean and North Atlantic. More than 60% of inflow across the BSO is transmuted into BSW, ferrying 60 MtC yr^{-1} from the atmosphere to the deep ocean and ∼1260 MtC yr^{-1} when advection from the Norwegian Sea is taken into consideration (Smedsrud et al., 2013). Critically, 25 Mt of anthropogenic carbon per year (Anderson et al., 1998; Smedsrud et al., 2013) is included within this atmospheric uptake, accounting for 50% of the uptake by the entire Arctic Ocean (Smedsrud et al., 2013). This observation suggests that the Barents Sea is potentially one of the most valuable regions in the world by area for carbon sequestration. However, predicted alterations to the influxes and proportions of water masses and a general warming of the BSB threatens the delicate balance of water masses and processes required for BSW formation.

Atlantification

The Barents Sea has been in a 'warm' phase for most of the 1990s, with a short stage of below average water temperatures in 1996-1997, followed by a period of marked warming towards the present day (Oziel et al., 2016). Between 1998-2008, mean SST of the Barents

region increased by 1^oC, with 2006 the warmest year on record at the time (ICES, 2008). Both SSTs and SATs measured in August 2016 for the southern domain were 5^oC warmer than the August mean of 1982-2010 (Timmermans, 2016), indicating that regional warming has continued and at a rate four times the global average. This recent warming is thought to be due to a process termed 'Atlantification', described as an increase in the proportion of AW present in the Barents Sea. The mechanism by which this process occurs has been demonstrated through analysis of a dataset spanning 1980-2011 (Oziel et al., 2016), indicating that the volume of the BSB occupied by AW has doubled within the studied time period and increased in temperature by 1.4^oC (Neukermans et al., 2018). This observation is consistent with findings that the area covered by AW has increased since 1970 (Dalpadado et al., 2012) and that recent sea-ice loss across the Barents Sea was caused not only by an increasing temperature of inflowing AW of 1^oC, but also by an increase in the volume at which it is delivered (+0.4 Sv) (Årthun et al., 2012).

Regional modelling studies have shown that heat transport has increased gradually from the Cool 70s period (Fig. A.3), resulting in the observed increase in SST (Årthun and Schrum, 2010). Not only has the increase in the presence of AW in the Barents Sea been established to the present day through modelling and observational data, but forward modelling has also predicted this process will continue into the future. Smedsrud et al. (2013) used an ice-ocean model (Regional Ocean Model System (ROMS)) forced with global simulations to look at a 2050 Barents Sea scenario. ROMS predicts an increase in average salinity of up to 1.3 psu (Fig. A.4d), which implies an increase in the region affected by pre-mixed, 'ideal' AW (Smedsrud et al., 2013). Complimentary to these findings, Koenigk and Brodeau (2014) show that heat transport into the Arctic Ocean has increased into the 21st century and predict it will continue to do so to 2050. These findings are based on coupled climate-model simulations carried out for every major Arctic Ocean gateway, including: the Fram Strait, Canadian Archipelago, Bering Strait and BSO. Crucially, it was found that the BSO dominates this increase (Koenigk and Brodeau, 2014). This observation has significant implications for the heat content of the Barents Sea, with knock-on effects for sea-ice cover and therefore primary productivity, as well as potentially driving a slowdown or inhibition of BSW generation (Oziel et al., 2016; Smedsrud et al., 2013).

In order to determine the potential influence of Atlantification on Barents Sea dynamics and climate, Oziel et al. (2016) incorporated a modelling study into their observational database analysis. The model was integrated according to the conditions observed between the previously discussed 1998-2000 winters, which were used as an analogue for future warming. The model and observational data provide contradictory interpretations. The former would suggest that BSW volume has in fact decreased in volume from 25% to <5% across the studied time period, concurrent with a northward shift in the PF in the central Barents Sea, as would be expected with the 3% increase in AW proportion derived

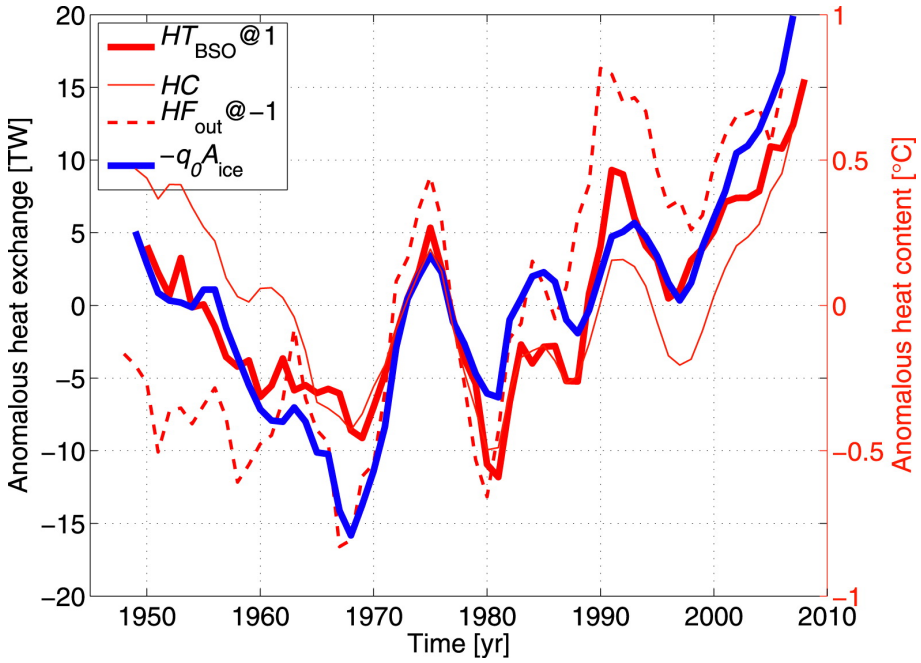

Figure A.3: Model results showing the effect of increased heat transport (due either to an increase in volumetric transport, or an increase in the temperature of inflow, or both contemporaneously) (HT_{BSO}) on sea ice cover (A_{ice}; inverted) and heat content of the BSB (HC). Lag response times denoted by '@'. Overall, an increased heat flux results in a reduction in sea ice cover and a consequential increase in heat loss from the ocean (HF_{out}). Taken from Årthun et al. (2012).

from the model. In contrast, observational data implies that BSW volume has remained stable. The interpretation for this discrepancy involves the presence of two frontal zones comprising a northern and southern branch of the PF (Fig. A.2), which bifurcate from the north eastern terminus of the Hopen Trench and delineate BSW from the other major water masses.

The observation that BSW has remained at a relatively consistent volume does not preclude an influence of Atlantification on the balance of Barents Sea water masses, as Oziel et al. (2016) suggest that an unchanged BSW volume requires a northward shift of the northern PF branch, in order to compensate for the observed equivalent shift in the southern branch. It should be noted that both the northern and southern extensions of the PF are only forced to shift in a northward direction from >40°E (Fig. 1.2), where the strict confines of bathymetry apply to a lesser degree. While it could be the case that the volume of BSW is less sensitive to Atlantification than previously thought, there is still a significant apparent northward shift in the position of BSW and thus an invasion of AW further east and northwards. This outcome would result in an expansion of the domain in which AW dominates at the expense of ArW (Lind and Ingvaldsen, 2012), which will have implications for dynamics through the whole water column by forcing the region into a warmer and more saline regime. Furthermore, it would be reasonable to suggest that should warming and Atlantification of the BSB continue, the formation of BSW may

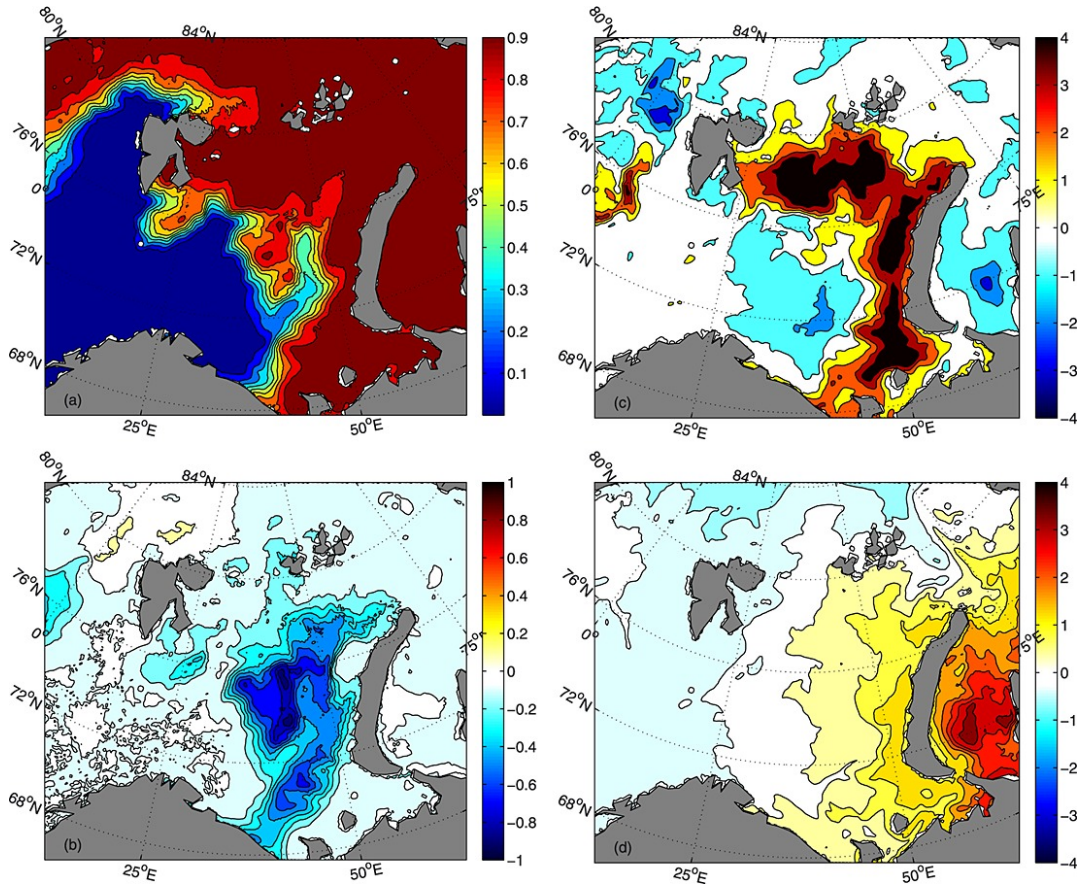

Figure A.4: Modelling study showing changes in Barents Sea conditions predicted for 2050 (Smedsrud et al., 2013). (a) Present sea ice concentration for March produced in the ROMS control run. The following subfigures are for 2050 relative to the present day simulation by ROMS. (b) Sea ice changes predicted for March in 2050. (c) Change in surface ocean temperature predicted for July 2050. (d) Salinity changes relative to present day at the surface for September 2050.

decrease in the future. For example, sea-ice formation on Novaya Zemlya Bank is pivotal in the BSW formation process, which will be under pressure by further rising temperatures driven by Atlantification.

A.3.2 Sea ice dynamics

Sea ice cover in the Barents Sea is highly seasonal, experiencing a late summer minimum (August-September) and a spring maximum (March-April). The majority of this ice is formed locally over winter in the northeastern archipelagoes of Novaya Zemlya Bank and Franz Josef Land, supplemented by the coastal regions surrounding Svalbard (Smedsrud et al., 2013). Coverage generally approaches 0.7-1.1$\times 10^6$ km^2 (Sakshaug et al., 1994; Vinje and Kvambek, 1991). The region south of the PF (AW realm) is permanently ice-free, while north of this region (ArW realm) sea-ice cover gradually increases in concentration towards the Franz-Victoria Trough (Fig. A.4a). The Barents Sea is therefore characterised by large regions of open water and a patchy, generally thin ice pack on account of its seasonal as opposed to multi-year nature (Smedsrud et al., 2013). However, ice cover has been gradually diminishing since 1850 (Shapiro et al., 2003). More recently (1998-2008) the region has experienced an accelerated decline, exhibiting the largest reduction in sea ice coverage across the Arctic Ocean, where annual average cover has decreased by 50% (2.18×10^5 km^2) at a rate of -58×10^3 km^2 decade^{-1} since 1980. As of 2012, sea-ice had attained its lowest level in six decades (Årthun et al., 2012). The Barents Sea, along with Baffin Bay, Greenland, are becoming the first permanently summer and autumn ice-free seas in the Arctic with projections further suggesting the BSB will be ice-free year round by 2050 (Smedsrud et al., 2013). This decline is currently having and will continue to have a significant impact on increasing air-sea exchange, deep water formation and primary productivity (Oziel et al., 2016).

Not only has there been a long-term decline, but ice conditions are also highly variable on interannual timescales in the Barents Sea. A great deal of the interannual variation can be accounted for by the warm and cold periods imposed by atmospheric modes and their influence on the rate of inflow across the BSO, while the temperature of infiltrating AW is also important. For example, the winter of 1979 bore unprecedented sea ice coverage under a cold regime, while the warm period of winter 2006 exhibited the minimum extent on record at the time with the majority of the BSB rendered ice free.

A numerical modelling study of a 1980-2011 water mass database showed a significant correlation between AO and the BSB AW proportion (Oziel et al., 2016). This ratifies previous work by Otterå et al. (2009), whose BCM study revealed a stable relationship between ice variability and AW inflow over the majority of the 600 year simulation (Smedsrud et al., 2013). However, this finding was not reflected in the observational data, where no correlation was found between AW inflow rate and sea ice cover, only between the relative volume of ArW and AW in the BSB and ice cover, where the correlation was

significant (Oziel et al., 2016). It has been suggested that the absence of a correlation between inflow rate and ice cover in the measurement derived dataset could simply be an artefact of a lack of data collection in the winter months (Oziel et al., 2016).

A field study of the Barents Sea MIZ (Ivanov et al., 2003), as well as empirical historical records from 1983 to present, show that winters during which ice cover is reduced, AW volume is high and vice-versa (Oziel et al., 2016). Contrary to the summertime dataset of Oziel et al. (2016), Vinje (2001) found that sea ice extent in the BSB is correlated significantly to anomalous heat transport from the Norwegian Sea with a lag time of two years. This was corroborated through a modelling study of sea ice variability (1979-2007) (Årthun et al., 2012), which identified the trend in sea ice coverage for this time period corresponded to a loss of 70×10^3 km^2 (5% (Smedsrud et al., 2013)) for every 10 TW (terawatt) of additional mean annual heat transport across the BSO (148×10^3 km^2 in total). This corresponds to a 12% increase in the area of open ocean in the Barents Sea in winter (60% to 72%) and a concurrent increase in mean BSB temperature of 0.9^{o}C (SST). Not only has the areal coverage of sea ice diminished in response to altered water mass proportions, but measurements of the thickness of fast ice at Hopen Island (1967-2007) has established that ice thickness has also been attenuated at a rate of 11 cm decade^{-1} (Gerland et al., 2008). Thinner Arctic sea ice at the end of the winter season results in easier melting for the following summer season and a compounding, positive feedback effect on the long term trend of sea ice across the region (Alexeev et al., 2017). Taking these empirical and model-based studies into account suggests that oceanic variability in terms of temperature and inflow rate across the BSO is the most influential driver of sea ice dynamics in the Barents Sea (Smedsrud et al., 2013).

While this mechanism can be employed to explain the temporal variability in Barents Sea ice cover of the ArW domain, at any given time the AW domain is ice-free and seasonal ice formation is generally considered to be inhibited. Consistent with this, by simulating the Barents Sea heat budget, Årthun et al. (2012) determined that the heat transport through the BSO determines the boundary for the AW domain the following year and thus, the sea ice extent. This observation supports the long-held assumption that sea ice extent at its seasonal maxima is dependent on the quantity of heat held in the water masses of the BSB in winter, given simply that a warmer ocean will take longer to cool to freezing point ($\sim$-1.8^{o}C). Therefore, ice melt in the Barents Sea is associated with an inflation of the region where wintertime freezing is inhibited, rather than through active melting of multi-year ice (Årthun et al., 2012; Smedsrud et al., 2013). Accordingly, anomalous heat transport will manifest itself as a northward-retreating MIZ, as has been observed at 40^{o}E, where the margin has receded by >240 km since 1980 (Årthun et al., 2012; Smedsrud et al., 2010). However, as anticipated this retreat is not emulated in the western basin on account of the relative stability of the PF, where the presence of ArW is maintained by bathymetric constraints (Fig. A.2).

Given that the discussed 'hot spots' of sea ice formation are in the eastern region, where the PF is most easily displaced, the process of Atlantification has been identified as contributing significantly to the slow down of sea ice (Fig. A.3) and therefore BSW formation (Årthun et al., 2012; Oziel et al., 2016). The ROMS study carried out by Smedsrud et al. (2013) suggested that a plausible scenario for 2050 is a sea ice minimum delayed to October, consisting of essentially no sea ice, and a maxima with extensive sea ice loss. The majority of ice loss is forecast to occur in the central and eastern limits of the BSB, where the largest shift in SST is also expected (Fig. A.4b and c). There is some potential for a temporary, partial recovery in sea ice cover in the region afforded by a decrease in inflow temperatures of individual years (Karaseva, 2010). However, should the predicted overall positive trend in heat transport transpire (Fig. A.3), wintertime cooling will become insufficient to generate notable volumes of sea ice (Årthun et al., 2012), with model projections anticipating a winter sea ice free Barents Sea within 2061-2088 (Onarheim and Årthun, 2017).

A.3.3 Marine ecosystems

Community structure

Barents Sea pelagic phytoplankton productivity and standing stocks are highly dynamic and vary on similar time and spatial scales as the climatic driving factors and distinct horizontal gradients in water mass characteristics. This variability is typical of polar ecosystems, which are known for their instability (Sakshaug, 1997). It is considered that the Barents Sea pelagic ecosystem is distributed into two distinct categories: 'true pelagic' and 'ice biota' (or 'sympagic') (Sakshaug et al., 1994). The true pelagic group is characterised by a dynamic community of phytoplankton (Table A.3) at the producer level, whose community structure fluctuates dependant upon the season. Despite interannual fluctuations in community stocks and seasonal changes in structure, it is considered absolute that a single 2-3 week bloom will occur within April-July (Wassmann and Olli, 2004).

During the late spring bloom period, up to 94% of nutrients delivered to the well-mixed euphotic zone are considered 'new', as they are delivered to the surface from deeper waters over winter. In this open system it is estimated that nutrient-rich AW is admixed into the surface layer with the following concentrations: 12-14 mmol m^{-3} of nitrate ($NO_3{}^-$), 0.9-1 mmol m^{-3} of phosphate ($PO_4{}^{3-}$) and 6-7 mmol m^{-3} of silicate (H_4SiO_4) (Rey et al., 1987; Sakshaug, 1997). As sea ice begins to melt north of the PF, the nutrient rich surface water is stabilised and flooded with sunlight, resulting in ideal conditions for phytoplankton growth. South of the PF under permanently ice-free conditions, water column stabilisation depends upon the formation of an insolation induced thermocline (Sakshaug, 1997). Under these replenished and stable conditions, communities thrive and are dominated by large

Table A.3: Annual average carbon biomass densities and productivities for key pelagic and benthic species for the entire Barents Sea over multiple years. Modified from (Sakshaug et al., 1994). 'DOC' is 'Dissolved Organic Carbon' and refers to the extracellular matter excreted by Phaeocytis Pouchetii (glycolic acid and carbohydrates, Sakshaug (1997)) and grazed by bacteria. Sedimentation refers to the export production that escapes the euphotic zone, which is highly episodic and so represents the average value. Capelin stock interannual variation: 30-700 kg C km^{-2}, Cod stock: 150-700 kg C km^{-2} (Sakshaug, 1997). Benthic data from (Kulakov et al., 2006). (a) range of benthic (secondary) productivity for whole region from (Kedra et al., 2013; Sakshaug, 1997)

Species	Biomass Density (kg C km^{-2})	Productivity (g C m^{-2} yr^{-1})
Bacteria	400	80
Phytoplankton (Total)	2000	110
Phytoplankton (New)	-	60
DOC	-	15
Sedimentation	-	45
Calanoids	2000	8
Krill	1000	1.5
Capelin	400	0.2
Polar Bears	0.1	0.00003
Macrobenthic	Biomass Density (g m^{-2})	Productivity (gC m^{-2} yr^{-1})
Coastal	<2000	0.5-70[a]
AW	<10-300	-
ArW	<10-100	-
MIZ	100->500	-

diatoms and the Arctic algal species *Phaeocytis pouchetii*. This algae produces extensive mats of gelatinous material that can be delivered efficiently to the deep ocean, despite exposure to aggressive bacterial attacks (Sakshaug et al., 1994; Wassmann et al., 1990). The stock of nutrients accumulated over winter is then deplete (Sakshaug, 1997), following which >83% of the available nutrients are regenerated within the upper reaches of the photic zone (Kristiansen and Farbrot, 1991). Meltwater-driven stabilisation then begins to hinder primary productivity by impeding water column mixing and nutrient replenishment from the deep ocean, establishing oligotrophic conditions (Sakshaug, 1997). Under this post-bloom closed system regime, smaller diatoms and flagellates prevail (Sakshaug et al., 1994).

Zooplankton species distribution differs across the AW and ArW domains. In the AW domain, the predominant zooplankton are copepods (*Calanus finmarchius*) and krill, while copepods (*Calanus glacialis*) dominate the ArW ecosystem (Sakshaug et al., 1994). Stocks of *C.finmarchius* show a significant range in productivities from 2-15 gC m^{-2} yr^{-1}, which is highly dependant on the autumn influx of AW months prior (Sakshaug et al., 1994). Similarly, the productivity of the *C.glacialis* population hinges on ice-cover in the Arctic domain, ranging from 1-8 gC m^{-2} yr^{-1} (Table A.3) from high to low sea ice cover respectively. Capelin (*Mallotus villosus*), a species of small fish, then forms the foundation of diets for higher trophic level species.

With regard to the sympagic flora, communities range from planktonic and pennate diatoms under marginal zones of seasonal ice and centric species under multi-year ice, which can form mats up to 1 m thick (Sakshaug et al., 1994). While ice algae is important locally in terms of biomass (up to 100 kgC m^{-2} of ice), given that seasonal ice now has an areal coverage of <30% (Smedsrud et al., 2013) and multi-year ice is rare in the Barents Sea, ice biota are thought to contribute little to the total biomass of the ecosystem as a whole (Sakshaug et al., 1994). They are also thought to contribute little to overall annual primary production (<10 gC m^{-2} yr^{-1} (Tamelander et al., 2006)), as typically ice biota are light-limited and as a consequence have slower growth rates than their pelagic counterparts (Sakshaug et al., 1994). Amphipods predominate as secondary producers for the sea ice ecosystem, which are crucial for cod stocks and in turn ringed seal and polar bear populations (Table A.3) (Ryg and Øritsland, 1991; Sakshaug et al., 1994).

Given the regular and substantial shifts in environmental conditions that occur in the Barents Sea (for example between the 'cold' and 'warm' climatic periods that span the length of Barents Sea history), one might expect equally significant changes in the ecosystem community structure of the region. During 'warm' phases of Barents Sea climate, large influxes of AW allow for adequate growth of critical zooplankton and fish stocks and represent periods of relative stability and high productivity across all trophic levels of the Barents Sea ecosystem (Sakshaug, 1997). In fact, simulations of primary producers for the whole Barents Sea show that populations are up to 30% more productive in warm years

with little sea ice (Slagstad and Stokke, 1994). Subsequent 'cold' years can then result in ecosystem imbalance or collapse, such as the 'capelin collapse' of 1988-1989 (Sakshaug, 1997). This collapse occurred due to the induction of less favourable growing conditions, introducing food shortages that rippled through the ecological pyramid (Sakshaug et al., 1994). This dynamism and sensitivity to cycling climate has fostered the consideration that the Barents Sea has in fact never seen 'ecological balance' (Sakshaug et al., 1994). However, Atlantification could promote higher regional productivity and a more stable 'Atlantic-style' ecosystem structure, as can be seen in the ecological records when warm periods associated with an increased proportion of AW predominate (Årthun et al., 2012; Oziel et al., 2016).

Primary production

Modelling of ecosystem dynamics in the Barents Sea indicates an organic matter production from primary producers of ∼125 gC m^{-2} yr^{-1} (Table A.3). 55% of this mean annual Barents Sea production corresponds to 'new' organic carbon composed of fresh nutrients delivered to the surface ocean from deeper waters (Kristiansen and Farbrot, 1991). Productivity in the Barents Sea is 25% higher than typical values for shelf seas globally (Sakshaug, 1997) and even greater in specific sites, such as Spitsbergen Bank where primary productivity can exceed 300 gC m^{-2} yr^{-1} (Sakshaug et al., 2009). The average primary productivity for Arctic Ocean shelves specifically is 20-400 gC m^{-2} yr^{-1}, which is significantly higher than those of Antarctic Shelves and the Ross sea (20-150 and 150 gC m^{-2} yr^{-1} respectively (Smith, 2010)) and demonstrates that the Barents Sea is amongst the most productive of polar ecosystems. It is thought that along with the Greenland Sea, the highest rates of areal total productivity in the Arctic are found in the Barents Sea, driven by the largest mean open water area (Bourgeois et al., 2017). On a global scale, rates of Barents Sea primary production are high and only surpassed in natural systems by the Anadyr waters in the Bering Sea (285 gC m^{-2} yr^{-1}), certain confined areas off Antarctica, as well as unique regions off the coast of west Africa and Peru (Sakshaug et al., 1994). Here, productivities can reach 300-500 gC m^{-2} yr^{-1} (Sakshaug, 1997) and are associated with the trade wind-driven Canary and Humboldt ('Peru') currents respectively. In these regions, upwelling occurs year-round on account of eastern boundary currents and Ekman transport in ocean-scale gyres.

Notably, AW areal average primary productivity is 125-200 gC m^{-2} yr^{-1}, consistent with ^{14}C measurements (Titov, 1995), which is three-fold higher than values calculated in northern ArW stations. Seasonal ice coverage reduces the average annual primary productivity in the ArW domain to <70 gC m^{-2} yr^{-1} (Sakshaug, 1997). Despite this annual average contrast, under spring bloom conditions both regions induce similar rates of 'new' biomass formation (30-50 gC m^{-2} over 2-3 weeks, Sakshaug (1997); Wassmann and Olli (2004)), implying that the annual areal contrast is due to the post bloom oligotrophic

conditions. The reduction relative to the AW domain in this time period is due to the meltwater influenced layer, which creates a strong and deep pycnocline (to 25-35 m depth), which inhibits light and further supply of 'new' nutrients via wind induced mixing. Stabilisation in the AW domain is much weaker as it relies solely upon insolation (Wassmann et al., 1999), allowing for wind-driven vertical mixing to depths of 40-80 m every 1-2 weeks through the passing of polar lows (Sakshaug, 1997; Sakshaug et al., 1995). This feature can also result in smaller, secondary peaks in primary productivity in the AW zone after the main spring bloom. Therefore, the anticipated increase in the number of polar low events per year associated with Atlantification (Alexeev et al., 2017; Smedsrud et al., 2013) could further emphasise the regional disparity in primary productivity. These observations are consistent with ocean-ecosystem primary productivity models, which generally predict a higher productivity AW domain (>100 gC m^{-2} yr^{-1}) and a less productive ArW region (<90 gC m^{-2} yr^{-1}) north of the PF (Ellingsen et al., 2008; Pathirana et al., 2014; Wassmann et al., 2010).

It is estimated that more than twice the primary production in the AW domain is 'new' as compared to the ArW domain (Sakshaug, 1997; Sakshaug et al., 1994). This is hypothesised to occur due to a deep pycnocline that forms during the summer growth period as sea ice melts. As a consequence of this, high productivity zones north of the polar front are confined to a 20-50 km wide band adjacent to the retreating ice edge, as nutrient-rich waters built up over the light-limited winter are uncovered (Nickel et al., 2008), in a process termed the 'ice-edge effect' (Gran, 1931; Sakshaug et al., 1994). While the formation of a stark pycnocline initially enhances primary productivity by stabilising the nutrient and light-rich surface waters, the combination with nutrient depletion reduces productivity in the ArW zone after the initial bloom period.

Overall, annual primary productivity increases southwards into the Atlantic domain and does not exhibit the same spatial or temporal limitation as the ArW region (Falk-Petersen et al., 2000). Therefore, under a modest climate change scenario, primary productivity in the Barents Sea is predicted to increase by an average of 8%, along with a modelled 1^{o}C warming of AW inflow over the next 50 years (Ellingsen et al., 2008). Crucially, the majority of this average rise in productivity is accounted for by the northern regions (Cochrane et al., 2009), associated with an increase in the areal extent of the more productive AW due to Atlantification, anthropogenically induced warming and associated sea ice retreat. These changes will have important implications for biogeochemical dynamics in the region from both an ecological and economic perspective.

Sedimentation and export production

It is estimated that 40-96% of total Barents Sea primary production (and 75% of the 'new' production) is delivered to the seafloor, dependent upon bloom composition, mixing dynamics and the water mass regime (Carmack and Wassmann, 2006; Cochrane et al.,

2009; Sakshaug et al., 1994; Wassmann et al., 1990). Reigstad et al. (2008) estimate that on average 36% of daily Barents Sea primary production along a 30^{o}E transect is exported as particulate organic carbon (POC) to 90 m depth, but export efficiencies up to 72% were observed at an ice free site strongly influenced by wind mixing, as well as at the PF. This represents a significant proportion given global estimates of export efficiency (i.e. transport of organic matter out of the euphotic zone) range between 10-40% (Eppley and Peterson, 1979; Henson et al., 2011), while Emerson and Hedges (2003) suggest that globally 90% of POC that exists in the euphotic zone is remineralised in the water column. The Barents Sea therefore has a much higher export efficiency than the Central Arctic Ocean, which averages 30% annually (Henson et al., 2015). This has important climatic implications. High levels of primary and export production act to reduce the summer partial pressure of CO_2 in the Barents Sea (Smedsrud et al., 2013). When coupled with efficient deep water formation in the region, the uptake density of CO_2 is estimated at 29-51 gC m^{-2} yr^{-1} (Smedsrud et al., 2013), which dwarfs the global average of 4 gC m^{-2} yr^{-1} (Takahashi et al., 2009).

Wassmann and Olli (2004) found that an extraordinarily high vertical POC flux at shallower depths (30-40 m, 2000 mgC m^{-2} d^{-1}) in late spring in the Barents Sea corresponded to a flux of 250-500 mgC m^{-2} d^{-1} below 200 m depth in both the ArW (MIZ) and AW domains. This value remained high over summer, reaching 260 mgC m^{-2} d^{-1} south of the PF (Wassmann and Olli, 2004). This flux at depth is comparable to strong coastal upwelling zones and is higher than most other shelf and coastal seas globally (Peña et al., 1999; Romero et al., 2000) and supports the hypothesis that regions with seasonal ice coverage are 'hot-spots' for carbon export and a potentially significant sink for CO_2. As a result, the consequences of future climate perturbations, such as warming and sea ice retreat could ripple into the carbon cycle and the extent to which the Barents Sea and Arctic Ocean can uptake anthropogenic carbon from the atmosphere.

As with most Barents Sea parameters, the magnitude of POC export fluctuates on both spatial and multiple temporal scales. Wassmann et al. (1999) suggests that POC export flux from the surface in the AW domain is 60-70 mgC m^{-2} d^{-1} and 20-50 mgC m^{-2} d^{-1} in the ArW domain, with very little deviation with water depth in early March (pre bloom). At the beginning of spring, high nutrient low chlorophyll (HNLC) conditions are ubiquitous throughout the Barents Sea region; as a result surface fluxes are driven by residual organic material from late-winter productivity (Wassmann and Olli, 2004). Wassmann and Olli (2004) found that in late spring-early summer under bloom conditions, vertical POC fluxes ranged from 300-1500 mgC m^{-2} d^{-1}, with a strong influence from water depth, correlating strongly to the degree of stratification. During these weeks, ArW sites displayed exports of >500 mgC m^{-2} d^{-1} within the pycnocline and a rapid decline in export efficiency at greater depth, while the depths of higher export (>500 mgC m^{-2} d^{-1}) in the AW extended at times to 90 m below the surface. Despite this contrast at moderate depths, near the

sediment-water interface flux magnitudes were almost indistinguishable in both realms (250-500 mgC m^{-2} d^{-1}) (Wassmann and Olli, 2004). Sites close to the PF in the same time period presented with lower POC flux magnitudes at shallow depths (700 mgC m^{-2} d^{-1}), yet unlike the other sites showed minimal attenuation with depth (Wassmann and Olli, 2004) and thus a higher flux to the sediment surface. This efficiency is attributed to physical mixing dynamics of frontal systems, which drive efficient delivery of POC to depth. In the late summer months (post bloom), export rates decreased but remained high and were greater under AW as compared to the ArW sites (100-400 mgC m^{-2} d^{-1} and 150 mgC m^{-2} d^{-1} respectively) (Wassmann and Olli, 2004) (Fig. A.5). For context, the highest surface POC export rates observed on the highly productive Chukchi Sea shelf and in the central Arctic Ocean during a transect study by Moran et al. (1997) were 450 and 85 mgC m^{-2} d^{-1} respectively.

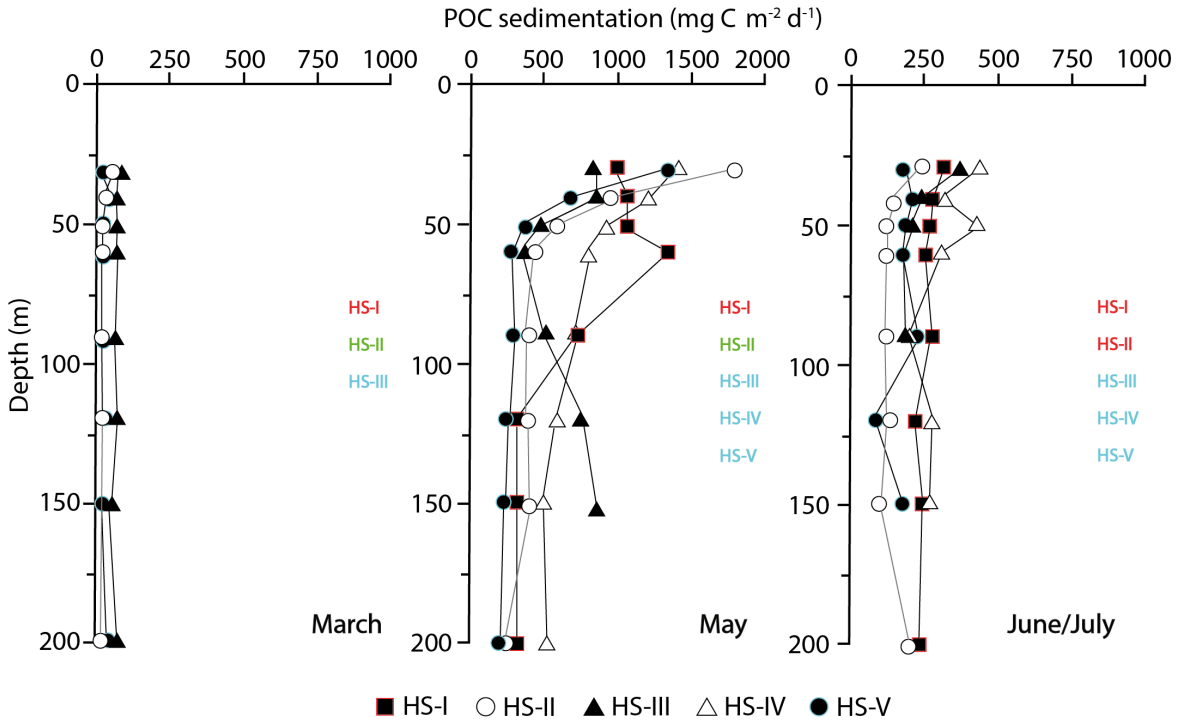

Figure A.5: Profiles of POC flux from the central Barents Sea measured over 24 hours using sediment traps over three cruises: March and May 1998 and June/July 1999. Measurements were taken along a north-south transect between 70-79°N and 30-34°E. Coloured site names within sub-figures denote the dominant water-mass domain in which the trap was located (red = AW, blue = ArW, green = PF), as each cruise transect differed but the same site names were appointed. Site HS-II during the May cruise was defined as the PF, AW domain. Fig. adapted from Wassmann and Olli (2004), domain category obtained from Olli et al. (2002b).

The composition of the POC may explain some of the spatial variability in export efficiencies observed across the Barents Sea shelf. Sites adjacent to Bear Island indicate that the POC derived from phytodetritus and their aggregates sink rapidly in the benthic boundary layer at a velocity of 0.7-1.0 cm s^{-1} (Thomsen and Graf, 1994; Thomsen et al.,

1994). This observation is significant considering an individual plankton may sink only a few metres per day (Riser et al., 2007)). Furthermore, Olli et al. (2002b) observed that 40% of sinking POC in the Barents Sea was composed of faecal pellets, and the rapidly sinking gelatinous algal species *P.Pouchetii* tends to dominate under nutrient replenished conditions (Sakshaug, 1997). Pellets along with diatom frustules and aggregates constitute the 'fast sinking' portion of POC globally, which can exceed 50-150 m day^{-1} (Iversen and Ploug, 2013; Riser et al., 2007; Wassmann et al., 2006b). Although Wiedmann et al. (2016) observed POC sinking rates up to 15.7 m s^{-1} at 60 m depth (6 m s^{-1} during the spring bloom) in Autumn at Adventfjorden off the west coast of Svalbard. These sinking velocities could potentially justify the efficiency at which the Barents Sea appears to ferry its carbon to depth.

Export efficiencies can also be modulated by grazing pressures by zooplankton, as well as physical mixing dynamics and POC composition. Grazing pressures along with POC fluxes show a disparity between the ArW and AW domains. Efficient grazing and thus low sedimentation of bloom products relies upon a matching of the zooplankton and phytoplankton blooms (Wassmann et al., 1990). South of the PF in the AW domain, phytoplankton blooms typically form in May-June, as the thermocline required to stabalise the surface layers is slow to form. A late forming bloom of long duration is ideal for zooplankton as it increases the probability that stock peaks between trophic levels will coincide (Bmstedt et al., 1991). As a result, in this region grazing pressure is typically high, which should reduce export efficiency and delivery to the sediment surface. North of the polar front however, it is thought that grazing pressure is lower on account of lower zooplankton stocks and rapid bloom development, thereby enhancing the sedimentation of organic matter (Sakshaug, 1997). However, Wassmann and Olli (2004) find that POC flux in late spring (post bloom) is equally high in both the MIZ and in the AW region. Given these findings, coupled with the observation that the majority of sinking organic material under bloom conditions is intact phytoplankton, it could be that grazing pressure under bloom conditions are similar across the two domains, with zooplankton struggling to cope with the high carbon production rates (Knies and Martinez, 2009; Wassmann et al., 2006a).

A.4 Benthic processes

Shelf sediments are particularly important for global biogeochemical cycling of nutrients. Despite representing just 8.6% of the global seafloor (Jørgensen, 1982), shelf sediments account for >80% of POC burial (Sarmiento and Gruber, 2006) and >55% of total sediment oxygen uptake (TSOC) (Thullner et al., 2009), used as an proxy for total organic carbon (TOC) remineralisation rates. However, shelf environments in the Arctic are undergoing significant and rapid changes in atmospheric processes, sea ice cover and water

mass characteristics. The contrast in environmental and ecological parameters between the northern and southern regions of the Barents Sea coupled with its year round accessibility (Smedsrud et al., 2013) and the well documented rapid sea ice retreat and Atlantification make for a unique natural laboratory for the study of sedimentary processes and their sensitivity to change. The influence of Atlantification on surface and pelagic processes is receiving increasingly more attention, but little is known of the potential impact on the benthic realm. This knowledge gap is critical, as these changes have cascading yet poorly constrained effects, which could have important implications for regional organic matter burial and nutrient recycling.

A.4.1 Pelagic-benthic coupling

A connection of the pelagic and benthic realms is referred to as coupling, whereby the order of the wording should denote the predominate direction of transfer. In the case of pelagic-benthic coupling, POC from surface ocean primary production flux towards the benthos and result in remineralisation and thus benthic productivity (Renaud et al., 2008b). Particularly strong, or 'tight' coupling occurs in regions where interference in the pelagial from zooplankton is minimal and sinking of material is rapid (e.g. during the spring bloom), delivering abundant POC to the SWI. A general paradigm exists for Arctic shelf sediments- that they are some of the most tightly coupled globally, due to a general mismatching of phyto and zooplankton blooms, as well as low water temperatures and high sinking velocities (Renaud et al., 2008a).

The suggestion that seasonally ice covered shelf regions are potential 'hot spots' for carbon burial and the sequestration of atmospheric CO_2 is driven by this tight coupling. Evidence for this is bolstered by work from Reigstad et al. (2011) and Kedra et al. (2013), demonstrating that despite present dissimilarities in benthic and pelagic community structures and productivities both north and south of the PF and between troughs and banks, 'permanent' carbon burial rates in the Barents Sea are relatively constant (19 $\pm$5 mgC m^{-2} d^{-1} or 7 gC m^{-2} yr^{-1}). This is found to be the case regardless of bloom phase or locality (Kedra et al., 2013; Reigstad et al., 2011), as while benthic secondary productivity can exceed 70 gC m^{-2} yr^{-1} (Kedra et al., 2013) on shallow banks, a mean demand of 0.5 gC m^{-2} yr^{-1} (Sakshaug et al., 1994) is similar to the POC flux below 200 m water depth in late spring.

However, analysis of carbon burial in sites previously analysed for POC remineralisation rates by Nickel et al. (2008); Vandieken et al. (2006b) lead to a different conclusion. Carbon burial in these sediments was found to be highest in troughs (Hopen Trench and Storfjorden), exceeding 7 mgC m^{-2} d^{-1}, while on shallow banks carbon burial was much lower, averaging 5.5 mgC m^{-2} d^{-1}, for a total range of 3.7-8.5 mgC m^{-2} d^{-1} (Carroll et al., 2008b). These datasets suggest a significant spatial heterogeneity in POC burial below the surface sediment (upper 10 cm), dependent not necessarily upon the water

mass regime or surface primary productivity, but instead on sedimentary features. Carroll et al. (2008b) suggest that while distance to the seafloor usually has a significant impact on burial efficiency, in the Barents Sea the complex topographic features have resulted in a hydrodynamic sorting of sediment, whereby finer sediments in the troughs have a greater affinity for carbon through sorption onto clay minerals. In contrast, higher energy, coarser sediment deposits of the north have a reduced capacity for permanent carbon burial deeper in the sediment. Carbon preservation at depth appears to be driven by physical processes (sedimentation rates, sediment type etc.), regardless of high surface productivities and surface carbon concentrations (Steinsund and Hald, 1994).

The origin and nature of the deposited POC is equally relevant to the importance of Arctic shelves as carbon sinks, due to the significant influence on benthic communities and metabolisms. Generally, marine sediments are composed of both terrestrially-derived organic matter (TOM) (from aeolian, fluvial, coastal erosion sources) and marine organic matter (MOM) in proportions that depend upon locality and the physical environment. TOM represents an older (pre-aged) POC fraction, which has previously been exposed to diagenetic reworking and remineralisation and thus can be considered a more refractory carbon pool (Hedges and Keil, 1995; Pathirana et al., 2014) relative to the fresher MOM derived from surface primary productivity.

It is common for Arctic sea ice to hold significant volumes of terrestrial material (Vinje and Kvambek, 1991), which is transported by fluvial systems to the Siberian and Laptev shelves (northeast of the Barents Sea). Sea ice formation in these regions then incorporates the terrestrial material and transports it southwards on the Transpolar Drift Stream and through the Fram Srait. Tamelander et al. (2008) and Wassmann and Olli (2004) note that of the material collected in sediment traps left beneath multi-year ice north of Svalbard in the Nansen Basin and in the northernmost BSB, TOM is the most important contributor to the POC flux. However, Holocene temporal scale (0-11 kyr) studies of central Barents Sea sediments estimate a TOM fraction of $\sim$5% (Carroll et al., 2008b) and often TOM is assumed negligible in the Barents Sea, given that fluvial input is low relative to other Arctic shelf seas and the majority of sea ice is first-year and thus assumed to be low in TOM (Pavlov et al., 2004; Tamelander et al., 2008). However, estimates for upper surface sediments across the Barents Sea suggest that on average 30% of TOC could be derived from terrestrial sources (Vetrov and Romankevich, 2004). Therefore, while on a site-specific scale TOM input may be negligible, for regional estimates (e.g. for carbon burial (Carroll et al., 2008b)) it could be assumed that between 0-30% of TOC is terrestrial. This is a conservative estimate, given that while previous studies (Knies and Martinez, 2009; Pathirana et al., 2014) have reproduced the estimates of Vetrov and Romankevich (2004) for AW sites, seasonally ice-covered regions close to the PF can present with TOM fraction of >50% of TOC, with an even greater proportion present in sediments of Svalbard fjords (Andreassen et al., 1996). However, it is recognised that the influence of TOM decreases

sharply with distance from shore and thus more distal sites will receive minor amounts of TOM.

The future balance of TOM/MOM delivery to the Arctic seafloor could have significant implications for benthic biogeochemical dynamics and rates of carbon oxidation in the sediments and should therefore be taken into account when considering organic matter degradation. Future work should focus on how these proportions may change, given the projected impacts of Atlantification and the greater proportion of MOM south of the PF. Theoretically, delivery of more labile compounds to the BSB over time would increase POC oxidation rates in favour of sulphate reduction as the predominant terminal electron acceptor (TEA) pathway (see section A.4.3).

A.4.2 Ecosystem

The distribution benthic organisms in the Barents Sea seafloor is highly dependent on the water mass regime (AW, ArW, PF/MIZ), ice-cover and primary productivity (Cochrane et al., 2009). The most diverse and prosperous communities are generally found in the fjords and coastal regions of Norway and Svalbard, where macrobenthic biomass densities ordinarily reach 1.5-2 kg m^{-2} (Kulakov et al., 2006). Kelp forests and coral reefs thrive here and provide a habitat for a rich diversity of species (ICES, 2008). Sediment within the troughs and deeper segments of the central Barents Sea are composed of fine sandy muds (Ivanov, 2011), wherein polychaetes dominate the benthic infauna (ICES, 2008) and detrital feeding echinoderms (mainly sea cucumbers) are also common (ICES, 2016). Filter feeding sponges prevail in the southwest regions close to the BSO, where macrobenthic biomass densities do not exceed 25 g m^{-2} (Kulakov et al., 2006). Whereas, on shallow banks (e.g. Great, Central and Spitsbergen) the sediment is composed of coarser sand (Ivanov, 2011) and gravels on account of higher energy current action. Here, predatory echinoderms (anemones and starfish) live alongside a great number of filter feeders (sea cucumbers, bivalves) (ICES, 2008) with an average biomass density of $\sim$300 g m^{-2} (Kulakov et al., 2006).

Carroll et al. (2008b), Cochrane et al. (2009) and Grebmeier et al. (1988) all observe higher benthic faunal densities and taxon richness underneath the PF, relative to the ArW and AW regions, especially in the western Barents Sea where the PF is stabilised by bathymetry. This phenomena is thought to be driven by tighter pelagic-benthic coupling delivering higher quality POC under intense physical mixing regimes. Average annual benthic secondary production in the Barents Sea is estimated as 0.5 gC m^{-2} yr^{-1} (Sakshaug, 1997), but can reach as high as 70 gC m^{-2} yr^{-1} on banks and in the MIZ (Kedra et al., 2013). This increase in productivity under the MIZ is attributed to the large pulse of food supplied to the sediment surface during the spring bloom (ICES, 2008). However, given that the MIZ locality is not ubiquitous year on year, especially in the eastern BSB, where the PF has a tendency to wander hundreds of kilometres, the organisms here must

be resilient to regular food shortages. Another suggestion as to the effect of the MIZ on benthic faunal abundance is that, rather than the increase being driven by pelagic productivity, it is instead a result of increased food quality on account of tighter pelagic-benthic coupling under bloom conditions (Carmack and Wassmann, 2006; Wassmann and Olli, 2004).

Given that the pelagic realm south of the PF is characterised by a higher annual primary productivity (Cochrane et al., 2009), benthic organisms are generally supplied with one large influx of food at the demise of the spring bloom, followed by more regular (albeit much smaller) 'meals' over their summer growth season (Sakshaug, 1997). In contrast, ecosystems north of the PF are typically food-limited, relying on short pulses of organic material delivered to the seafloor just once a year as the receeding MIZ productivity window passes overhead (Cochrane et al., 2009). Therefore, as would be expected, benthic community structure differs across the PF.

It is generally accepted that the Barents Sea is separated into two 'biocenoses', representing a northern and a central/southern grouping (Zenkevich, 1963). The biomass of the northern group is reported to be dominated by echinoderms then molluscs with some influence from polychaetes and other species. In contrast, the southern biocenosis can be dominated in equal proportion by echinoderms, molluscs and polychaetes with even less influence from crustaceans and other species (Zenkevich, 1963), but more often than not the dominant fauna is polychaetes (Cochrane et al., 2009). Therefore, the north-south divide in biodiversity is not a stark contrast in species, but instead presents itself in the balance of faunal abundance and 'evenness' in community structure (Cochrane et al., 2009). Food limitation in the northern region exhibits a higher evenness and lower abundance, while the macrobenthos of the more productive AW (central and southern) region present with higher abundance and a tendency for dominance by a particular species (Cochrane et al., 2009). This response by the benthos of a tendency towards dominance and increased abundance with food supply is widespread and is reported in lower latitude communities, although for larger contrasts in food supply than is seen across the PF (Cochrane et al., 2009; Pearson and Rosenberg, 1978). Cochrane et al. (2009) found that although faunal composition in communities differed in terms of their abundance between the northern and southern regions, they found no 'typical' Arctic or Atlantic fauna- each fauna was present in both domains. Although, given the typical dominance and abundance of polychaetes in AW sediments, further expansion of the southern biocenosis could reasonably be expected under future climate change scenarios and with Atlantification.

However, while an increased POC flux to the seafloor may arise due to an increase in the area of open ocean over time, Grebmeier et al. (2006) note an alternative regime shift in the Bering Sea that could be a foreshadow of change for other Arctic shelf seas. The Bering Sea has seen significant warming of 0.5-2.0^{o}C since the late 1970s (Grebmeier et al., 2006), which has resulted in notable changes to biogeochemical cycling and community

structure. This regime shift has led the Bering Sea from a 'typical' Arctic environment consisting of low standing stocks of zooplankton, wherein a large proportion of energy is processed by the benthos, to a system dominated more by pelagic processes (Cochrane et al., 2009; Renaud et al., 2008a). This system no longer follows the well-documented positive correlation in the Arctic of organic matter delivery and benthic biomass, as well as the observation that the highest benthic biomasses are associated with ice-free regions (Carroll et al., 2008b; Grebmeier et al., 1988). Instead, this system has reduced benthic biomass as a result of lower phytoplankton stocks and concomitant weakened pelagic-benthic coupling (Cochrane et al., 2009) (i.e. a transfer from pelagic productivity to benthic respiration), which is ordinarily notably strong on Arctic shelves (Renaud et al., 2008b). Grazing activity has increased as a result of reduced ice cover in the Bering Sea, just as in the Chukchi Sea (Lalande et al., 2007), which ultimately has led to a reduction in economically relevant fish stocks that feed on macrobenthic organisms, a lower benthic biomass and importantly a lower uptake of carbon by the sediment (Grebmeier et al., 2006). It is unclear as to whether future changes in the Barents Sea will reflect those that occur on the Bering Shelf, however if they were to, changes to the benthos in terms of biogeochemical dynamics and community structure may not be as simple as an increase in the areal extent of the central/southern faunal grouping.

A.4.3 Sediment biogeochemistry

Ocean sediments are vital for the cycling of ecologically important chemical species. The deposition of POC on the seafloor drives a complex and dynamic reaction network that forces POC into the dissolved phase through a series of degradation pathways, thereby recycling nutrients and ultimately producing dissolved organic carbon (DOC). Concentration gradients form between the sediment and bottom waters as a result of these processes, forming diffusive gradients across the sediment-water interface. The resulting molecular diffusion, as well as contributions from advection and biological process (e.g. bioirrigation and bioturbation) result in benthic fluxes, which deliver solutes (e.g. macro/micro nutrients and alkalinity) back to the water column. This process couples the pelagic and benthic realms, directly influencing pH, carbon and nutrient cycling.

The degradation of POC during burial relies on a plethora of different bacterial functional groups and metabolisms. Heterotrophic microbes utilise the POC to obtain energy from it through the transfer of electrons from an electron donor (POC in this case) to a terminal electron acceptor (TEA). In theory, these reactions are not simultaneous and instead follow a sequential pattern with depth ($O_{2(aq)}$, $NO_3{}^-{}_{(aq)}$, $Fe(III)_{(s)}$, $Mn(IV)_{(s)}$, $SO_4{}^{2-}{}_{(aq)}$ and finally methanogenesis, where there is a complete absence of external oxidants, i.e. electron transfer is between POC compounds) determined by the standard free energy yield of each reaction pathway, with more exergonic reactions (per mole electrons transferred) taking precedence (LaRowe and Van Cappellen, 2011) (Fig. A.6, Table A.4).

It is assumed that each reaction pathway will occur until the substrate or TEA is no longer available, or has reached a limiting concentration, whereby the following degradation pathway becomes favourable (Van Cappellen and Wang, 1996). In reality these redox zones can overlap spatially, as they have in the Barents Sea (Kostka et al., 1999; Nickel et al., 2008; Vandieken et al., 2006a) and on temperate shelf seas due to a variable POC and TEA substrate supply and reactivity (Canfield et al., 1993b). In the deep ocean (>1000 m water depth), up to 90-95% of organic carbon remineralisation in sediments is through aerobic respiration, whereas in the neritic zone (≤200 m), the aerobic layer is very thin (a few mm) (Jørgensen, 1982; Monien et al., 2014).

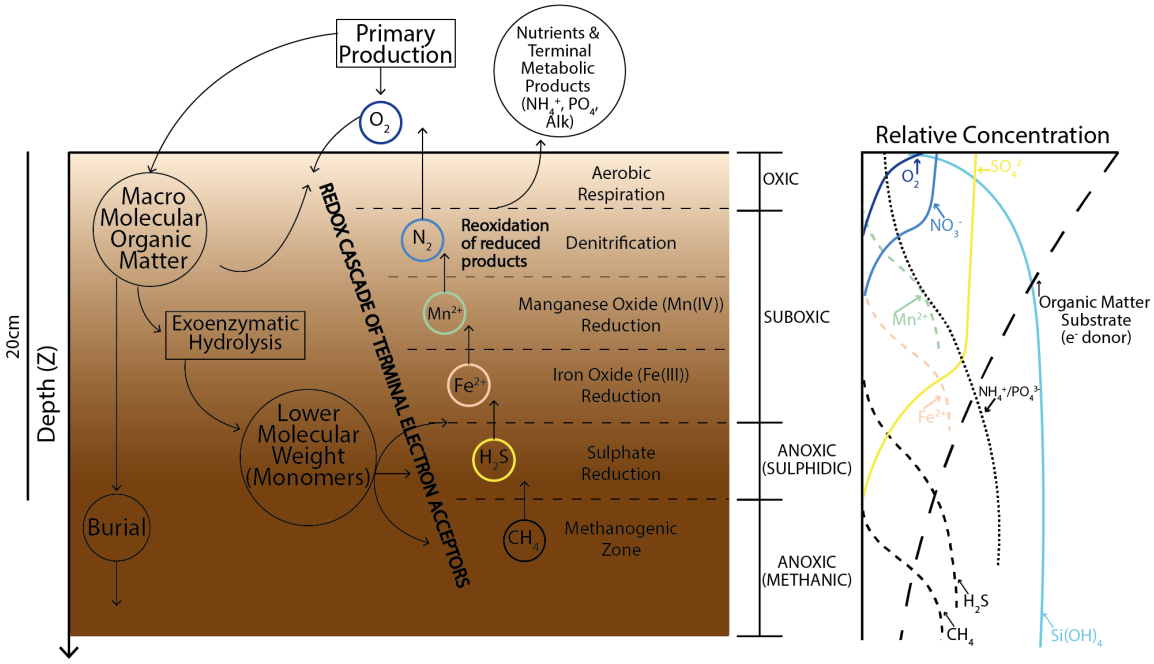

Figure A.6: Idealised organic carbon early diagenesis schematic, showing the sequence of hydrolysis and metabolic reactions involved in the degradation of organic matter in marine sediments and the concentration gradients that form as a result of those processes.

Sulphate reduction (SR) is therefore the most important process on continental shelves, accounting for 25-50% of the TOC oxidation rate on average (Jørgensen, 1982; Thullner et al., 2009), which reduces the relative global importance of aerobic respiration to 65% (Emerson and Hedges, 2003). This proportion is debated, with model-based estimates suggesting that O_2 accounts for just 15% of global carbon mineralisation, with 76% from SR (Thullner et al., 2009) (Fig. A.8). The combination of a thin oxic layer and high average sedimentation rates (15 cm kyr^{-1}) on shelves relative to the deep ocean (<3 cm kyr^{-1}, Emerson and Hedges (2003)) allows for the activation of anaerobic pathways in their sediments. The importance of this in relation to sediment pore water chemistry, is that shelf environments are able to recycle and flux a wider variety of solutes into the water column and so more readily impact the cycling of important micronutrients, such as iron

Table A.4: Pathways of organic matter oxidation and their respective Gibbs free energy yields (ΔG^0) per mole of organic carbon oxidised (Sarmiento and Gruber, 2006; Schulz et al., 2000). The stoichiometry of these reactions are different to those of Anderson (1995) or Thullner et al. (2009), as they involve a more complex mixture of organic compounds. For simplicity, CH_2O here refers to sucrose. Free energy changes for degradation reactions are given as per mole CH_2O (ΔG^0 at 25^oc) from (Morel and Hering, 1993).

Reaction	Stoichiometry	ΔG^0 (kJ mol^{-1})
(1) Aerobic Respiration	$CH_2O + O_2 \longrightarrow CO_2 + H_2O$	-476
(2) Denitrification	$5\,CH_2O + 4\,NO_3^- \longrightarrow 2\,N_2 + 4\,HCO_3^- + CO_2 + 3\,H_2O$	-452
(3) Manganese Oxide Reduction	$CH_2O + 3\,CO_2 + H_2O + 2\,MnO_2 \longrightarrow 2\,Mn^{2+} + 4\,HCO_3^-$	-388
(4) Iron Oxide Reduction	$CH_2O + 7\,CO_2 + 4\,Fe(OH)_3 \longrightarrow 4\,Fe^{2+} + 8\,HCO_3^- + 3\,H_2O$	-187
(5) Sulphate Reduction	$2\,CH_2O + SO_4^{2-} \longrightarrow H_2S + 2\,HCO_3^-$	-82
(6) Methane Fermentation (Methanogenesis)	$2\,CH_2O \longrightarrow CO_2 + CH_4$	-71

(Fe) and manganese (Mn). For example, while contributing a 'negligible' portion of global POC mineralisation (1-3%) in both model (Thullner et al., 2009) and observational-based estimates (Sarmiento and Gruber, 2006) (Fig. A.8), shelf sediments account for 84% of global Fe oxide reduction (Thullner et al., 2009) and thus this domain is critical for Fe cycling.

Total organic carbon

Organic carbon drives a complex reaction network, which results in the fluxing of ecologically relevant solutes back in to the water column. However, the flux magnitude and TOC content of the sediment has a significant impact on the relative importance of individual TEA pathways and total carbon remineralisation rates. Thus, the magnitude of POC delivery can in part modulate which solutes are fluxed across the SWI.

Sites north (south) of the Barents Sea PF are generally lower (higher) in TOC, inferring that seasonal ice cover limits the time a site is under open water conditions, thereby reducing annual POC deposition fluxes (Cochrane et al., 2009; Nickel et al., 2008; Vandieken et al., 2006a,b). As a result of the higher TOC content, TSOC both south of the PF and west of Svalbard exhibit higher values relative to the ArW-influenced eastern fjords and in open water sediments north of the PF (Table A.5). This is true of all inflow shelves of the Arctic Ocean (including Bering and Chukchi), which present with TSOC rates of ∼11.8 mmol m^{-2} d^{-1}, the highest of which were observed in the Barents Sea in an Arctic-wide data compilation by Bourgeois et al. (2017) (Fig. A.7). This TSOC value is more than two-fold greater than both outflow (e.g. Greenland) and interior (e.g Laptev and Kara)

shelf seas, mean published values for which are 3.9 mmol m^{-2} d^{-1} and 6.2 mmol m^{-2} d^{-1} respectively (Bourgeois et al., 2017) (Fig. A.7). This observation is mainly due to higher annual primary productivities driven by the largest average open water areas and the influx of nutrient-rich waters (Pacific/Atlantic) (Bourgeois et al., 2017). Vandieken et al. (2006b) therefore suggest that Atlantification of the BSB should increase the mean carbon content of sediments by increasing the duration of the open water season across the region and driving a modelled 8% increase in average primary productivity (Ellingsen et al., 2008). However, work by Pathirana et al. (2014) yields an alternative conclusion. They suggest that a retreating MIZ will in fact reduce carbon storage capacity of Barents Sea sediments, evidenced by higher TOC contents currently found across the PF (Knies and Martinez, 2009) (Fig. 4.14) and higher modelled TOC across ArW sediments (1.8-3 wt% and 0.2-1.8 wt% in the ArW and AW region respectively). These conclusions are antithetical and would have considerable and inverse effects on sediment biogeochemical dynamics in the region.

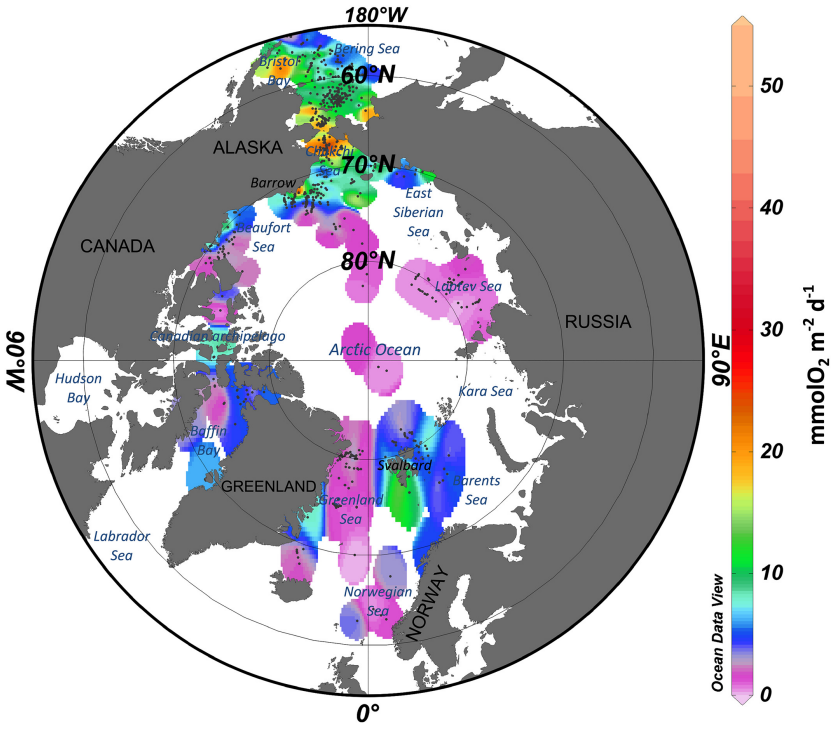

Figure A.7: Pan-Arctic Ocean compilation of total sediment oxygen consumption (TSOC) rates from Bourgeois et al. (2017). Interpolation carried out using weighted-average gridding method. Black crosses are station localities, extracted from 30 publications and 16 databases- Bourgeois et al. (2017) and references therein.

Fig. 4.14 presents a compilation of available TOC data for the Barents Sea, suggesting that the contrast in conclusions discussed above could be an artefact of both nomenclature and primary productivity estimates. Pathirana et al. (2014) and Knies and Martinez (2009) define the PF as the MIZ, suggesting that the highest Barents Sea productivities are observed across this boundary as modelled by Steinsund and Hald (1994). The data

compilation is consistent with this assumption, in that the highest TOC contents trace the PF. However, analysis of POC fluxes indicate that under bloom conditions, the PF presents with a flux of 700 mgC m^{-2} d^{-1} at the surface, while the highest values were in fact north of this in the retreating MIZ, with a flux of >1500 mgC m^{-2} d^{-1}. This highlights that, while on a decadal scale the PF represents the mean sea ice extent, these boundaries do not invariably coincide (Slagstad and Stokke, 1994; Wassmann and Olli, 2004). Furthermore, Wassmann and Olli (2004) calculate very little attenuation of POC sinking fluxes with depth at the PF sites. This is on account of efficient physical mixing dynamics, therefore while primary productivity may have been reduced in the upper water column relative to the MIZ, POC retention and reworking increased on account of the well developed pycnoclines both north and south of the PF. Perhaps then, the heightened TOC observed under PF sites could in fact be a consequence of the physical mixing dynamics, rather than heightened surface productivity, given that below 250 m POC fluxes were indistinguishable in both the AW and ArW (MIZ) zones (Wassmann and Olli, 2004). This is consistent with Cochrane et al. (2009), who found that stations underneath the Barents Sea PF presented with the highest macrofaunal abundances, despite a reduced water column productivity realtive to north and south of the front. They hypothesise that it is not necessarily a high pelagic producticity that supports benthic communities, but rather the higher quality of food transported to the SWI under PF and MIZ regimes. Furthermore, Pathirana et al. (2014) recognise that their modelled primary productivity is significantly lower than estimates found in the literature.

Estimates of primary productivity from observations and ocean-ecosystem modelling range between 100-200 gC m^{-2} yr^{-1} south of the PF and <70-90 gC m^{-2} yr^{-1} in an ArW regime (Ellingsen et al., 2008; Sakshaug, 1997; Sakshaug et al., 1994; Wassmann et al., 2010). Coupled with comparable export efficiencies at 250 m depth under bloom conditions and over winter in both regions, as well as a higher export efficiency under AW conditions over summer (Wassmann and Olli, 2004), TOC contents should theoretically be higher in the southern Barents Sea. Contrary to this, primary productivites modelled by Pathirana et al. (2014) that were back-calculated from deposited material predict higher rates in the north (90 gC m^{-2} yr^{-1}) than the south (<50 gC m^{-2} yr^{-1}), likely due to contrasting modelling techniques compared with similar previous studies.

To conclude, it is recognised then that the PF region represents a zone of high POC export efficiency. However, there are two schools of thought as to whether a northward migration of the MIZ and PF will increase or decrease sediment TOC. Under a Pathirana et al. (2014) and Knies and Martinez (2009) regime, this retreat would represent an expansion of the lower productivity AW zone, contrary to the consensus that the AW region is more productive overall due to the factors discussed in section A.3.3. Barents Sea primary production has increased since 1998, with some studies suggesting an increase of 20% between 1998-2009 with the increasing area of open water (Arrigo and Van Dijken,

2011) and another suggesting it doubled between 1998 and 2017 (Dalpadado et al., 2020), however Wassmann and Reigstad (2011) still predict a longer-term decline in southern Barents Sea primary productivity. They suggest that an increase in primary productivity and POC flux to the seafloor is expected in regions where conditions are evolving from having multi-year and seasonal sea ice cover to longer stints that are ice free (e.g. the northern Barents Sea). Whereas, increased thermal stratification in year-round ice-free regions (e.g. the southern Barents Sea) could inhibit nutrient replenishment resulting from the passing of polar lows, thereby reducing POC delivery and benthic TSOC as a result (Bourgeois et al., 2017; Wassmann and Reigstad, 2011). These hypotheses suggest that while a reduction in sea ice cover could initially increase TSOC rates (for the wider Arctic Ocean, as well as the Barents Sea), a longer-term decline could decrease POC delivery to the seafloor (Bourgeois et al., 2017).

Iron-manganese reduction

Both iron and manganese can be used by bacteria to breakdown organic matter within seafloor sediments during respiration (Table A.4). However, trace metal reduction is considered negligible in a global ocean carbon remineralisation rate context, largely due to a ubiquitously low concentration of solid metals. Not only that, but also because bacteria have to compete with abiotic pathways as oxidised and reduced metals can react spontaneously with a plethora of chemical-compounds (Nickel et al., 2008). Dissimilatory Fe and Mn reduction (DIR and DMR respectively) are estimated to contribute just 1-3% collectively to total POC remineralisation in marine sediments (Sarmiento and Gruber, 2006; Thullner et al., 2009).

A global data compilation put together in this study (Table A.5), indicates that DMR is insignificant at all sites except for two: the deepest Skaggerak station (S9) and the Panama Basin (PB). The common factor enabling DMR to contribute almost 100% of POC oxidation rates is the solid phase oxide concentration (Aller, 1990; Aller et al., 1986; Canfield et al., 1993b). DMR is only influential in specific locations as most sites present with <20 μmol Mn cm^{-3} to a maximum sediment depth of 2 cm. However, at PB and S9 labile oxides (Fe and Mn) are found as deep as 10 cm and in concentrations of 200-600 μmol cm^{-3}.

The depositional environments required to achieve such high concentrations are relatively unique: the Panama Basin oxides are of hydrothermal provenance, while the Skaggerak is referred to as a sink for reduced Mn released by sediments in the Baltic Sea (Canfield et al., 1993b; Thamdrup and Canfield, 1996). Sedimentation of metal oxides is not sufficient to sustain organotrophic metal reduction alone (Nickel et al., 2008). Burial of oxides drives <1% of POC oxidation (Canfield et al., 1993b; Thamdrup and Canfield, 2000), therefore sediment mixing must occur to maintain the high concentration of metals through reoxidation of their reduced products (Fe^{2+} and Mn^{2+}), either through physical

processes (e.g. periodic resuspension on the Amazon shelf) or more commonly through macrofaunal activity (e.g. biomixing/bioturbation and burrow flushing/bioirrigation at station S9). The coupling of these transport and redox processes can result in any particular cation being cycled 8-10 times on average, with the potential for 100 cycles before its permanent burial or transport back to the water column (Canfield et al., 1993b; Thullner et al., 2009). In the case of Mn, turnover times vary in the region of a few days to weeks (Thamdrup and Canfield, 2000). Fe cycling is slower, occurring on a 70-300 day timescale (Canfield et al., 1993b; Thamdrup and Canfield, 2000), but in certain environments physical mixing and subsequent reoxidation (recycling) is sufficient to support Fe oxides as a predominant TEA. Electron fluxes driven by periodic reoxidation far outweigh the TEA capacity of the metal when initially deposited (Van Cappellen and Wang, 1996). Not only does mixing induce organotrophic metal reduction through reoxidation, but also transports younger, more labile POC compounds to depth, further energising anaerobic pathways of mineralisation.

DIR is unquestionably more influential for POC mineralisation on a global scale than DMR, the rates of which are consistently an order of magnitude lower. Site-specific contributions range between 12-70% for a range of continental shelf sediments and environments (Thamdrup and Canfield, 2000), while it is estimated that for global shelves (<350 m water depth), the average DIR contribution is 17% (22% of anaerobic respiration) (Nickel et al., 2008; Thamdrup and Canfield, 2000) (Fig. A.8, Table A.5). 86% of global reactive Fe oxide deposition occurs on continental shelves in larger quantities than those of Mn oxides. In a similar fashion to the limiting Mn oxide concentration for DMR ($\sim$20 μmol cm^{-3}), rates of DIR are thought to increase with the concentration of labile, poorly crystalline Fe(III) oxides (Canfield et al., 1993b; Thamdrup and Canfield, 1996, 2000), which is supported through mixing and periodic reoxidation. <1% of global shelf POC mineralisation was accounted for by DIR in a model-based estimate by Thullner et al. (2009), which is significantly less than that derived from laboratory studies (Thamdrup and Canfield, 2000). However the significance of this value is uncertain, with Thullner et al. (2009) suggesting that the global mean contribution of DMR/DIR to shelf mineralisation may be low due to a lack of available data on labile oxide deposition, and that considerable contributions of DIR/DMR could be provincial in nature.

As bioturbation is the primary mechanism for sediment mixing and turnover in most sites where metal reduction is prominent, the efficiency of such reduction is dependent upon parameters that influence biomass abundance and macrobenthic infaunal composition (Thamdrup and Canfield, 2000). For example, sites C6-26 in Chile have lower DIR rates compared to C40-41 (Table A.5) on account of low bottom water O_2 limiting biomass density, while a complete absence of DIR at site SV2 in Svalbard is attributed to an increased POC flux reducing the depth of mixing (Glud et al., 1998; Thamdrup and Canfield, 2000). In contrast, stations exhibiting a high density of deep-burrowing infauna

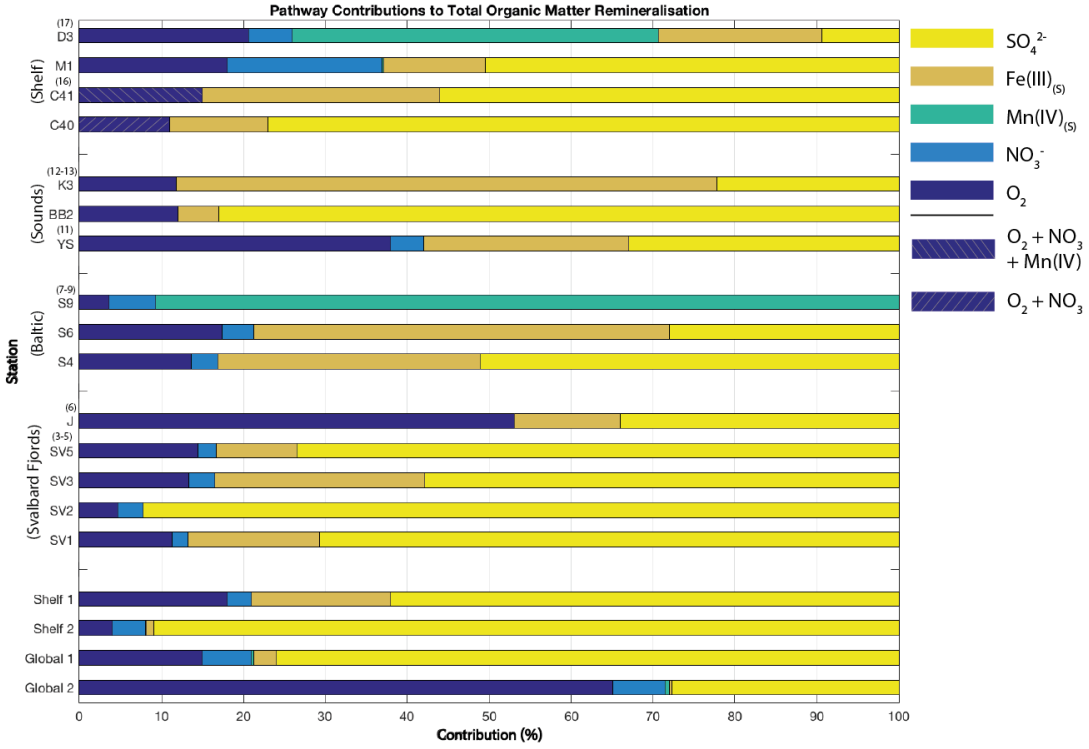

Figure A.8: A global compilation of the contribution of various TEA pathways to POC mineralisation in a range of marine sediments. Reference numbers refer to those of Table A.5. Locations are grouped by environment. Note that shelf sediments from (16) have grouped contributions from multiple oxidants. 'Global 2' is an estimate of TEA contributions to global organic carbon mineralisation from all marine sediments from experimentally-derived data (Sarmiento and Gruber, 2006). 'Global 1' is a model-based estimate (1G) of the same scale (Thullner et al., 2009), while 'Shelf 2' is an estimate of TEA contributions for <350 m depth from the same study. Both estimates present antithetical theories in relation to the importance of O_2 and SO_4^{2-} as TEAs, however both recognise the minor importance of metal reduction on a global scale. Note that these proportions are for surface sediments; methanogenesis contributes between 5-9.8% of global organic carbon mineralisation but only when much deeper sediment (m scale) and more recalcitrant carbon fractions are considered (Sarmiento and Gruber, 2006; Thullner et al., 2009). 'Shelf 1' from Thamdrup and Canfield (2000) estimates a much higher proportion of 17% after removing 'unusual' sites affected by anoxia (Amazon Shelf muds, Panama Basin), however this is based on a compilation of data where sites have been analysed for interesting features, such as high Fe reduction rates thus could represent a sampling bias.

(e.g. Polchaetes) have correspondingly higher DIR rates (e.g. XII Barents Sea (Vandieken et al., 2006b) and S4-6 Skaggerak (Canfield et al., 1993b)). However, an infinite increase in biomixing intensity does not correspond to an ever-increasing contribution of DIR/DMR to the oxidation of POC. For example, one of three stations in the Barents Sea exhibited the highest polychaete tube density and turnover of Fe/Mn cations, but the lowest contribution of DIR/DMR to the total POC oxidation (69% of anaerobic), given that the overall rate of oxidation increased with the mixing intensity, thereby favouring SR (Vandieken et al., 2006b). Indeed, a modelling study found that DIR rates decrease with increasing overall mineralisation rates, as Fe oxides begin to react with H_2S, a reduced product of SR (Van Cappellen and Wang, 1996). This observation implies that an intermediate POC supply is favourable for metal reduction, given that biomixing increases with POC sedimentation (Thamdrup and Canfield, 2000) and over-mixing begins to favour SR.

This periodic reoxidation and recycling of metals between their solid and dissolved phases drives a process termed 'rejuvenation', which is highly influential for the reactivity of the compounds in question. Older Fe oxides (e.g. goethite) are less labile as a result of a high level of crystallinity. However, after metal oxides reductively dissolve on burial to the anoxic zone, dissolved Fe^{2+} and Mn^{2+} are able to adsorb onto sediment particulates or precipitate as authigenic sulphides in the presence of H_2S, or as carbonate and phosphate mineral phases at depth. They are then transported back towards the SWI through particle mixing (usually biomixing), or flushed upwards through bioirrigation if in an aqueous phase. They then re-precipitate as hydroxides in the upper sediment layers as 'fresher', more bioavailable nanoparticulates (Monien et al., 2014). This mechanism has been suggested to facilitate the delivery of glacially-derived Fe to neighbouring shelf seas (Wehrmann et al., 2014).

The Barents Sea is another particularly interesting area with regard to the TEA pathways used in the breakdown of POC within the seafloor. Five Barents Sea sites were analysed across two studies by Vandieken et al. (2006b) and Nickel et al. (2008), forming a transect along 30^{o}E (north and east of Svalbard) traversing the PF, spanning both the ArW and AW sectors. Lower TOC contents (1.4-1.5 wt%) and sediment accumulation rates (0.5-1 mm yr^{-1}) were found in four of the sites (VIII, X, XII, XVII), in combination with high concentrations of solid phase reactive Fe (84-108 μmol cm^{-3}) and Mn (30-60 μmol cm^{-3}) oxides. At these localities, DMR/DIR were found to contribute 69-98% of the anaerobic POC mineralisation rate in the upper 12 cm during anoxic sediment bag incubation experiments of core slices (Table A.5). The remainder of the anaerobic remineralisation rate was found to be associated with SR. The contribution of aerobic respiration to the total POC mineralisation rates were not explicitly measured, although this value is typically ∼12-20% of the total rate in shelf sediments (Table A.5).

The lower TOC content in the Barents Sea sediments was attributed to seasonal sea ice cover reducing the timeframe available for the deposition of phytodetritus (>70% in the

northern stations during sampling). This is in contrast to the ice-free AW Hopen Trench station (XVIII), which was characterised by a higher TOC (2.6 wt%), sediment accumulation rate (1.3 mm yr^{-1}), remineralisation rate and a lower labile metal oxide content (<2.2 μmol cm^{-3} Mn(IV), <37 μmol cm^{-3} Fe(III) oxide) (Table A.5). At this station, just 24% of anaerobic remineralisation was accounted for by DIR/DMR and >80% by SR, the rates of which were five-fold higher than at the northern sites. The predominance of DIR/DMR over SR at four of the sites was attributed the fact that, as TOC content increases, so do remineralisation rates. This reflects the consensus that low-intermediate supply of POC (coupled with higher metal oxide concentrations and bioturbation) favours metal reduction in ocean sediments (Burdige, 1993). This hypothesis is supported by work in fjords west and south of Svalbard (SV2-5 and J) under the influence of AW, as well as in fjords of Greenland (YS) (Glud et al., 1998; Kostka et al., 1999; Rysgaard et al., 1998; Vandieken et al., 2006b) (Table A.5). At these sites, metal reduction contributes just 0-26% of total carbon oxidation (0-43% of anaerobic) in the upper layers and sediments present with much higher overall remineralisation rates than the open water Barents Sea sites discussed above (10-24 *vs* 1.3-7.7 mmol m^{-2} d^{-1}). Low concentrations of labile Mn(IV) and Fe(III) (0 and <40 μmol cm^{-3} respectively) further substantiates the low contribution of DMR/DIR at these locations relative to sites east and north of Svalbard (Nickel et al., 2008; Vandieken et al., 2006b).

Organic carbon substrate availability is considered one of the most important factors in determining the relative importance of TEA pathways (Nickel et al., 2008). Therefore, as a result of the increased TOC content at the Hopen Trench, overall mineralisation rates increase, rapidly assimilating oxygen and labile metal oxides as TEAs. This increases the relative importance of SR as an oxidation pathway, as sulphate concentrations are ubiquitously high in ocean bottom waters and are thus unlikely to become exhausted (Nickel et al., 2008). Therefore, as is the case for the majority of Barents Sea parameters, an ArW and AW regime could also be ascribed to sedimentary biogeochemical processes based on these findings. This would imply that Atlantification could cause a shift in the relative importance of DIR/DMR with respect to POC remineralisation. This highlights a critical research question that must be answered in order to determine how sediment chemical dynamics may change.

If the reconstructions of Knies and Martinez (2009) and Pathirana et al. (2014) are a reasonable representation of future change, the region of higher annual primary productivity (ArW) is to shrink, thereby potentially reducing POC delivery to the seafloor. Contrary to this, laboratory-based work (Nickel et al., 2008; Sakshaug, 1997; Vandieken et al., 2006b), as well as data from ocean-ecosystem modelling experiments (Ellingsen et al., 2008; Wassmann et al., 2010) would suggest that primary productivity and TOC contents are higher in the AW zone. The growth of this region would potentially then increase POC delivery to the seafloor across the BSB, increase overall remineralisation

rates and therefore the relative importance of SR compared to metals. This hypothesis is consistent with the findings of Wassmann and Olli (2004), who observe similar POC fluxes either side of the PF at depth during the spring bloom, but higher throughout summer in the Atlantic region. This must be reconciled with the potential for the composition of POC delivery to change. Given that a much higher proportion of TOC in the ArW realm is composed of TOM (Knies and Martinez, 2009), the quality of POC delivery could increase with Atlantification, which would likely also increase sediment POC mineralisation rates. Not only this, but while annual POC delivery to the seafloor is higher across southern sites (Wassmann and Olli, 2004), would a northward migration of the PF (where the most efficient delivery of POC to the seafloor occurs in the Barents Sea) increase sedimentary TOC content overall?

Changes to DIR in shelf sediments of the Arctic could have considerable implications for pelgaic ecosystem dynamics. It has been suggested that at lower bottom water temperatures, reaction kinetics are low enough to allow reduced Fe^{2+} to flux across the SWI and be entrained in bottom water currents. The discussed mechanism of Fe rejuvination therefore not only increases the bioavailability of Fe compounds, but could also transport them further off-shelf (Monien et al., 2014), potentially representing a conveyor for delivering micronutrients from the fringes of fjord systems and shelf seas to open waters.

Recent work by Vieira et al. (2018) suggests that up to 10-25% of the benthic Fe flux (2.5 μmol m^{-2} d^{-1}) emanating from Chukchi Sea sediments is transported off-shelf, representing a 'major' source of micronutrients to the central Arctic Ocean. Similarly, DIR and the associated benthic Fe flux appear to be intensifying in newly ice-free areas of the Western Antarctic Peninsula, on account of a heightened accumulation of glacially-derived Fe-rich fines and a decrease in labile organic matter availability (Monien et al., 2014). The benthic flux of bioavailable Fe supplied from sediments of the Antarctic shelf to the HNLC Southern Ocean is now estimated to be equivalent to that provided by icebergs and significantly more than the aeolian flux (Monien et al., 2014). These findings are interesting given the suggestion that the contribution of DIR to POC mineralisation in the Barents Sea could decrease with Atlantification (Vandieken et al., 2006b).

The sensitivity of the relative contribution of TEA pathways to POC remineralisation in the Barents Sea therefore represents a source of uncertainty that should be addressed. This is especially important given the projected increase in riverine runoff to the region (Bowling et al., 2000) and the influence enhanced meltwater runoff has had on TEA pathways in sediments of King George Island (Monien et al., 2014). Any changes to POC delivery will not only affect benthic fluxes of Fe, but also of macronutrients (nitrate, ammonium and phosphate) and alkalinity. At present, SWI fluxes of these solutes have all been found to be positive on inflow shelves of the Arctic Ocean and negative on the interior and outflow shelves (Bourgeois et al., 2017). Therefore a stimulation or attenuation in benthic activity with climate change will have significant and widespread implications

for nutrient cycling in the region.

Table A.5: Global compilation of sediment biogeochemical characteristics from a range of marine sediments (continued below*).

Site	Area	Depth (m)	Temp (^{o}C)	Sediment Accumulation (mm yr^{-1})	TOC (wt%)	Fe Oxide[d] (μmol cm^{-3})	Mn Oxide (μmol cm^{-3})	TSOC (mmol m^{-2} d^{-1})	Anaerobic C[c] Oxidation Rate (mmol C m^{-2} d^{-1})	SR[a] (mmol m^{-2} d^{-1})	DIR/DMR[b] (% anaerobic C mineralised)
Barents											
VIII[(1)]	North	503	2.9	1.0	1.5	<275	<60	2.1	2.2	0.1 (0.2)	90
X	North	303	2.5	0.6	1.4	<110	<110	1.5	1.5	0.1 (0.2)	87
XII	North	286	2.3	0.5	1.5	<125	<60	3.5	4.3	0.22 (0.44)	69
XVII[(2)]	Central	280	0	0.7	1.4	<84	<30	1.9	1.3	0.03 (0.06)	99
XVIII	South	340	2.2	1.3	2.6	<37	<2.2	3.7	6.7	0.15 (0.3)	24
Fjords											
SV1[(3−5)]	Norway	329	7	1.3	0.6	<20	<1.5	4.7	11.8 (13)	5.0 (10)	18.6 (11.3)
SV2	Svalbard	155	7	5.9	1.5	<50	<3	8.1	23.1 (24.2)	12.0 (24)	0 (4.7)
SV3	Svalbard	115	2.6	2.5	1.8	<100	<18	4.2	10.31 (11.9)	2.6 (4.2)	29.6 (13.3)
SV4	Svalbard	138	0.2	2.5	1.8	nd	nd	4.7	nd	nd	nd
SV5	Svalbard	175	-1.7	2.1	2.4	<125	<18	3.6	9.42 (11)	4.4 (8.8)	11.5 (14.4)
J[(6)]	Svalbard	212	1.5	nd	2	<112	<1.5	4.2	3.3 (7.1)	1.2 (2.4)	43 (53)
Polar											
S4[(7−9)]	Skagerrak	190	5	2	nd	<60	<2.9	9.2	13.7 (15.8)	4.0 (8.0)	25 (13.6)
S6	Skagerrak	380	5	1.8	nd	<60	<3.5	9.9	8.5 (10.2)	1.5 (3.0)	62 (17.4)
S9	Skagerrak	695	5	1	nd	<150	<175	8.1	10.5 (10.9)	<0.1	94 (3.6)
N[(10)(f)]	Bering Shelf	70	2	0.1-1	nd	21.3	0.95	9.1	nd (7)	nd	15.6[e] (nd)
Mid	Bering Shelf	65	2	0.1-1	nd	41.2	1.1	9	nd (6.9)	nd	7.8 (nd)
Out	Bering Shelf	127	2	0.1-1	nd	16.7	0.38	7.2	nd (5.4)	nd	4.4 (nd)
Off	Bering Shelf	2216	2	0.1-1	nd	9.4	13.6	4	nd (3.1)	nd	3.9 (nd)
Sounds											
YS[(11)]	Greenland	36	-2	2.3	1.4	<48	<1.25	5-13[(g)]	3.9 (6.3, 5-12)	0.8-1.7 (1.6-3.4)[(h)]	40.5 (38)
BB2 [(12−13)]	Great Belt	25	nd	0.3	3.2	<16	<3	nd	11.4 (13)	5.4 (10.8)	5 (12)
K3	Kattegat	56	nd	6.2	2.2	<45	<1	nd	39.6 (44.9)	5 (10)	75 (11.8)
Temperate											
Freshwater											
TW[(14)]	Talladega	<1	22	nd	20	<75	<0.75	nd	59-117	3-4.5 (6-9)	38-55 ('min')
Saltmarsh											
BVL[(15)(k)]	Georgia	<1	30	nd	15	<125	ND	nd	80	<2	100 (0)
NUC	Georgia	<1	30	nd	15	<16	ND	nd	49	20	0
Shelf											
C6-26[(16)]	Chile	34-122	11.4	nd	2.5-5.8	<20	ND	nd	<60-112	30-56 (60-112)	0 (0)
C40	Chile	1015	6	nd	3.8	<30	ND	nd	<11.9	4.8 (9.6)	13 (<12)
C41	Chile	2000	3.9	nd	4	<35	<0.5	nd	<9.3	2.7 (5.4)	34 (<15)
M1[(17)]	East Sea	1453	1.3	1.5-3	4	<5	<1	7.1	14 (17.1)	4.3 (8.6)	15.4 (18)
D3	East Sea	2154	0.6	0.7	2.7	<20	<220	2.5	7.2 (9.2)	0.43 (0.9)	82 (20.6)
Tropical											
Shelf											
11-123[(18−19)]	Amazon	10-50	28	5-50	0.55-0.77	80-200	nd	11.8 (10.5-13)[(i)]	44 (55)	'min'	>50 (20)[(j)]
Abyssal											
PB[(20)]	Panama	3890	1.8	0.3[a]	2.5	nd	<290	2.3	2	0	100 (0)

Table A.5: * nd: not determined; ND = not detected. (1) Vandieken et al. (2006b); (2) Nickel et al. (2008); (3) Glud et al. (1998); (4) Kostka et al. (1999); (5) Jørgensen et al. (2005); (6) Vandieken et al. (2006a); (7) Wang and Van Cappellen (1996); (8) Canfield et al. (1993b); (9) Canfield et al. (1993a); (10) Esch et al. (2013); (11) Rysgaard et al. (1998); (12) Jensen et al. (2003); (13) Jørgensen et al. (1990); (14) Roden and Wetzel (1996); (15) Kostka et al. (2002); (16)Thamdrup and Canfield (1996); (17) Hyun et al. (2017); (18) Aller et al. (1986); (19) Aller et al. (1991); (20) Aller (1990). Sediment accumulation rates for refs (1) and (2) from Zaborska et al. (2008) and for (20) from Swift (1977). (a) Integrated SR with carbon equivalents in brackets, assuming a stoichiometry of 0.5:1 ($SO_4{}^{2-}$ reduced to C oxidised). (b) Contribution (%) of DMR and DIR to anaerobic mineralisation with the aerobic proportion to total in brackets. (c) Anaerobic C mineralisation rates with total rate in brackets. (d) Solid phase concentrations are given as < maxima (generally 1-4 cm depth) and are labile fraction only. (e) Total C mineralisaition rate (anaeorbic rates were not explicitly determined). (f) N = northern shelf; Mid shelf; Out = Outer shelf; Off = Off shelf. (g) TSOC 5 mmol m^{-2} d^{-1} under ice cover and 13 mmol m^{-2} d^{-1} ice free. (h) Anaerobic C mineralisation given as an annual average and total rate '()' given as a mean and seasonal range (12 mmol C m^{-2} d^{-1} in late July, 5 mid June), SRR as a seasonal range only. There's a tendency for higher rates in the open water period. (i) TSOC measured as diffusive uptake only (minimal bioirrigation). (j) 'Most' anaerobic C remineralisation attributed metal reduction (minimum % given). (k) BVL = bioturbated, vegetated. NUC = non bioturbated/vegetated. Depth-integrated SR 0-20 cm for (1) (2) (6) and (18), 0-6 cm (15), 0-15 cm (11) and 0-10 cm for the remainder. C oxidation rates and TEA contributions experimentally calculated for all for 0-10 cm depth interval, bar 0-6 cm (15) and 0-20 cm (18) and 0-25 cm (20). DIR sole pathway at BVL, DMR sole pathway at PB & S9, not present at C6-41, Sv1-Sv5, YS, TW, J, BVL & NUC, YS <1%.

Bibliography

Abbott, A. N., Löhr, S., and Trethewy, M. (2019). Are clay minerals the primary control on the oceanic rare earth element budget? *Front. Mar. Sci.*, 6(504).

Abramson, L., Wirick, S., Lee, C., Jacobsen, C., and Brandes, J. A. (2009). The use of soft X-ray spectromicroscopy to investigate the distribution and composition of organic matter in a diatom frustule and a biomimetic analog. *Deep. Res. II*, 56:1369–1380.

Aguilera, D. R., Jourabchi, P., Spiteri, C., and Regnier, P. (2005). A knowledge-based reactive transport approach for the simulation of biogeochemical dynamics in Earth systems. *Geochem. Geophys. Geosystems.*, 6(7).

Airs, R. L., Atkinson, J. E., and Keely, B. J. (2001). Development and application of a high resolution liquid chromatographic method for the analysis of complex pigment distributions. *J. Chromatogr. A*, 917(1-2):167–177.

Airs, R. L. and Keely, B. J. (2000). A novel approach for sensitivity enhancement in atmospheric pressure chemical ionisation liquid chromatography/mass spectrometry of chlorophylls. *Rapid Commun. Mass Spectrom.*, 14(3):125–128.

Aksenov, Y., Bacon, S., Coward, A. C., and Nurser, A. J. (2010). The North Atlantic inflow to the Arctic Ocean: High-resolution model study. *J. Mar. Syst.*, 79(1-2):1–22.

Alexeev, V. A., Walsh, J. E., Ivanov, V. V., Semenov, V. A., and Smirnov, A. V. (2017). Warming in the Nordic Seas, North Atlantic storms and thinning Arctic sea ice. *Environ. Geol.*, 12(084011).

Aller, R. C. (1990). Bioturbation and Manganese Cycling in Hemipelagic Sediments. *Philos. Trans. Royal Soc. A*, 331(1616).

Aller, R. C. (2014). 8.11 - Sedimentary Diagenesis, Depositional Environments, and Benthic Fluxes. *Treatise on Geochemistry (Second Edition)*, 8:293–334.

Aller, R. C., Aller, J. Y., Blair, N. E., Mackin, J. E., Rude, P. D., Stupakoff, I., Patchineelam, S., Boehme, S. E., and Knoppers, B. (1991). Biogeochemical processes in Amazon Shelf sediments. *Oceanography*, 4(1):27 – 32.

Aller, R. C., Mackin, J. E., and Cox, R. T. (1986). Diagenesis of Fe and S in Amazon inner shelf muds: apparent dominance of Fe reduction and implications for the genesis of ironstones. *Cont. Shelf Res.*, 6(1-2):263–289.

Anderson, L. A. (1995). On the hydrogen and oxygen content of marine phytoplankton. *Deep. Res. I*, 42(9):1675–1680.

Anderson, L. G., Dyrssen, D. W., Jones, E. P., and Lowings, M. G. (1983). Inputs and outputs of salt, fresh water, alkalinity, and silica in the Arctic Ocean. *Deep. Res. A*, 30:87–94.

Anderson, L. G., Olsson, K., and Chierici, M. (1998). A carbon budget for the Arctic Ocean. *Global Biogeochem. Cycles*, 12(3):455–465.

Andreassen, I., Noting, E. M., and Wassmann, P. (1996). Vertical particle flux on the shelf off northern Spitsbergen, Norway. *Mar. Ecol. Prog. Ser.*, 137(1-3):215–228.

Andrén, H. (2004). *Studies of Arctificial Mass Bias in Isotopic Measurements by Inductively Coupled Plasma Mass Spectrometry.* PhD thesis, Luleå University of Technology.

Antajan, E., Chrétiennot-Dinet, M. J., Leblanc, C., Daro, M. H., and Lancelot, C. (2004). 19'-Hexanoyloxyfucoxanthin may not be the appropriate pigment to trace occurrence and fate of Phaeocystis: The case of P. globosa in Belgian coastal waters. *J. Sea Res.*, 52:165–177.

Araújo, D. F., Boaventuraa, G., Viers, J., Mulholland, D., Weiss, D., Araújo, D., Lima, B., Ruiz, I., Machado, W., Babinski, M., and Dantas, E. (2017). Ion Exchange Chromatography and Mass Bias Correction for Accurate and Precise Zn Isotope Ratio Measurements in Environmental Reference Materials by MC-ICP-MS. *J. Braz. Chem. Soc*, 28(2).

Arrigo, K. R. and Van Dijken, G. L. (2011). Secular trends in Arctic Ocean net primary production. *J. Geophys. Res.*, 116(C09011).

Årthun, M. (2011). Ocean surface heat flux variability in the Barents Sea. *J. Mar. Syst.*, 83(1-2):88–98.

Årthun, M., Eldevik, T., Smedsrud, L. H., Skagseth, and Ingvaldsen, R. B. (2012). Quantifying the influence of atlantic heat on barents sea ice variability and retreat. *J. Clim.*, 25(13):4736–4743.

Årthun, M. and Schrum, C. (2010). Ocean surface heat flux variability in the Barents Sea. *J. Mar. Syst.*, 83(1-2):88–98.

Backman, J., Jakobsson, M., Løvlie, R., Polyak, L., and Febo, L. A. (2004). Is the central Arctic Ocean a sediment starved basin? *Quat. Sci. Rev.*, 23(11-13):1435–1454.

Bailey, H., Hubbard, A., Klein, E. S., Mustonen, K. R., Akers, P. D., Marttila, H., and Welker, J. M. (2021). Arctic sea-ice loss fuels extreme European snowfall. *Nat. Geosci.*, 14:283–288.

Baldermann, A., Banerjee, S., Czuppon, G., Dietzel, M., Farkaš, J., Loehr, S., Moser, U., Scheiblhofer, E., Wright, N. M., and Zack, T. (2022). Impact of green clay authigenesis on element sequestration in marine settings. *Nat. Commun.*, 13(1527).

Barão, L., Vandevenne, F., Clymans, W., Frings, P., Ragueneau, O., Meire, P., Conley, D. J., and Struyf, E. (2015). Alkaline-extractable silicon from land to ocean: A challenge for biogenic silicon determination. *Limnol. Oceanogr.: Methods*, 13(7):329–344.

Barnes, D. (2019). Changing Arctic Ocean Seafloor JR18006 Cruise Report, RRS James

Clark Ross. Technical report.

Baronas, J. J., Hammond, D. E., Rouxel, O. J., and Monteverde, D. R. (2019). A first look at dissolved ge isotopes in marine sediments. *Front. Earth Sci.*, 7(162).

Barton, B. I., Lenn, Y. D., and Lique, C. (2018). Observed atlantification of the Barents Sea causes the Polar Front to limit the expansion of winter sea ice. *J. Phys. Oceanogr.*, 48(8):1849–1866.

Bayon, G., Delvigne, C., Ponzevera, E., Borges, A. V., Darchambeau, F., De Deckker, P., Lambert, T., Monin, L., Toucanne, S., and André, L. (2018). The silicon isotopic composition of fine-grained river sediments and its relation to climate and lithology. *Geochim. Cosmochim. Acta*, 229:147–161.

Beeskow, B. and Rachold, V. (2003). Geochemistry on water profiles from the Kara Sea. PANGAEA.

Bengtsson, L., Semenov, V. A., and Johannessen, O. M. (2004). The early twentieth-century warming in the arctic - A possible mechanism. *J. Clim.*, 17(20):4045–4057.

Berelson, W., McManus, J., Coale, K., Johnson, K., Burdige, D., Kilgore, T., Colodner, D., Chavez, F., Kudela, R., and Boucher, J. (2003). A time series of benthic flux measurements from Monterey Bay, CA. *Cont. Shelf Res.*, 23:457–481.

Berner, R. (1980). *Early diagenesis: a theoretical approach*. Princeton University Press, Princeton, NJ.

Bernhardt, A., Oelze, M., Bouchez, J., von Blanckenburg, F., Mohtadi, M., Christl, M., and Wittmann, H. (2020). 10Be/9Be Ratios Reveal Marine Authigenic Clay Formation. *Geophys. Res. Lett.*, 47.

Bmstedt, U., Eilertson, H. C., Tande, K. S., Slagstad, D., and Skjoldal, H. R. (1991). Copepod grazing and its potential impact on the phytoplankton development in the Barents Sea. *Polar Res.*, 10(2).

Boetius, A., Albrecht, S., Bakker, K., Bienhold, C., Felden, J., Fernández-Méndez, M., Hendricks, S., Katlein, C., Lalande, C., Krumpen, T., Nicolaus, M., Peeken, I., Rabe, B., Rogacheva, A., Rybakova, E., Somavilla, R., Wenzhöfer, F., and Felden, J. (2013). Export of algal biomass from the melting arctic sea ice. *Science*, 339(6126):1430–1432.

Boudreau, B. P. (1996). The diffusive tortuosity of fine-grained unlithified sediments. *Geochim. Cosmochim. Acta*, 60(16):3139–3142.

Boudreau, B. P. (1997). *Diagenetic models and their implementation: modelling transport and reactions in aquatic sediments*. Springer, New York, 1st edition.

Bourgeois, S., Archambault, P., and Witte, U. (2017). Organic matter remineralization in marine sediments: A Pan-Arctic synthesis. *Global Biogeochem. Cycles*, 31(1):190–213.

Boutorh, J., Moriceau, B., Gallinari, M., Ragueneau, O., and Bucciarelli, E. (2016). Effect of trace metal-limited growth on the postmortem dissolution of the marine diatom Pseudo-nitzschia delicatissima. *Global Biogeochem. Cycles*, 30(1):57–69.

Bowling, L., Lettenmaier, D., and Matheussen, B. (2000). Hydroclimatology of the Arctic

Drainage Basin. In Lewis, E., Jones, E., Lemke, P., Prowse, T., and Wadhams, P., editors, *The Freshwater Budget of the Arctic Ocean*, pages 57–90. Kluwer Academic Publishers, Dordrecht.

Brzezinski, M. A., Closset, I., Jones, J. L., de Souza, G. F., and Maden, C. (2021). New Constraints on the Physical and Biological Controls on the Silicon Isotopic Composition of the Arctic Ocean. *Front. Mar. Sci.*, 8(699762).

Buffle, J., De Vitre, R. R., Perret, D., and Leppard, G. G. (1989). Physico-chemical characteristics of a colloidal iron phosphate species formed at the oxic-anoxic interface of a eutrophic lake. *Geochim. Cosmochim. Acta*, 53:399–408.

Burdige, D. (1993). The biogeochemistry of manganese and iron reduction in marine sediments. *Earth-Sci. Rev.*, 35(3):249–284.

Burdige, D. (2006). *Geochemistry of Marine Sediments*. Princeton University Press, Princeton, NJ.

Canfield, D., Jørgensen, B., Fossing, H., Glud, R., Gundersen, J., Ramsing, N., Thamdrup, B., Hansen, J., Nielsen, L., and Hall, P. (1993a). Pathways of organic carbon oxidation in three continental margin sediments. *Mar. Geol.*, 113(1-2):27–40.

Canfield, D. E., Thamdrup, B., and Hansen, J. W. (1993b). The anaerobic degradation of organic matter in Danish coastal sediments: Iron reduction, manganese reduction, and sulfate reduction. *Geochim. Cosmochim. Acta*, 57(16):3867–3883.

Cardinal, D., Alleman, L. Y., De Jong, J., Ziegler, K., and André, L. (2003). Isotopic composition of silicon measured by multicollector plasma source mass spectrometry in dry plasma mode. *J. Anal. At. Spectrom.*, 18:213–218.

Carmack, E. and Wassmann, P. (2006). Food webs and physical-biological coupling on pan-Arctic shelves: Unifying concepts and comprehensive perspectives. *Prog. Oceanogr.*, 71(2-4):446–477.

Carroll, J. L., Zaborska, A., Papucci, C., Schirone, A., Carroll, M. L., and Pempkowiak, J. (2008a). Accumulation of organic carbon in western Barents Sea sediments. *Deep. Res. II*, 55(10-21):2361–2371.

Carroll, M. L., Denisenko, S. G., Renaud, P. E., and Ambrose, W. G. (2008b). Benthic infauna of the seasonally ice-covered western Barents Sea: Patterns and relationships to environmental forcing. *Deep. Res. II*, 55(20-21):2340–2351.

Carter, S. J. and Colman, S. M. (1994). Biogenic Silica in Lake Baikal Sediments: Results From 1990–1992 American Cores. *J. Great Lakes Res.*, 20(4):751–760.

Cassarino, L. (2018). *From micro to macro: silicon isotope fractionation during biogenic opal formation*. PhD thesis, University of Bristol.

Cassarino, L., Coath, C. D., Xavier, J. R., and Hendry, K. R. (2018). Silicon isotopes of deep sea sponges: New insights into biomineralisation and skeletal structure. *Biogeosciences*, 15:6959–6977.

Cassarino, L., Hendry, K. R., Henley, S. F., MacDonald, E., Arndt, S., Freitas, F. S., Pike,

J., and Firing, Y. L. (2020). Sedimentary Nutrient Supply in Productive Hot Spots off the West Antarctic Peninsula Revealed by Silicon Isotopes. *Global Biogeochem. Cycles*, 34(12).

Cermelj, B., Bertuzzi, A., and Faganeli, J. (1997). Modelling of pore water nutrient distribution and benthic fluxes in shallow coastal waters (Gulf of Trieste, Northern Adriatic). *Water Air Soil Pollut.*, 99:435–444.

Chemtob, S. M., Rossman, G. R., Young, E. D., Ziegler, K., Moynier, F., Eiler, J. M., and Hurowitz, J. A. (2015). Silicon isotope systematics of acidic weathering of fresh basalts, Kilauea Volcano, Hawai'i. *Geochim. Cosmochim. Acta*, 169:63–81.

Clarkson, M. O., Poulton, S. W., Guilbaud, R., and Wood, R. A. (2014). Assessing the utility of Fe/Al and Fe-speciation to record water column redox conditions in carbonate-rich sediments. *Chem. Geol.*, 382:111–122.

Cochrane, S. K., Denisenko, S. G., Renaud, P. E., Emblow, C. S., Ambrose, W. G., Ellingsen, I. H., and Skardhamar, J. (2009). Benthic macrofauna and productivity regimes in the Barents Sea - Ecological implications in a changing Arctic. *J. Sea Res.*, 61(4):222–233.

Conley, D. (1987). *Mechanisms controlling silica flux from sediments and implications for biogeochemical cycling of silica in Lake Michigan.* PhD thesis, University of Michigan.

Conley, D. J. (1998). An interlaboratory comparison for the measurement of biogenic silica in sediments. *Mar. Chem.*, 63(1-2):39–48.

Cuadros, J., Dekov, V. M., Arroyo, X., and Nieto, F. (2011). Smectite formation in submarine hydrothermal sediments: Samples from the HMS Challenger expedition (1872-1876). *Clays Clay Miner.*, 59(2):147–164.

Cutter, G. A., Casciotti, K., Croot, P. L., Geibert, W., Heimbürger, L.-E., Lohan, M., Planquette, H., and van de Flierdt, T. (2017). Sampling and Sample-handling Protocols for GEOTRACES Cruises. Version 3, August 2017. *GEOTRACES Community Practices.*

Dale, A. W., Paul, K. M., Clemens, D., Scholz, F., Schroller-Lomnitz, U., Wallmann, K., Geilert, S., Hensen, C., Plass, A., Liebetrau, V., Grasse, P., and Sommer, S. (2021). Recycling and Burial of Biogenic Silica in an Open Margin Oxygen Minimum Zone. *Global Biogeochem. Cycles*, 35(2).

Dalpadado, P., Arrigo, K. R., Hjøllo, S. S., Rey, F., Ingvaldsen, R. B., Sperfeld, E., Van Dijken, G. L., Stige, L. C., Olsen, A., and Ottersen, G. (2014). Productivity in the Barents Sea - Response to recent climate variability. *PLoS ONE*, 9(5).

Dalpadado, P., Arrigo, K. R., van Dijken, G. L., Skjoldal, H. R., Bagøien, E., Dolgov, A. V., Prokopchuk, I. P., and Sperfeld, E. (2020). Climate effects on temporal and spatial dynamics of phytoplankton and zooplankton in the Barents Sea. *Prog. Oceanogr.*, 185(102320).

Dalpadado, P., Ingvaldsen, R. B., Stige, L. C., Bogstad, B., Knutsen, T., Ottersen, G.,

and Ellertsen, B. (2012). Climate effects on Barents Sea ecosystem dynamics. *ICES J. Mar. Sci.*, 69(7):1303–1316.

Dankers, R. and Middelkoop, H. (2008). River discharge and freshwater runoff to the Barents Sea under present and future climate conditions. *Clim. Change*, 87:131–153.

De La Rocha, C. L. (2002). Measurement of silicon stable isotope natural abundances via multicollector inductively coupled plasma mass spectrometry (MC-ICP-MS). *Geochem. Geophys. Geosystems.*, 3(8):1–8.

De la Rocha, C. L. (2003). Silicon isotope fractionation by marine sponges and the reconstruction of the silicon isotope composition of ancient deep water. *Geology*, 31(5):423–426.

De La Rocha, C. L., Brzezinski, M. A., and DeNiro, M. J. (1997). Fractionation of silicon isotopes by marine diatoms during biogenic silica formation. *Geochim. Cosmochim. Acta*, 61(23):5051–5056.

De Oliveira Souza, M., Ribeiro, M. A., Carneiro, M. T. W. D., Athayde, G. P. B., De Castro, E. V. R., Da Silva, F. L. F., Matos, W. O., and De Queiroz Ferreira, R. (2015). Evaluation and determination of chloride in crude oil based on the counterions Na, Ca, Mg, Sr and Fe, quantified via ICP-OES in the crude oil aqueous extract. *Fuel*, 154:181–187.

de Souza, G. F., Reynolds, B. C., Rickli, J., Frank, M., Saito, M. A., Gerringa, L. J., and Bourdon, B. (2012). Southern Ocean control of silicon stable isotope distribution in the deep Atlantic Ocean. *Global Biogeochem. Cycles*, 26(2):GB2035.

Degerlund, M. and Eilertsen, H. C. (2010). Main Species Characteristics of Phytoplankton Spring Blooms in NE Atlantic and Arctic Waters (68-80° N). *Estuaries Coast*, 33:242–269.

Delstanche, S., Opfergelt, S., Cardinal, D., Elsass, F., André, L., and Delvaux, B. (2009). Silicon isotopic fractionation during adsorption of aqueous monosilicic acid onto iron oxide. *Geochim. Cosmochim. Acta*, 73:923–924.

Demarest, M. S., Brzezinski, M. A., and Beucher, C. P. (2009). Fractionation of silicon isotopes during biogenic silica dissolution. *Geochim. Cosmochim. Acta*, 73:5572–5583.

DeMaster, D. (1981). The supply and accumulation of silica in the marine environment. *Geochim. Cosmochim. Acta*, 45(10):1715–1732.

DeMaster, D. (2001). Marine Silica Cycle. In *Encyclopedia of Ocean Sciences*, pages 1659–1667. Academic Press.

Demaster, D. J. (1992). Cycling and accumulation of biogenic silica and organic matter in high-latitude environments: the Ross Sea. *Oceanography*, 5(3).

DeMaster, D. J. (2002). The accumulation and cycling of biogenic silica in the Southern Ocean: Revisiting the marine silica budget. *Deep. Res. II*, 49(16):3155–3167.

DeMaster, D. J. (2019). The global marine silica budget: Sources and sinks. In *Encyclopedia of Ocean Sciences*, pages 473–483. Elsevier Ltd.

DeMaster, D. J., Knapp, G. B., and Nittrouer, C. A. (1983). Biological uptake and accumulation of silica on the Amazon continental shelf. *Geochim. Cosmochim. Acta*, 47:1713–1723.

DeMaster, D. J., Nelson, T. M., Harden, S. L., and Nittrouer, C. A. (1991). The cycling and accumulation of biogenic silica and organic carbon in Antarctic deep-sea and continental margin environments. *Mar. Chem.*, 35:489–502.

DeMaster, D. J., Ragueneau, O., and Nittrouer, C. A. (1996). Preservation efficiencies and accumulation rates for biogenic silica and organic C, N, and P in high-latitude sediments: The Ross Sea. *J. Geophys. Res. Oceans*, 101(C8):18,501–18,518.

DePaolo, D. J. (2011). Surface kinetic model for isotopic and trace element fractionation during precipitation of calcite from aqueous solutions. *Geochim. Cosmochim. Acta*, 75(4):1039–1056.

Ding, T., Jiang, S., Wan, D., Li, Y., Li, J., Song, H., Liu, Z., and Yao, X. (1996). *Silicon isotope geochemistry*. Geological Publishing House, Beijing, China.

Ding, T., Wan, D., Bai, R., Zhang, Z., Shen, Y., and Meng, R. (2005). Silicon isotope abundance ratios and atomic weights of NBS-28 and other reference materials. *Geochim. Cosmochim. Acta*, 69(23):5487–5494.

Dixit, S. and Van Cappellen, P. (2003). Predicting benthic fluxes of silicic acid from deep-sea sediments. *J. Geophys. Res.: Oceans*, 108(C10).

Dixit, S., Van Cappellen, P., and Van Bennekom, A. J. (2001). Processes controlling solubility of biogenic silica and pore water build-up of silicic acid in marine sediments. *Mar. Chem.*, 73:333–352.

Docquier, D., Fuentes-Franco, R., Koenigk, T., and Fichefet, T. (2020). Sea Ice—Ocean Interactions in the Barents Sea Modeled at Different Resolutions. *Front. Earth Sci.*, 8(172).

Doering, K., Ehlert, C., Pahnke, K., Frank, M., Schneider, R., and Grasse, P. (2021). Silicon Isotope Signatures of Radiolaria Reveal Taxon-Specific Differences in Isotope Fractionation. *Front. Mar. Sci.*, 8(666896).

Downes, P. P., Goult, S. J., Woodward, E. M. S., Widdicombe, C. E., Tait, K., and Dixon, J. L. (2021). Phosphorus dynamics in the Barents Sea. *Limnol. Oceanogr.*, 66:S326–S342.

Dumont, E., Brand, T., and Hopkins, J. (2019). CTD data from NERC CAO JR16006 cruise.

Dunlea, A. G., Murray, R. W., Santiago Ramos, D. P., and Higgins, J. A. (2017). Cenozoic global cooling and increased seawater Mg/Ca via reduced reverse weathering. *Nat. Commun.*, 8(844).

Dutkiewicz, A., Müller, R. D., O'Callaghan, S., and Jónasson, H. (2015). Census of seafloor sediments in the world's ocean. *Geology*, 43(9):795–798.

Dybwad, C., Assmy, P., Olsen, L. M., Peeken, I., Nikolopoulos, A., Krumpen, T., Randel-

hoff, A., Tatarek, A., Wiktor, J. M., and Reigstad, M. (2021). Carbon Export in the Seasonal Sea Ice Zone North of Svalbard From Winter to Late Summer. *Front. Mar. Sci.*, 7(525800).

Egan, K. E., Rickaby, R. E., Leng, M. J., Hendry, K. R., Hermoso, M., Sloane, H. J., Bostock, H., and Halliday, A. N. (2012). Diatom silicon isotopes as a proxy for silicic acid utilisation: A Southern Ocean core top calibration. *Geochim. Cosmochim. Acta*, 96:174–192.

Ehlert, C., Doering, K., Wallmann, K., Scholz, F., Sommer, S., Grasse, P., Geilert, S., and Frank, M. (2016a). Stable silicon isotope signatures of marine pore waters – Biogenic opal dissolution versus authigenic clay mineral formation. *Geochim. Cosmochim. Acta*, 191:102–117.

Ehlert, C., Reckhardt, A., Greskowiak, J., Liguori, B. T., Böning, P., Paffrath, R., Brumsack, H. J., and Pahnke, K. (2016b). Transformation of silicon in a sandy beach ecosystem: Insights from stable silicon isotopes from fresh and saline groundwaters. *Chem. Geol.*, 440:207–218.

Ellingsen, I. H., Dalpadado, P., Slagstad, D., and Loeng, H. (2008). Impact of climatic change on the biological production in the Barents Sea. *Clim. Change*, 87(1-2):155–175.

Elverhøi, A. (1984). Glacigenic and associated marine sediments in the Weddell Sea, fjords of Spitsbergen and the Barents Sea: A review. *Mar. Geol.*, 57:53–88.

Elverhøi, A. and Solheim, A. (1983). The Barents Sea ice sheet - a sedimentological discussion. *Polar Res.*, 1:23–42.

Emerson, S. and Hedges, J. (2003). Sediment Diagenesis and Benthic Flux. *Treatise on Geochemistry*, 6:293–319.

Engström, E., Rodushkin, I., Baxter, D. C., and Öhlander, B. (2006). Chromatographic purification for the determination of dissolved silicon isotopic compositions in natural waters by high-resolution multicollector inductively coupled plasma mass spectrometry. *Anal. Chem.*, 78:250–257.

Eppley, R. W. and Peterson, B. J. (1979). Particulate organic matter flux and planktonic new production in the deep ocean. *Nature*, 282:677–680.

Esch, M. E., Shull, D. H., Devol, A. H., and Moran, S. B. (2013). Regional patterns of bioturbation and iron and manganese reduction in the sediments of the southeastern Bering Sea. *Deep. Res. II*, 94:80–94.

Fabre, S., Jeandel, C., Zambardi, T., Roustan, M., and Almar, R. (2019). An Overlooked Silica Source of the Modern Oceans: Are Sandy Beaches the Key? *Front. Earth Sci.*, 7(231).

Fadeev, E., Rogge, A., Ramondenc, S., Nöthig, E.-M., Wekerle, C., Bienhold, C., Salter, I., Waite, A. M., Hehemann, L., Boetius, A., and Iversen, M. H. (2021). Sea ice presence is linked to higher carbon export and vertical microbial connectivity in the Eurasian Arctic Ocean. *Commun. Biol.*, 4(1255).

Fahl, K., Stein, R., Gaye-Haake, B., Gebhardt, C., Kodina, L., Unger, D., and Ittekkot, V. (2003). Biomarkers in surface sediments from the Ob and Yenisei estuaries and the southern Kara Sea: Evidence for particulate organic carbon sources, pathways, and degradation. In Stein, R., Fahl, K., Fütterer, D., Galimov, E., and Stepanets, O., editors, *Siberian River Run-off in the Kara Sea: Characterisation, Quantification, Variability, and Environmental Significance*, pages 329–488. Elsevier, Amsterdam.

Falk-Petersen, S., Hop, H., Budgell, W. P., Hegseth, E. N., Korsnes, R., Løyning, T. B., Børre Ørbæk, J., Kawamura, T., and Shirasawa, K. (2000). Physical and ecological processes in the marginal ice zone of the northern Barents Sea during the summer melt period. *J. Mar. Syst.*, 27(1-3):131–159.

Fanning, K. A. and Schink, D. R. (1969). Interaction of Marine Sediments with Dissolved Silica. *Limnol. Oceanogr.*, 14(1):59–68.

Faust, J. C., Stevenson, M., Abbott, G., and Knies, J. (2020). Does Arctic warming reduce preservation of organic matter in Barents Sea sediments? *Philos. Trans. Royal Soc. A*, 378(2181).

Faust, J. C., Tessin, A., Fisher, B. J., Zindorf, M., Papadaki, S., Hendry, K. R., Doyle, K. A., and März, C. (2021). Millennial scale persistence of organic carbon bound to iron in Arctic marine sediments. *Nat. Commun.*, 12(275).

Feely, R. A., Baker, E. T., Lebon, G. T., Gendron, J. F., Massoth, G. J., and Mordy, C. W. (1998). Chemical variations of hydrothermal particles in the 1996 Gorda Ridge event and chronic plumes. *Deep. Res. II*, 45:2637–2664.

Fetterer, F., Savoie, M., Helfrich, S., and Clemente-Colón, P. (2010). *Multisensor Analyzed Sea Ice Extent - Northern Hemisphere (MASIE-NH), Version 1.* U.S. National Ice Center and National Snow and Ice Data Center, Boulder, Colorado USA.

Fischer, W. W. and Knoll, A. H. (2009). An iron shuttle for deepwater silica in late Archean and early Paleoproterozoic iron formation. *Geol. Soc. Am. Bull.*, 121(1-2):222–235.

Flower, R. J. (1993). Diatom preservation: experiments and observations on dissolution and breakage in modern and fossil material. *Hydrobiologia*, 269:473–484.

Freitas, F. S., Hendry, K. R., Henley, S. F., Faust, J. C., Tessin, A. C., Stevenson, M. A., Abbott, G. D., März, C., and Arndt, S. (2020). Benthic-pelagic coupling in the Barents Sea: an integrated data-model framework. *Philos. Trans. Royal Soc. A*, 378(2181).

Freitas, F. S., Pika, P. A., Kasten, S., Jorgensen, B. B., Rassmann, J., Rabouille, C., Thomas, S., Sass, H., Pancost, R. D., and Arndt, S. (2021). New insights into large-scale trends of apparent organic matter reactivity in marine sediments and patterns of benthic carbon transformation. *Biogeosciences*, 18:4651–4679.

Frings, P. (2017). Revisiting the dissolution of biogenic Si in marine sediments: a key term in the ocean Si budget. *Acta Geochim.*, 36:429–432.

Frings, P. J., Clymans, W., Fontorbe, G., De La Rocha, C. L., and Conley, D. J. (2016). The continental Si cycle and its impact on the ocean Si isotope budget. *Chem. Geol.*,

425:12–36.

Frings, P. J., De La Rocha, C., Struyf, E., van Pelt, D., Schoelynck, J., Hudson, M. M., Gondwe, M. J., Wolski, P., Mosimane, K., Gray, W., Schaller, J., and Conley, D. J. (2014). Tracing silicon cycling in the Okavango Delta, a sub-tropical flood-pulse wetland using silicon isotopes. *Geochim. Cosmochim. Acta*, 142:132–148.

Fripiat, F., Cavagna, A. J., Dehairs, F., De Brauwere, A., André, L., and Cardinal, D. (2012). Processes controlling the Si-isotopic composition in the Southern Ocean and application for paleoceanography. *Biogeosciences*, 9:2443–2457.

Gallinari, M., Ragueneau, O., Corrin, L., DeMaster, D. J., and Tréguer, P. (2002). The importance of water column processes on the dissolution properties of biogenic silica in deep-sea sediments I. Solubility. *Geochim. Cosmochim. Acta*, 66(15):2701–2717.

Gallinari, M., Ragueneau, O., DeMaster, D. J., Hartnett, H., Rickert, D., and Thomas, C. (2008). Influence of seasonal phytodetritus deposition on biogenic silica dissolution in marine sediments-Potential effects on preservation. *Deep. Res. II*, 55(22-23):2451–2464.

Gehlen, M., Malschaert, H., and Van Raaphorst, W. R. (1995). Spatial and temporal variability of benthic silica fluxes in the southeastern North Sea. *Cont. Shelf Res.*, 15(13):1675–1696.

Geilert, S., Grasse, P., Doering, K., Wallmann, K., Ehlert, C., Scholz, F., Frank, M., Schmidt, M., and Hensen, C. (2020a). Impact of ambient conditions on the Si isotope fractionation in marine pore fluids during early diagenesis. *Biogeosciences*, 17:1745–1763.

Geilert, S., Grasse, P., Wallmann, K., Liebetrau, V., and Menzies, C. D. (2020b). Serpentine alteration as source of high dissolved silicon and elevated δ30Si values to the marine Si cycle. *Nat. Commun.*, 11(5123).

Geilert, S., Vroon, P. Z., Roerdink, D. L., Van Cappellen, P., and van Bergen, M. J. (2014). Silicon isotope fractionation during abiotic silica precipitation at low temperatures: Inferences from flow-through experiments. *Geochim. Cosmochim. Acta*, 142:95–114.

Georg, R. B., Reynolds, B. C., Frank, M., and Halliday, A. N. (2006). New sample preparation techniques for the determination of Si isotopic compositions using MC-ICPMS. *Chem. Geol.*, 235(1-2):95–104.

Georg, R. B., Reynolds, B. C., West, A. J., Burton, K. W., and Halliday, A. N. (2007). Silicon isotope variations accompanying basalt weathering in Iceland. *Earth Planet. Sci. Lett.*, 261(3-4):476–490.

Georg, R. B., Zhu, C., Reynolds, B. C., and Halliday, A. N. (2009). Stable silicon isotopes of groundwater, feldspars, and clay coatings in the Navajo Sandstone aquifer, Black Mesa, Arizona, USA. *Geochim. Cosmochim. Acta*, 73:2229–2241.

Gerland, S., Renner, A. H., Godtliebsen, F., Divine, D., and Løyning, T. B. (2008). Decrease of sea ice thickness at Hopen, Barents Sea, during 1966-2007. *Geophys. Res. Lett.*, 35(6).

Giesbrecht, K. E. (2019). *Biogenic Silica Dynamics of Arctic Marine Ecosystems*. PhD thesis, University of Victoria.

Giesbrecht, K. E. and Varela, D. E. (2021). Summertime Biogenic Silica Production and Silicon Limitation in the Pacific Arctic Region From 2006 to 2016. *Global Biogeochem. Cycles*, 35(1).

Glud, R. N., Holby, O., Hoffmann, F., and Canfield, D. E. (1998). Benthic mineralization and exchange in Arctic sediments (Svalbard, Norway). *Mar. Ecol. Prog. Ser.*, 173:237–251.

Gordeev, V. V., Martin, J. M., Sidorov, I. S., and Sidorova, M. V. (1996). A reassessment of the Eurasian river input of water, sediment, major elements, and nutrients to the Arctic ocean. *Am. J. Sci.*, 296:664–691.

Gran, H. (1931). On the conditions for the production of plankton in the sea. *Conseil Perm. Internat. pour I'Explor. de la Mer. Rapp. et Proces-Verb.*, 75:37–46.

Grasse, P., Brzezinski, M. A., Cardinal, D., de Souza, G. F., Andersson, P., Closset, I., Cao, Z., Dai, M., Ehlert, C., Estrade, N., François, R., Frank, M., Jiang, G., Jones, J. L., Kooijman, E., Liu, Q., Lu, D., Pahnke, K., Ponzevera, E., Schmitt, M., Sun, X., Sutton, J. N., Thil, F., Weis, D., Wetzel, F., Zhang, A., Zhang, J., and Zhang, Z. (2017). GEOTRACES inter-calibration of the stable silicon isotope composition of dissolved silicic acid in seawater. *J. Anal. At. Spectrom.*, 32(3):562–578.

Grebmeier, J., McRoy, C., and Feder, H. (1988). Pelagic-benthic coupling on the shelf of the northern Bering and Chukchi Seas. I. Food supply source and benthic bio-mass. *Mar. Ecol. Prog. Ser.*, 48:57–67.

Grebmeier, J. M., Overland, J. E., Moore, S. E., Farley, E. V., Carmack, E. C., Cooper, L. W., Frey, K. E., Helle, J. H., McLaughlin, F. A., and McNutt, S. L. (2006). A major ecosystem shift in the northern Bering sea. *Science*, 311(5766):1461–1464.

Grotti, M., Soggia, F., Ardini, F., Bazzano, A., Moroni, B., Vivani, R., Cappelletti, D., and Misic, C. (2017). Trace elements in surface sediments from Kongsfjorden, Svalbard: occurrence, sources and bioavailability. *Int. J. Environ. Anal. Chem*, 97(5):401–418.

Gruber, C., Harlavan, Y., Pousty, D., Winkler, D., and Ganor, J. (2019). Enhanced chemical weathering of albite under seawater conditions and its potential effect on the Sr ocean budget. *Geochim. Cosmochim. Acta*, 261:20–34.

Hach (2019). Silica, Heteropoly Blue Method 8186.

Hammond, D. E., Cummins, K. M., Mcmanus, J., Berelson, W. M., Smith, G., and Spagnoli, F. (2004). Methods for measuring benthic nutrient flux on the California Margin: Comparing shipboard core incubations to in situ lander results. *Limnol. Oceanogr.: Methods*, 2(6):146–159.

Hatton, J. E. (2019). *Silicon Cycling in Subglacial Environments: An Investigation into Glacial Silicon Isotope Systematics*. PhD thesis, University of Bristol.

Hatton, J. E., Hendry, K. R., Hawkings, J. R., Wadham, J. L., Opfergelt, S., Kohler,

T. J., Yde, J. C., Stibal, M., and Žárský, J. D. (2019). Silicon isotopes in Arctic and sub-Arctic glacial meltwaters: The role of subglacial weathering in the silicon cycle. *Proc. Math. Phys. Eng. Sci.*, 475(2228).

Hátún, H., Azetsu-Scott, K., Somavilla, R., Rey, F., Johnson, C., Mathis, M., Mikolajewicz, U., Coupel, P., Tremblay, J., Hartman, S., Pacariz, S. V., Salter, I., and Ólafsson, J. (2017). The subpolar gyre regulates silicate concentrations in the North Atlantic. *Sci. Rep.*, 7(14576).

Haug, T., Bogstad, B., Chierici, M., Gjøsæter, H., Hallfredsson, E. H., Høines, Å. S., Hoel, A. H., Ingvaldsen, R. B., Jørgensen, L. L., Knutsen, T., Loeng, H., Naustvoll, L. J., Røttingen, I., and Sunnanå, K. (2017). Future harvest of living resources in the Arctic Ocean north of the Nordic and Barents Seas: A review of possibilities and constraints. *Fish. Res.*, 188:38–57.

Hawkings, J. R., Wadham, J. L., Benning, L. G., Hendry, K. R., Tranter, M., Tedstone, A., Nienow, P., and Raiswell, R. (2017). Ice sheets as a missing source of silica to the polar oceans. *Nat. Commun.*, 8(14198).

Hedges, J. I. and Keil, R. G. (1995). Sedimentary organic matter preservation: an assessment and speculative synthesis. *Mar. Chem.*, 49(2-3):81–115.

Hendry, K. R. and Andersen, M. B. (2013). The zinc isotopic composition of siliceous marine sponges: Investigating nature's sediment traps. *Chem. Geol.*, 354:33–41.

Hendry, K. R. and Brzezinski, M. A. (2014). Using silicon isotopes to understand the role of the Southern Ocean in modern and ancient biogeochemistry and climate. *Quat. Sci. Rev.*, 89:13–26.

Hendry, K. R., Georg, R. B., Rickaby, R. E., Robinson, L. F., and Halliday, A. N. (2010). Deep ocean nutrients during the Last Glacial Maximum deduced from sponge silicon isotopic compositions. *Earth Planet. Sci. Lett.*, 292(3-4):290–300.

Hendry, K. R., Huvenne, V. A., Robinson, L. F., Annett, A., Badger, M., Jacobel, A. W., Ng, H. C., Opher, J., Pickering, R. A., Taylor, M. L., Bates, S. L., Cooper, A., Cushman, G. G., Goodwin, C., Hoy, S., Rowland, G., Samperiz, A., Williams, J. A., Achterberg, E. P., Arrowsmith, C., Alexander Brearley, J., Henley, S. F., Krause, J. W., Leng, M. J., Li, T., McManus, J. F., Meredith, M. P., Perkins, R., and Woodward, E. M. S. (2019). The biogeochemical impact of glacial meltwater from Southwest Greenland. *Prog. Oceanogr.*, 176(102126).

Hendry, K. R., Leng, M. J., Robinson, L. F., Sloane, H. J., Blusztjan, J., Rickaby, R. E., Georg, R. B., and Halliday, A. N. (2011). Silicon isotopes in Antarctic sponges: An interlaboratory comparison. *Antarct. Sci.*, 23:34–42.

Hendry, K. R. and Robinson, L. F. (2012). The relationship between silicon isotope fractionation in sponges and silicic acid concentration: Modern and core-top studies of biogenic opal. *Geochim. Cosmochim. Acta*, 81:1–12.

Henson, S. A., Sanders, R., Madsen, E., Morris, P. J., Le Moigne, F., and Quartly, G. D.

(2011). A reduced estimate of the strength of the ocean's biological carbon pump. *Geophys. Res. Lett.*, 38(L04606).

Henson, S. A., Yool, A., and Sanders, R. (2015). Variability in efficiency of particulate organic carbon export: A model study. *Global Biogeochem. Cycles*, 29(1).

Hodal, H. and Kristiansen, S. (2008). The importance of small-celled phytoplankton in spring blooms at the marginal ice zone in the northern Barents Sea. *Deep. Res. II*, 55(20-21):2176–2185.

Holmes, R. M., McClelland, J. W., Peterson, B. J., Tank, S. E., Bulygina, E., Eglinton, T. I., Gordeev, V. V., Gurtovaya, T. Y., Raymond, P. A., Repeta, D. J., Staples, R., Striegl, R. G., Zhulidov, A. V., and Zimov, S. A. (2012). Seasonal and Annual Fluxes of Nutrients and Organic Matter from Large Rivers to the Arctic Ocean and Surrounding Seas. *Estuaries Coast*, 35(2):369–382.

Honjo, S., Manganini, S. J., Krishfield, R. A., and Francois, R. (2008). Particulate organic carbon fluxes to the ocean interior and factors controlling the biological pump: A synthesis of global sediment trap programs since 1983. *Prog. Oceanogr.*, 76:217–285.

Hopkins, J. (2018). The Changing Arctic Ocean Cruise JR16006, RRS James Clark Ross, Cruise Report No.51. Technical report.

Hou, Y., Hammond, D. E., Berelson, W. M., Kemnitz, N., Adkins, J. F., and Lunstrum, A. (2019). Spatial patterns of benthic silica flux in the North Pacific reflect upper ocean production. *Deep. Res. I*, 148:25–33.

Hughes, H. J., Delvigne, C., Korntheuer, M., De Jong, J., André, L., and Cardinal, D. (2011). Controlling the mass bias introduced by anionic and organic matrices in silicon isotopic measurements by MC-ICP-MS. *J. Anal. At. Spectrom.*, 26(9):1892–1896.

Hughes, H. J., Sondag, F., Santos, R. V., André, L., and Cardinal, D. (2013). The riverine silicon isotope composition of the Amazon Basin. *Geochim. Cosmochim. Acta*, 121:637–651.

Hulth, S., Blackburn, H., and Hall, P. (1994). Arctic sediments (Svalbard): consumption and microdistribution of oxygen. *Mar. Chem.*, 46:293–316.

Hulth, S., Hall, P., Blackburn, T. H., and Landen, A. (1996). Arctic sediments (Svalbard): pore water and solid phase distributions of C, N, P and Si. *Polar Biol.*, 16:447–462.

Hurd, D. (1983). Physical and chemical properties of siliceous skeletons. In Aston, S. R., editor, *Silicon Geochemistry and Biogeochemistry*, pages 187–244. Academic Press, London.

Hurd, D. C. (1972). Factors affecting solution rate of biogenic opal in seawater. *Earth Planet. Sci. Lett.*, 15(4):411–417.

Hurd, D. C. (1973). Interactions of biogenic opal, sediment and seawater in the Central Equatorial Pacific. *Geochim. Cosmochim. Acta*, 37:2257–2282.

Hurd, D. C., Fraley, C., and Fugate, J. K. (1979). Silica Apparent Solubilities and Rates of Dissolution and Precipitation for ca. 25 Common Minerals at 1°-2°C, pH 7.5-8.5 in

Seawater. In Jenne, E., editor, *Chemical Modeling in Aqueous Systems*, chapter 21, pages 413–445. American Chemical Society, Washington, DC.

Hutchins, D. A. and Bruland, K. W. (1998). Iron-limited diatom growth and Si:N uptake ratios in a coastal upwelling regime. *Nature*, 393:561–564.

Hyun, J. H., Kim, S. H., Mok, J. S., Cho, H., Lee, T., Vandieken, V., and Thamdrup, B. (2017). Manganese and iron reduction dominate organic carbon oxidation in surface sediments of the deep Ulleung Basin, East Sea. *Biogeosciences*, 14:941–958.

ICES (2008). *The Barents Sea and the Norwegian Sea*.

ICES (2016). Barents Sea Ecoregion – Ecosystem overview. *ICES Advice 2016, Book 9*.

Ikeda, M. (1990). Decadal oscillations of the air-ice-ocean system in the northern hemisphere. *Atmos. - Ocean*, 28(1):106–139.

Ingvaldsen, R., Loeng, H., and Asplin, L. (2002). Variability in the Atlantic inflow to the Barents Sea based on a one-year time series from moored current meters. *Cont. Shelf Res.*, 22(3):505–519.

Ingvaldsen, R. B., Assmann, K. M., Primicerio, R., Fossheim, M., Polyakov, I. V., and Dolgov, A. V. (2021). Physical manifestations and ecological implications of Arctic Atlantification. *Nat. Rev. Earth Environ.*, 2:874–889.

IPCC (2021). Summary for Policymakers. In Masson-Delmotte, V., Zhai, P., Pirani, A., Connors, S., Péan, C., Berger, S., Caud, N., Chen, Y., Goldfarb, L., Gomis, M., Huang, M., Leitzell, K., Lonnoy, E., J.B.R., Matthews, Maycock, T., Waterfield, T., Yelekçi, O., Yu, R., and Zhou, B., editors, *Climate Change 2021: The Physical Science Basis. Contribution of Working Group I to the Sixth Assessment Report of the Intergovernmental Panel on Climate Change*, pages 3–32. Cambridge University Press, Cambridge, United Kingdom and New York, NY, USA.

Isson, T. T. and Planavsky, N. J. (2018). Reverse weathering as a long-term stabilizer of marine pH and planetary climate. *Nature*, 560:471–475.

Ivanov, B. V., Gerland, S., Winther, J. G., and Goodwin, H. (2003). Energy exchange processes in the marginal ice zone of the Barents Sea, Arctic Ocean, during spring 1999. *J. Glaciol.*, 49(166):415–419.

Ivanov, G. (2011). Bottom sediments of Barents Sea: distribution and sorption capacity. In Lyubin, P., Jørgensen, L., Anisimova, N., Manushin, I., Prohorova, T., Zakharov, D., Viaznikova, V., Juravleva, N., Golikov, A., Morov, A., Zimina, O., and Lyubina, O., editors, *Biological – Geological Seabed Mapping and Monitoring in the Barents Sea*, chapter 2.2, pages 18–21. Murmansk.

Iversen, M. H. and Ploug, H. (2013). Temperature effects on carbon-specific respiration rate and sinking velocity of diatom aggregates – potential implications for deep ocean export processes. *Biogeosciences*, 10:4073–4085.

Jakobsson, M., Grantz, A., Kristoffersen, Y., and Macnab, R. (2003). Physiographic provinces of the Arctic Ocean seafloor. *Geol. Soc. Am. Bull.*, 115(12):1443–1455.

Jakobsson, M., Mayer, L., Coakley, B., Dowdeswell, J. A., Forbes, S., Fridman, B., Hodnesdal, H., Noormets, R., Pedersen, R., Rebesco, M., Schenke, H. W., Zarayskaya, Y., Accettella, D., Armstrong, A., Anderson, R. M., Bienhoff, P., Camerlenghi, A., Church, I., Edwards, M., Gardner, J. V., Hall, J. K., Hell, B., Hestvik, O., Kristoffersen, Y., Marcussen, C., Mohammad, R., Mosher, D., Nghiem, S. V., Pedrosa, M. T., Travaglini, P. G., and Weatherall, P. (2012). The International Bathymetric Chart of the Arctic Ocean (IBCAO) Version 3.0. *Geophys. Res. Lett.*, 39(12).

Janssen, F., Huettel, M., and Witte, U. (2005). Pore-water advection and solute fluxes in permeable marine sediments (II): Benthic respiration at three sandy sites with different permeabilities (German Bight, North Sea). *Limnol. Oceanogr.*, 50(3):779–792.

Jeandel, C. and Oelkers, E. H. (2015). The influence of terrigenous particulate material dissolution on ocean chemistry and global element cycles. *Chem. Geol.*, 395:50–66.

Jeandel, C., Peucker-Ehrenbrink, B., Jones, M. T., Pearce, C. R., Oelkers, E. H., Godderis, Y., Lacan, F., Aumont, O., and Arsouze, T. (2011). Ocean margins: The missing term in oceanic element budgets? *Eos*, 92(26):217–224.

Jensen, M. M., Thamdrup, B., Rysgaard, S., Holmer, M., and Fossing, H. (2003). Rates and regulation of microbial iron reduction in sediments of the Baltic-North Sea transition. *Biogeochemistry*, 65:295–317.

Jia, J., Liu, Z., Bechtel, A., Strobl, S. A., and Sun, P. (2013). Tectonic and climate control of oil shale deposition in the Upper Cretaceous Qingshankou Formation (Songliao Basin, NE China). *Int. J. Earth Sci.*, 102:1717–1734.

Jones, E. P. and Anderson, L. G. (1986). On the origin of the chemical properties of the Arctic Ocean halocline. *J. Geophys. Res.*, 91:10759–10767.

Jones, E. P. and Coote, A. R. (1980). Nutrient Distributions in the Canadian Archipelago: Indicators of Summer Water Mass and Flow Characteristics. *Can. J. Fish. Aquat. Sci.*, 37:589–599.

Jones, M. T., Pearce, C. R., and Oelkers, E. H. (2012). An experimental study of the interaction of basaltic riverine particulate material and seawater. *Geochim. Cosmochim. Acta*, 77:108–120.

Jørgensen, B., Bang, M., and Blackburn, H. (1990). Anaerobic mineralization in marine sediments from the Baltic Sea-North Sea transition. *Mar. Ecol. Prog. Ser.*, 59:39–94.

Jørgensen, B. B. (1982). Mineralization of organic matter in the sea bed - The role of sulphate reduction. *Nature*, 296:643–645.

Jørgensen, B. B., Glud, R. N., and Holby, O. (2005). Oxygen distribution and bioirrigation in Arctic fjord sediments (Svalbard, Barents Sea). *Mar. Ecol. Prog. Ser.*, 2:85–95.

Kamatani, A. (1982). Dissolution rates of silica from diatoms decomposing at various temperatures. *Mar. Biol.*, 68:91–96.

Kamatani, A. and Oku, O. (2000). Measuring biogenic silica in marine sediments. *Mar. Chem.*, 68(3):219–229.

Karaseva, T. (2010). Survey report from the joint Norwegian/Russian ecosystem survey in the Barents Sea August–October 2009. Technical report, IMR/PINRO, Bergen.

Karl, D. M. and Tien, G. (1992). MAGIC: A sensitive and precise method for measuring dissolved phosphorus in aquatic environments. *Limnol. Oceanogr.*, 37(1):105–116.

Kedra, M., Renaud, P. E., Andrade, H., Goszczko, I., and Ambrose, W. G. (2013). Benthic community structure, diversity, and productivity in the shallow Barents Sea bank (Svalbard Bank). *Mar. Biol.*, 160:805–819.

Kemp, E., Roseburrough, R., Elliott, E., and Krause, J. (2021). Spatial Variability of Sediment Amorphous Silica and its Reactivity in a Northern Gulf of Mexico Estuary and Coastal Zone. *Gulf Caribb. Res.*, 32.

Kennedy, C. B., Scott, S. D., and Ferris, F. G. (2003). Ultrastructure and potential subseafloor evidence of bacteriogenic iron oxides from Axial Volcano, Juan de Fuca Ridge, north-east Pacific Ocean. *FEMS Microbiol. Ecol.*, 43(2):247–254.

Khalil, K., Rabouille, C., Gallinari, M., Soetaert, K., DeMaster, D. J., and Ragueneau, O. (2007). Constraining biogenic silica dissolution in marine sediments: A comparison between diagenetic models and experimental dissolution rates. *Mar. Chem.*, 106:223–238.

Kim, J., Dong, H., Seabaugh, J., Newell, S. W., and Eberl, D. D. (2004). Role of Microbes in the Smectite-to-Illite Reaction. *Science*, 303:830–832.

King, S., Froelich, P., and Jahnke, R. (2000). Early diagenesis of germanium in sediments of the Antarctic South Atlantic: In search of the missing Ge sink. *Geochim. Cosmochim. Acta*, 64(8):1375–1390.

Knies, J. and Martinez, P. (2009). Organic matter sedimentation in the western Barents Sea region: Terrestrial and marine contribution based on isotopic composition and organic nitrogen content. *Nor. J. Geol.*, 89(1):79–89.

Knies, J. and Stein, R. (1998). New aspects of organic carbon deposition and its paleoceanographic implications along the Northern Barents Sea Margin during the last 30,000 years. *Paleoceanography*, 13(4):384–394.

Koenigk, T. and Brodeau, L. (2014). Ocean heat transport into the Arctic in the twentieth and twenty-first century in EC-Earth. *Clim. Dyn.*, 42:3101–3120.

Koning, E., Epping, E., and Van Raaphorst, W. (2002). Determining biogenic silica in marine samples by tracking silicate and aluminium concentrations in alkaline leaching solutions. *Aquat. Geochem.*, 8:37–67.

Kostka, J. E., Gribsholt, B., Petrie, E., Dalton, D., Skelton, H., and Kristensen, E. (2002). The rates and pathways of carbon oxidation in bioturbated saltmarsh sediments. *Limnol. Oceanogr.*, 47(1):230–240.

Kostka, J. E., Thamdrup, B., Glud, R. N., and Canfield, D. E. (1999). Rates and pathways of carbon oxidation in permanently cold Arctic sediments. *Mar. Ecol. Prog. Ser.*, 180:7–21.

Krause, J. W., Darrow, E. S., Pickering, R. A., Carmichael, R. H., Larson, A. M., and Basaldua, J. L. (2017). Reactive silica fractions in coastal lagoon sediments from the northern Gulf of Mexico. *Cont. Shelf Res.*, 151:8–14.

Krause, J. W., Duarte, C. M., Marquez, I. A., Assmy, P., Fernández-Méndez, M., Wiedmann, I., Wassmann, P., Kristiansen, S., and Agustí, S. (2018). Biogenic silica production and diatom dynamics in the Svalbard region during spring. *Biogeosciences*, 15(21):6503–6517.

Krause, J. W., Schulz, I. K., Rowe, K. A., Dobbins, W., Winding, M. H., Sejr, M. K., Duarte, C. M., and Agustí, S. (2019). Silicic acid limitation drives bloom termination and potential carbon sequestration in an Arctic bloom. *Sci. Rep.*, 9(8149).

Krissansen-Totton, J. and Catling, D. C. (2020). A coupled carbon-silicon cycle model over Earth history: Reverse weathering as a possible explanation of a warm mid-Proterozoic climate. *Earth Planet. Sci. Lett.*, 537(116181).

Kristiansen, S. and Farbrot, T. (1991). Nitrogen uptake rates in phytoplankton and ice algae in the Barents Sea. *Polar Res.*, 10(1):187–192.

Krom, M. D., Cliff, R. A., Eijsink, L. M., Herut, B., and Chester, R. (1999). The characterisation of Saharan dusts and Nile particulate matter in surface sediments from the Levantine basin using Sr isotopes. *Mar. Geol.*, 155(3-4):319–330.

Kulakov, M., Pogrebov, V., Timofeyev, S., Nhernova, M., and Kiyko, O. (2006). Ecosystem of the Barents and Kara Seas Coastal Segment. *The Sea*, 14b:1139–1177.

Kulikov, N. (2004). Amorphous silica contents in bottom sediments from the Kara Sea. PANGAEA.

Lalande, C., Bauerfeind, E., Nöthig, E. M., and Beszczynska-Möller, A. (2013a). Impact of a warm anomaly on export fluxes of biogenic matter in the eastern Fram Strait. *Prog. Oceanogr.*, 109:70–77.

Lalande, C., Bauerfeind, E., Nöthig, E. M., and Beszczynska-Möller, A. (2013b). Impact of a warm anomaly on export fluxes of biogenic matter in the eastern Fram Strait. *Prog. Oceanogr.*, 109:70–77.

Lalande, C., Grebmeier, J. M., Wassmann, P., Cooper, L. W., Flint, M. V., and Sergeeva, V. M. (2007). Export fluxes of biogenic matter in the presence and absence of seasonal sea ice cover in the Chukchi Sea. *Cont. Shelf Res.*, 27(15):2051–2065.

Lalande, C., Moriceau, B., Leynaert, A., and Morata, N. (2016). Spatial and temporal variability in export fluxes of biogenic matter in Kongsfjorden. *Polar Biol.*, 39:1725–1738.

LaRowe, D. E. and Van Cappellen, P. (2011). Degradation of natural organic matter: A thermodynamic analysis. *Geochim. Cosmochim. Acta*, 75(8):2030–2042.

Laruelle, G. G., Roubeix, V., Sferratore, A., Brodherr, B., Ciuffa, D., Conley, D. J., Dürr, H. H., Garnier, J., Lancelot, C., LeThiPhuong, Q., Meunier, J. D., Meybeck, M., Michalopoulos, P., Moriceau, B., Ni Longphuirt, S., Loucaides, S., Papush, L.,

Presti, M., Ragueneau, O., Regnier, P., Saccone, L., Slomp, C. P., Spiteri, C., and Van Cappellen, P. (2009). Anthropogenic perturbations of the silicon cycle at the global scale: Key role of the land-ocean transition. *Global Biogeochem. Cycles*, 23(4).

Lawson, D. S., Hurd, D. C., and Pankratz, H. S. (1978). Silica dissolution rates of decomposing phytoplankton assemblages at various temperatures. *Am. J. Sci.*, 278:1373–1393.

Lehtimäki, M., Sinkko, H., and Tallberg, P. (2016). The role of oxygen conditions in the microbial dissolution of biogenic silica under brackish conditions. *Biogeochemistry*, 129:355–371.

Lein, A., Pimenov, N., Rusanov, I., Pavlova, G., Savvichec, A., and Verkhovskayaya, Z. (2008). Methane Cycle in the Barents Sea. *Lithol. Miner. Resour.*, 43(5):405–428.

Lerman, A., Mackenzie, F. T., and Bricker, O. P. (1975). Rates of dissolution of aluminosilicates in seawater. *Earth Planet. Sci. Lett.*, 25(1):82–88.

Levitus, S., Matishov, G., Seidov, D., and Smolyar, I. (2009). Barents Sea multidecadal variability. *Geophys. Res. Lett.*, 36(19).

Li, Y., Hou, K., Wan, D., Zhang, Z., and Yue, G. (2014). Precambrian banded iron formations in the north china craton: Silicon and oxygen isotopes and genetic implications. *Ore Geol. Rev.*, 57:299–307.

Li, Y. H. and Gregory, S. (1974). Diffusion of ions in seawater and in deep-sea sediments. *Geochim. Cosmochim. Acta*, 38(5):703–714.

Lien, V. S., Vikebø, F. B., and Skagseth, O. (2013). One mechanism contributing to co-variability of the Atlantic inflow branches to the Arctic. *Nat. Commun.*, 4(1488).

Liguori, B. T., Ehlert, C., and Pahnke, K. (2020). The Influence of Water Mass Mixing and Particle Dissolution on the Silicon Cycle in the Central Arctic Ocean. *Front. Earth Sci.*, 7(202).

Lind, S. and Ingvaldsen, R. B. (2012). Variability and impacts of Atlantic Water entering the Barents Sea from the north. *Deep. Res. I*, 62:70–88.

Lind, S., Ingvaldsen, R. B., and Furevik, T. (2018). Arctic warming hotspot in the northern Barents Sea linked to declining sea-ice import. *Nature Climate Change*, 8:634–639.

Liu, D., Yuan, P., Tian, Q., Liu, H., Deng, L., Song, Y., Zhou, J., Losic, D., Zhou, J., Song, H., Guo, H., and Fan, W. (2019). Lake sedimentary biogenic silica from diatoms constitutes a significant global sink for aluminium. *Nat. Commun.*, 10(4829).

Liu, G., Qiu, S., Liu, B., Pu, Y., Gao, Z., Wang, J., Jin, R., and Zhou, J. (2017a). Microbial reduction of Fe(III)-bearing clay minerals in the presence of humic acids. *Sci. Rep.*, 7(45354).

Liu, J., Ye, S., Allen Laws, E., Xue, C., Yuan, H., Ding, X., Zhao, G., Yang, S., He, L., Wang, J., Pei, S., Wang, Y., and Lu, Q. (2017b). Sedimentary environment evolution and biogenic silica records over 33,000 years in the Liaohe delta, China. *Limnol. Oceanogr.*, 62(2):474–489.

Liu, S. M., Ye, X. W., Zhang, J., and Zhao, Y. F. (2002). Problems with biogenic silica

measurement in marginal seas. *Mar. Geol.*, 192(4):383–392.

Liu, S. M., Zhang, J., and Li, R. X. (2005). Ecological significance of biogenic silica in the East China Sea. *Mar. Ecol. Prog. Ser.*, 290:15–26.

Loeng, H. (1991). Features of the physical oceanographic conditions of the Barents Sea. *Polar Res.*, 10(1):5–18.

Lomas, M. W., Baer, S. E., Acton, S., and Krause, J. W. (2019). Pumped up by the cold: Elemental quotas and stoichiometry of cold-water diatoms. *Front. Mar. Sci.*, 6(286).

Loucaides, S., Koning, E., and Van Cappellen, P. (2012a). Effect of pressure on silica solubility of diatom frustules in the oceans: Results from long-term laboratory and field incubations. *Mar. Chem.*, 136-137:1–6.

Loucaides, S., Michalopoulos, P., Presti, M., Koning, E., Behrends, T., and Van Cappellen, P. (2010). Seawater-mediated interactions between diatomaceous silica and terrigenous sediments: Results from long-term incubation experiments. *Chem. Geol.*, 270:68–79.

Loucaides, S., van Cappellen, P., Roubeix, V., Moriceau, B., and Ragueneau, O. (2012b). Controls on the Recycling and Preservation of Biogenic Silica from Biomineralization to Burial. *Silicon*, 4(1):7–22.

Luchetta, A., Ponitz, P., and Ilyin, G. (2021). Chemical oceanography during POLARSTERN cruise ARK-IX/4. PANGAEA.

Lybrand, R. A., Austin, J. C., Fedenko, J., Gallery, R. E., Rooney, E., Schroeder, P. A., Zaharescu, D. G., and Qafoku, O. (2019). A coupled microscopy approach to assess the nano-landscape of weathering. *Sci. Rep.*, 9(5377).

Macdonald, R. W., Anderson, L. G., Christensen, J. P., Miller, L. A., Semiletov, I. P., and Stein, R. (2010). The Arctic Ocean. In Liu, K. K., Atkinson, L., Quinones, R., and Talaue-McManus, L., editors, *Carbon and nutrient fluxes in continental margins: a global synthesis*, chapter 6.2, pages 291–303. Sperling-Verlag, Berlin.

Mackenzie, F. and Garrels, R. (1965). Silicates: Reactivity with Sea Water. *Science*, 150(3692):57–58.

Mackenzie, F. T., Garrels, R. M., Bricker, O. P., and Bickley, F. (1967). Silica in sea water: Control by silica minerals. *Science*, 155(3768):1404–1405.

Mackin, J. E. and Aller, R. C. (1984). Dissolved Al in sediments and waters of the East China Sea: Implications for authigenic mineral formation. *Geochim. Cosmochim. Acta*, 48:281–297.

Maiti, K., Carroll, J. L., and Benitez-Nelson, C. R. (2010). Sedimentation and particle dynamics in the seasonal ice zone of the Barents Sea. *J. Mar. Syst.*, 79(1-2):185–198.

Makarevich, P. R., Larionov, V. V., Vodopyanova, V. V., Bulavina, A. S., Ishkulova, T. G., Venger, M. P., Pastukhov, I. A., and Vashchenko, A. V. (2022). Phytoplankton of the Barents Sea at the Polar Front in Spring. *Oceanology*, 61:930–943.

Maldonado, M., Carmona, M. C., Velásquez, Z., Puig, A., Cruzado, A., López, A., and Young, C. M. (2005). Siliceous sponges as a silicon sink: An overlooked aspect of

benthopelagic coupling in the marine silicon cycle. *Limnol. Oceanogr.*, 50(3):799–809.

Maldonado, M., López-Acosta, M., Sitjà, C., García-Puig, M., Galobart, C., Ercilla, G., and Leynaert, A. (2019). Sponge skeletons as an important sink of silicon in the global oceans. *Nat. Geosci.*, 12:815–822.

Martin, W. and Bender, M. (1988). The variability of benthic fluxes and sedimentary remineralization rates in response to seasonally variable organic carbon rain rates in the deep sea; a modeling study. *Am. J. Sci.*, 288(6):561–574.

März, C., Meinhardt, A. K., Schnetger, B., and Brumsack, H. J. (2015). Silica diagenesis and benthic fluxes in the Arctic Ocean. *Mar. Chem.*, 171:1–9.

Mason, T. F., Weiss, D. J., Horstwood, M., Parrish, R. R., Russell, S. S., Mullane, E., and Coles, B. J. (2004). High-precision Cu and Zn isotope analysis by plasma source mass spectrometry Part 2. † Correcting for mass discrimination effects. *J. Anal. At. Spectrom.*, 19(2):218–226.

Mathewson, J. H. (2003). Oceanography, Chemical. In Meyers, R. A., editor, *Encyclopedia of Physical Science and Technology (Third Edition)*, pages 99–115. Academic Press.

Mauritzen, C. (1996). Production of dense overflow waters feeding the North Atlantic across the Greenland-Scotland Ridge. Part 2: An inverse model. *Deep. Res. I*, 43(6):807–835.

Mavromatis, V., Rinder, T., Prokushkin, A. S., Pokrovsky, O. S., Korets, M. A., Chmeleff, J., and Oelkers, E. H. (2016). The effect of permafrost, vegetation, and lithology on Mg and Si isotope composition of the Yenisey River and its tributaries at the end of the spring flood. *Geochim. Cosmochim. Acta*, 191:32–46.

McLennan, S. M. (2001). Relationships between the trace element composition of sedimentary rocks and upper continental crust. *Geochem. Geophys. Geosystems.*, 2(4).

McManus, J., Hammond, D. E., Berelson, W. M., Kilgore, T. E., DeMaster, D. J., Ragueneau, O. G., and Collier, R. W. (1995). Early diagenesis of biogenic opal: Dissolution rates, kinetics, and paleoceanographic implications. *Deep. Res. II*, 42(2-3):871–903.

Michalopoulos, P. and Aller, R. C. (1995). Rapid clay mineral formation in Amazon delta sediments: Reverse weathering and oceanic elemental cycles. *Science*, 270:614–617.

Michalopoulos, P. and Aller, R. C. (2004). Early diagenesis of biogenic silica in the Amazon delta: Alteration, authigenic clay formation, and storage. *Geochim. Cosmochim. Acta*, 68(5):1061–1085.

Middag, R., de Baar, H. J., Laan, P., and Bakker, K. (2009). Dissolved aluminium and the silicon cycle in the Arctic Ocean. *Mar. Chem.*, 115(3-4):176–195.

Middelburg, J. J., Soetaert, K., and Herman, P. M. (1997). Empirical relationships for use in global diagenetic models. *Deep. Res. I*, 44(2):327–344.

Milligan, A. J., Varela, D. E., Brzezinski, M. A., and Morel, F. M. (2004). Dynamics of silicon metabolism and silicon isotopic discrimination in a marine diatom as a function of pCO2. *Limnol. Oceanogr.*, 49:322–329.

Mogollón, J. M., Dale, A. W., Fossing, H., and Regnier, P. (2012). Timescales for the development of methanogenesis and free gas layers in recently-deposited sediments of Arkona Basin (Baltic Sea). *Biogeosciences*, 9:1915–1933.

Monien, P., Lettmann, K. A., Monien, D., Asendorf, S., W, A. C., Lim, C. H., Thal, J., Schnetger, B., and Brumsack, H. J. (2014). Redox conditions and trace metal cycling in coastal sediments from the maritime Antarctic. *Geochim. Cosmochim. Acta*, 141:26–44.

Moran, S. B., Ellis, K. M., and Smith, J. N. (1997). 234Th/238U disequilibrium in the central Arctic Ocean: Implications for particulate organic carbon export. *Deep. Res. II*, 44(8):1593–1606.

Morata, D., Polvé, M., Valdés, A., Belmar, M., Dinator, M. I., Silva, M., Leiva, M. A., Aigouy, T., and Morales, J. R. (2008). Characterisation of aerosol from Santiago, Chile: An integrated PIXE-SEM-EDX study. *Environ. Geol.*, 56:81–95.

Morata, N., Michaud, E., and Włodarska-Kowalczuk, M. (2013). Impact of early food input on the Arctic benthos activities during the polar night. *Polar Biol.*, 38(1):99–114.

Morel, F. and Hering, J. (1993). *Principles and Applications of Aquatic Chemistry*. John Wiley & Sons, Inc., New York.

Morin, G. P., Vigier, N., and Verney-Carron, A. (2015). Enhanced dissolution of basaltic glass in brackish waters: Impact on biogeochemical cycles. *Earth Planet. Sci. Lett.*, 417:1–8.

Morley, D. W., Leng, M. J., Mackay, A. W., Sloane, H. J., Rioual, P., and Battarbee, R. W. (2004). Cleaning of lake sediment samples for diatom oxygen isotope analysis. *J. Paleolimnol.*, 31:391–401.

Mortlock, R. A. and Froelich, P. N. (1989). A simple method for the rapid determination of biogenic opal in pelagic marine sediments. *Deep. Res. A*, 36(9):1415–1426.

Nakicenovic, N. and Swart, R. (2000). Emission Scenarios. Technical report.

Nelson, D. M. and Brzezinski, M. A. (1997). Diatom growth and productivity in an oligotropic midocean gyre: A 3-yr record from the Sargasso Sea near Bermuda. *Limnol. Oceanogr.*, 42(3):473–486.

Nelson, D. M., Tréguer, P., Brzezinski, M. A., Leynaert, A., and Quéguiner, B. (1995). Production and dissolution of biogenic silica in the ocean: Revised global estimates, comparison with regional data and relationship to biogenic sedimentation. *Global Biogeochem. Cycles*, 9(3):359–372.

Neukermans, G., Oziel, L., and Babin, M. (2018). Increased intrusion of warming Atlantic water leads to rapid expansion of temperate phytoplankton in the Arctic. *Glob. Change Biol.*, 24(6):2545–2553.

Ng, H. C., Cassarino, L., Pickering, R. A., Woodward, E. M. S., Hammond, S. J., and Hendry, K. R. (2020). Sediment efflux of silicon on the Greenland margin and implications for the marine silicon cycle. *Earth Planet. Sci. Lett.*, 529(115877).

Nickel, M., Vandieken, V., Brüchert, V., and Jørgensen, B. B. (2008). Microbial Mn(IV)

and Fe(III) reduction in northern Barents Sea sediments under different conditions of ice cover and organic carbon deposition. *Deep. Res. II*, 55:2390–2398.

Niemistö, J., Kononets, M., Ekeroth, N., Tallberg, P., Tengberg, A., and Hall, P. O. (2018). Benthic fluxes of oxygen and inorganic nutrients in the archipelago of Gulf of Finland, Baltic Sea – Effects of sediment resuspension measured in situ. *J. Sea Res.*, 135:95–106.

Odin, G. and Matter, A. (1981). De glauconiarum origine. *Sedimentology*, 28(5):611–641.

Odin, G. S. and Fröhlich, F. (1988). Chapter C3 Glaucony from the Kerguelen Plateau (Southern Indian Ocean). *Dev. Sedimentol.*, 45:277–294.

Oelze, M., von Blanckenburg, F., Hoellen, D., Dietzel, M., and Bouchez, J. (2014). Si stable isotope fractionation during adsorption and the competition between kinetic and equilibrium isotope fractionation: Implications for weathering systems. *Chem. Geol.*, 380:161–171.

Olli, K., Wexels Riser, C., Wassmann, P., Ratkova, T., Arashkevich, E., and Pasternak, A. (2002a). Seasonal variation in vertical flux of biogenic matter in the marginal ice zone and the central Barents Sea. *J. Mar. Syst.*, 38:189 – 204.

Olli, K., Wexels Riser, C., Wassmann, P., Ratkova, T., Arashkevich, E., and Pasternak, A. (2002b). Seasonal variation in vertical flux of biogenic matter in the marginal ice zone and the central Barents Sea. *J. Mar. Syst.*, 38(1-2):189–204.

Onarheim, I. H. and Årthun, M. (2017). Toward an ice-free Barents Sea. *Geophys. Res. Lett.*, 44(16):8387–8395.

Opfergelt, S., de Bournonville, G., Cardinal, D., André, L., Delstanche, S., and Delvaux, B. (2009). Impact of soil weathering degree on silicon isotopic fractionation during adsorption onto iron oxides in basaltic ash soils, Cameroon. *Geochim. Cosmochim. Acta*, 73(24):7226–7240.

Opfergelt, S. and Delmelle, P. (2012). Silicon isotopes and continental weathering processes: Assessing controls on Si transfer to the ocean. *C. R. - Geosci.*, 344(11-12):723–738.

Orkney, A., Platt, T., Narayanaswamy, B. E., Kostakis, I., and Bouman, H. A. (2020). Bio-optical evidence for increasing Phaeocystis dominance in the Barents Sea: Increasing Phaeocystis in Barents Sea. *Philos. Trans. Royal Soc. A*, 378(2181).

Orsi, T. H. and Dunn, D. A. (1991). Correlations between sound velocity and related properties of glacio-marine sediments: Barents sea. *Geo-Mar. Lett.*, 11:79–83.

Otterå, O. H., Bentsen, M., Bethke, I., and Kvamstø, N. G. (2009). Simulated pre-industrial climate in Bergen Climate Model (version 2): model description and large-scale circulation features. *Geosci. Model Dev.*, 2:197–212.

Ozhigin, V., Ingvaldsen, R., Loeng, H., Boitsov, V., and Karsakov, A. (2011). Introduction to the Barents Sea. In Jakobsen, T. and Ozhigin, V., editors, *The Barents Sea Ecosystem, Resources, Management. Half a Century of Russian-Norwegian Cooperation*, pages

39–76. Tapir Academic Press.

Oziel, L., Baudena, A., Ardyna, M., Massicotte, P., Randelhoff, A., Sallée, J. B., Ingvaldsen, R. B., Devred, E., and Babin, M. (2020). Faster Atlantic currents drive poleward expansion of temperate phytoplankton in the Arctic Ocean. *Nat. Commun.*, 11(1705).

Oziel, L., Neukermans, G., Ardyna, M., Lancelot, C., Tison, J. L., Wassmann, P., Sirven, J., Ruiz-Pino, D., and Gascard, J. C. (2017). Role for Atlantic inflows and sea ice loss on shifting phytoplankton blooms in the Barents Sea. *J. Geophys. Res.: Oceans*, 122(6):5121–5139.

Oziel, L., Sirven, J., and Gascard, J. C. (2016). The Barents Sea frontal zones and water masses variability (1980-2011). *Ocean Sci.*, 12:169–184.

Pacariz, S. V., Hátún, H., Jacobsen, J. A., Johnson, C., Eliasen, S., and Rey, F. (2016). Nutrient-driven poleward expansion of the Northeast Atlantic mackerel (Scomber scombrus) stock: A new hypothesis. *Elementa*, 4(7059).

Parsons, A. R., Bourke, R. H., Muench, R. D., Chiu, C.-S., Lynch, J. F., Miller, J. H., Plueddemann, A. J., and Pawlowicz, R. (1996). The Barents Sea Polar Front in summer. *J. Geophys. Res. Oceans*, 101(C6):14201–14221.

Pathirana, I., Knies, J., Felix, M., and Mann, U. (2014). Towards an improved organic carbon budget for the western Barents Sea shelf. *Clim. Past*, 10:569–587.

Pattan, J. N., Parthiban, G., Gupta, S. M., and Mir, I. A. (2012). Fe speciation and Fe/Al ratio in the sediments of southeastern Arabian Sea as an indicator of climate change. *Quat. Int.*, 250:19–26.

Pavlov, V., Pavlova, O., and Korsnes, R. (2004). Sea ice fluxes and drift trajectories from potential pollution sources, computed with a statistical sea ice model of the Arctic Ocean. *J. Mar. Syst.*, 48(1-4):133–157.

Pearson, T. and Rosenberg, R. (1978). Macrobenthic succession in relation to organic enrichment and pollution of the marine environment. *Oceanogr. Mar. Biol.*, 16:229–311.

Peña, M. A., Denman, K. L., Calvert, S. E., Thomson, R. E., and Forbes, J. R. (1999). The seasonal cycle in sinking particle fluxes off Vancouver Island, British Columbia. *Deep. Res. II*, 46(11-12):2969–2992.

Petoukhov, V. and Semenov, V. A. (2010). A link between reduced Barents-Kara sea ice and cold winter extremes over northern continents. *J. Geophys. Res. Atmos.*, 115(D21).

Pfannkuche, O. and Thiel, H. (1987). Meiobenthic stocks and benthic activity on the NE-Svalbard shelf and in the Nansen Basin. *Polar Biol.*, 7:253–266.

Pickering, R. (2020). *Silica Cycling at the Sediment Water Interface of Coastal Systems.* PhD thesis, The University of South Alabama College of Arts and Sciences.

Pickering, R., Cassarino, L., Hendry, K., Wang, X., Maiti, K., and Krause, J. (2020). Using Stable Isotopes to Disentangle Marine SedimentarySignals in Reactive Silicon Pools. *Geophys. Res. Lett.*, 47(15).

Piepenburg, D., Blackburn, T. H., VonDorrien, C. F., Gutt, J., Hall, P. O., Hulth, S., Kendall, M. A., Opalinski, K. W., Rachor, E., and Schmid, M. K. (1995). Partitioning of benthic community respiration in the Arctic (northwestern Barents Sea). *Mar. Ecol. Prog. Ser.*, 118(1-3):199–213.

Pirrung, M., Illner, P., and Matthiessen, J. (2008). Biogenic barium in surface sediments of the European Nordic Seas. *Mar. Geol.*, 250(1-2):89–103.

Pokrovsky, O. S., Reynolds, B. C., Prokushkin, A. S., Schott, J., and Viers, J. (2013). Silicon isotope variations in Central Siberian rivers during basalt weathering in permafrost-dominated larch forests. *Chem. Geol.*, 335:103–116.

Pokrovsky, O. S., Viers, J., Shirokova, L. S., Shevchenko, V. P., Filipov, A. S., and Dupré, B. (2010). Dissolved, suspended, and colloidal fluxes of organic carbon, major and trace elements in the Severnaya Dvina River and its tributary. *Chem. Geol.*, 273:136–149.

Polyakov, I. V., Pnyushkov, A. V., Alkire, M. B., Ashik, I. M., Baumann, T. M., Carmack, E. C., Goszczko, I., Guthrie, J., Ivanov, V. V., Kanzow, T., Krishfield, R., Kwok, R., Sundfjord, A., Morison, J., Rember, R., and Yulin, A. (2017). Greater role for Atlantic inflows on sea-ice loss in the Eurasian Basin of the Arctic Ocean. *Science*, 365(6335):285–291.

Presti, M. and Michalopoulos, P. (2008). Estimating the contribution of the authigenic mineral component to the long-term reactive silica accumulation on the western shelf of the Mississippi River Delta. *Cont. Shelf Res.*, 28(6):823–838.

Price, N. B., Brand, T., Pates, J. M., Mowbray, S., Theocharis, A., Civitarese, G., Miserocchi, S., Heussner, S., and Lindsay, F. (1999). Horizontal distributions of biogenic and lithogenic elements of suspended particulate matter in the Mediterranean Sea. *Prog. Oceanogr.*, 44(1-3):191–218.

Qin, Y. C., Weng, H. X., Jin, H., Chen, J., and Tian, R. X. (2012). Estimation of authigenic alteration of biogenic and reactive silica in Pearl River estuarine sediments using wet-chemical digestion methods. *Environ. Earth Sci.*, 65:1855–1864.

Rabouille, C., Gaillard, J. F., Tréguer, P., and Vincendeau, M. A. (1997). Biogenic silica recycling in surficial sediments across the Polar Front of the Southern Ocean (Indian Sector). *Deep. Res. II*, 44(5):1151–1176.

Ragueneau, O., Chauvaud, L., Leynaert, A., Thouzeau, G., Paulet, Y. M., Bonnet, S., Lorrain, A., Grall, J., Corvaisier, R., Le Hir, M., Jean, F., and Clavier, J. (2002). Direct evidence of a biologically active coastal silicate pump: Ecological implications. *Limnol. Oceanogr.*, 47(6):1849–1854.

Ragueneau, O., Gallinari, M., Corrin, L., Grandel, S., Hall, P., Hauvespre, A., Lampitt, R. S., Rickert, D., Stahl, H., Tengberg, A., and Witbaard, R. (2001). The benthic silica cycle in the Northeast Atlantic: Annual mass balance, seasonality, and importance of non-steady-state processes for the early diagenesis of biogenic opal in deep-sea sediments. *Prog. Oceanogr.*, 50(1-4):171–200.

Ragueneau, O., Regaudie-de Gioux, A., Moriceau, B., Gallinari, M., Vangriesheim, A., Baurand, F., and Khripounoff, A. (2009). A benthic Si mass balance on the Congo margin: Origin of the 4000 m DSi anomaly and implications for the transfer of Si from land to ocean. *Deep. Res. II*, 56(23):2197–2207.

Ragueneau, O., Savoye, N., Del Amo, Y., Cotten, J., Tardiveau, B., and Leynaert, A. (2005). A new method for the measurement of biogenic silica in suspended matter of coastal waters: Using Si:Al ratios to correct for the mineral interference. *Cont. Shelf Res.*, 25:5–6.

Ragueneau, O. and Tréguer, P. (1994). Determination of biogenic silica in coastal waters: applicability and limits of the alkaline digestion method. *Mar. Chem.*, 45(1-2):43–51.

Ragueneau, O., Tréguer, P., Leynaert, A., Anderson, R. F., Brzezinski, M. A., DeMaster, D. J., Dugdale, R. C., Dymond, J., Fischer, G., François, R., Heinze, C., Maier-Reimer, E., Martin-Jézéquel, V., Nelson, D. M., and Quéguiner, B. (2000). A review of the Si cycle in the modern ocean: Recent progress and missing gaps in the application of biogenic opal as a paleoproductivity proxy. *Glob. Planet. Change*, 26(4):317–365.

Rahman, S., Aller, R. C., and Cochran, J. K. (2016). Cosmogenic 32Si as a tracer of biogenic silica burial and diagenesis: Major deltaic sinks in the silica cycle. *Geophys. Res. Lett.*, 43(13):7124–7132.

Rahman, S., Aller, R. C., and Cochran, J. K. (2017). The Missing Silica Sink: Revisiting the Marine Sedimentary Si Cycle Using Cosmogenic 32Si. *Global Biogeochem. Cycles*, 31(10):1559–1578.

Rahn, K. A. (1976). Silicon and aluminum in atmospheric aerosols: Crust-air fractionation? *Atmos. Environ.*, 10:597–601.

Raiswell, R., Newton, R., Bottrell, S. H., Coburn, P. M., Briggs, D. E., Bond, D. P., and Poulton, S. W. (2008). Turbidite depositional influences on the diagenesis of Beecher's Trilobite Bed and the Hunsrück Slate; sites of soft tissue pyritization. *Am. J. Sci.*, 308(2):105–129.

Rebreanu, L., Vanderborght, J. P., and Chou, L. (2008). The diffusion coefficient of dissolved silica revisited. *Mar. Chem.*, 112:230–233.

Regnier, P., Jourabchi, P., and Slomp, C. P. (2003). Reactive-transport modeling as a technique for understanding coupled biogeochemical processes in surface and subsurface environments. *Neth. J. Geosci.*, 82(1):5–18.

Regnier, P., O'Kane, J., Steefel, C., and Vanderborght, J. (2002). Modeling complex multi-component reactive-transport systems: towards a simulation environment based on the concept of a Knowledge Base. *Appl. Math. Model.*, 26(9):913–927.

Reigstad, M., Carroll, J. L., Slagstad, D., Ellingsen, I., and Wassmann, P. (2011). Intra-regional comparison of productivity, carbon flux and ecosystem composition within the northern Barents Sea. *Prog. Oceanogr.*, 90(1):33–46.

Reigstad, M., Wassmann, P., Wexels Riser, C., Øygarden, S., and Rey, F. (2002). Vari-

ations in hydrography, nutrients and chlorophyll a in the marginal ice-zone and the central Barents Sea. *J. Mar. Syst.*, 38:9–29.

Reigstad, M., Wexels Riser, C., Wassmann, P., and Ratkova, T. (2008). Vertical export of particulate organic carbon: Attenuation, composition and loss rates in the northern Barents Sea. *Deep. Res. II*, 55(20-21):2308–2319.

Ren, H., Brunelle, B. G., Sigman, D. M., and Robinson, R. S. (2013). Diagenetic aluminum uptake into diatom frustules and the preservation of diatom-bound organic nitrogen. *Mar. Chem.*, 155:92–101.

Renaud, P. E., Carroll, M. L., and Ambrose, W. G. (2008a). Effect of Global Warming on Arctic Sea-Floor Communities and its Consequences for Higher Trophic Levels. In Duarte, C., editor, *Impacts of Global Warming on Polar Ecosystems*, chapter 5, pages 139–179. Bilbao.

Renaud, P. E., Morata, N., Carroll, M. L., Denisenko, S. G., and Reigstad, M. (2008b). Pelagic-benthic coupling in the western Barents Sea: Processes and time scales. *Deep. Res. II*, 55(20-21):2372–2380.

Rey, F. (2012). Declining silicate concentrations in the Norwegian and Barents Seas. *ICES J. Mar. Sci.*, 69(2):208–212.

Rey, F., Skjoldal, H., and Slagstad, D. (1987). Primary production in relation to climatic changes in the Barents Sea. In Loeng, H., editor, *The effect of oceanographic conditions on distribution and population dynamics of commercial fish stocks in the Barents Sea : proceedings of the third Soviet-Norwegian Symposium, Murmansk*, pages 29–46. Institute of Marine Research, Bergen, Murmansk.

Reynolds, B. C., Aggarwal, J., André, L., Baxter, D., Beucher, C., Brzezinski, M. A., Engström, E., Georg, R. B., Land, M., Leng, M. J., Opfergelt, S., Rodushkin, I., Sloane, H. J., Van Den Boorn, S. H., Vroon, P. Z., and Cardinal, D. (2007). An inter-laboratory comparison of Si isotope reference materials. *J. Anal. At. Spectrom.*, 22(5):561–568.

Reynolds, B. C., Frank, M., and Halliday, A. N. (2006). Silicon isotope fractionation during nutrient utilization in the North Pacific. *Earth Planet. Sci. Lett.*, 244:431–443.

Rickert, D. (2000). *Dissolution kinetics of biogenic silica in marine environments*. PhD thesis, Christian-Albrecht University of Kiel.

Rickert, D., Schlüter, M., and Wallmann, K. (2002). Dissolution kinetics of biogenic silica from the water column to the sediments. *Geochim. Cosmochim. Acta*, 66(3):439–455.

Rimstidt, J. D. and Barnes, H. L. (1980). The kinetics of silica-water reactions. *Geochim. Cosmochim. Acta*, 44:1683–1699.

Riser, C. W., Reigstad, M., Wassmann, P., Arashkevich, E., and Falk-Petersen, S. (2007). Export or retention? Copepod abundance, faecal pellet production and vertical flux in the marginal ice zone through snap shots from the northern Barents Sea. *Polar Biol.*, 30:719–730.

Roden, E. E. and Wetzel, R. G. (1996). Organic carbon oxidation and suppression of

methane production by microbial Fe(III) oxide reduction in vegetated and unvegetated freshwater wetland sediments. *Limnol. Oceanogr.*, 41(8):1733–1748.

Romero, N., Silverberg, N., Roy, S., and Lovejoy, C. (2000). Sediment trap observations from the Gulf of St. Lawrence and the continental margin of eastern Canada. *Deep. Res. II*, 47(3-4):545–583.

Rosén, P., Vogel, H., Cunningham, L., Reuss, N., Conley, D. J., and Persson, P. (2010). Fourier transform infrared spectroscopy, a new method for rapid determination of total organic and inorganic carbon and biogenic silica concentration in lake sediments. *J. Paleolimnol.*, 43:247–259.

Rude, P. D. and Aller, R. C. (1994). Fluorine uptake by Amazon continental shelf sediment and its impact on the global fluorine cycle. *Cont. Shelf Res.*, 14:883–907.

Rudels, B., Jones, E. P., Anderson, L. G., and Kattner, G. (1994). On the Intermediate Depth Waters of the Arctic Ocean. In Johannessen, O. M., Muench, R. D., and Overland, J. E., editors, *The Polar Oceans and their role in shaping the global environment*, pages 33–46. American Geophysical Union, Washington.

Ryg, M. and Øritsland, N. A. (1991). Estimates of energy expenditure and energy consumption of ringed seals (Phoca hispida) throughout the year. *Polar Res.*, 10(2):595–602.

Rynearson, T. A., Richardson, K., Lampitt, R. S., Sieracki, M. E., Poulton, A. J., Lyngsgaard, M. M., and Perry, M. J. (2013). Major contribution of diatom resting spores to vertical flux in the sub-polar North Atlantic. *Deep. Res. I*, 82:60–71.

Rysgaard, S., Thamdrup, B., Risgaard-Petersen, N., Fossing, H., Berg, P., Christensen, P. B., and Dalsgaard, T. (1998). Seasonal carbon and nutrient mineralization in a high-Arctic coastal marine sediment, Young Sound, Northeast Greenland. *Mar. Ecol. Prog. Ser.*, 175:261–276.

Sakshaug, E. (1997). Biomass and productivity distributions and their variability in the Barents Sea. *ICES J. Mar. Sci.*, 54(3):341–350.

Sakshaug, E., Bjørge, A., Gulliksen, B., Loeng, H., and Mehlum, F. (1994). Structure, biomass distribution, and energetics of the pelagic ecosystem in the Barents Sea: A synopsis. *Polar Biol.*, 14(6):405–411.

Sakshaug, E., Johnsen, G., Kristiansen, S., von Quillfeldt, C., Rey, F., Slagstad, D., and Thingstad, F. (2009). Phytoplankton and primary production. In Sakshaug, E., Johnsen, G., and Kovacs, K., editors, *Ecosystem Barents Sea*, chapter 7, pages 167–209. Tapir Academic Press, Trondheim.

Sakshaug, E., Rey, F., and Slagstad, D. (1995). Wind forcing of marine primary production in the northern atmospheric low-pressure belt. In Skjodal, H., Hopkins, C., Erikstad, K., and Leinaas, H., editors, *Ecology of Fjords and Coastal Waters*, pages 15–25. Elsevier.

Sañé, E., Isla, E., Bárcena, M. Á., and DeMaster, D. J. (2013). A Shift in the Biogenic Silica of Sediment in the Larsen B Continental Shelf, Off the Eastern Antarctic Peninsula,

Resulting from Climate Change. *PLoS ONE*, 8(1).

Sarmiento, J. L. and Gruber, N. (2006). *Ocean Biogeochemical Dynamics Sarmiento*. Princeton University Press, Princeton, NJ.

Savage, P. S., Georg, R. B., Armytage, R. M., Williams, H. M., and Halliday, A. N. (2010). Silicon isotope homogeneity in the mantle. *Earth Planet. Sci. Lett.*, 295:139–146.

Savage, P. S., Georg, R. B., Williams, H. M., Turner, S., Halliday, A. N., and Chappell, B. W. (2012). The silicon isotope composition of granites. *Geochim. Cosmochim. Acta*, 92:184–202.

Sayles, F. L., Deuser, W. G., Goudreau, J. E., Dickinson, W. H., Jickells, T. D., and King, P. (1996). The benthic cycle of biogenic opal at the Bermuda Atlantic Time Series site. *Deep. Res. I*, 43(4):383–409.

Sayles, F. L., Martin, W. R., Chase, Z., and Anderson, R. F. (2001). Benthic remineralization and burial of biogenic SiO2, CaCO3, organic carbon, and detrital material in the Southern Ocean along a transect at 170° West. *Deep. Res. II*, 48(19-20):4323–4383.

Sayles, F. L., Martin, W. R., and Deuser, W. G. (1994). Response of benthic oxygen demand to particulate organic carbon supply in the deep sea near Bermuda. *Nature*, 371:686–689.

Schink, D. R., Guinasso, N. L., and Fanning, K. A. (1975). Processes affecting the concentration of silica at the sediment-water interface of the Atlantic Ocean. *J. Geophys. Res.*, 80(21):3013–3031.

Schlüter, M. and Sauter, E. (2000). Biogenic silica cycle in surface sediments of the Greenland Sea. *J. Mar. Syst.*, 23(4):333–342.

Schoolmeester, T., Gjerdi, H., Crump, J., B, A., Fabres, J., Johnsen, K., Puikkonen, L., Kurvits, T., and Baker, E. (2019). *Global Linkages – A graphic look at the changing Arctic (rev.1).* UN Environment and GRID-Arendal, Nairobi and Arendal.

Schoster, F., Behrends, M., Muller, R., Stein, R., and Washner, M. (2000). Modern river discharge and pathways of supplied material in the Eurasian Arctic Ocean: Evidence from mineral assemblagesand major and minor element distribution. *Int. J. Earth Sci.*, 89:486–495.

Schulz, H. D., Zabel, M., Fütterer, D. K., Breitzke, M., Rullkötter, J., Jørgensen, B. B., Hensen, C., Schulz, H. N., Haese, R. R., Kasten, S., Schneider, R. R., Bickert, T., Glasby, G. P., Herzig, P. M., Hannington, M. D., Bohrmann, G., and Torres, M. E. (2000). *Marine Geochemistry*. Springer, 1 edition.

Serreze, M. C., Barrett, A. P., Slater, A. G., Steele, M., Zhang, J., and Trenberth, K. E. (2007). The large-scale energy budget of the Arctic. *J. Geophys. Res. Atmos.*, 112(D11).

Shapiro, I., Colony, R., and Vinje, T. (2003). April sea ice extent in the Barents Sea, 1850-2001. *Polar Res.*, 22(1):5–10.

Shevchenko, V. P., Pokrovsky, O. S., Filippov, A. S., Lisitsyn, A. P., Bobrov, V. A., Bogunov, A. Y., Zavernina, N. N., Zolotykh, E. O., Isaeva, A. B., Kokryatskaya, N. M.,

Korobov, V. B., Kravchishina, M. D., Novigatsky, A. N., and Politova, N. V. (2010). On the elemental composition of suspended matter of the Severnaya Dvina River (White Sea region). *Dokl. Earth Sci.*, 430(2):228–234.

Siever, R. (1968). Establishment of equilibrium between clays and sea water. *Earth Planet. Sci. Lett.*, 5:106–110.

Slagstad, D. (1984). A Model of Phytoplankton Production in the Marginal Sea-Ice Zone of the Barents Sea. *Model. Identif. Control*, 5(3):129–140.

Slagstad, D. and Stokke, S. (1994). Simulation of current fields, hydrography, ice cover, and primary production in the northern Barents Sea (English Summary). *Fisken og havet*, 9:1–46.

Smedsrud, L. H., Esau, I., Ingvaldsen, R. B., Eldevik, T., Haugan, P. M., Li, C., Lien, V. S., Olsen, A., Omar, A. M., Risebrobakken, B., Sandø, A. B., Semenov, V. A., and Sorokina, S. A. (2013). The role of the Barents Sea in the Arctic climate system. *Rev. Geophys.*, 51(3):415–449.

Smedsrud, L. H., Ingvaldsen, R., Nilsen, J. E., and Skagseth (2010). Heat in the Barents Sea: Transport, storage, and surface fluxes. *Ocean Sci.*, 6(1):219–234.

Smith, J. N., Ellis, K. M., Naes, K., Dahle, S., and Matishov, D. (1995). Sedimentation and mixing rates of radionuclides in Barents Sea sediments off Novaya Zemlya. *Deep. Res. II*, 42(6):1471–1493.

Smith, W. (2010). Polar Margins. In Liu, K., Atkinson, L., Quinones, R., and McManus, L., editors, *Carbon and Nutrient Fluxes in Continental Margins: A Global Synthesis*, chapter 6, pages 289–331. Springer, Berlin.

Solan, M. (2018). The Changing Arctic Ocean: Cruise Report, RRS James Clark Ross JR17007. Technical report.

Solan, M., Ward, E. R., Wood, C. L., Reed, A. J., Grange, L. J., and Godbold, J. A. (2020). Climate-driven benthic invertebrate activity and biogeochemical functioning across the Barents Sea polar front: Climate driven benthic activity. *Philos. Trans. Royal Soc. A*, 378(2181).

Song, Y. H. and Choi, M. S. (2009). REE geochemistry of fine-grained sediments from major rivers around the Yellow Sea. *Chem. Geol.*, 266(3-4):328–342.

Srithongouthai, S., Sonoyama, Y. I., Tada, K., and Montani, S. (2003). The influence of environmental variability on silicate exchange rates between sediment and water in a shallow-water coastal ecosystem, the Seto Inland Sea, Japan. *Mar. Pollut. Bull.*, 47:10–17.

Stamm, F. M., Méheut, M., Zambardi, T., Chmeleff, J., Schott, J., and Oelkers, E. H. (2020). Extreme silicon isotope fractionation due to Si organic complexation: Implications for silica biomineralization. *Earth Planet. Sci. Lett.*, 541(116287).

Staudigel, H., Yayanos, A., Chastain, R., Davies, G., Verdurmen, E. A., Schiffman, P., Bourcier, R., and De Baar, H. (1998). Biologically mediated dissolution of volcanic glass

in seawater. *Earth Planet. Sci. Lett.*, 164:233–244.

Steinsund, P. I. and Hald, M. (1994). Recent calcium carbonate dissolution in the Barents Sea: Paleoceanographic applications. *Mar. Geol.*, 78(3).

Strickland, J. and Parsons, T. (1972). *A Practical Handbook of Seawater Analysis*, volume 167. Fisheries Research Board of Canada, Ottawa.

Stroeve, J. and Notz, D. (2018). Changing state of Arctic sea ice across all seasons. *Environ. Res. Lett.*, 13(103001).

Sun, X., Mörth, C. M., Porcelli, D., Kutscher, L., Hirst, C., Murphy, M. J., Maximov, T., Petrov, R. E., Humborg, C., Schmitt, M., and Andersson, P. S. (2018). Stable silicon isotopic compositions of the Lena River and its tributaries: Implications for silicon delivery to the Arctic Ocean. *Geochim. Cosmochim. Acta*, 241:120–133.

Sun, X., Olofsson, M., Andersson, P. S., Fry, B., Legrand, C., Humborg, C., and Mörth, C. M. (2014). Effects of growth and dissolution on the fractionation of silicon isotopes by estuarine diatoms. *Geochim. Cosmochim. Acta*, 130:156–166.

Sun, Z., Li, J., Huang, W., Dong, H., Little, C. T., and Li, J. (2015). Generation of hydrothermal Fe-Si oxyhydroxide deposit on the Southwest Indian Ridge and its implication for the origin of ancient banded iron formations. *J. Geophys. Res. Biogeosci.*, 120(1):187–203.

Sutton, J. N., André, L., Cardinal, D., Conley, D. J., de Souza, G. F., Dean, J., Dodd, J., Ehlert, C., Ellwood, M. J., Frings, P. J., Grasse, P., Hendry, K., Leng, M. J., Michalopoulos, P., Panizzo, V. N., and Swann, G. E. (2018). A review of the stable isotope bio-geochemistry of the global silicon cycle and its associated trace elements. *Front. Earth Sci.*, 5(112).

Sutton, J. N., Varela, D. E., Brzezinski, M. A., and Beucher, C. P. (2013). Species-dependent silicon isotope fractionation by marine diatoms. *Geochim. Cosmochim. Acta*, 104:300–309.

Swift, S. (1977). Holocene Rates of Sediment Accumulation in the Panama Basin, Eastern Equatorial Pacific: Pelagic Sedimentation and Lateral Transport. *J. Geol.*, 85(3):301–319.

Syvertsen, E. E. (1991). Ice algae in the Barents Sea: types of assemblages, origin, fate and role in the ice-edge phytoplankton bloom. *Polar Res.*, 10(1):277–288.

Taitel-Goldman, N., Ezersky, V., and Mogilyanski, D. (2009). High-resolution transmission electron microscopy study of Fe-Mn oxides in the hydrothermal sediments of the Red Sea deeps system. *Clays Clay Miner.*, 57(4):465–475.

Takahashi, T., Sutherland, S. C., Wanninkhof, R., Sweeney, C., Feely, R. A., Chipman, D. W., Hales, B., Friederich, G., Chavez, F., Sabine, C., Watson, A., Bakker, D. C., Schuster, U., Metzl, N., Yoshikawa-Inoue, H., Ishii, M., Midorikawa, T., Nojiri, Y., Körtzinger, A., Steinhoff, T., Hoppema, M., Olafsson, J., Arnarson, T. S., Tilbrook, B., Johannessen, T., Olsen, A., Bellerby, R., Wong, C. S., Delille, B., Bates, N. R., and

de Baar, H. J. (2009). Climatological mean and decadal change in surface ocean pCO2, and net sea-air CO2 flux over the global oceans. *Deep. Res. II*, 56(8-10):554–577.

Tamelander, T., Reigstad, M., Hop, H., Carroll, M. L., and Wassmann, P. (2008). Pelagic and sympagic contribution of organic matter to zooplankton and vertical export in the Barents Sea marginal ice zone. *Deep. Res. II*, 55(20-21):2330–2339.

Tamelander, T., Renaud, P. E., Hop, H., Carroll, M. L., Ambrose, W. G., and Hobson, K. A. (2006). Trophic relationships and pelagic-benthic coupling during summer in the Barents Sea Marginal Ice Zone, revealed by stable carbon and nitrogen isotope measurements. *Mar. Ecol. Prog. Ser.*, 310:33–46.

Testa, J. M., Brady, D. C., Di Toro, D. M., Boynton, W. R., Cornwell, J. C., and Kemp, W. M. (2013). Sediment flux modeling: Simulating nitrogen, phosphorus, and silica cycles. *Estuar. Coast. Shelf Sci.*, 131:245–263.

Thamdrup, B. and Canfield, D. E. (1996). Pathways of carbon oxidation in continental margin sediments off central Chile. *Limnol. Oceanogr.*, 41(8):1629–1650.

Thamdrup, B. and Canfield, D. E. (2000). Benthic Respiration in Aquatic Sediments. In *Methods of Ecosystem Science*. Springer.

Thompson, D. W. and Wallace, J. M. (1998). The Arctic oscillation signature in the wintertime geopotential height and temperature fields. *Geophys. Res. Lett.*, 25(9):1297–1300.

Thomsen, L. and Graf, G. (1994). Boundary-Layer Characteristics of the Continental-Margin of the Western Barents Sea. *Oceanol. Acta*, 17(6).

Thomsen, L., Graf, G., Martens, V., and Steen, E. (1994). An instrument for sampling water from the benthic boundary layer. *Cont. Shelf Res.*, 14(7):871–882.

Thullner, M., Dale, A. W., and Regnier, P. (2009). Global-scale quantification of mineralization pathways in marine sediments: A reaction-transport modeling approach. *Geochem. Geophys. Geosystems.*, 10(10).

Timmermans, M. (2016). Sea Surface Temperature. Technical report.

Titov, O. (1995). Seasonal Dynamics of Primary Production in the Barents Sea. In *ICES CM 1995/Mini*, volume 16.

Tobo, Y., Demott, P. J., Hill, T. C., Prenni, A. J., Swoboda-Colberg, N. G., Franc, G. D., and Kreidenweis, S. M. (2014). Organic matter matters for ice nuclei of agricultural soil origin. *Atmos. Chem. Phys.*, 14(7):9705–9728.

Torres-Valdés, S., Tsubouchi, T., Bacon, S., Naveira-Garabato, A. C., Sanders, R., McLaughlin, F. A., Petrie, B., Kattner, G., Azetsu-Scott, K., and Whitledge, T. E. (2013). Export of nutrients from the Arctic Ocean. *J. Geophys. Res. Oceans*, 118(4):1625–1644.

Tréguer, P., Bowler, C., Moriceau, B., Dutkiewicz, S., Gehlen, M., Aumont, O., Bittner, L., Dugdale, R., Finkel, Z., Iudicone, D., Jahn, O., Guidi, L., Lasbleiz, M., Leblanc, K., Levy, M., and Pondaven, P. (2018). Influence of diatom diversity on the ocean biological

carbon pump. *Nat. Geosci.*, 11:27–37.

Tréguer, P., Nelson, D. M., Van Bennekom, A. J., DeMaster, D. J., Leynaert, A., and Quéguiner, B. (1995). The silica balance in the world ocean: A reestimate. *Science*, 268:375–379.

Tréguer, P. J. and De La Rocha, C. L. (2013). The World Ocean Silica Cycle. *Ann. Rev. Marine Sci.*, 5:477–501.

Tréguer, P. J., Sutton, J. N., Brzezinski, M., Charette, M. A., Devries, T., Dutkiewicz, S., Ehlert, C., Hawkings, J., Leynaert, A., Liu, S. M., Monferrer, N. L., López-Acosta, M., Maldonado, M., Rahman, S., Ran, L., and Rouxel, O. (2021). Reviews and syntheses: The biogeochemical cycle of silicon in the modern ocean. *Biogeosciences*, 18:1269–1289.

Trower, E. J. and Fischer, W. W. (2019). Precambrian Si isotope mass balance, weathering, and the significance of the authigenic clay silica sink. *Sediment. Geol.*, 384:1–11.

Turner, J. T. (2015). Zooplankton fecal pellets, marine snow, phytodetritus and the ocean's biological pump. *Prog. Oceanogr.*, 130:205–248.

Tyler, J. J., Leng, M. J., and Sloane, H. J. (2007). The effects of organic removal treatment on the integrity of δ18O measurements from biogenic silica. *J. Paleolimnol.*, 37:491–497.

Tyler, J. J., Leng, M. J., Sloane, H. J., Sachse, D., and Gleixner, G. (2008). Oxygen isotope ratios of sedimentary biogenic silica reflect the European transcontinental climate gradient. *J. Quat. Sci.*, 23(4):341–350.

Van Bennekom, A. J., Buma, A. G., and Nolting, R. F. (1991). Dissolved aluminium in the Weddell-Scotia Confluence and effect of Al on the dissolution kinetics of biogenic silica. *Mar. Chem.*, 35:423–434.

van Bennekom, A. J., Fred Jansen, J. H., van der Gaast, S. J., van Iperen, J. M., and Pieters, J. (1989). Aluminium-rich opal: an intermediate in the preservation of biogenic silica in the Zaire (Congo) deep-sea fan. *Deep. Res. A*, 36(2):173–190.

Van Beusekom, J. E., Van Bennekom, A. J., Tréguer, P., and Morvan, J. (1997). Aluminium and silicic acid in water and sediments of the Enderby and Crozet Basins. *Deep. Res. II*, 44(5):987–1003.

Van Cappellen, P., Dixit, S., and van Beusekom, J. (2002). Biogenic silica dissolution in the oceans: Reconciling experimental and field-based dissolution rates. *Global Biogeochem. Cycles*, 16(4):23–1–23–10.

Van Cappellen, P. and Qiu, L. (1997a). Biogenic silica dissolution in sediments of the Southern Ocean. I. Solubility. *Deep. Res. II*, 44:1109–1128.

Van Cappellen, P. and Qiu, L. (1997b). Biogenic silica dissolution in sediments of the Southern Ocean. II. Kinetics. *Deep. Res. II*, 44(5):1129–1149.

Van Cappellen, P. and Wang, Y. (1996). Cycling of iron and manganese in surface sediments: A general theory for the coupled transport and reaction of carbon, oxygen, nitrogen, sulfur, iron, and manganese. *Am. J. Sci.*, 296:197–243.

Van Den Boorn, S. H., Vroon, P. Z., and Van Bergen, M. J. (2009). Sulfur-induced offsets

in MC-ICP-MS silicon-isotope measurements. *J. Anal. At. Spectrom.*, 24(8):1111–1114.

Vandevivere, P., Welch, S. A., Ullman, W. J., and Kirchman, D. L. (1994). Enhanced dissolution of silicate minerals by bacteria at near-neutral pH. *Microb. Ecol.*, 27(3):241–251.

Vandieken, V., Finke, N., and Jørgensen, B. B. (2006a). Pathways of carbon oxidation in an Arctic fjord sediment (Svalbard) and isolation of psychrophilic and psychrotolerant Fe(III)-reducing bacteria. *Mar. Ecol. Prog. Ser.*, 322:29–41.

Vandieken, V., Nickel, M., and Jørgensen, B. B. (2006b). Carbon mineralization in Arctic sediments northeast of Svalbard: Mn(IV) and Fe(III) reduction as principal anaerobic respiratory pathways. *Mar. Ecol. Prog. Ser.*, 322:15–27.

Varela, D. E., Brzezinski, M. A., Beucher, C. P., Jones, J. L., Giesbrecht, K. E., Lansard, B., and Mucci, A. (2016). Heavy silicon isotopic composition of silicic acid and biogenic silica in Arctic waters over the Beaufort shelf and the Canada Basin. *Global Biogeochem. Cycles*, 30(6):804–824.

Varkouhi, S. and Wells, J. (2020). The relation between temperature and silica benthic exchange rates and implications for near-seabed formation of diagenetic opal. *Results Geophys. Sci.*, 1-4(100002).

Vernet, M., Matrai, P. A., and Andreassen, I. (1998). Synthesis of particulate and extracellular carbon by phytoplankton at the marginal ice zone in the Barents Sea. *J. Geophys. Res.: Oceans*, 103(C1):1023–1037.

Vetrov, A. and Romankevich, E. (2004). The Barents Sea: distribution, sources, variability and burial of organic carbon. In Stein, R. and Macdonald, R., editors, *The Organic Carbon Cycle in the Arctic Ocean*, pages 266–278. Springer, Berlin.

Vieira, L., Achterberg, E., Scholten, J., Beck, A., Liebetrau, V., Mills, M., and Arrigo, K. (2018). Benthic fluxes of trace metals in the Chukchi Sea and their transport into the Arctic Ocean. *Mar. Chem.*, 208:43–55.

Viers, J., Dupré, B., and Gaillardet, J. (2009). Chemical composition of suspended sediments in World Rivers: New insights from a new database. *Sci. Total Environ.*, 407(2):853–868.

Vinje, T. (2001). Anomalies and trends of sea-ice extent and atmospheric circulation in the Nordic Seas during the period 1864-1998. *J. Clim.*, 14(3):255–267.

Vinje, T. and Kvambek, A. (1991). Barents Sea drift ice characteristics. *Polar Res.*, 10(1):59–68.

Viscosi-Shirley, C., Mammone, K., Pisias, N., and Dymond, J. (2003). Clay mineralogy and multi-element chemistry of surface sediments on the Siberian-Arctic shelf: Implications for sediment provenance and grain size sorting. *Cont. Shelf Res.*, 23(11-13):1175–1200.

Vogt, C. and Knies, J. (2009). Sediment pathways in the western Barents Sea inferred from clay mineral assemblages in surface sediments. *Nor. J. Geol.*, 89:41–55.

Vogt, C., Lauterjung, J., and Fischer, R. X. (2002). Investigation of the clay fraction (<2

μm) of the clay minerals society reference clays. *Clays Clay Miner.*, 50(3):388–400.

Volz, J., Riedinger, N., Hardisty, D., and Kasten, S. (2020). Data report: solid-phase major and minor elements and iron and sulfur species in sediments of the Anholt Basin, Baltic Sea collected during IODP Expedition 347. *Proceedings of the Integrated Ocean Drilling Program*, 347.

Vorhies, J. S. and Gaines, R. R. (2009). Microbial dissolution of clay minerals as a source of iron and silica in marine sediments. *Nat. Geosci.*, 2(3):221–225.

Walker, J. C., Hays, P. B., and Kasting, J. F. (1981). A negative feedback mechanism for the long-term stabilization of Earth's surface temperature. *J. Geophys. Res.*, 86(C10):9776–9782.

Wang, C., Zhu, H., Wang, P., Hou, J., Ao, Y., and Fan, X. (2015a). Early diagenetic alterations of biogenic and reactive silica in the surface sediment of the Yangtze Estuary. *Cont. Shelf Res.*, 99:1–11.

Wang, L., Zhang, C., and Shi, X. (2015b). The burial of biogenic silica, organic carbon and organic nitrogen in the sediments of the East China Sea. *J. Ocean Univ. China*, 14(3):464–470.

Wang, W., Wei, H. Z., Jiang, S. Y., Liu, X., Lei, F., Lin, Y. B., and Zhao, Y. (2019). Silicon isotope geochemistry: Fractionation linked to silicon complexations and its geological applications. *Molecules*, 24(7):1415.

Wang, Y. and Van Cappellen, P. (1996). A multicomponent reactive transport model of early diagenesis: Application to redox cycling in coastal marine sediments. *Geochim. Cosmochim. Acta*, 60(16):2993–3014.

Wang, Z., Li, R., Cui, L., Fu, H., Lin, J., and Chen, J. (2018). Characterization and acid-mobilization study for typical iron-bearing clay mineral. *J. Environ. Sci. (China)*, 71:222–232.

Ward, J., Hendry, K., Arndt, S., Faust, J., Freitas, F., Henley, S. F., Krause, J., Maerz, C., Ng, H. C., and Pickering, R. (2022). Stable Silicon Isotopes Uncover a Mineralogical Control on the Benthic Silicon Cycle in the Arctic Barents Sea. *Geochim. Cosmochim. Acta (in press)*.

Wassmann, P. and Olli, K. (2004). Central Barents Sea and Northern Spitsbergen. In Stein, R. and Macdonald, R. W., editors, *The Organic Carbon Cycle in the Arctic Ocean*, pages 112–114. Springer, Berlin.

Wassmann, P., Ratkova, T., Andreassen, I., Vernet, M., Pedersen, G., and Rey, F. (1999). Spring bloom development in the marginal ice zone and the central Barents Sea. *Mar. Ecol.*, 20(3-4):321–346.

Wassmann, P. and Reigstad, M. (2011). Future Arctic Ocean seasonal ice zones and implications for pelagic-benthic coupling. *Oceanography*, 24(3):220–231.

Wassmann, P., Reigstad, M., Haug, T., Rudels, B., Carroll, M. L., Hop, H., Gabrielsen, G. W., Falk-Petersen, S., Denisenko, S. G., Arashkevich, E., Slagstad, D., and Pavlova,

O. (2006a). Food webs and carbon flux in the Barents Sea. *Prog. Oceanogr.*, 71(2-4):232–287.

Wassmann, P., Slagstad, D., and Ellingsen, I. (2010). Primary production and climatic variability in the European sector of the Arctic Ocean prior to 2007: Preliminary results. *Polar Biol.*, 33:1641–1650.

Wassmann, P., Slagstad, D., Riser, C. W., and Reigstad, M. (2006b). Modelling the ecosystem dynamics of the Barents Sea including the marginal ice zone: II. Carbon flux and interannual variability. *J. Mar. Syst.*, 59(1-2):1–24.

Wassmann, P., Vernet, M., Mitchell, B., and Rey, F. (1990). Mass sedimentation of Phaeocystis pouchetii in the Barents Sea. *Mar. Ecol. Prog. Ser.*, 66:183–195.

Wehausen, R. and Brumsack, H. J. (1999). Cyclic variations in the chemical composition of eastern Mediterranean Pliocene sediments: A key for understanding sapropel formation. *Mar. Geol.*, 153(1-4):161–176.

Wehrmann, L. M., Formolo, M. J., Owens, J. D., Raiswell, R., Ferdelman, T. G., Riedinger, N., and Lyons, T. W. (2014). Iron and manganese speciation and cycling in glacially influenced high-latitude fjord sediments (West Spitsbergen, Svalbard): Evidence for a benthic recycling-transport mechanism. *Geochim. Cosmochim. Acta*, 141:628–655.

Welsby, H. J., Hendry, K. R., and Perkins, R. G. (2016). The role of benthic biofilm production in the mediation of silicon cycling in the Severn Estuary, UK. *Estuar. Coast. Shelf Sci.*, 176:124–134.

Wessels, M., Mohaupt, K., Kümmerlin, R., and Lenhard, A. (1999). Reconstructing past eutrophication trends from diatoms and biogenic silica in the sediment and the pelagic zone of Lake Constance, Germany. *J. Paleolimnol.*, 21:171–192.

Westacott, S., Planavsky, N. J., Zhao, M. Y., and Hull, P. M. (2021). Revisiting the sedimentary record of the rise of diatoms. *PNAS*, 118(27).

Wetzel, F., de Souza, G. F., and Reynolds, B. C. (2014). What controls silicon isotope fractionation during dissolution of diatom opal? *Geochim. Cosmochim. Acta*, 131:128–137.

Wickbold, R. (1959). Die Anreicherung sehr kleiner Mengen Kieselsäure durch Ionenaustausch. *Fresenius J. Anal. Chem.*, 171(2):81–87.

Wiedmann, I., Ershova, E., Bluhm, B. A., Nöthig, E. M., Gradinger, R. R., Kosobokova, K., and Boetius, A. (2020). What Feeds the Benthos in the Arctic Basins? Assembling a Carbon Budget for the Deep Arctic Ocean. *Front. Mar. Sci.*, 7(224).

Wiedmann, I., Reigstad, M., Marquardt, M., Vader, A., and Gabrielsen, T. M. (2016). Seasonality of vertical flux and sinking particle characteristics in an ice-free high arctic fjord-Different from subarctic fjords? *J. Mar. Syst.*, 154(B):192–205.

Willey, J. D. (1978). Release and uptake of dissolved silica in seawater by marine sediments. *Mar. Chem.*, 7:53–65.

Wollast, R. (1974). The Silica Problem. In Goldberg, E., editor, *The Sea, Volume 5: The*

Global Coastal Ocean, chapter 11, pages 359–392. Harvard University Press.

Wu, B., Liu, S. M., and Ren, J. L. (2017). Dissolution kinetics of biogenic silica and tentative silicon balance in the Yellow Sea. *Limnol. Oceanogr.*, 62:1512–1525.

Wu, B., Lu, C., and Liu, S. M. (2015). Dynamics of biogenic silica dissolution in Jiaozhou Bay, western Yellow Sea. *Mar. Chem.*, 174:58–66.

Xu, H., Jiang, S., Li, J., Pu, R., Wang, J., Jin, W., Sha, L., and Li, D. (2020). Biogenic silica and organic carbon records in zhoushan coastal sea over the past one hundred years and their environmental indications. *Int. J. Environ. Res. Public Health*, 17(3890).

Xu, Z., Li, T., Li, G., Hedding, D. W., Wang, Y., Gou, L. F., Zhao, L., and Chen, J. (2022). Lithium isotopic composition of soil pore water: Responses to evapotranspiration. *Geology*, 50(2):194–198.

Yang, S. and Christensen, J. H. (2012). Arctic sea ice reduction and European cold winters in CMIP5 climate change experiments. *Geophys. Res. Lett.*, 39(20).

Yang, X., Yang, H., Li, W., and Li, P. (2016). Distribution of biogenic silica in sediments of the Yellow River (upper and middle reaches). *Chem. Eng. Trans.*, 55:361–366.

Young, E. D., Galy, A., and Nagahara, H. (2002). Kinetic and equilibrium mass-dependent isotope fractionation laws in nature and their geochemical and cosmochemical significance. *Geochim. Cosmochim. Acta*, 66(6):1095–1104.

Yuan, H., Cheng, C., Chen, K., and Bao, Z. (2016). Standard-sample bracketing calibration method combined with Mg as an internal standard for silicon isotopic compositions using multi-collector inductively coupled plasma mass spectrometry. *Acta Geochim.*, 35(4):421–427.

Zaborska, A., Carroll, J. L., Papucci, C., Torricelli, L., Carroll, M. L., Walkusz-Miotk, J., and Pempkowiak, J. (2008). Recent sediment accumulation rates for the Western margin of the Barents Sea. *Deep. Res. II*, 55(20-21):2352–2360.

Zeebe, R. E., Ridgwell, A., and Zachos, J. C. (2016). Anthropogenic carbon release rate unprecedented during the past 66 million years. *Nat. Commun.*, 9:325–329.

Zenkevich, L. (1963). *The Biology of the Seas of the USSR*. Interscience Publishers, New York.

Zheng, X. Y., Beard, B. L., Reddy, T. R., Roden, E. E., and Johnson, C. M. (2016). Abiologic silicon isotope fractionation between aqueous Si and Fe(III)-Si gel in simulated Archean seawater: Implications for Si isotope records in Precambrian sedimentary rocks. *Geochim. Cosmochim. Acta*, 187:102–122.

Zhu, C., Liu, Z., Zhang, Y., Wang, C., Scheafer, A., Lu, P., Zhang, G., Georg, R. B., lin Yuan, H., and Rimstidt, J. D. (2016). Measuring silicate mineral dissolution rates using Si isotope doping. *Chem. Geol.*, 445:146–163.

Ziegler, K., Chadwick, O. A., Brzezinski, M. A., and Kelly, E. F. (2005a). Natural variations of δ30Si ratios during progressive basalt weathering, Hawaiian Islands. *Geochim. Cosmochim. Acta*, 69:4597–4610.

Ziegler, K., Chadwick, O. A., White, A. F., and Brzezinski, M. A. (2005b). δ30Si systematics in a granitic saprolite, Puerto Rico. *Geology*, 33:817–820.